PORTUGALIAE PHYSICA

64

PORTUGALIAE
PHYSICA

ELECTRON DENSITY AND SPIN DENSITY STUDIES (*)

P. J. BROWN

Institut Laue-Langevin, Grenoble, France

ABSTRACT — The paper reviews some of the problems encountered in the measurement and interpretation of electron-density measurements. The experimental problems are compared with those encountered in parallel studies of spin density distributions. To illustrate this comparison an outline of the polarized neutron technique for spin density determinations is given. Finally two examples of spin density determinations are described to illustrate the application of the techniques.

1 — INTRODUCTION

The aim of the present paper is to review some of the problems which are currently faced by experimentalists who use X-ray and neutron scattering techniques to study the electron densities in crystalline solids. It will start by reviewing some experimental problems which must now be overcome in studies of charge densities in materials containing elements outside the first two rows of the periodic table. The second part of the paper shows how some of these problems can be alleviated in measurements of spin rather than charge density and outlines the theoretical and experimental basis of spin density measurements using polarized neutrons. In the last section of the paper two examples of recent studies using the polarized neutron technique are presented.

Portgal. Phys. — Vol. 13, fasc. 1-2, pp. 1-22, 1982

1

2 — CHARGE DENSITY MEASUREMENTS

In this discussion of charge density measurements it is assumed that the reader is familiar with the X-ray scattering techniques used in recording diffraction intensities suitable for charge density studies and has some knowledge of the methods used in their analysis. In this section some of the questions currently being debated with regard to such measurements, both of an experimental and a more philosophical nature will be discussed.

2.1 — *Experimental Problems*

2.1.1 — Range of applicability

In almost all cases the purpose of making charge density measurements is to determine in what way the electron density is modified when an assembly of free atoms is brought together to form a crystal. To a first approximation only the valence or outer shells of the atoms are modified in this process, so that only these electrons can be said to be of interest. On the other hand all the elctrons in the crystal contribute to the scattered X-ray intensity so that the fraction of the scattering contributed by the valence electrons goes down as the atomic number of the constituent goes up. Until recently, except in a very few cases, meaningful charge density studies were restricted to compounds of elements in the first two rows of the periodic table. Now, with improved accuracy in the diffraction measurements, studies of crystals containing first period transition metals, or even heavier elements are attempted. It seems unlikely that X-ray diffraction will ever be a very suitable technique to study charge densities of materials in which the electrons of interest comprise less that about 5 % of the total.

2.1.2 — Determination of the Scale Factor

The scale factor in a charge density investigation is an important parameter since it fixes the absolute values of charge density. In many studies the scale factor is left as a variable of

the least squares refinement and this appears to be a valid procedure for crystals containing light atoms in which the temperature parameters have been fixed using neutron diffraction measurements. In such a case the derivation of the scale factor depends on the assumption that the scattering at high angles is correctly given by the sum of the free atoms form factors. Such a procedure may no longer be valid for heavier atoms such as transition metals in which the valence electrons may still give some contribution to the scattering at the limit of measurement.

2.1.3 — Temperature Factors

The classical technique for charge density determination pioneered by Coppens [1] and known as the X-n technique relied on obtaining accurate temperature and thermal parameters from a neutron diffraction study. These were then used as a basis to calculate the X-ray structure factors corresponding to the sum of free atoms. Fourier transformation of their differences from the observed X-ray structure factors then gave the so-called X-n map. An alternative technique is to use the higher angle X-ray data to derive the positional and thermal parameters, and this then leads to an «X-X» map. Each of these techniques has its problems; for example there are sometimes significant differences between the temperature factors derived from neutron and X-ray experiments, this will give rise to important features on the X-n map which are not due to valence electrons. On the other hand temperature factors of light atoms from high angle X-ray data may not be sufficiently precise, and with heavier atoms temperature factors may become correlated with valence electron deformations. These problems become much less acute if the X-ray measurements have been made on an absolute scale.

2.1.4 — Extinction

The recent treatments of extinction by Becker and Coppens [2], [3] and Thornley and Nelmes [4] make it possible to describe the extinction properties of the crystal by a relatively small number of parameters which can be fitted in the least squares

refinement. These extinction models seem to work quite well even in the case of relatively large extinction. They can probably be used with confidence to correct extinction in a charge density study as long as it does not reduce the observed intensities by more than about 20 %. The refined parameters are of very doubtful significance.

2.1.5 — Multiple Scattering

Multiple scattering is closely related to extinction since both involve repeated Bragg scattering. It is unlikely that multiple scattering will pose a severe problem in a crystal for which the extinction is small. The presence of multiple scattering may be revealed by inequivalence of equivalent reflections or the occurrence of significant intensity in space group absences. Where detected it may be possible to avoid it by making measurements at different wavelengths or by rotating about the scattering vector.

2.1.6 — Thermal Diffuse Scattering

The inclusion of significant amounts of thermal diffuse scattering (TDS) in integrated intensity measurements, particularly at high angles is unavoidable. Under favourable circumstances (Cooper and Rouse [5], Rouse and Cooper [6], Cochran [7]) it may only lead to errors in the temperature factors and may be one of the reasons why temperature factors derived from X-ray and neutron diffraction studies do not agree. It should be borne in mind that the amount of TDS included in an integrated intensity measurement depends on the scan width and slit sizes, and is less important in an experimental set-up that gives good resolution at high angles.

2.2 — *Presentation of the Results of Charge Density Studies*

2.2.1 — Fourier Techniques

The most straightforward method of presenting the results of a study of charge density is as a Fourier synthesis, the coefficients

4

in the synthesis being differences between the observed X-ray structure factors and a model based on positional and thermal parameters from neutron (X-n), or high angle X-ray (X-X) data. Such maps, whilst demonstrating in a clear way the spatial features of the valence electron density such as delocalisation along a bond or lone-pair densities, suffer from deficiencies in the experimental data. They are of necessarily limited resolution since the maximum angle for data collection is limited. Even within these limits there may be missing data because of other experimental difficulties. It is therefore not always possible to be sure that some features of these maps are «real» effects and not artefacts of the missing data.

2.2.2 — The Multipole Expansion

As an alternative to expanding the electron density in its Fourier components is possible to make an expansion in spherical harmonic components about the atomic centres, each harmonic component having an associated radial density function. Such a procedure was first suggested by Kuorki Suonio [8] who showed how to derive the spherical harmonic components directly from the measured structure factors. His technique being based on a Fourier expansion suffers from the same problems as outlined above. An alternative procedure introduced by Stewart [9], [10] and others is to model the spherical harmonic expansion by a limited number of parameters giving the magnitude of the harmonic components and the shape of their associated radial distributions. These parameters are then determined from the observed structure factors by least squares analysis.

The validity of the multipole expansion method rests on the physically reasonable supposition that the valence electron density is associated with the atomic centres and its wave-functions can be well represented by linear combinations of atomic orbitals. It is this supposition that makes it possible to terminate the expansion after relatively few terms leaving the ratio of observations to parameters favourable for least squares refinement. The advantage of the multipole technique is that it gives an

analytical expression for the charge density involving relatively few parameters. The multipole representation can then be used to expand the charge density itself or to calculate other properties which depend on it. It must however always be borne in mind that the derivation of any property which implies a higher reso- lution than that imposed by the limit of data collection has no experimental justification.

2.2.3 — The «free atom» model

Whether a Fourier or a multipole technique is used the charge density represented is usually the difference between a «free atom» model and the observations. Several different bases for the «free atom» model are used by different groups and it is as well to be sure that the same basis has been used for subtraction before comparing results. The two most frequently used models are the true free atom model in which the sum of the neutral free atom form factors is used and the prepared atom model in which the form factors appropriate to the atom or ion in the state nearest to that expected in the solid is used. To take a simple example: for NaCl the free atom model would use the sum of the neutral sodium and chlorine atoms whereas the prepared atom model would use the form factors for Na^+ and Cl^-. Clearly the difference density, often called the defor- mation density would be completely different in the two cases.

2.2.4 — Fitting the data to a model

Perhaps the most satisfactory method of using the results of a charge density study would be to compare them with a theoretical model which could include a few adjustable parameters to be fitted to the data by least squares. Unfortunately such models are hardly ever available for crystals on which charge density sutdies have been made. There have been some attempts to correlate the parameters obtained in multipole analyses with Mulliken population numbers, but these are of doubtful theoretical validity. It is to be hoped that studies undertaken in the future will cover cases where a fit of theoretical parameters to the experiments is possible.

2.3 — *Objectives of Charge Density Studies*

It has now been clearly demonstrated that it is possible with careful measurements on well chosen materials to measure charge densities with sufficient precision to show effects which are associated with chemical bonding. The question of what use are such charge density maps, may now be asked. The first and most obvious purpose of such studies is to serve as a test for theoretical calculation. For relatively simple molecules, it is now claimed that theoretical wave functions can be calculated to any required degree of accuracy. A proper comparison between theory and experiment is more difficult to obtain mainly because most theoretical calculations pertain to molecules and not to crystals. There are of course many cases where the number of electrons in the molecule is such that self consistent ab-initio calculations would be too costly or time-consuming and recourse is made to more approximate theoretical methods. Here the comparison between theory and experiment can be used to select the most appropriate of several possible approximate methods.

In cases where good theoretical models are not available one may ask whether it is possible to use the results of charge density studies to derive other chemical properties such as electrostatic potentials, dipole and higher moments which can be compared with results obtained using other techniques. Such comparisons usually turn out to be disappointing because of the difficulty of adequately accounting for the very different spatial resolutions associated with the different types of experiment.

The areas where perhaps the most can be expected from the results of charge density measurements are those where theoretical calculations are the most difficult and one may hope that deformation charge densities will help in understanding chemical and physical properties. In many electron systems such as organo metallic compounds or transition metal alloys or compounds there are very few reliable calculations of electron distribution. In the case of metals rather good band structure calculations are sometimes available but as has often been pointed out the spatial properties of the eigenvectors provide a much more rigorous test of the correctness of a theoretical model than

Portgal. Phys. — Vol. 13, fasc. 1-2, pp. 1-22, 1982

7

do the eigenvalues. In these many-electron systems X-ray scattering determinations become difficult for reasons pointed out at the beginning of this section. On the other hand amongst the transition elements exchange correlation becomes important, resulting in significant numbers of unpaired electrons. For these systems magnetic neutron scattering may be used to probe the distribution of these unpaired electrons. In the final sections of this paper a brief account will be given of the polarized neutron technique for determining unpaired electron density with two examples of its use.

3 — MEASUREMENT OF UNPAIRED ELECTRON DENSITY (SPIN DENSITY)

The magnetic interaction between neutron beam and the unpaired electron density in a crystal offers the possibility of studying the spatial distribution of just those unpaired electrons. This technique, complementary to the X-ray scattering studies avoids a number of the experimental problems outlined in Section 2.1.

3.1 — *Experimental Problems*

3.1.1 — Range of application

In most cases magnetic neutron scattering is by electrons with unpaired spins, and these are just those with energies near to the Fermi energy and therefore involved in solid state interactions and chemical bonding. The core electrons are paired and contribute little if anything to the magnetic scattering. Thus magnetic neutron scattering, where applicable, is sensitive to just those electrons which are of interest to the solid state physicist. The technique can therefore be applied to any magnetic material regardless of atomic number. For example, studies of actinide compounds have shed light on the roles played by 5f and 6d electrons in their magnetism and cohesion.

3.1.2 — Scale Factor

The results of magnetic scattering studies are easily placed on an absolute scale by reference to the neutron nuclear scattering which can be measured under exactly the same experimental conditions.

3.1.3 — Temperature Factors

As for the scale factor, the temperature factors can be determined under the same conditions as the magnetic structure factors. There remains some question as to whether the magnetic electrons will undergo the same thermal vibrations as the atomic nuclei. Up to the present time there is little evidence that any inequality in these factors is sufficiently important to falsify the results.

3.1.4 — Extinction

Extinction is equally important in magnetic scattering studies as in X-ray scattering studies. It may often be more acute since in general larger crystals must be used. If the magnetic scattering occurs as a small perturbation of the nuclear scattering then a reliable correction can be made so long as an empirical expression for the observed intensity in terms of the kinematical intensity can be established (Delapalme et al., [11]). When the magnetic scattering is of the same order of magnitude as the nuclear scattering extinction corrections must be made with care; often observations at a number of different wavelengths are required (Bonnet et al. [12]).

3.1.5 — Multiple Scattering

Multiple scattering can falsify magnetic scattering measurements in just the same way as X-ray scattering measurements, and can be avoided in the same ways.

3.1.6 — Thermal Diffuse Scattering

TDS does not present a problem for magnetic scattering measurements using polarized neutrons which do not require integrated intensity measurements.

3.2 — *Magnetic Neutron Scattering an the Polarized Beam Technique*

3.2.1 — The Magnetic Structure Factor and Magnetic Form Factors

The neutron is scattered in a magnetic material because of the interaction between its magnetic moment and magnetic fields in the material. In just the same way as for X-ray scattering one can define a magnetic structure factor

$$\mathbf{M}\ (\mathbf{k}) = \int_{\text{cell}} \mathbf{M}\ (\mathbf{r})\ e^{i\mathbf{k}.\mathbf{r}}\ d\mathbf{r} \tag{1}$$

where $\mathbf{M}\ (\mathbf{r})$ is the intensity of magnetization or magnetization density in the material. The principal difference from the X-ray or nuclear structure factor is that $\mathbf{M}\ (\mathbf{k})$ being the Fourier transform of a vector is itself a vector. The intensity of scattered neutrons is not directly related to the magnetic structure factor but to its projection on the plane perpendicular to the scattering plane. The generalised magnetic interaction vector is then given by

$$\mathbf{M}_{\perp}(\mathbf{k}) = \hat{\mathbf{k}} \times \mathbf{M}\ (\mathbf{k}) \times \hat{\mathbf{k}} \tag{2}$$

and the cross-section for magnetic elastic scattering of unpolarized neutrons

$$\left(\frac{d\sigma}{d\omega}\right)_{\text{magn. el.}} = |\mathbf{M}_{\perp}\ (\mathbf{k})|^{2} \tag{3}$$

10

Portgal. Phys. — Vol. 13, fasc. 1-2, pp. 1-22, 1982

If the magnetization density can be divided amongst well defined atoms or ions then one can define a magnetic form factor for each atom

$$f(k) = \left(\int m(r) \, e^{ik.r} \, dr \right) / \left(\int m(r) \, dr \right) \qquad (4)$$

where $m(r)$ is the magnetization density associated with the atom. The magnetic structure factor can be written easily in terms of from factors as

$$M(k) = \sum_n f_n(k) \, M_n \, e^{ik.r_n} \qquad (5)$$

Here $f_n(k)$ is the form factor for the nth atom at a distance r_n from the origin and M_n is the magnetic moment on this atom. The sum is over all atoms in the unit cell.

When the magnetization is due to electrons in a single unfilled shell one may write the form factor as

$$f(k) = \sum_l A_l(k) <J_l(|k|)> \qquad (6)$$

where

$$<J_l(|k|)> = \int_0^\infty U^2(r) \, J_l(kr) \, dr \qquad (7)$$

Here $J_l(kr)$ is the spherical Bessel function of order l and $U^2(r)$ the radial distribution function of electrons in the open shell. The coefficients $A_l(k)$ depend both on the direction of the scattering vector k and on the magnetic configuration. For a spherically symmetric spin-only ion such as the Mn^{2+} $3d^5$ configuration only A_0 is finite. For the general spin-only case with d electrons A_0, A_2 and A_4 can be non-zero. The situatiton is more complicated when some orbital moment is present. The orbital magnetization density at a point is not due to the electrons at that point but to all electrons contributing to current loops closing around the point. An approximation to the spherical form factor valid for small k when orbital moment is present is given by the dipole approximation (Marshall and Lovesey [13]) as

$$f(k) = 2S<J_0(k)> + L(<J_0(k)> + <J_2(k)>) \qquad (8)$$

where S and L represent the spin and orbital angular momenta of the ion. Fig. 1 shows the k dependence of the three integrals $< J_0 >$, $< J_2 >$ and $< J_4 >$ for the Mn^{2+} ion. Also shown for comparison is the total charge X-ray form factor.
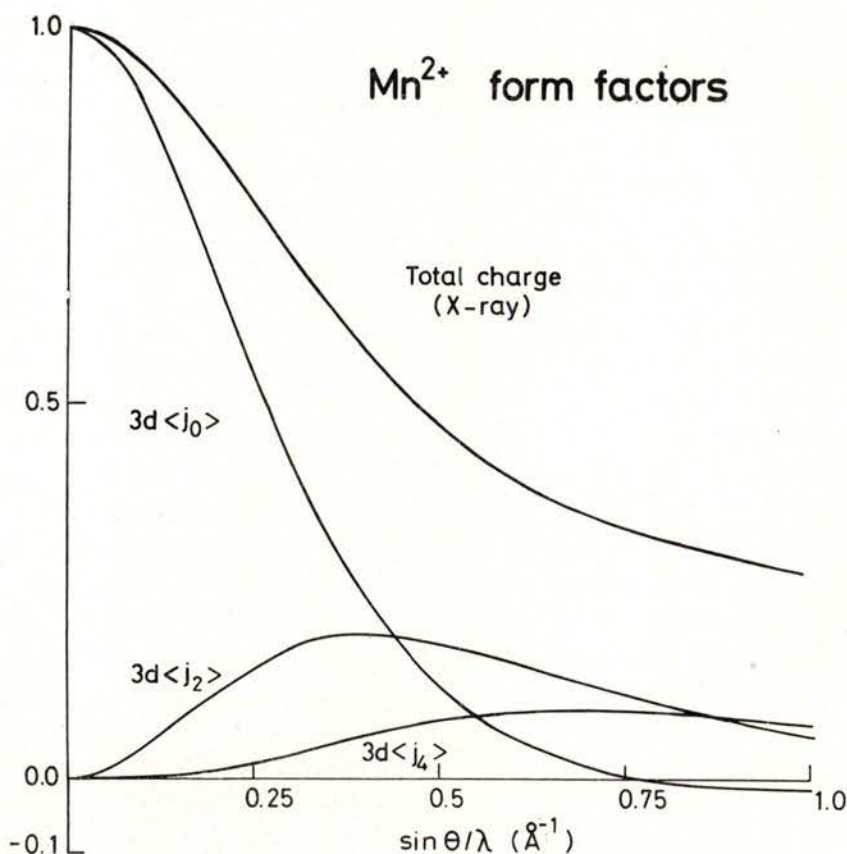

Fig. 1 — The total charge and 3d form factors for the Mn^{2+} ion.

3.2.2 — Scattering of Polarized Neutrons

The cross-section for scattering of polarized neutrons is the sum of two terms, one corresponding to scattering without change

of spin state and the other («spin-flip» cross-section) comprises neutrons whose spin was changed by the scattering.

$$\frac{d\sigma}{d\omega}(\uparrow\uparrow) \propto |N(k) + \hat{u} \cdot M_{\perp}(k)|^2 \tag{9}$$

$$\frac{d\sigma}{d\omega}(\uparrow\downarrow) \propto |\hat{u} \times M_{\perp}(k)|^2 \tag{10}$$

Here $N(k)$ is the neutron-nuclear structure factor and $\hat{u}$ a unit vector parallel to the neutron polarization. The non-spin flip cross-section is polarization dependent if there is interference between nuclear and magnetic scattering. The flipping ratio which is the ratio between the cross-sections for two opposite neutron spins is

$$R = \frac{|N(k)|^2 + |M_{\perp}(k)|^2 + N^*(k)\,\hat{u}\cdot M_{\perp}(k) + N(k)\,\hat{u}\;M^*_{\perp}(k)}{|N(k)|^2 + |M_{\perp}(k)|^2 - N^*(k)\,\hat{u}\cdot M_{\perp}(k) - N(k)\,\hat{u}\cdot M^*_{\perp}(k)} \tag{11}$$

and it is this flipping ratio which is measured in most polarized neutron experiments.

An instrument for making polarized neutron measurements is shown in Fig. 2. A monochromatic polarized beam is produced
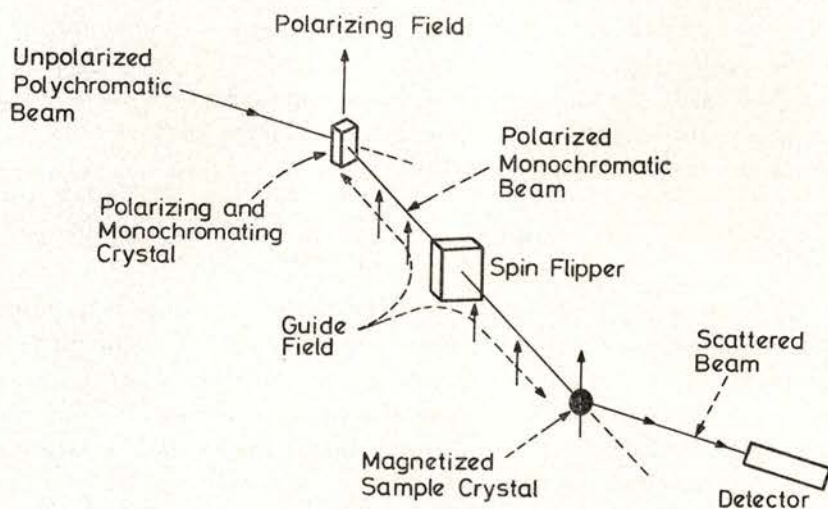

Fig. 2 — Schematic representation of a polarized neutron diffractometer.

Portgal. Phys. — Vol. 13, fasc. 1-2, pp. 1-22, 1982

13

by a crystal which has zero cross-section for one spin state. The polarization is retained between polarizer and specimen by magnetic guide fields. At some point in this path a «spin-flipper» is introduced whose function is to reverse the polarization when it is «on» and to leave it unchanged when it is «off». In an experiment the diffractometer and sample are set so that the peak of a Bragg reflection enters the counter and the ratio between the counting rates for the two neutron spin states is determined.

In the simple case that both $N(k)$ and $M(k)$ are real (centrosymmetric structures) and the polarization is parallel to the magnetization and perpendicular to k the flipping ratio R becomes

$$R = \frac{N(k)^2 + M(k)^2 + 2\ N(k)\ M(k)}{N(k)^2 + M(k)^2 - 2\ N(k)\ M(k)} = \left(\frac{1+\gamma}{1-\gamma}\right)^2 \qquad (12)$$

where $\gamma = M(k) / N(k)$.

In general R can only differ from unity if there is magnetic and nuclear scattering in the same reflection. This condition is satisfied if any part of the magnetization has the same periodicity as the nuclear structure as is the case in a ferromagnet or in a paramagnet in an applied field. It is not satisfied by antiferromagnetic structures in which the magnetic cell is some multiple of the nuclear one.

The ratio γ is obtained from the flipping ratio R by solving the quadratic equation (12). The result assuming perfect polarization and complete spin reversal is

$$\gamma = (R + 1 \pm \sqrt{4R}) / (R - 1) \qquad (13)$$

The choice of root depends on whether the absolute magnitude of the magnetic scattering is greater or less than that of the nuclear scattering. There is no uncertainty in the sign of γ which shows that the polarized neutron technique determines the sign of the magnetic scattering with respect to that of the nuclear scattering in centrosymmetric structures.

One of the major advantages of the polarized neutron technique is that integrated intensities are not needed — it is just the

ratio between peak counting ratios for the two spin states that is measured and this ratio can be obtained with high accuracy. In most cases magnetic neutron scattering is much weaker than nuclear scattering and $|\gamma|$ is significantly less than one. For small γ (13) can be simplified to

$$R = 1 + 4\gamma \qquad (14)$$

The sensitivity of the polarized neutron technique is demonstrated by comparing (14) with the fraction of the integrated intensity due to magnetic scattering

$$\Delta I / I = 1 + \gamma^2 \qquad (15)$$

The technique can be used to measure extremely small γ since down to 0.1 % accuracy or better there is little except the counting statistics to limit the accuracy with which R can be measured. Measurements of very small γ values do however require long counting times and high incident intensity. To give some idea of the orders of magnitude involved the counting rate at a high flux reactor from a strong reflection of a simple crystal will probably not much exceed 10^4 cps, which implies measurement times from a few minutes to several days.

To illustrate the use of the technique the last two sections of this paper will be used to describe two recent studies carried out at the Institute Laue-Langevin, one showing the measurement of a very small magnetic moment in a paramagnetic metal (Rhadhakrishna and Brown [14]) and the other demonstrating how covalent bonding affects the magnetic form factor in an ionic compound (Brown, Ziebeck and Radhakrishna [15]).

4 — THE PARAMAGNETIC FORM FACTOR OF TECHNETIUM

Technetium, which is the 4d analogue of manganese in the 3d and rhenium in the 5d transition series, does not occur naturally. It can be obtained as the radioactive isotope ^{99}Tc, a soft β-emitter with a half life of 5×10^5 years. Technetium is a hexagonal close-packed metal, it has a paramagnetic susceptibility which remains essentially constant at 10^{-6} emu/g over the temperature

Portgal. Phys. — Vol. 13, fasc. 1-2, pp. 1-22, 1982

15

range 80-1400 K. The form factor of technetium is of interest because of the rather strange from factors found for other hexagonal close-packed metals (Moon et al. [16]) such as scandium, yttrium and titanium which indicate considerable delocalisation of the magnetic electrons.

An applied field of 4.8 T induces an aligned moment of 0.94 ± 10^3 μ_B per atom of technetium and the expected γ value at the lowest angle reflection is aout 2×10^{-4} showing that measurement of the paramagnetic magnetization density is at the lower limit of possibility. However, large single crystals of technetium have been grown by Kostorz and Michailovitch [17] and two were lent to us by the Oak Ridge National Laboratory. These crystals gave counting rates greater than 10^5/s and the rate used was limited by the detector dead time. In about 28 days measuring time we were able to determine the flipping ratios of the eight lowest angle reflections with an accuracy of around one part in 10^4. At this level of precision in flipping ratio measurements account must be taken of small systematic errors implicit in the measurement technique. Moon et al. [18] discuss some of these errors which are most troublesome if the crystal rocking curve is narrow or the crystal slightly mis-set. In the case of technetium the rocking curves were quite broad (0.25° f. whm) and an on-line maximisation option in the diffractometer control package was used to ensure that the crystal was set to the centre of the reflection for each measurement. The precision of the flipping ratios was estimated from the degree of reproducibility between repeated measurements of all available equivalent reflections; in no case was the reproducibility found to be significantly different from that expected from the counting statistics.

Several different physical effects must be taken into account before the paramagnetic structure factors can be obtained from the flipping ratios, the most important of these are extinction, diamagnetism and Schwinger scattering. To determine the degree of extinction a separate experiment was carried out using unpolarized neutrons. The integrated intensities of reflections were measured at three different wavelengths in zero field; the results showed the effect of extinction on the flipping ratios to be negligible. Calculation of the diamagnetic scattering and Schwinger scattering showed them to be of the same order of magnitude

as the experimental errors. Once corrected for these effects the resultant magnetic structure amplitudes are the Fourier components of the paramagnetic magnetization density. They are converted to points on the paramagnetic form factor by dividing by the geomet-
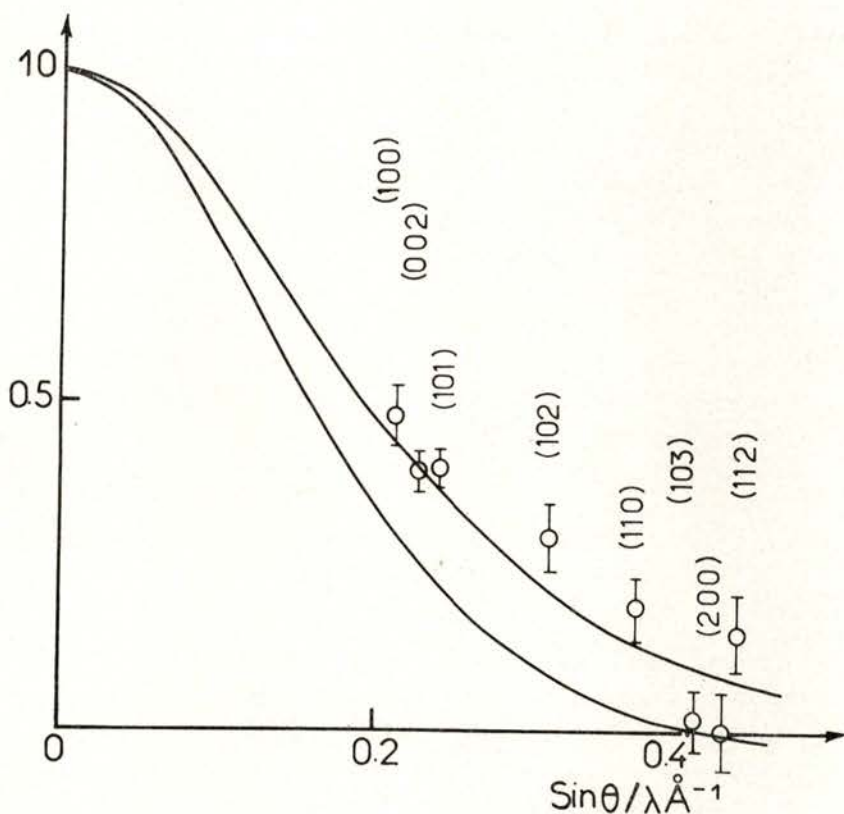

Fig. 3 — The paramagnetic form factor of technetium. The experimental points with their estimated errors are shown. The lower full curve corresponds to the spin-only form factor for Tc 4d electrons. The upper full curve is the form factor in the dipole approximation with 70 % orbital moment.

ric structure factors and the value of the bulk magnetization per cell. The bulk magnetization must also be corrected for the dia-magnetic moment. The results are shown in Fig. 3; they fall on a

reasonably smooth curve unlike those for scandium, yttrium and titanium. This confirms that the behaviour of these latter elements is due to their early positions in the transition series rather than to their hexagonal structures. The experimental points lie well above the lower full curve of figure 3 which represents the spin-only form factor for Tc 4d electrons. This is not unexpected since a temperature independent susceptibility may have a large Van-Vleck orbital component. The experimental data have been fitted to a Tc 4d form factor in the dipole approximation (equation (8)) allowing the ratio of spin to orbital moment to vary. The result suggests that 70 % of the moment is orbital, and the resultant form factor is shown in the upper solid curve of figure 3. This model gives a reasonably good account of the experimental data; further refinement must await a good calculation of the technetium band structure. This study of technetium is an example of the measurement of a very small magnetization in a very simple structure. The results will provide a stringent test of any band structure calculation.

5 — COVALENT EFFECTS IN THE MAGNETIZATION DENSITIES OF $CrCl_3$ AND $CrBr_3$

Magnetization measurements on chromium tri-bromide and chromium tri-chloride show that at 4.2 K fields of some 0.3 T are sufficient to produce essentially parallel alignment of all the chromium moments. Under these conditions the polarized neutron scattering technique can be used to study their magnetization density distributions. Both $CrCl_3$ and $CrBr_3$ have the rhombhedral $FeCl_3$ structure at low temperatures, the chromium ions are octahedrally co-ordinated by halide ligands and the octahedra share three of their twelve edges to form sheets which lie perpendicular to the triad axis. Single crystals of both compounds were grown for us at the M. P. I. Stuttgart. They were mounted with a $< 01.0>$ axis parallel to the diffractometer ω axis which is the magnetization and polarization direction. The flipping ratios of all reflections in the zero, first and second layers were measured at 4.2 K in an applied field of 1.4 T. The $\sin\theta/\lambda$ limit was 0.5 for $CrCl_3$ and 0.75 for

$CrBr_3$. Integrated intensities measured in a separate experiment with unpolarized neutrons were used to determine the structural parameters and temperature factors at 4.2 K.

Magnetic structure factors were obtained from the observed flipping ratios using the structural parameters at 4.2 K to give the nuclear structure factors. The magnetic structure factors can be displayed as a form factor by dividing through by the chromium geometric structure factors. The form factors so obtained were compared with a theoretical Cr^{3+} free ion 3d form factor. In both compounds the experimental curve drops much more sharply at low angles but the outer parts of both experimental and theoretical curves have rather closely the same shape. In $CrBr_3$ where the measurements extend to $\sin\theta/\lambda = 0.75$ experimental and theoretical curves drop to zero at about the same angle.

The difference in shape between the experimental and theoretical free ion form factors is not unexpected since covalency in these compounds should be significant. For a ferromagnetically aligned material the delocalisation associated with transferred spin should lead to a narrower form factor. To quantify this effect the magnitude of the 3d-like part of the scatterring has been estimated by fitting the moment value of a Cr^{3+} spherical 3d form factor to those data with $\sin\theta/\lambda > 0.25$. Reasonable fits were obtained with $\mu_{3d} = 2.46(4)$ for $CrBr_3$ and $2.24(6)$ for $CrCl_3$. Magnetization and resonance measurements on chromic salts suggest that the 3d electrons in $CrCl_3$ and $CrBr_3$ should be described by the orbital singlet $^4\Gamma_2$ obtained as ground state from a ^4F term under an octahedral field. The scattering from this state is not isotropic and the calculated anisotropy of its form factor reproduces rather well the anisotropy of the observations as may be seen from Fig. 4. In a simple model including covalent effects, the magnetization density can be split into a 3d part, a ligand part and an overlap part, this latter being negative for antibonding orbitals. Hence the magnetisation density may be written

$$\rho(r) = N(\rho_{3d}(r) + A^2 \rho_{ligand}(r) - A \rho_{overlap}(r))$$

N is a normalising constant obtained by integrating the density over a unit cell so that $N = (1 + 3A^2 - 3AS)^{-1}$ where S is the

Portgal. Phys. — Vol. 13, fasc. 1-2, pp. 1-22, 1982

19

value of the overlap integral. Since the observed 3d moment is reduced in $CrCl_3$ and $CrBr_3$, N must be less than unity and hence $A > S$. A lower limit of $A^2 > 0.04$ is given if S is very small. A preliminary investigation of the delocalised moment has
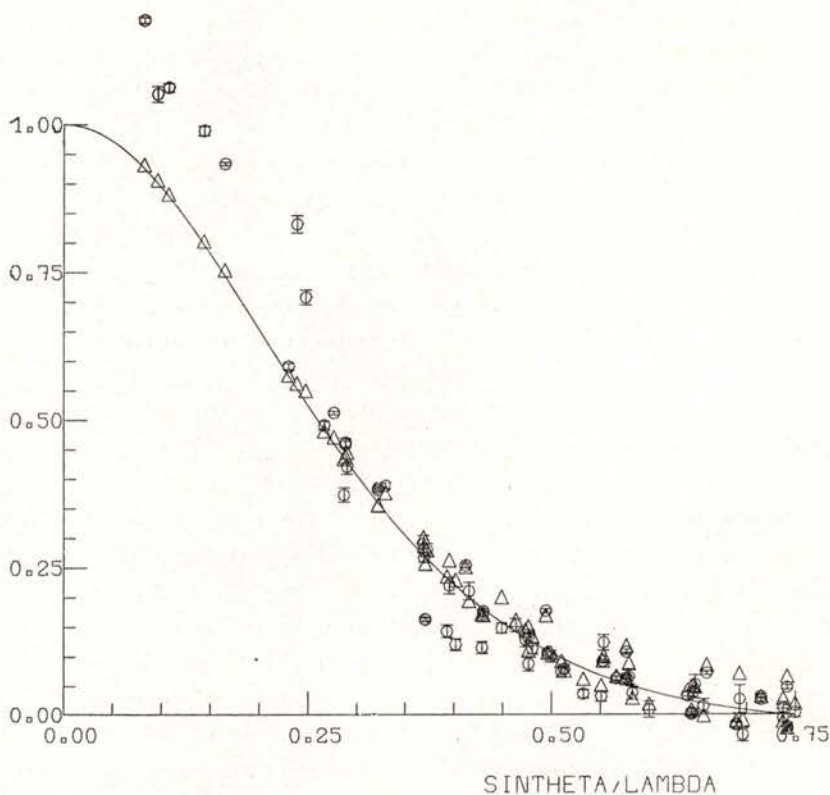

Fig. 4 — The form factor derived from h0l reflections in $CrBr_3$: circles mark observed values with their error bars and the triangles correspond to the calculation for Cr^{3+} $^4\Gamma_2$. The full curve is the spherical 3d form factor for a Cr^{3+} free ion.

been made using Fourier techniques. These give some evidence for magnetic density transferred towards ligand sites but the most significant feature of the maps is an accumulation of density

between near neighbour chromium ions within the chromium layer as can be seen in Fig. 5. This density demonstrates the importance of the shared edges of the octahedron of halide ions in the description of covalent interactions in these compounds.
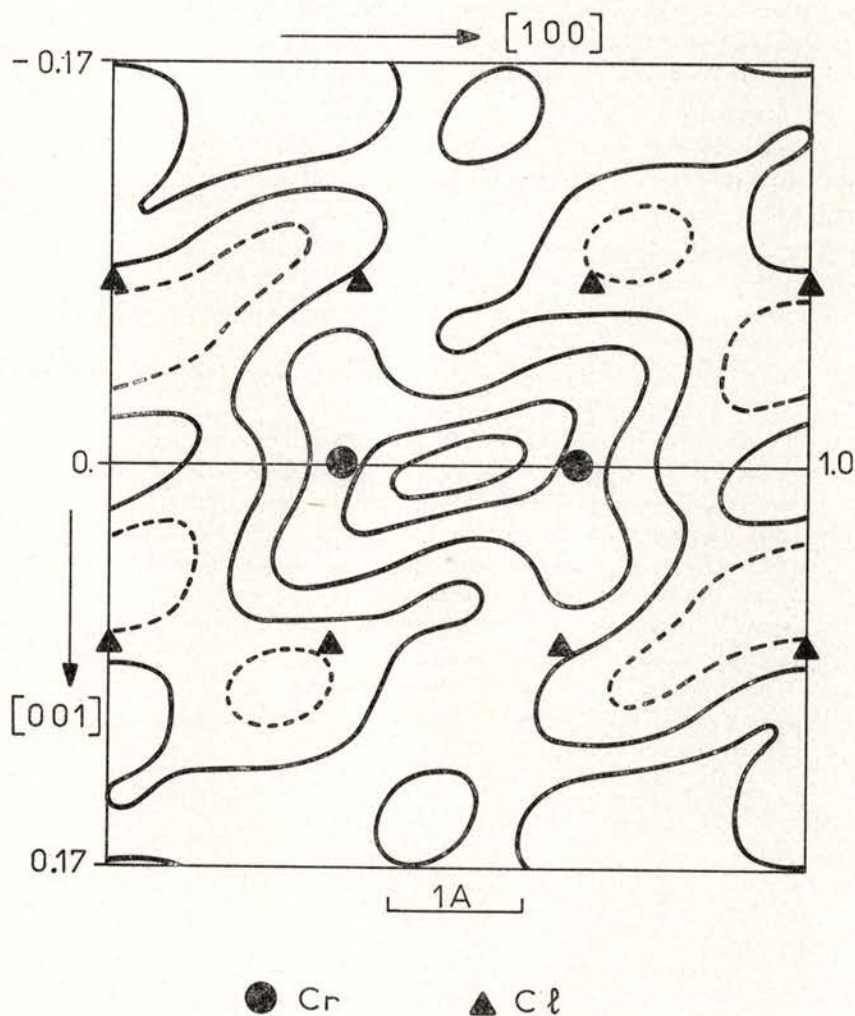

● Cr   ▲ Cℓ

Fig. 5 — Fourier projection of the delocalised spin density in $CrCl_3$ on the (10.1) plane. The projected positions of Cr^{3+} and Cl^- ions are shown. The contour interval is 0.05 $\mu_B/Å^2$; negative contours are shown as dashed lines.

REFERENCES

[1] Coppens, P., *Science*, **158**, 1577 (1967).

[2] Becker, P. and Coppens, P., *Acta Cryst.*, **A30**, 129 (1974).

[3] Becker, P. and Coppens, P., *Acta Cryst.*, **A31**, 417 (1975).

[4] Thornley, F. R. and Nelmes, R. J., *Acta Cryst.*, **A30**, 748 (1974).

[5] Cooper, M. J. and Rouse, K. D., *Acta Cryst.*, **A24**, 405 (1968).

[6] Rouse, K. D. and Cooper, M. J., *Acta Cryst.*, **A25**, 615 (1969).

[7] Cochran, W., *Acta Cryst.*, **A25**, 95 (1969).

[8] Kurki Suonio, K., *Report Series in Physics 3/69*, University of Helsinki.

[9] Stewart, R. F., *J. Chem. Phys.*, **58**, 1668 (1973).

[10] Stewart, R. F., *Acta Cryst.*, **A32**, 565 (1976).

[11] Delapalme, A., Lander, G. H. and Brown, P. J., *J. Phys.*, **C11**, 1441 (1978).

[12] Bonnet, M., Delapalme, A., Becker, P. and Fuess, H., *Acta Cryst.*, **A32**, 945 (1976).

[13] Marshall, W. and Lovesey, S. W., *Theory of thermal neutron scattering*, p. 156, O.U.P. (1971).

[14] Radhakrishna, P. and Brown, P. J., *J. Phys.*, **F10**, 489 (1980).

[15] Brown, P. J., Ziebeck, K. R. A. and Radhakrishna, P., *Argonne Conference on Neutron Scattering* Aug. 1981 (In press).

[16] Moon, R. M., Koehler, W. C. and Cable, J. N., *Proceedings of the Conference on Neutron Scattering*, Gatlinburg Tennessee p. 577 (CONF-760-601-P2) National Technical Information Service US Department of Commerce, Springfield Virginia.

[17] Kostorz, G. and Michaelovitch, S., in *Proc. 12th Int. Conf. on Low Temp. Phys.* p. 341, Academic Press of Japan (1970).

[18] Moon, R. M., Koehler, W. C. and Shull, C. G., *Nucl. Instrum. Meth.*, **129**, 515 (1975).

PRECISION MOLECULAR GEOMETRY DETERMINATION: LOW TEMPERATURE NEUTRON DIFFRACTION VERSUS AB-INITIO MOLECULAR ORBITAL CALCULATIONS (*)

G. A. Jeffrey and J. R. Ruble

Department of Crystallography, University of Pittsburgh,
Pittsburgh, PA 15260, U.S.A.

R. K. McMullan

Department of Chemistry, Brookhaven National Laboratory,
Upton, NY 11973, U.S.A.

D. J. DeFrees, J. S. Binkley and J. A. Pople

Department of Chemistry, Carnegie-Mellon University,
Pittsburgh, PA 15213, U.S.A.

ABSTRACT — Four molecules have been studied by single crystal neutron diffraction: acetamide at 23 K, fluoroacetamide at 20 K, formamide oxime at 16 K, and 1,2-diformyl hydrazine at 15 K. *Ab-initio* molecular orbital calculations were carried out using GAUSSIAN-80 at the Hartree-Fock level with a 3-21G basis set. For acetamide and 1,2-diformyl hydrazine, the conformation of the molecules in the crystal is not that of the calculated minimum energy. The observed bond lengths, when corrected for thermal motion effects, differ from those calculated by *ab-initio* geometry optimization. These differences are reduced when corrections are applied to the theoretical values for polarization, electron correlation and hydrogen bonding. Except in the case of $C=N$ and $N-O$ bonds, the residual discrepancies are comparable with the experimental errors (σ's, 0.0002 to 0.0012 Å). Larger discrepancies occur in X-H bonds due to the inadequacy of thermal riding-motion corrections assuming harmonic motion.

1 — INTRODUCTION

In the past ten years, the determination of the crystal structures of organic and organometallic molecules with molecular

Portgal. Phys. — Vol. 13, fasc. 1-2, pp. 23-38, 1982

23

weights of less than 500 daltons by X-ray diffraction has changed from an intellectually stimulating and challenging problem to a routine methodology. This is a consequence of developments in computer technology and some very clever programming of these computers by small groups of gifted crystallographers. Computer-controlled diffractometers collect the diffraction data and structure-solving and refinement packages complete the analysis. The computers provide the final numerical data and computer graphics display the results visually. Of the 800 crystal structures reported in *Acta Crystallographica Section B* for 1980, in less than one hundred was there any serious difficulty in solving the phase problem.

As a consequence, crystal structure analysis has moved out of physics to become a routine tool of analytical chemistry. Crystallographers have sought their intellectual satisfaction by applying their methodology and interests in stimulating ways in other fields of science where the geometrical arrangement of atoms in the crystalline state has relevance to the interpretation of macroscopic phenomena. Most spectacular has been the impact of crystallography on the biological sciences, leading to the birth of a new specialty in the field, molecular biology. The under-standing of biological function and malfunction has moved from the microscopic scale to the atomic scale of the Angstrom unit, with important consequences in the medical sciences.

In this paper, we will be discussing an interaction between Crystallography and Quantum Chemistry. It is over 50 years since Dirac claimed quantum mechanics to be capable of explaining all of chemistry and most of physics. Since that time, both of these fields have expanded much faster than even the simpler phenomena have been explained by any solutions to the wave equations, however approximate. What quantum mechanics has provided is a convenient and generally acceptable descriptive language for explaining *qualitatively* certain chemical and phys-ical phenomena in terms of electronic and nuclear behaviour. Despite the great growth in computing power over the past twenty years, the number of *quantitative* comparisons between the results of *ab-initio* quantum theory and experimental measure-ments are relatively few. The magnitude of the computing power for *ab-initio* methods has forced the use of semi-empirical

methods where quantum mechanical concepts are combined with quantities obtained from experimental observations.

In recent years, the development of the GAUSSIAN series of programs [1] has made possible the *ab-initio* nuclear geometry energy optimization of molecules containing first row elements which are large enough to form crystals at room temperatures. This interests the crystallographer who believes that crystal analysis by X-ray or neutron diffraction is the method, *par excellence*, of measuring the atomic geometry of molecules of this size. In this paper, we report the results of this comparison between theory and experiment. The molecules and crystal structures we have studied are shown in Table 1.

TABLE 1 — Molecules studied *

	Space group	Molecular symmetry	Temperature (K)	R-factor	E.s.d (Å × 10)
Acetamide	R3c	1	23	0.021	10-20
Fluoroacetamide	P1̄	m	20	0.023	4-8
Formamide oxime	$P2_12_12_1$	1	16	0.017	4-8
Diformyl hydrazine	$P2_1/c$	1	15	0.024	4-7

* The details of these results are reported elsewhere [2].

2 — THE THEORETICAL METHOD

The nuclear geometry minimization was carried out with *ab-initio* molecular orbital (LCAO) theory at the Hartree-Fock level using the 3-21G split-valence basis set incorporated in the GAUSSIAN-78 and -80 programs. All geometrical parameters were minimized. In appropriate cases, the final minimization was preceded by global searches of minimized energy conformations using the smaller STO-3G basis set. Comparison with spectroscopic microwave data on simpler molecules gives good reason to believe that at the HF/3-21G level of approximation,

the agreement in bond lengths with experimental values is within 0.05 Å. Table 2 gives the differences between theory and experiment for these simpler molecules at different levels

TABLE 2 — Molecular geometry from quantum mechanics: $\Delta_{\text{theory-exp.}}$ (Å)

Ab-initio M.O. calculations using Pople methodology [3]

Basis sets	Electronic Correlations				
	Hartree-Fock	Moller Plesset Perturbations			
		MP1	MP2	MP3	∞
STO-3G	0.010 d				
3-21G 4-31G	0.000 a 0.033 b 0.006 c 0.039 d				
6-31G *	0.018 a 0.014 b 0.009 c 0.029 d		0.006 a 0.012 b 0.008 c	0.005 a 0.012 b 0.008 c	
6-31G **					
↓ ∞					Schrödinger Equation

a C-N in methylamine
b C-H in formaldehyde
c N-H in methylamine   } vs microwave spectroscopy
d N-O in formaldoxime

of approximation. Table 3 shows a similar comparison in a different form.

These results show that in certain cases, i.e. for the C-N bond in methylamine, there is a cancellation of errors in the

TABLE 3 — Effects of level of approximation on bond lengths in some small molecules

Bond	Molecule	HF/3-21G [4]	HF/6-31G * [4]	MP3/6-31G * [5]	Spectroscopy [6] ±(0.005-0.010)
C–C	Ethane	1.542	1.528	1.526	1.526
C=O	Formaldehyde	1.207	1.184	1.210	1.208
C–N	Methylamine	1.472	1.453	1.466	1.471
N–O	Hydroxylamine	1.469	1.403	1.444	1.453
C=N	Methylenimine	1.256	1.250	1.275	1.273
C–H	Methane	1.083	1.084	1.091	1.094
	Formaldehyde	1.083	1.092	1.104	1.116
N–H	Ammonia	1.002	1.002	1.017	1.012
O–H	Methanol	0.946	0.946	0.967	0.956

lower level approximations. The poorer agreement is observed
for multiple bonds, as in $C=O$, and for bonds between electro-
negative atoms, as in N-O, as shown in Table 4. This suggests
that the calculated theoretical bond langths are sensitive to the
effects of electron correlation. The molecules shown in Table 1
contain between 32 and 46 electrons. Extension to molecules
with more than 50 electrons involves excessive computing, which
increases approximately as the fourth power of the number of
electrons. Calculations at higher levels for molecules of this size
is also not feasible, since each advance to a higher level in
Table 2, involves a factor of about ten in computing.

3 — THE EXPERIMENTAL METHOD

All the crystal structures shown in Table 1 have been deter-
mined previously by X-ray diffraction. The experimental data
for this work was collected at the Brookhaven High Flux Reactor
using monochromated neutrons. The crystals were maintained at
the temperatures indicated in Table 1, using a DISPLEX (CS-202)
closed-cycle refrigerator. The intensities were corrected for
absorption and extinction. The nuclear parameters were refined
by full-matrix least-squares [7], using an anisotropic extinction
parameter [8] where necessary. The thermal motion was analyzed
by the segmented-body analysis method, ORSBA [9]. The bond
lengths were corrected for the libration effect and for riding-
motion [10] in the case of those involving hydrogen atoms.

The use of neutron diffraction permits the direct comparison
with the theoretically calculated nuclear geometries. With present
low-temperature technology, lower temperatures can be obtained
on neutron diffractometers than on X-ray instruments.

4 — COMPARISON BETWEEN THEORY AND EXPERIMENT

Agreement between the theoretical and experimental molecular
geometries is not expected for the following reasons:

1 — Molecule at rest versus molecule undergoing thermal
and zero point motion.

TABLE 4 — Experimental and theoretical molecular dimensions (Å) of acetamide at 23 K and fluoro-acetamide at 20 K

The σ values in parentheses refer to the last significant figure

Bond	CH₃CONH₂				FCH₂CONH₂		
	Experimental at 23 K		Theoretical	E.D.	Experimental at 20 K		Theoretical
	Observed	Corrected			Observed	Corrected	
C – C	1.5094(10)	1.513	1.516	1.519(6)	1.51109(5)	1.512	1.517
C = O	1.2468(12)	1.250	1.216	1.220(3)	1.2437(5)	1.246	1.216
C – N	1.3351(11)	1.337	1.358	1.380(4)	1.3242(2)	1.327	1.341
C – F					1.3906(5)	1.391	1.405
C – H(1)	1.085(2)	1.125	1.085				
C – H(2)	1.076(2)	1.119	1.082	1.124(10)	1.0942(7)	1.112	1.078
C – H(2′)	1.076(2)	1.119	1.079		1.0937(8)	1.112	1.078
N – H(3)	1.023(2)	1.036	0.998		1.0227(8)	1.037	0.997
N – H(4)	1.023(2)	1.037	0.994	1.022(11)	1.0138(7)	1.037	0.994

2 — Isolated molecule versus molecule in the crystal field. Distortion of molecules due to hydrogen bonds, polar interactions, and van der Waals' forces.

3 — Approximations in the *ab-initio* theory due to deficiencies in basis set and electron correlation.

Of these, thermal motion, hydrogen-bonding, and approximations in the theory were expected to be significant in terms of the experimental errors of the neutron diffraction measurements. All these crystals contain hydrogen-bonded molecules. They would not be crystals at room temperature otherwise. The necessity to use crystals whcih have melting points above room temperature is a technicality concerned with the efficient utilization of a scarce neutron facility. Procedures are being developed at Brookhaven National Laboratory to grow and examine low-melting crystals outside the neutron beam and transfer them to the cryostat without melting. This would permit similar studies of simple molecules where higher level theory can be applied.

At the start of these experiments, we were by no means certain that we could unscramble these three effects, which are likely to be all of the same order of magnitude; that is, between 0.01 and 0.05 Å. However, we were sure we would learn something new in trying to do so. Unsuccessful experiments are frequently more informative than successful ones.

The first interesting result that we obtained was that for two of these molecules, acetamide and diformyl hydrazine, the conformation of the molecules in the crystal is not that of the calculated minimum energy for the isolated molecules at rest. The molecule of acetamide is shown in Fig. 1. The thermal ellipsoids are at 75 % probability instead of the more usual 50 %. The relatively large thermal ellipsoids of the C-H bonds at 23 K were unexpected. Acetamide is an asymmetric molecule in an asymmetric crystal structure, space group R3c. In contrast, the theoretical minimum energy conformation of acetamide has m symmetry with one of the C-H bonds in the plane of the molecule. At the HF/3-21G level, the observed asymmetric conformation is calculated to be 1.5 kJ/mol higher than the symmetrical molecule. We can speculate that this is due to better van der Waals' packing

of the methyl groups on adjacent molecules, but we have no proof of this and the reason may, in fact, be more subtle.
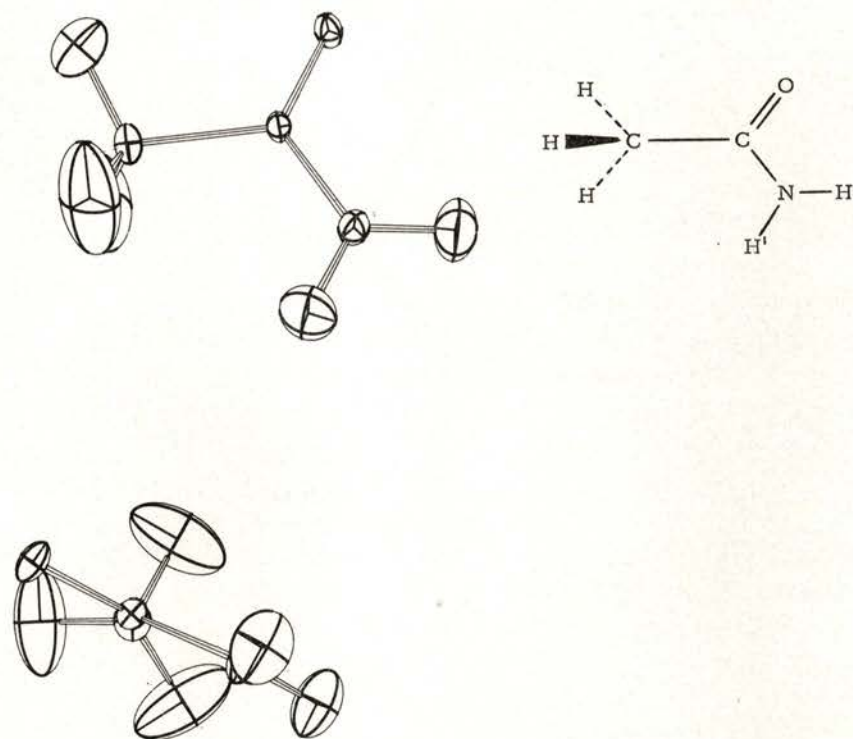

Fig. 1 — Thermal ellipsoids for acetamide (hexagonal form) at 23 K, shown at 75 % probability. Top: atomic notation and view perpendicular to C, N, O plane. Bottom: view in direction of C(2)-C(1) bond.

In monofluoroacetamide, shown in Fig. 2, both the observed and calculated molecules have the same m conformation, with the C-F bond in the plane of the molecule. The bond lengths for these two molecules are shown in Table 4. For the bonds not involving hydrogens, the thermal motion corrections are ≈ 0.002 Å. The uncertainty in these corrections, due to the assumption in the models used and of harmonic motion, is likely to be about
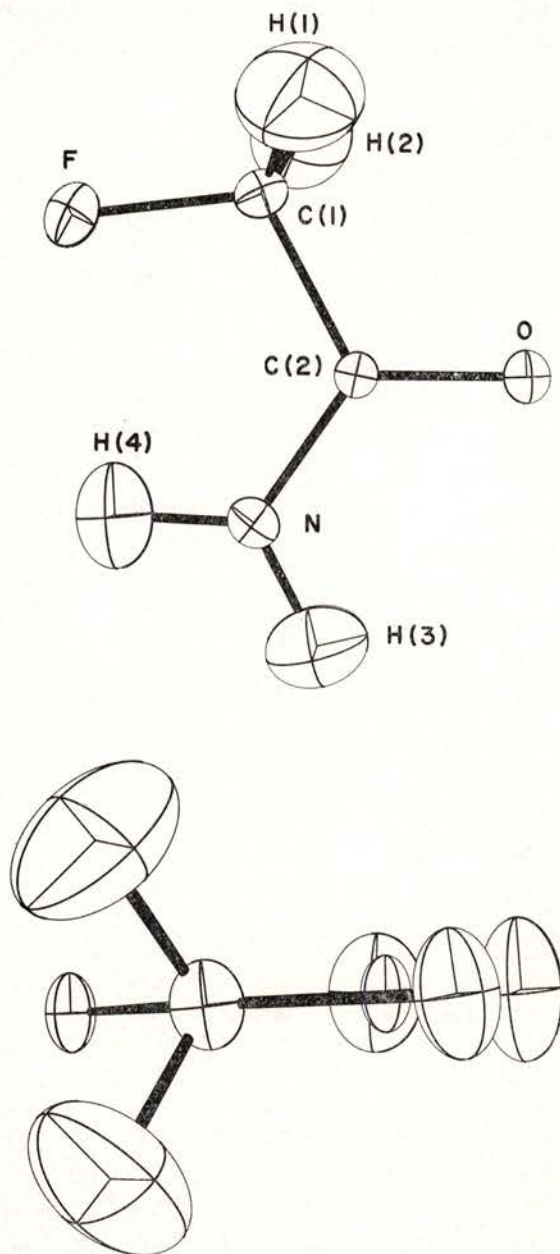
Fig. 2 — Atomic notation and thermal ellipsoids (75 %) for monofluoro-acetamide at 20 K, viewed normal to and in the plane of the molecule.

10 %, i.e. of the same magnitude as the experimental standard deviations. In other words, the application of thermal motion corrections approximately doubles the uncertainty of the experimental results.

The significant result is for the observed and calculated C-N and C=O distances. The C-N bonds are observed 0.021 Å shorter than those calculated, and the C=O bonds are observed 0.034 Å longer. This we interpreted as due to hydrogen-bonding in the crystal. To verify this, a HF/3-21G calculation was carried out on the formamide closed hydrogen-bonded dimer. These results are shown in Fig. 3. The values in parentheses are for the monomer. At this level of theory, the hydrogen-bonding diminishes the C-N bonds by 0.023 Å and lengthens the C=O bonds by 0.018 Å. In view of the disparity between the dimer model and the acetamide crystal structure, this agreement is very satisfactory. The theory also predicts a lengthening of the N-H bonds by 0.018 Å when involved in hydrogen-bonding.

The comparison of the experimental and observed X-H bond lengths is obscured by the large thermal riding-motion corrections shown in Table 3. Clearly, the agreement between experiment and theory for X-H bonds is better if the thermal motion effect is ignored. The reason for that, we believe, is because the effect of the riding-motion, which leads to a shortening of the observed bond lengths, is compensated for by the anharmonicity of the internal stretching motion, which increases the bond length to that of a bond in a molecule *at rest*. At these low temperatures, these two effects appear to almost cancel.

Another significant source of discrepancy between theory and experiment is the level of approximation in the theory. This can be estimated from the results of the higher order calculations on simple molecules containing the same bonds, shown in Tables 1 and 2.

Both corrections for hydrogen-bonding and basis set and electron correlation deficiencies can be applied to give residual discrepancies shown in Table 5. These residuals are less than 0.010 Å, except for the C-N bond in fluoroacetamide and the C-H bond lengths. This is better agreement than we anticipated, in view of the approximation of the simple hydrogen-bonding model and deficiencies in the thermal motion and *ab-initio*
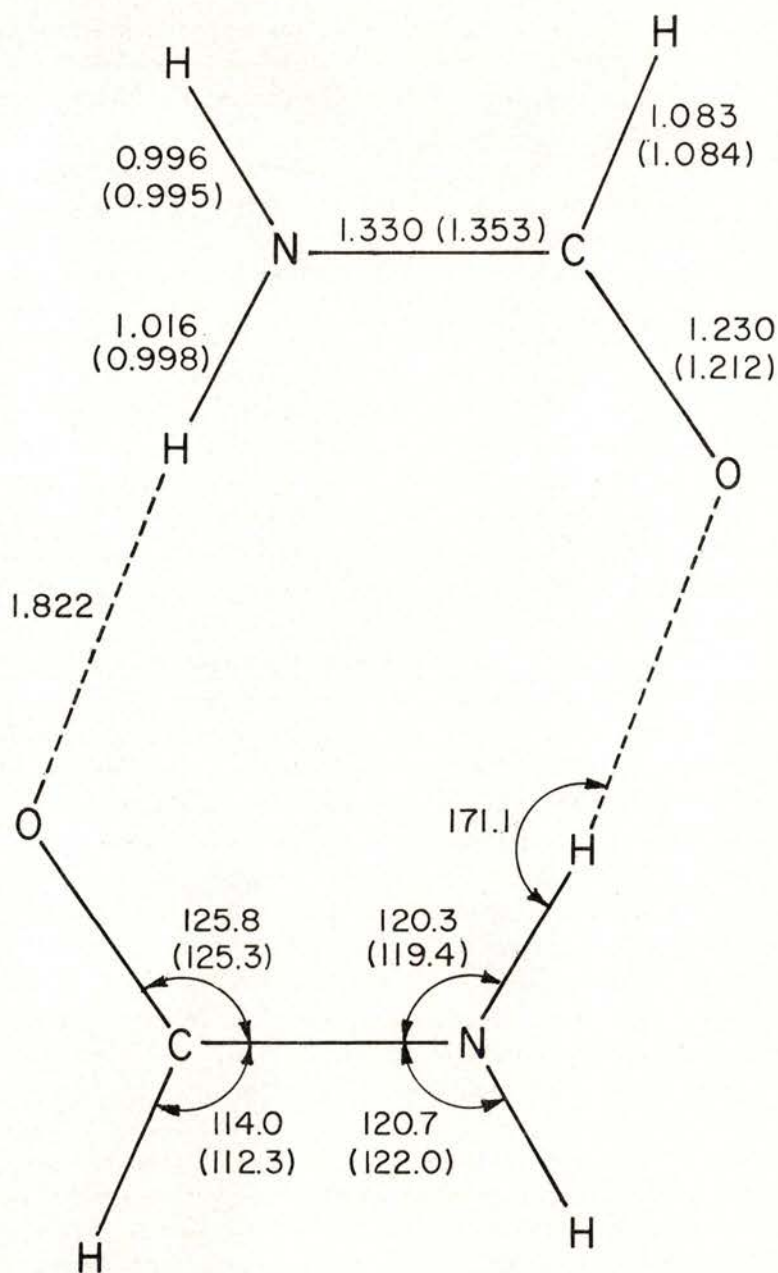
Fig. 3 — Theoretical geometry optimization of formamide and the hydrogen-bonded formamide dimer with HF/3-21G, using GAUSSIAN 80. The values in parentheses refer to the monomer.

TABLE 5 — Analysis of bond length discrepancies in acetamide
and fluoroacetamide

Upper values are for acetamide, lower values for fluoroacetamide

Bond	Δ Theory-Experiment	Higher Level Extrapolation	H-bonding Extrapolation	Residual Δ
C=O	−0.034	+0.014 [a]	+0.018	−0.002
	−0.030			+0.002
C−N	+0.021	−0.006 [b]	−0.023	−0.008
	+0.015			−0.014
N−H	−0.041	+0.015 [c]	+0.020	−0.006
	−0.041			−0.006
C−C	+0.003	−0.003 [d]		0.000
	+0.005			+0.002
C−H	−0.037	+0.011 [e]		−0.026
	−0.034			−0.023

[a] MP2/6-31G * formaldehyde
[b] MP2/6-31G * methylamine
[c] MP2/6-31G * ammonia
[d] HF/6-31G * acetaldehyde
[e] MP2/6-31G * methane

theories used. Very similar results were obtained for formamide oxime, as shown in Table 6.

In diformyl hydrazine, the theoretical minimum energy conformation for the isolated molecule has symmetry 2. As with hydrazine itself, the $>N—N<$ bonds are not coplanar. In the crystal structure, the molecules are planar with m symmetry. This is certainly due to the strong hydrogen-bonded layer arrangement in the crystals, shown in Fig. 4. The energy difference between the calculated non-planar conformation and the observed planar conformation is small, 5.4 kJ/mol. This is much smaller than the 108 kJ/mol difference between the non-planar and planar conformation for hydrazine [4].

TABLE 6 — Analysis of bond length discrepancies in formamide oxime

Bond	Neutron diffraction, 16 K		Δ Theory-experiment	H-bonding	Δ HF/3-21G → MP3/6-31G*	Residual
	Observed	Corrected				
C—N(1)	1.3347(4)	1.351	+0.002		−0.006 a	−0.004
C—N(2)	1.2959(4)	1.299	−0.030		+0.019 b	−0.011
N(2)—O	1.4283(4)	1.435	+0.034		−0.025 c	+0.009
N—H	1.0120(8)	1.026	−0.036	+0.020	+0.015 a	−0.001
	1.0162(8)	1.032	−0.036			
C—H	1.0899(8)	1.101	−0.040		+0.020 d	−0.020
O—H	0.9906(8)	1.002	−0.037	+0.005	+0.011 e	−0.021

a methylamine   b methylenimine   c hydroxylamine   d formaldehyde   e methanol

Fig. 4 (facing page) — Hydrogen bonding in the crystal structure of 1,2-diformyl hydrazine. Values in [ ] are bond lengths (Å) and bond angles (°) corrected for thermal motion. The plane of the diagram is $(10\bar{2})$.
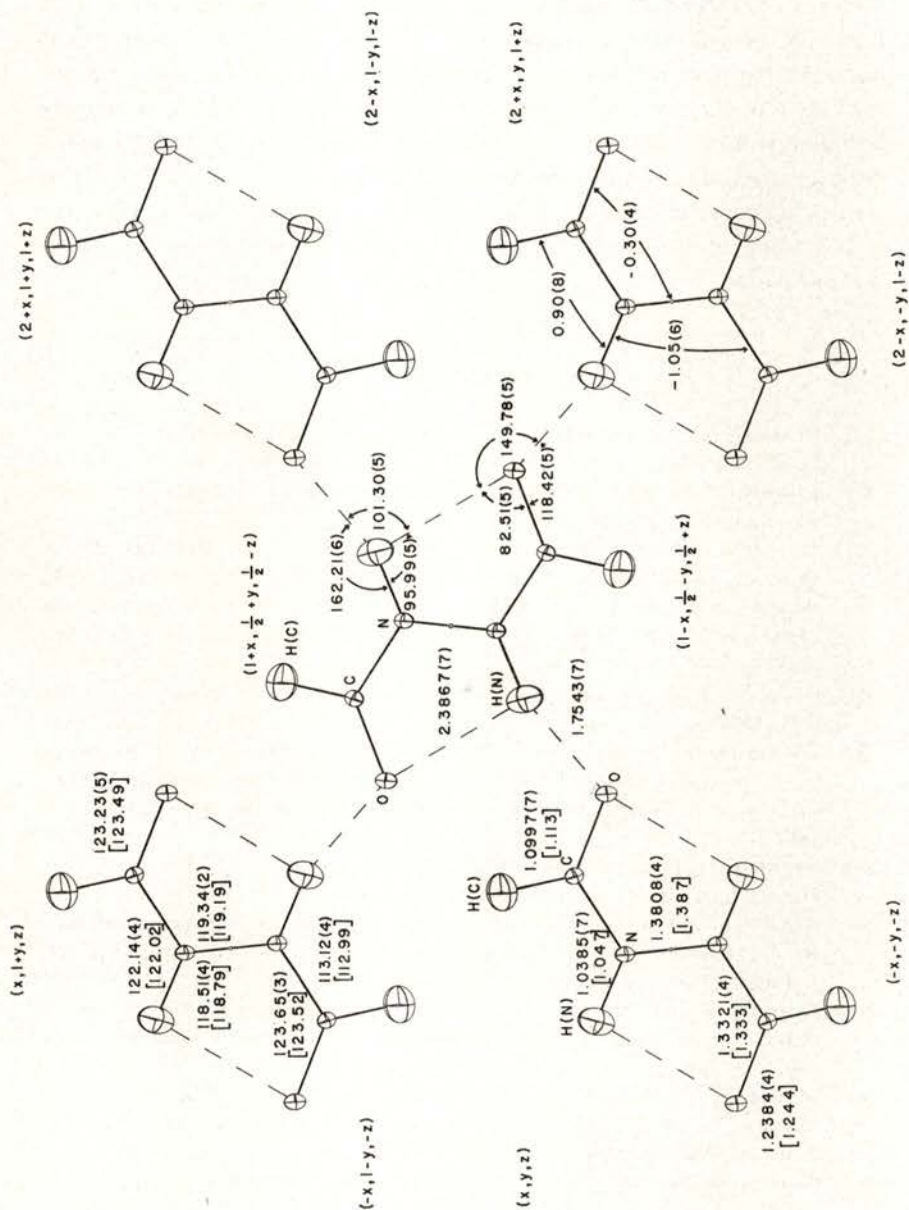
In summary, the agreement in bond lengths between *ab-initio* M.O. theory at the HF/3-21G level of approximation and neutron diffraction structure analyses at <25 K, is generally better than 0.015 Å, as shown in Table 6. A notable exception is the N-O bond in formamide oxime. The predominance of negative values in Table 6 suggests that the corrections for thermal motion are being systematically over-estimated and that better and possibly simpler methods should be sought. The X-H bond lengths show better agreement between theory and experiment, if it is assumed that riding-motion and anharmonicity effects cancel at these temperatures.

REFERENCES

[1] BINKLEY, J. S., WHITESIDE, R. A., KRISHNAN, R., SEEGER, R., DeFREES, D. J., SCHLEGEL, H. B., TOPIOL, S., KAHN, L. R., POPLE, J. A., *Quantum Chemistry Program Exchange*, 13, 406 (1980). Indiana University Bloomington, Indiana, USA.

[2] JEFFREY, G. A., RUBLE, J. R., McMULLAN, R. K., DeFREES, D. J., BINKLEY, J. S., POPLE, J. A., *Acta Cryst.*, B36, 2292 (1980); JEFFREY, G. A., RUBLE, J. R., McMULLAN, R. K., DeFREES, D. J., POPLE, J. A., *Acta Cryst.*, B37, 1381 (1981); *Ibid.*, B37, 1885 (1981); *Ibid.*, B38, in press (1982).

[3] BINKLEY, J. S., POPLE, J. A., HEHRE, W. J., *J. Amer. Chem. Soc.*, 102, 939 (1980).

[4] WHITESIDE, R. A., BINKLEY, J. S., KRISHNAN, R., FRISCH, M. J., DeFREES, D. J., SCHLEGEL, H. B., POPLE, J. A., *Carnegie-Mellon Quantum Chemistry Archive*, Carnegie-Mellon University, Pittsburgh, PA 15213, USA, 1981.

[5] DeFREES, D. J., LEVI, B. A., POLLACK, S. K., HEHRE, W. J., BINKLEY, J. S., POPLE, J. A., *J. Amer. Chem. Soc.*, 101, 4085 (1979).

[6] HARMONY, M. D., LAURIE, V. W., KUCZKOWSKI, R. L., SCHWENDEMAN, R. H., RAMSAY, D. A., LOVAS, F. J., LAFFERTY, W. J., MAKI, A. G., *J. Phys. Chem. Res. Data*, 8, 619 (1979).

[7] BUSING, W. R., MARTIN, K. O., LEVY, H. A., *ORFLS*. Report ORNL--TM-305, Oak Ridge National Laboratory, Oak Ridge, Tennessee, USA, 1962.

[8] BECKER, P. J., COPPENS, P., *Acta Cryst.*, A31, 417 (1975).

[9] JOHNSON, C. K., *ORSBA*, in *Thermal Neutron Diffraction*, edited by B. T. M. Willis, Oxford University Press, Chapt., 9, p. 132 (1970).

[10] BUSING, W. R., LEVY, H. A., *Acta Cryst.*, 17, 142 (1964).

FERROELASTICITY AND FERROELASTIC TRANSFORMATIONS (*)

D. M. C. GUIMARÃES

Department of Physics of Aveiro University
3800 AVEIRO — Portugal

ABSTRACT — Ferroelastic transformations can be calculated, when an n-fold pseudo-rotation exists (the n-fold rotation being a symmetry element of the prototype lost in the lower symmetry ferroelastic phase), by means of a transformation (rotation of axes) corresponding to the reorientation of the lattice vectors if distortion of the ferroelastic structure is taken into account.

1 — FERROELASTICITY

Ferroelasticity was recognized in 1969 as a new crystal property by K. Aizu [1]. A crystal is ferroelastic if it possesses two or more equally stable orientational states which differ in spontaneous strain, and if a suitably applied external mechanical stress can reproducibly transform one of these states into the others. Spontaneous strain is measured in relation to the prototype structure. The crystal symmetry is reduced, in the ferroelastic state, to a subgroup of a higher symmetry class (corresponding to the prototype structure) by a small distortion. The classification of potentially ferroelastic materials (from the point of view of symmetry) was developed by Aizu [2].

We discuss here the relation between the property of ferroelasticity and the crystal structure i.e. the incidence of this on the phenomenon of lattice reorientation under the effect of mechanical stress. As examples of the concepts in question we use samarium orthoaluminate, $Sm\ Al\ O_3$, and lead orthophosphate, $Pb_3\ (PO_4)_2$.

---

2 — FERROELASTICITY AND STRUCTURE
IN SAMARIUM ORTHOALUMINATE

2.1 — *Description of the structure*

Crystals of Sm Al O$_3$ grow in a ferroelastic phase (Abrahams et al., [3]) whose structure corresponds to an hettotype of the perovskite family (Megaw, [4]).
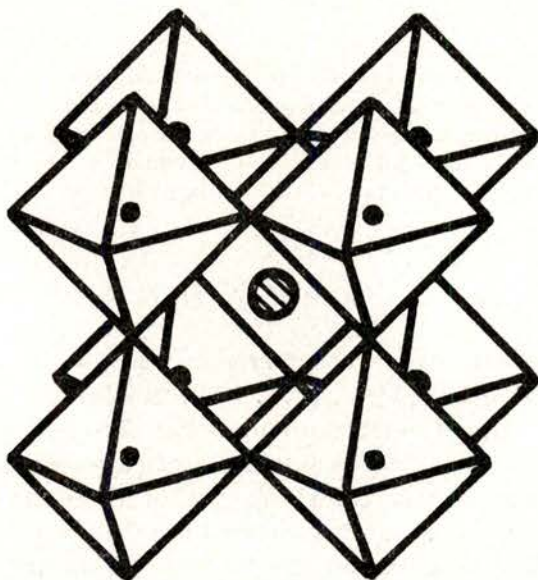
Fig. 1 — Ideal perovskite structure, ABO$_3$. Perspective view of the lattice, showing the octahedra: full circles B , hatched circle A , O atoms at the corners of the octahedra.

Fig. 1 shows the ideal perovskite structure. The general formula is A B O$_3$ (A and B are cations) and the lattice is primitive cubic. The structure can be simply described as a framework of B O$_6$ octahedra sharing corners, with the large A atom in the cavity between octahedra. This is the aristotype of the perovskite family. Note that the general formula of this family is A B X$_3$, in analogy with A B O$_3$, X being an anion.

40

Portgal. Phys. — Vol. 13, fasc. 1-2, pp. 39-52, 1982

The prototype structure of Sm Al O$_3$ is also an hettotype of the perovskite family. In this case the group O$_6$ around the Al cation becomes a tetragonal bipyramid instead of an octahedron; the point group in this ideal structure is 4/m m m.
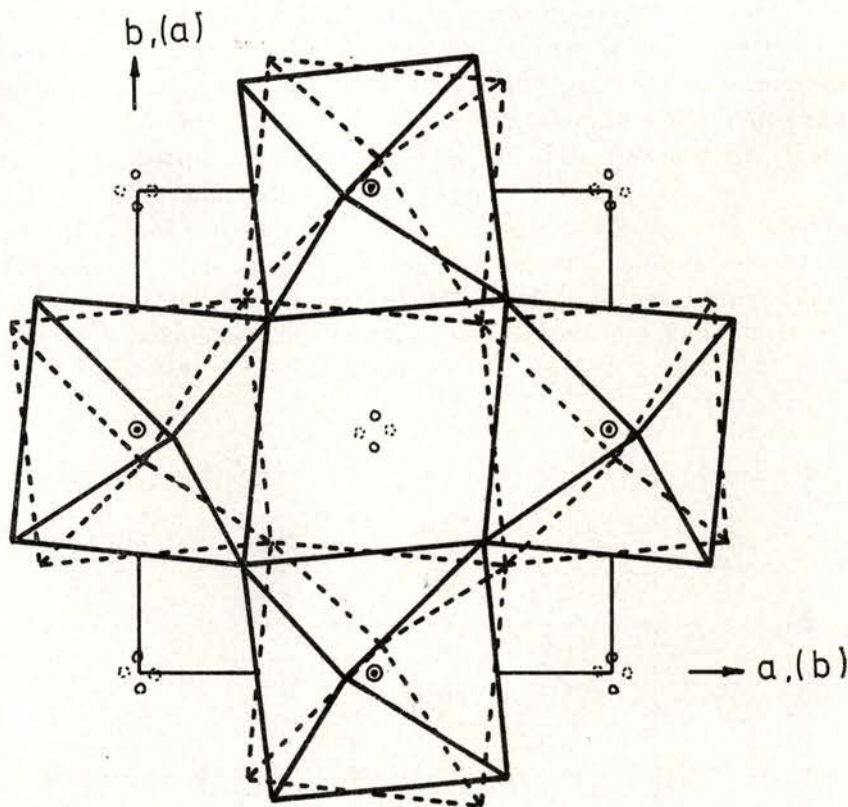
Fig. 2 — Atomic positions in Sm Al O$_3$, in initial *a b c* orientation (solid outlines) and in orientation *b a c* after ferroelastic transformation (dashed outlines). (from Abrahams et al., [3]).

In the real ferroelastic phase the groups Al O$_6$ tilt relative to one another; the distortion may occur in two different ways which correspond to two well determined orientations of the crystal lattice. The point group is m m m. The two stable states are energetically equivalent and only distinguishable by their orientation in space. Fig. 2 shows the atomic positions in both

orientation states. In this example, the ferroelastic phase is orthorhombic, pseudo-tetragonal. By means of an adequate compressive stress along the [100] or [010] crystallographic directions, small atomic movements occur (of the order of tenths of Å) which give rise to ferroelastic switching from one state to the other. The phenomenon is clearly observed in polarized light.

Point group m m m is a subgroup of 4/m m m. Besides all symmetry elements of the ferroelastic structure, the prototype has other symmetry elements, such as rotations by $\pi/2$ and $3\pi/2$ about the fourfold axis. These rotations, when applied to one of the ferroelastic states transform it into the other. There is a geometric correspondence between the stable ferroelastic states that is established by the symmetry elements of the prototype which have been lost in the ferroelastic phase.

Fig. 3 indicates in a diagram (taken down the c axial direction) how the axes in the prototype are chosen in order to refer to
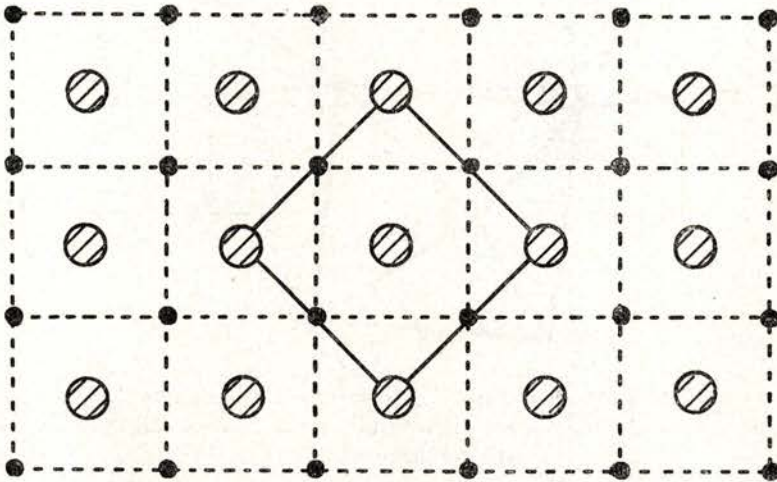
Fig. 3 — Choice of axes in the prototype, coincident with the axes in the ferroelastic phase of Sm Al O$_3$. [Projection in (001)].

them the distortion of the ferroelastic phase. It is seen (the axial length c duplicates) that there is a quadruplication of the unit cell in the ferroelastic phase.

The preparation of the crystals, lattice constants and atomic coordinates in samarium orthoaluminate are described by Abrahams et al., [3]. We give here the indispensable data for the analysis of the ferroelastic transformation that is dealt with in section 2.2.

The lattice constants are

$$a = 5.291075 \pm 0.000024 \text{ Å}$$
$$b = 5.290479 \pm 0.000024 \text{ Å}$$
$$c = 7.474200 \pm 0.000051 \text{ Å}$$

2.2 — *Ferroelastic transformation in samarium orthoaluminate*

According to a well known criterion about the structural basis of ferroelasticity (Abrahams et al., [5]) — this criterion being applicable only when two possible ferroelastic domains are in question — every atom in Sm Al O_3 at x_1, y_1, z_1 is pseudo-symmetrically related to another atom of the same kind, with coordinates x_2, y_2, z_2, by the equation

$$x_1, y_1, z_1 = (1/2 - y_2, 1/2 - x_2, 1/2 + z_2) + \Delta \qquad (1)$$

where Δ is an atomic displacement of the order of tenths of Å.

On the basis of the transformation relation (1), Abrahams et al. calculate the coordinates of every atom, after the ferroelastic switching to the other orientational state (the axes of reference being the initial ones) as well as the atomic displacements Δ that take place in the transformation.

Considering the symmetry relations between the prototype and the ferroelastic phase we do here the same determinations and obtain the same results. This method is quite general, since ferroelastic transformations can be carried out in this way also in the case of more than two ferroelastic domains.

Let us refer the prototype structure to the axes of the ferroelastic phase which is a small distortion of the first. Having in mind one of the ferroelastic states, let us rotate the lattice by $\pi/2$ around the c^* axis direction (pseudo-fourfold axis). Supposing the domains related by fourfold clockwise rotation, the axes for the transformation of coordinates must be correspondingly rotated anti-clockwise.

If the axes a and b are considered of equal length, the simple transformation of coordinates (x', y', z' are the coordinates in domain 2 referred to the original axes of domain 1) is

$$\begin{bmatrix} x' \\ y' \\ z' \end{bmatrix} = \begin{bmatrix} 0 & 1 & 0 \\ -1 & 0 & 0 \\ 0 & 0 & 1 \end{bmatrix} \begin{bmatrix} x \\ y \\ z \end{bmatrix} \qquad (2)$$

Note that ratio a/b is different from 1. From a geometric point of view, the exact transformation of coordinates would be

$$\begin{bmatrix} x' \\ y' \\ z' \end{bmatrix} = \begin{bmatrix} 0 & b/a & 0 \\ -a/b & 0 & 0 \\ 0 & 0 & 1 \end{bmatrix} \begin{bmatrix} x \\ y \\ z \end{bmatrix} \qquad (3)$$

The use of (2) instead of (3) doesn't really alter the results, due to the precision with which the atomic coordinates are known. This is not the case of ferroelastic transformations in other materials, such as $Pb_3 (PO_4)_2$, to which we refer further on.

When relations of type (1) are used, simplifications similar to the one we have emphasized here are implicit.

The ferroelastic transformation in Sm Al O_3, obtained by use of the method we have just outlined, is detailed in Table 1. The first column of this Table indicates the identity of the atom in the ferroelastic state 1 whose position in ferroelastic state 2 one wants to determine by means of relations (2); its coordinates are given in the second column. The third column gives the identity of the atom (Atom*) which must be considered to obtain the required ferroelastic transformation. In the fourth column the coordinates of Atom* are given; and in the fifth those of the particular Atom* to be chosen to carry out transformation (2) (x, y, z coordinates). In the sixth column the result of the ferroelastic transformation is written and in the seventh the atomic displacement undergone by the initial atom. *The reference axes remain those that have been initially chosen in ferroelastic state 1.* In the transformed lattice, the identity of the atom after the ferroelastic transformation is the same as Atom*. Note that, in the prototype, coordinates x', y', z' (result of the ferroelastic transformation) coincide with the initial coordinates of the atom, denoted by XYZ in the second column of Table 1.

TABLE 1 — Atomic coordinates and displacement vectores Δ in ferroelastic transformation of Sm Al O$_3$

Atom	Coordinates	Atom*	Coordinates	Coordinates*	Result	Δ (Å)
Sm-1	$X = -0.00501$ $Y = 0.02402$ $Z = 1/4$	Sm-1	$X' = -0.00501$ $Y' = 0.02402$ $Z' = 1/4$	$x = -0.00501$ $y = 0.02402$ $z = 1/4$	$x' = 0.02402$ $y' = 0.00501$ $z' = 1/4$	0.184
Sm-2	$X = 0.00501$ $Y = -0.02402$ $Z = 3/4$	Sm-2	$X' = 0.00501$ $Y' = -0.02402$ $Z' = 3/4$	$x = 0.00501$ $y = -0.02402$ $z = 3/4$	$x' = -0.02402$ $y' = -0.00501$ $z' = 3/4$	0.184
Sm-3	$X = 0.49499$ $Y = 0.47598$ $Z = 3/4$	Sm-3	$X' = 0.49499$ $Y' = 0.47598$ $Z' = 3/4$	$x = -0.50501$ $y = 0.47598$ $z = 3/4$	$x' = 0.47598$ $y' = 0.50501$ $z' = 3/4$	0.184
Sm-4	$X = 0.50501$ $Y = 0.52402$ $Z = 1/4$	Sm-4	$X' = 0.50501$ $Y' = 0.52402$ $Z' = 1/4$	$x = -0.49499$ $y = 0.52402$ $z = 1/4$	$x' = 0.52402$ $y' = 0.49499$ $z' = 1/4$	0.184
Al-1	$X = 0$ $Y = 1/2$ $Z = 0$	Al-2	$X' = 1/2$ $Y' = 0$ $Z' = 0$	$x = 1/2$ $y = 0$ $z = 0$	$x' = 0$ $y' = 1/2$ $z' = 0$	0
Al-2	$X = 1/2$ $Y = 0$ $Z = 0$	Al-1	$X' = 0$ $Y' = 1/2$ $Z' = 0$	$x = 0$ $y = 1/2$ $z = 0$	$x' = 1/2$ $y' = 0$ $z' = 0$	0
Al-3	$X = 1/2$ $Y = 0$ $Z = 1/2$	Al-4	$X' = 0$ $Y' = 1/2$ $Z' = 1/2$	$x = 0$ $y = 1/2$ $z = 1/2$	$x' = 1/2$ $y' = 0$ $z' = 1/2$	0

TABLE 1 — (continuation)

Atom	Coordinates	Atom*	Coordinates	Coordinates*	Result	Δ (Å)
Al-4	X = 0 Y = 1/2 Z = 1/2	Al-3	X' = 1/2 Y' = 0 Z' = 1/2	x = − 1/2 y = 0 z = 1/2	x' = 0 y' = 1/2 z' = 1/2	0
0 (1)-1	X = 0.0644 Y = 0.4903 Z = 1/4	0 (1)-4	X' = 0.4356 Y' = 0.9903 Z' = 1/4	x = − 0.5644 y = − 0.0097 z = 1/4	x' = − 0.0097 y' = 0.5644 z' = 1/4	0.554
0 (1)-2	X = − 0.0644 Y = 0.5097 Z = 3/4	0 (1)-3	X' = 0.5644 Y' = 0.0097 Z' = 3/4	x = − 0.4356 y = 0.0097 z = 3/4	x' = 0.0097 y' = 0.4356 z' = 3/4	0.554
0 (1)-3	X = 0.5644 Y = 0.0097 Z = 3/4	0 (1)-2	X' = − 0.0644 Y' = 0.5097 Z' = 3/4	x = − 0.0644 y = 0.5097 z = 3/4	x' = 0.5097 y' = 0.0644 z' = 3/4	0.409
0 (1)-4	X = 0.4356 Y = 0.9903 Z = 1/4	0 (1)-1	X' = 0.0644 Y' = 0.4903 Z' = 1/4	x = 0.0644 y = 0.4903 z = 1/4	x' = 0.4903 y' = − 0.0644 z' = 1/4	0.409
0 (2)-1	X = − 0.2766 Y = 0.2770 Z = 0.0335	0 (2)-8	X' = 0.7766 Y' = 0.7770 Z' = 0.0335	x = − 0.2234 y = − 0.2230 z = 0.0335	x' = − 0.2230 y' = 0.2234 z' = 0.0335	0.401
0 (2)-2	X = 0.7766 Y = 0.7770 Z = 0.4665	0 (2)-3	X' = 0.2766 Y' = − 0.2770 Z' = 0.5335	x = − 0.7234 y = 0.7230 z = 0.5335	x' = 0.7230 y' = 0.7234 z' = 0.5335	0.642

TABLE 1 — (continuation)

Atom	Coordinates	Atom*	Coordinates	Coordinates*	Result	Δ (Å)
0 (2)-3	X = 0.2766 Y = -0.2770 Z = 0.5335	0 (2)-6	X' = 0.2234 Y' = 0.2230 Z' = 0.5335	x = 0.2234 y = 0.2230 z = 0.5335	x' = 0.2230 y' = -0.2234 z' = 0.5335	0.401
0 (2)-4	X = 0.2234 Y = 0.2230 Z = -0.0335	0 (2)-1	X' = -0.2766 Y' = 0.2770 Z' = 0.0335	x = -0.2766 y = 0.2770 z = 0.0335	x' = 0.2770 y' = 0.2766 z' = 0.0335	0.642
0 (2)-5	X = 0.2766 Y = -0.2770 Z = -0.0335	0 (2)-4	X' = 0.2234 Y' = 0.2230 Z' = -0.0335	x = 0.2234 y = 0.2230 z = -0.0335	x' = 0.2230 y' = -0.2234 z' = -0.0335	0.401
0 (2)-6	X = 0.2234 Y = 0.2230 Z = 0.4665	0 (2)-7	X' = -0.2766 Y' = 0.2770 Z' = 0.4665	x = -0.2766 y = 0.2770 z = 0.4665	x' = 0.2770 y' = 0.2766 z' = 0.4665	0.642
0 (2)-7	X = -0.2766 Y = 0.2770 Z = 0.4665	0 (2)-2	X' = 0.7766 Y' = 0.7770 Z' = 0.4665	x = -0.2234 y = -0.2230 z = 0.4665	x' = -0.2230 y' = 0.2234 z' = 0.4665	0.401
0 (2)-8	X = 0.7766 Y = 0.7770 Z = 0.0335	0 (2)-5	X' = 0.2766 Y' = -0.2770 Z' = -0.0335	x = -0.7234 y = 0.7230 z = -0.0335	x' = 0.7230 y' = 0.7234 z' = -0.0335	0.642

In short, if atoms with coordinates XYZ and xyz are independent crystallographic atoms of the same kind, we can write

$$(XYZ) = R (xyz) + \Delta \tag{4}$$

where R (xyz) is a transformation (a clockwise rotation of the lattice by $\theta = \pi/2$ around the pseudo-fourfold axis) that causes reorientation of the lattice vectors; Δ is an atomic displacement of the order of tenths of Å and represents the effective displacement of the atom with coordinates XYZ in the process of ferroelastic switching from one domain to the other.

An atom that is situated on the fourfold axis in the prototype, may occur in the ferroelastic phase in one of two possible positions (according to the domain it is in) that are symmetrically placed around the pseudo-fourfold axis:

$$XYZ - \text{domain } 1 \quad ; \quad R (XYZ) - \text{domain } 2.$$

3 — FERROELASTICITY AND STRUCTURE IN LEAD ORTHOPHOSPHATE

In lead orthophosphate, $Pb_3 (PO_4)_2$, there are in general triplets of crystallographically-independent atoms of the same kind that are pseudo-symmetrically related by a pseudo-threefold rotation (Guimarães, [6]).

The material undergoes a phase transition to a high temperature phase at about 180 C.

3.1 — *Structure and ferroelastic domains in lead orthophosphate*

The high and low temperature structures are fully described in the literature. Fig. 4 shows the stereogram of the symmetry change.

The high temperature phase (prototypic phase or β phase) whose structure is rhombohedral (point group $\bar{3}m$) may be referred to the monoclinic axes of the low temperature phase

(ferroelastic phase or α phase, point group 2/m) and this is convenient for the study of spontaneous strain (Guimarães, [7]) and ferroelastic transformations.
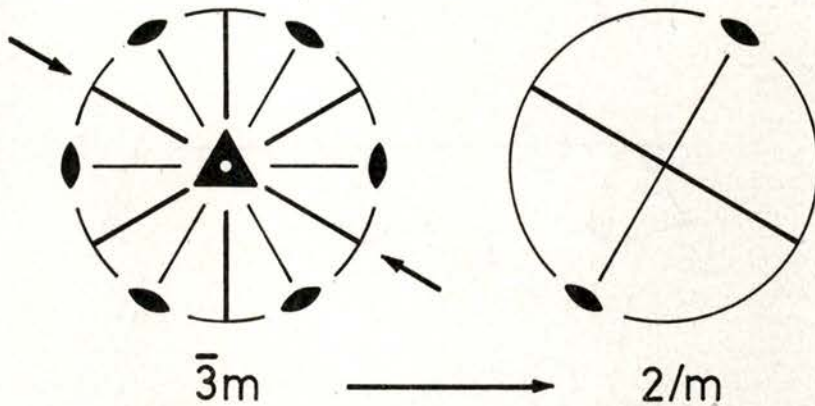
Fig. 4 — Stereogram of the symmetry change in the phase transition of $Pb_3 (PO_4)_2$.

The projection of the ferroelastic structure on the monoclinic (010) plane is shown in Fig. 5. The pseudo-threefold axis is along a_m^* and passes through the point $(0, 1/4, 1/4)$ with respect to the centre of symmetry.

There are in the α phase three possible orientations of ferroelastic domains, related to one another by a threefold rotation about the pseudo-threefold axis.

3.2 — *Ferroelastic transformations in lead orthophosphate*

The real monoclinic ferroelastic lattice is slightly distorted in relation to the monoclinic ideal sub-lattice of the rhombohedral β phase.

$Pb_3 (PO_4)_2$ was the first example of a ferroelastic material with more than two domains where it was possible to find a structural explanation of the ferroelastic properties and to set up a scheme for the achievement of ferroelastic transformations.
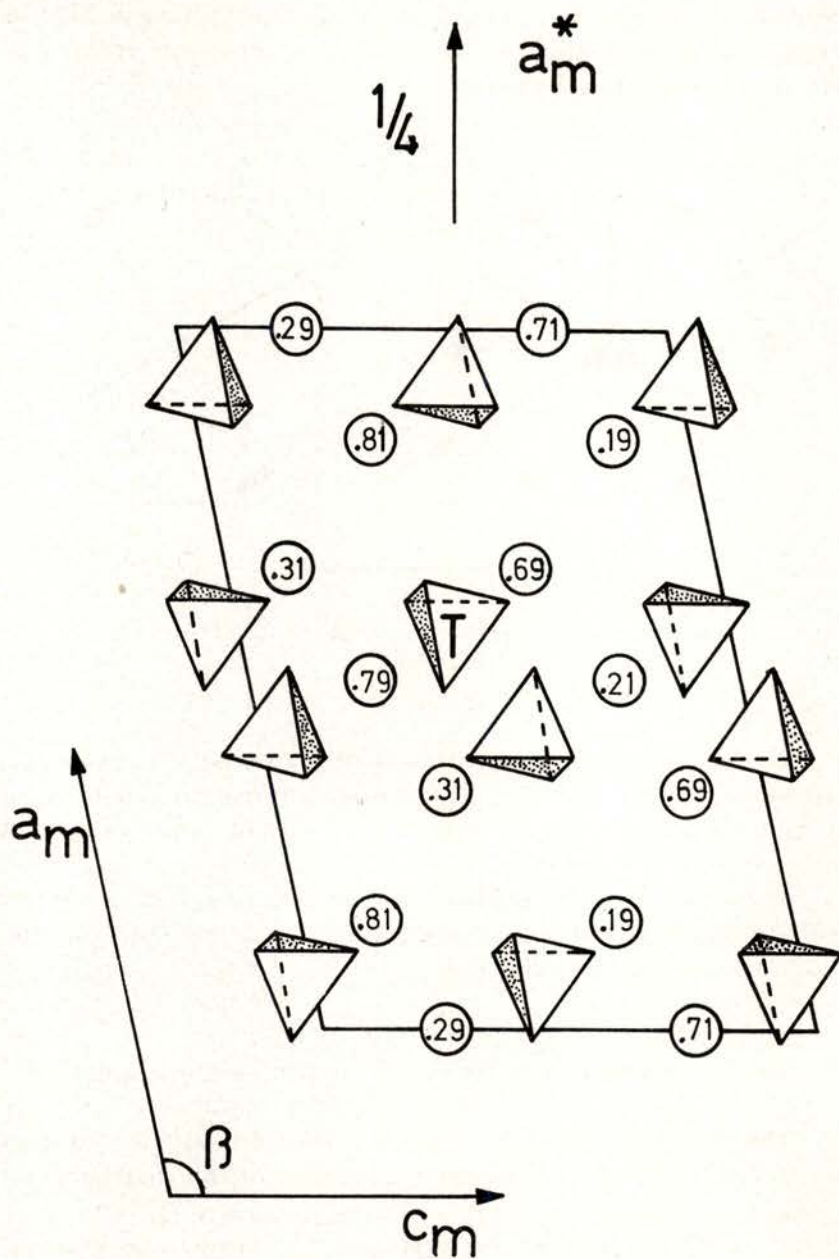
Fig. 5 — Projection of the Pb$_3$(PO$_4$)$_2$ ferroelastic structure on the (010) monoclinic plane (origin on centre of symmetry). The y coordinates are given inside the circles.

This method has proved to be general and includes the materials studied previously, with two domains only.

Atomic coordinates are denoted x^1, y^1, z^1 in domain 1; x^2, y^2, z^2 in domain 2; and x^3, y^3, z^3 in domain 3 (Guimarães, [6]). To obtain coordinates in domains 2 and 3, the lattice is rotated by $2\pi/3$ and $2 \times 2\pi/3$, respectively, about the reciprocal a_m^* axis that is common to the three domains (pseudo-threefold axis). The domains are considered in this case disposed around a_m^* anti-clockwisely, and the rotations of axes for the transformations of coordinates are, accordingly, clockwise.

The result is the following ($u = c_m/b_m$):

$$
\begin{bmatrix} x^2 \\ y^2 \\ z^2 \end{bmatrix} = \begin{bmatrix} 1 & 0 & 0 \\ \dfrac{\sqrt{3}}{2}\, u\, \dfrac{a_m}{c_m} \cos\beta & -\dfrac{1}{2} & \dfrac{\sqrt{3}}{2}\, u \\ -\dfrac{3}{2}\, \dfrac{a_m}{c_m} \cos\beta & -\dfrac{\sqrt{3}}{2} \cdot \dfrac{1}{u} & -\dfrac{1}{2} \end{bmatrix} \begin{bmatrix} x^1 \\ y^1 \\ z^1 \end{bmatrix} \tag{5}
$$

and

$$
\begin{bmatrix} x^3 \\ y^3 \\ z^3 \end{bmatrix} = \begin{bmatrix} 1 & 0 & 0 \\ -\dfrac{\sqrt{3}}{2}\, u\, \dfrac{a_m}{c_m} \cos\beta & -\dfrac{1}{2} & -\dfrac{\sqrt{3}}{2}\, u \\ -\dfrac{3}{2}\, \dfrac{a_m}{c_m} \cos\beta & \dfrac{\sqrt{3}}{2} \cdot \dfrac{1}{u} & -\dfrac{1}{2} \end{bmatrix} \begin{bmatrix} x^1 \\ y^1 \\ z^1 \end{bmatrix} \tag{6}
$$

In the high temperature phase $(a_m/c_m) \cos\beta = -1/3$ and the quantity u is equal to $\sqrt{3}$. Matrices (5) and (6) include the transformation matrices that are obtained when the ferroelastic distortion is absent and take into account the distortion present when the structure is in its low-temperature modification. By adequate use of (5) and (6) the transformed coordinates in domains 2 and 3 are obtained, *axes of reference being those chosen for domain 1.*

Portgal. Phys. — Vol. 13, fasc. 1-2, pp. 39-52, 1982

51

We make here only a short reference to the use of the method. Consider the PO$_4$ tetrahedron marked T in Fig. 5.

Atoms 0(1), 0(2) and 0(3), which form this tetrahedron with P and 0(4) almost aligned along the pseudo-threefold axis, are crystallographically independent in the α phase; they are pseudosymmetrically related by the pseudo-threefold rotation and interchange identity in the ferroelastic transformations. Note that although we are relating two atomic positions by a rotation, we emphasize that the *actual* movement of the atoms in question is only a small displacement.

REFERENCES

[1] K. AIZU, *J. Phys. Soc. Japan*, 27, 387 (1969).

[2] K. AIZU, *Phys. Rev.* B2, 754 (1970).

[3] S. C. ABRAHAMS, J. L. BERNSTEIN and J. P. REMEIKA, *Mat. Res. Bull.*, 9, 1613 (1974).

[4] H. D. MEGAW, *Crystal Structures: a Working Approach*, W. B. Saunders Company (1973).

[5] S. C. ABRAHAMS and E. T. KEVE, *Ferroelectrics*, 2, 129 (1971).

[6] D. M. C. GUIMARÃES, *Acta Cryst.*, A35, 108 (1979).

[7] D. M. C. GUIMARÃES, *Phase Transitions*, 1, 143 (1979).

A CRYSTALLIZATION STUDY OF Se_{1-x} Bi_x (x = 0.05 at) BY CALORIMETRIC METHODS (*)

H. Miranda, F. L. Cumbrera, A. Conde, R. Márquez

Departamento de Optica y Sección de Física del Centro Coordinado del C.S.I.C.
Universidad de Sevilla. Spain

ABSTRACT — Crystallization kinetics of the amorphous $Se_{0.95}$ $Bi_{0.05}$ alloy, prepared by quenching of the melt at 850 K, has been studied by calorimetric DSC measurements. The estimated activation energy is 1.18 eV/at. Heterogenous nucleation is found to be preponderant during 80 % of the time taken by the whole crystallization process. The estimated critical cooling rate of 6.2 K/s is much smaller than the experimental one ($\sim 10^8$ K/s) and this produces a high quantity of homogeneity faults.

1 — INTRODUCTION

As is well known pure selenium and selenium alloys have a remarkable ability to amorphize by different methods. The system Se_{1-x} Bi_x takes advantage of such a good ability for amorphization while it introduces a small amount of Bi that improves the transport properties [1].

In this paper some results about the crystallization kinetics of Se_{1-x} Bi_x (x = 0.05 at) are reported. The time dependence of the crystallized fraction is analyzed to estimate the preponderant mechanism in the crystallization process.

The critical cooling rate of amorphization for this alloy is determined and the temperature dependence of viscosity is established from the time-temperature-transformation curve.

Structural and electron-transport studies for this system are in progress.

---

2 — EXPERIMENTAL

High purity selenium and bismuth (99.999 %) were mixed and enclosed in an evacuated and sealed glass ampule, then held at 850 K for 5 days to make the mixture homogeneous, and finally quenched into water. X-ray diffraction and DTA preliminary runs showed the amorphous character of the samples.

Calorimetric measurements were carried out using a Perkin-Elmer DSC 1 B Differential Scanning Calorimeter, calibrated with indium standards of melting point 429 K, which needs not a remarkable temperature correction in our range of interest [2]. Five heating rates (2, 4, 8, 16 and 32 K/min) were explored for samples in a weight range 10 to 20 mg. All the experiments gave values of $T_{me} = 483 \pm 3$ K for the melting point and $T_g = 305 \pm 2$ K, for the glass-transition temperature of the alloy and dispersion in these values is within the experimental uncertainty. Nevertheless Larmagnac et al. [3] have recently showed some results about a dependence of T_g on heating rate and ageing for amorphous selenium.

For crystallization kinetics studies, an isothermal annealing run was performed at a temperature slightly below 340 K, which is the lowest crystallization temperature found in continuous heating experiments, i.e., that corresponding to a heating rate of 2 degrees per minute. The total time for the crystallization process to be concluded was 44 min for samples of 15 mg. This is a result to be taken into account in order to disregard annealing at much lower temperatures for thermal analysis purposes, if a precision curve integrator is not available.

3 — RESULTS AND DISCUSSION

Kissinger [4] provides an useful method to evaluate the activation energy involved in the process of crystallization, based in the shift of temperature T_m at the maximum of the crystallization peak with the heating rate. It consists of measuring the function — $\ln (\phi/T_m^2)$ versus T_m^{-1}, where ϕ represents the heating

rate. Such a function is plotted in Fig. 1 and a fitting coefficient of 0.998 was found. The activation energy calculated turned out to be 1.18 eV/at for this Se-Bi alloy.
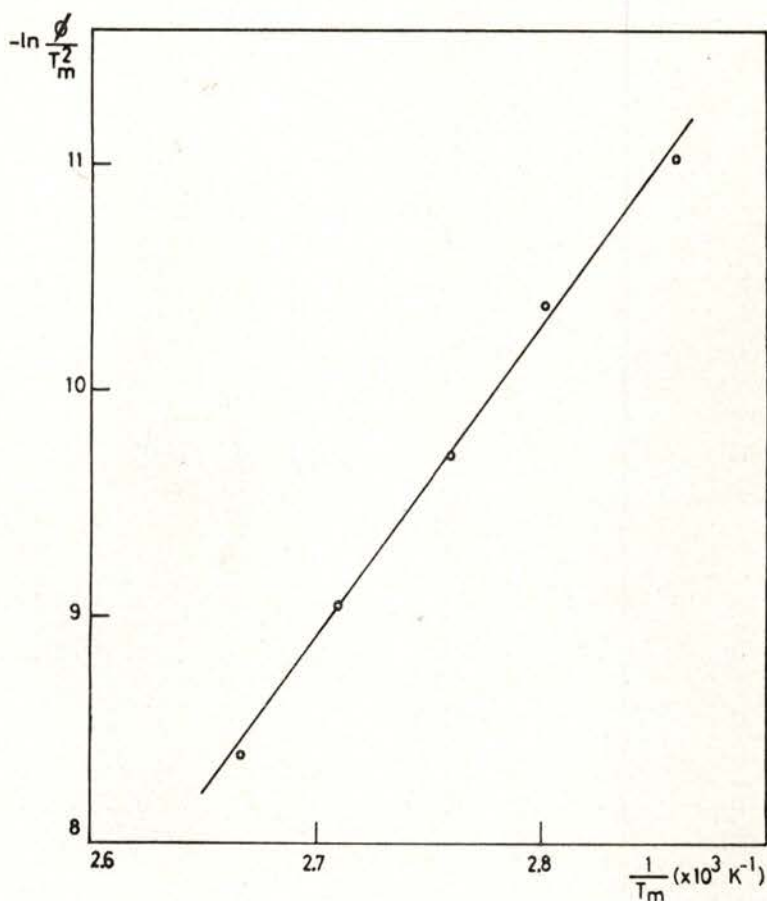
Fig. 1—Evaluation of activation energy by the Kissinger method. E=1.18 eV/at.

The isothermal annealing at a temperature close to the lowest crystallization temperature allows to determine the time evolution of the crystallized fraction α (t), as is plotted in Fig. 2. It is a standard sigmoidal curve, the three characteristic stages in crystallization being present. There is a very short period of germination, due to the initial existence of a great amount of

defects and homogeneity faults that become centres of hetero-
geneous nucleation in crystallization processes. It is followed
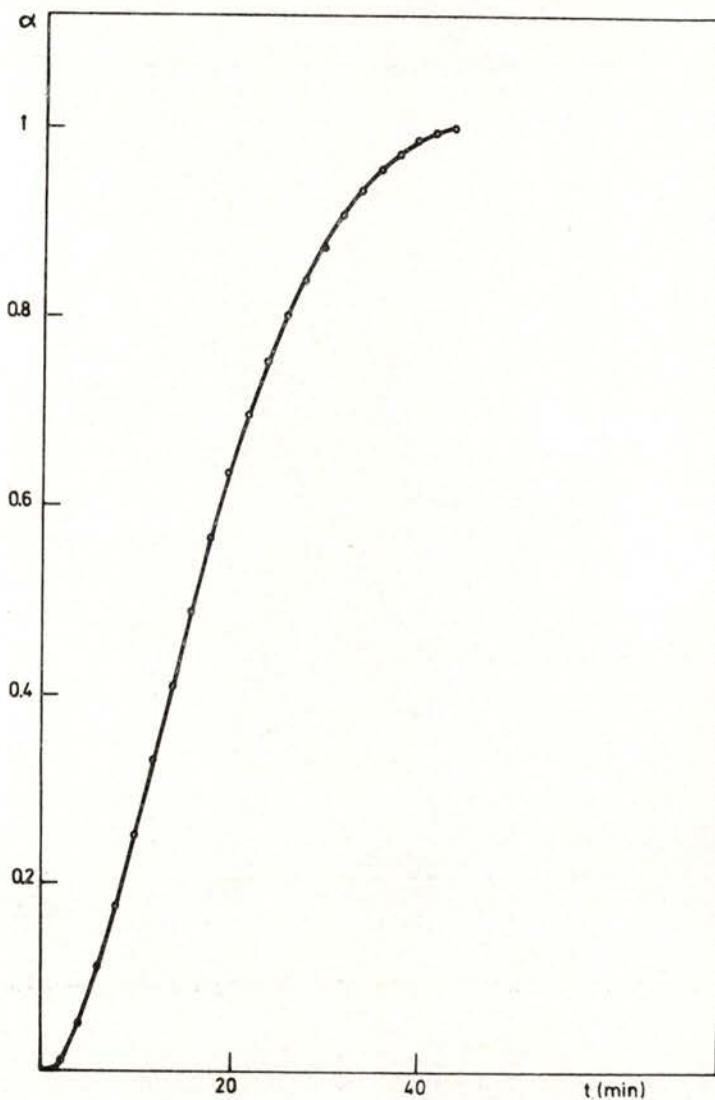
Fig. 2 — Time evolution of crystallized fraction.

by a much longer period of acceleration of the process, and then
by a final decay until the crystallization is completed. Following

Germain et al. [5] an order of magnitude for the different crystal growth mechanisms can be derived by determining the power r that affects the time t in the most significant terms of the polynomy $\ln [1/(1-\alpha)] = \lambda \ t^r$.

Fig. 3 shows a plot of $\ln \{ \ln [1/(1-\alpha)] \}$ vs $\ln$ t. The first straight stage gives values $r = 1.81$ and $\lambda = 4.38 \times 10^{-3}$ min^{-2},
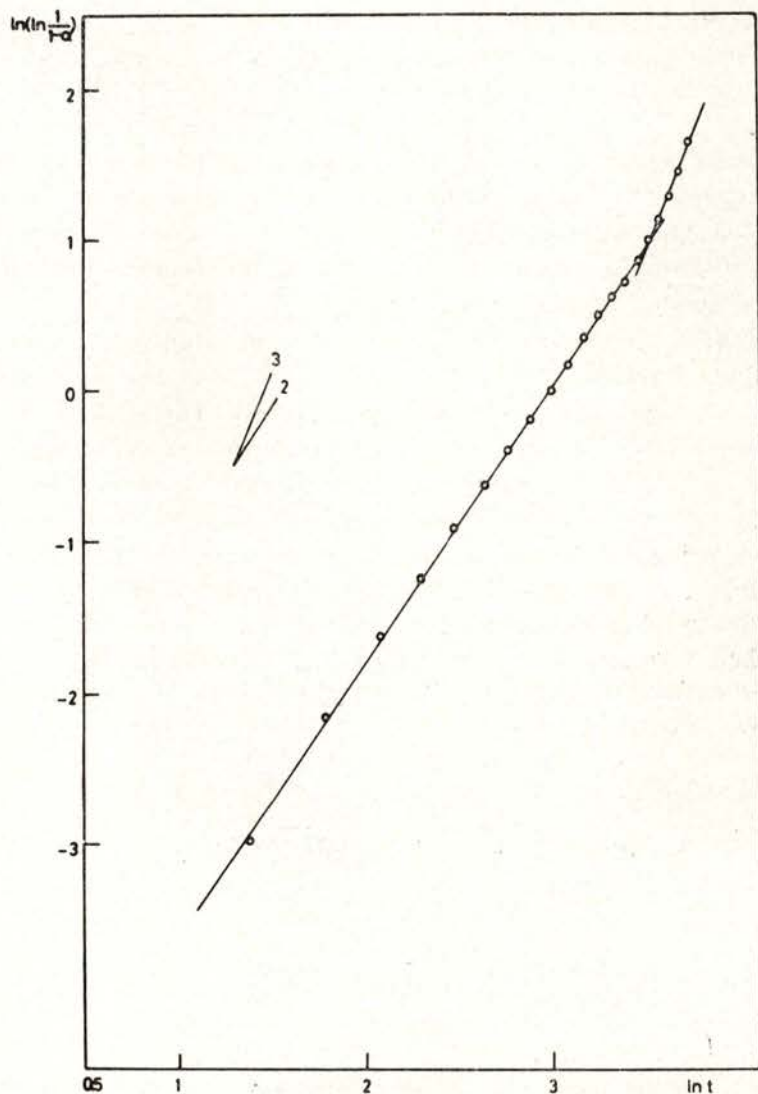
Fig. 3 — Kinetics of amorphous-crystal transformation.

with a fitting coefficient of 0.999. Such a power r ~ 2, for a bulk induced crystallization, allows λ to be $\lambda = (p/S) \, \pi \, V_g^2$, where V_g is the crystal growth rate and p/S is the initial number of crystallites per unit area, that will contribute to heterogeneous growth. Assuming a typical value of $V_g = 10$ Å s^{-1}, we obtain a crystallite concentration $p/S = 3.9 \times 10^7$ cm^{-2}.

The second stage in Fig. 3 gives $r = 3.14$, $\lambda = 4 \times 10^{-5}$ min^{-2} (fitting coefficient 0.996) and a power r ~ 3 leads to describe $\lambda = (\pi/3) \, n \, V_g^2$, where n is the homogeneous nucleation rate per unit area. So the resulting nucleation rate is $n = 1.1 \times 10^6$ cm^{-2} min^{-1}.

Those results show that, if the same V_g is still assumed, the homogeneous nucleation does not become preponderant until about 35 min after the beginning of crystallization, which is about 80 % of full time, and it is due to the presence of such a large number of nucleation centres.

In order to determine the glass-forming ability, a suitable crystalline fraction of 3.10^{-2} was measured from the total area of thermograms. A time-temperature-transformation (TTT) curve is drawn in Fig. 4, where the lower part (points o) is experimental and the rest (points +) is extrapolated by the use of the kinetics expression for the crystallization fraction $\alpha \sim (\pi/3) \, I \, u^3 \, t^4$, I and u being the homogeneous nucleation rate and the crystal growth rate respectively [6]. Such an extrapolation may be done through the calculation of another interesting parameter: the liquid quenched viscosity η in the range T_{me} (melting point) to T_g (glass-transition temperature). Viscosity is evaluated from the experimental data using Uhlmann theory [7] through the expressions

$$I = \frac{N_v^\circ \, K \, T}{3 \, \pi \, a_o^3 \, \eta} \, \exp \left[-\frac{16 \, \pi}{3} \, \frac{\sigma^3 \, T_{me}^4}{(\Delta H_{me})^2 \, (\Delta T)^2 \, RT^3} \right]$$

and

$$n = \frac{f \, K \, T}{3 \, \pi \, a_o^2 \, \eta} \left[1 - \exp \left(-\frac{\Delta H_{me} \, \Delta T}{R \, T \, T_{me}} \right) \right]$$

where N_v° is the mean volume concentration of atoms, a_o is the atomic diameter, σ is the molar free interface enthalpy between
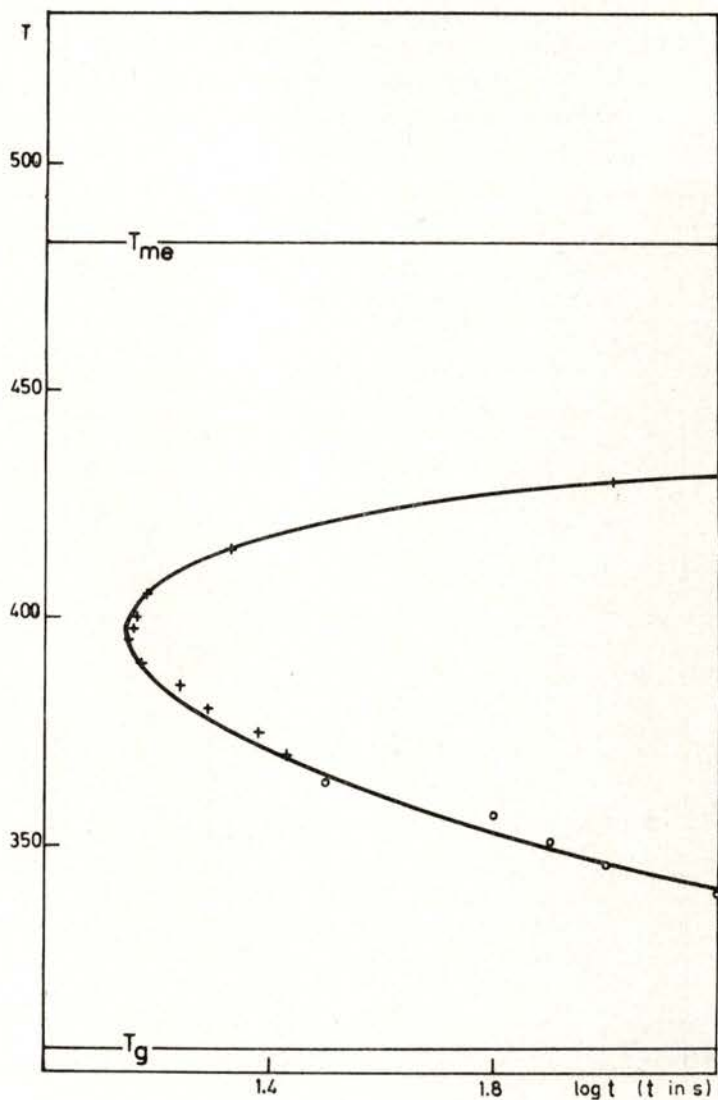
Fig. 4 — Time-Temperature-Transformation (TTT) curve between T$_{me}$ and T$_g$.
(o: experimental; +: calculated).

nucleus and liquid, ΔH_{me} the molar enthalpy of fusion, $\Delta T = T_{me} - T$ and f the fraction of sites at the crystal-liquid interface. To calculate η, N_v^o is known from the alloy density ($\rho = 4.6$ g.cm^{-3}),

ΔH_{me} measured is 1700 J/at.g, and assumptions made in [8] remain valid so that $a_o = 4$ Å, $f = 1$ and $\sigma = 0.32$ ΔH_{me}.

Fig. 5 shows the temperature dependence of viscosity where the full line is experimental and the dashed portion is calculated
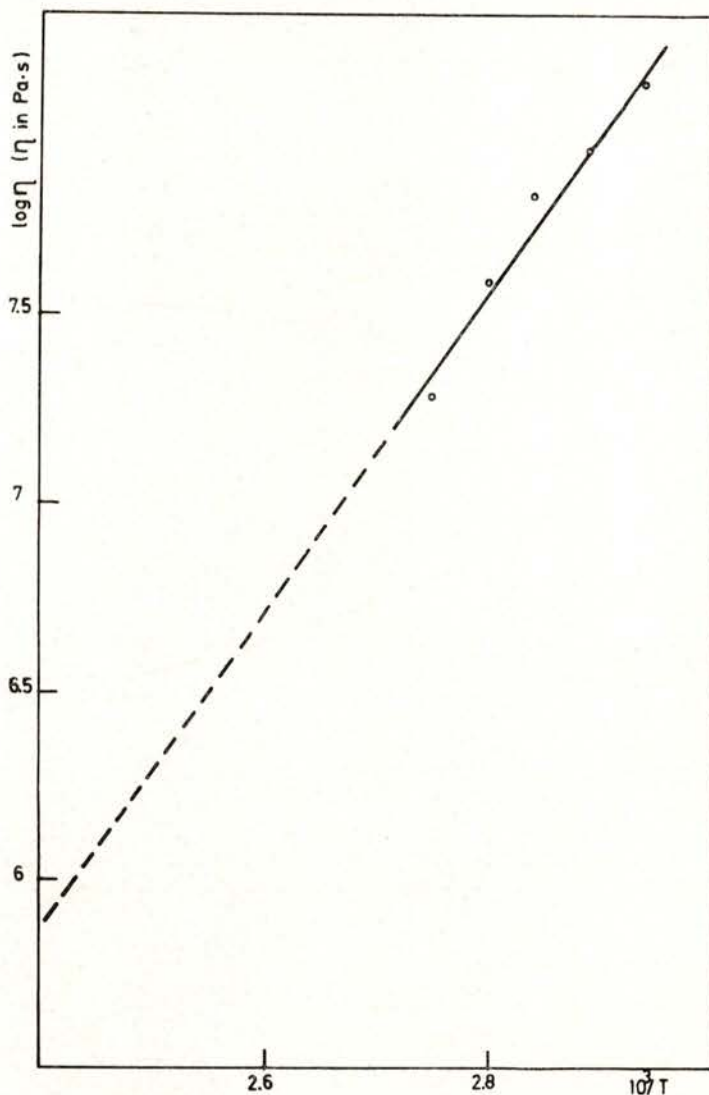
Fig. 5 — Temperature dependence of viscosity η (Full line: experimental; dashed line: calculated).

60

Portgal. Phys. — Vol. 13, fasc. 1-2, pp. 53-61, 1982

from an Arrhenius equation $\eta = A \exp (a/T)$, with $A = 4.2 \times 10^{-5}$ Pa.s and $a = 4260$ K.

Temperature T_n and time t_n being 395 K and 14.1 s, respectively, at the nose of the TTT curve, the corresponding value for the critical cooling rate R_c, to get the alloy amorphous is: $R_c = (T_{me} - T_n)/t_n = 6.2$ K s^{-1}, which is well below what is achieved with a quenching technique. This value of the critical cooling rate is consistent with the known ability of amorphization of selenium alloys, but is more restricting than the estimated for ternary alloys [8].

The experimental cooling rate ($\sim 10^3$ K.s^{-1}) is much higher than the critical value; this could explain the high amount of homogeneity faults and, therefore, the preponderance of an heterogeneous nucleation mechanism along the crystallization process.

REFERENCES

[1] Tohge, N., Minami, T., Tanaka, M. J., *J. Non-Cryst. Sol.*, **37**, 23 (1980); *J. Appl. Phys.*, **51**, 1048 (1980).

[2] McNaughton, J. L., Mortimer, C. T., *Differential Scanning Calorimetry*, p. 9. Reprinted from «IRS; Phys. Chem. Series 2, vol. **10** (1975)».

[3] Larmagnac, J. P., Grenet, J., Michon, P., *J. Non-Cryst. Sol.* **45**, 157 (1981).

[4] Kissinger, H. E., *Analy. Chem.*, **29**, 1703 (1957).

[5] Germain, P., Squelard, S., Bourgoin, J. C., Gheorghiu, A., *J. Appl. Phys.*, **50**, 6986 (1979).

[6] Uhlmann, D. R., *J. Non-Cryst. Sol.*, **7**, 337 (1972).

[7] Uhlmann, D. R., *Mat. Sci. Res.*, vol. **4** (Plenum Press, N. Y.), p. 172 (1969).

[8] Clavaguera, N., Clavaguera-Mora, M. T., Casas-Vazquez, J., *J. Non--Cryst. Sol.*, **22**, 23 (1976).

CHARACTERIZATION OF AMORPHOUS $Se_{1-x} Bi_x$ (x = 0.05 at) COEVAPORATED THIN FILMS (*)

A. MUÑOZ, J. LEAL, A. CONDE, R. MÁRQUEZ

Departamento de Optica y Sección de Física del Centro Coordinado del C.S.I.C.
Universidad de Sevilla. Spain.

ABSTRACT — Thermal evolution of amorphous $Se_{1-x} Bi_x$ (x = 0.05 at) coevaporated thin films has been characterized by electrical resistivity measurements and electron microscopy observations. Optical measurements on amorphous and crystallized films have been performed by ellipsometric methods.

1 — INTRODUCTION

The electronic properties of amorphous chalcogenide semiconductors can be modified or controlled by addition of some impurities; the effects of various kinds of foreign atoms on electrical conductivity, optical absorption, etc., have been extensively studied [1].

Bi-doped chalcogenides exhibit a striking feature: they show n-type conduction [2], [3] as opposed to the more common p-type conduction observed in chalcogenide semiconductors.

In this paper some initial results on the $Se_{1-x} Bi_x$ system (x = 0.05 at.) relative to crystallization and optical properties are reported. The aim of the work is to study possible differences between coevaporated thin films and the melt-quenched material of the same composition.

2 — EXPERIMENTAL

Thin films of $Se_{1-x} Bi_x$ were prepared by vacuum thermal evaporation (~ 10^{-4} Pa) of high-purity selenium and bismuth from two separate allumina crucibles. Glass and allumina substrates were used and kept during deposition at a temperature of ~ 170 K by liquid nitrogen refrigeration.

(*) Presented at the VII Iberoamerican Congress of Crystallography (21-26 September 1981, Coimbra, Portugal).

The film composition could be varied simply by controlling the crucible temperatures and for this work a value of $x \simeq 0.5 \%$ at was selected. Composition and thickness of films were monitored during evaporation by a quartz oscillator device and the evaporation rate was 1.5 nm s^{-1} approximately.

For *in situ* electrical measurements films of thickness in the range between 50 and 500 nm were deposited onto allumina substrates in which Au electrical contacts had been evaporated previously. Electrical measurements were performed on films inside the evaporation chamber after concluding the film formation and a Keithley 602 electrometer was used.

Films for electron microscopy observation and optical measurements were deposited onto glass substrates and a higher thickness ($\sim$ 1500 nm) was used in the last case. Ellipsometric measurements were carried out on a classical device (Fig. 1) using a iodine lamp, a holographic grating monochromator and a quarter-wave plate for the Na wavelength λ of 589 nm. The measurements were made by null setting the polarizer and the analyser, which gave two characteristic parameters: Δ defined as the phase angle change, and Ψ defined as the arctangent of the amplitude ratio change [4]. In such measurements we could have two experimental parameters but there are three unknowns which are the refractive index n, the extinction coefficient k and the film thickness d. However, for films thicker than 1 μm the effect of the reflection at the substrate surface is negligeable and the film thickness can be considered as infinite for short wavelengths.

In this work, the shortest and longest wavelengths used were 300 nm and 750 mm respectively owing to restrictions
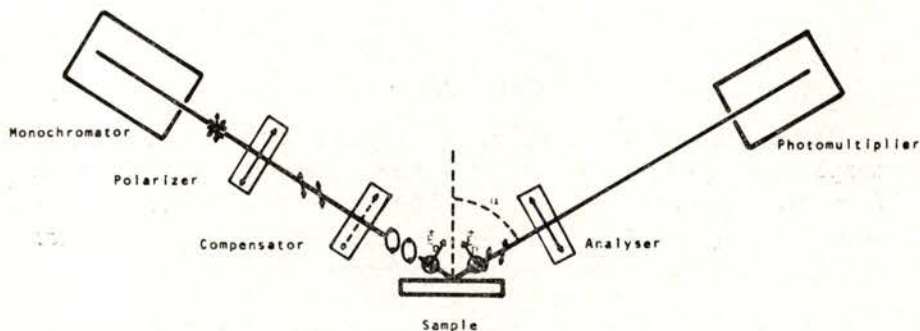
Fig. 1 — A schematic drawing of ellipsometric device.

64

Portgal. Phys. — Vol. 13, fasc. 1-2, pp. 63-74, 1982

imposed by the quality of the optical elements of the ellipsometric device. All measurements were performed at ∼ 300 K in a dark room.

3 — RESULTS

3.1 — *Electrical resistivity*

Thermal evolution of electrical resistivity of films was studied between the deposition temperature (∼ 170 K) and 400 K at a heating rate of 4 K min⁻¹ approximately. For thicknesses in the explored range (50 to 500 nm) the ρ *vs* T curves exhibit the same qualitative features and Fig. 2 shows the temperature variation of electrical resistivity for a film of 80 nm thickness.
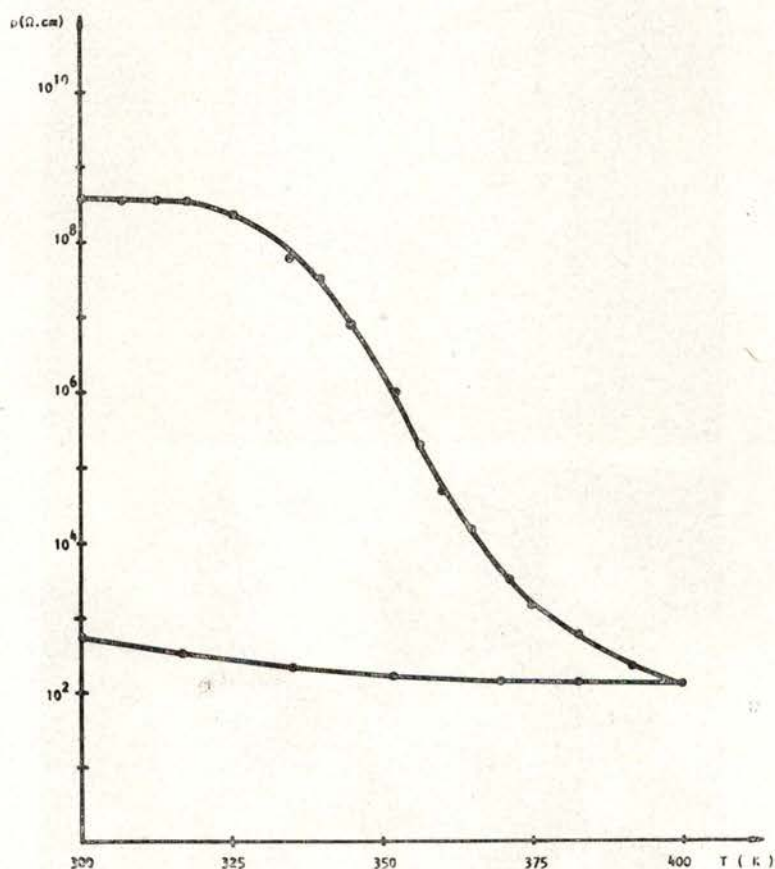
Fig. 2—Temperature dependence of electrical resistivity for a 80 nm thick film.
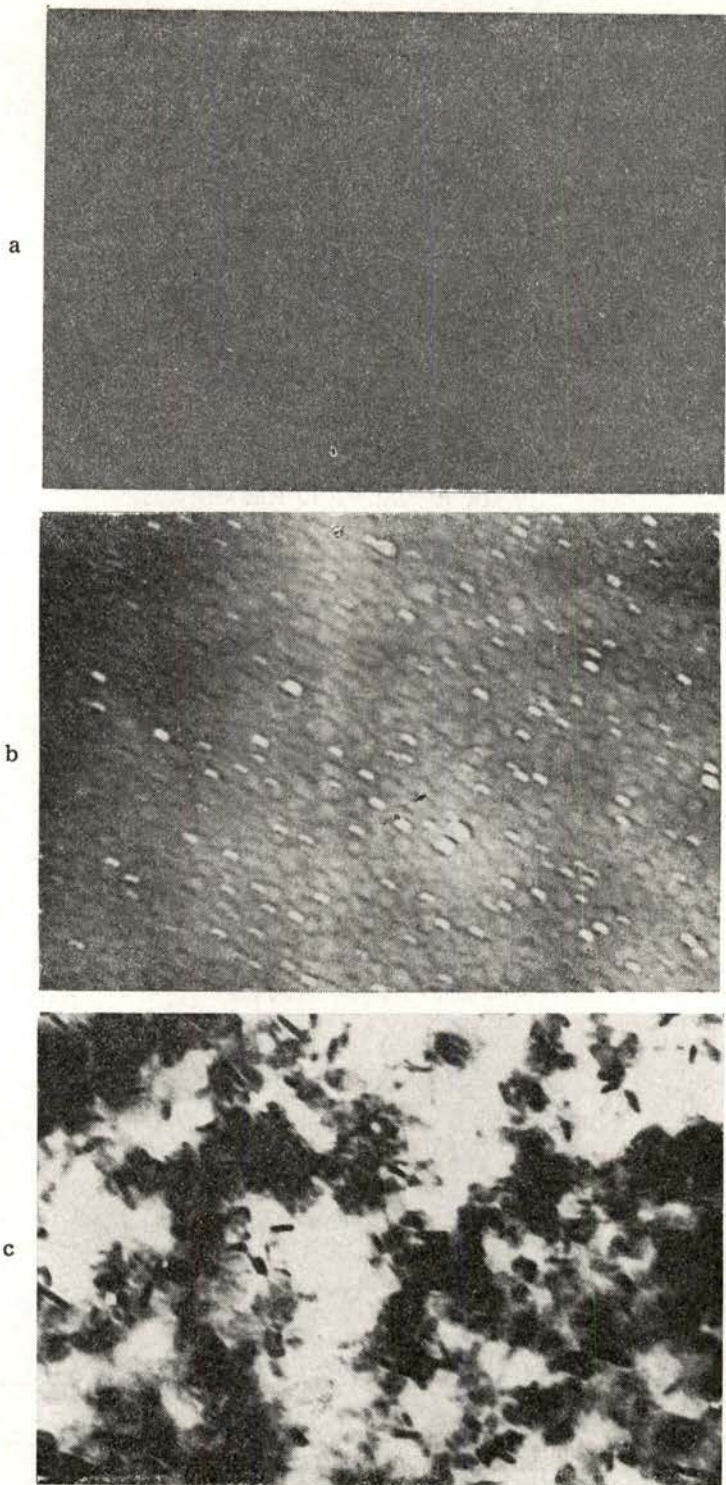
Fig. 3 — Electron micrographs (x 110,000): a) amorphous film, b) intermediate stage of crystallization process and c) crystallized film.
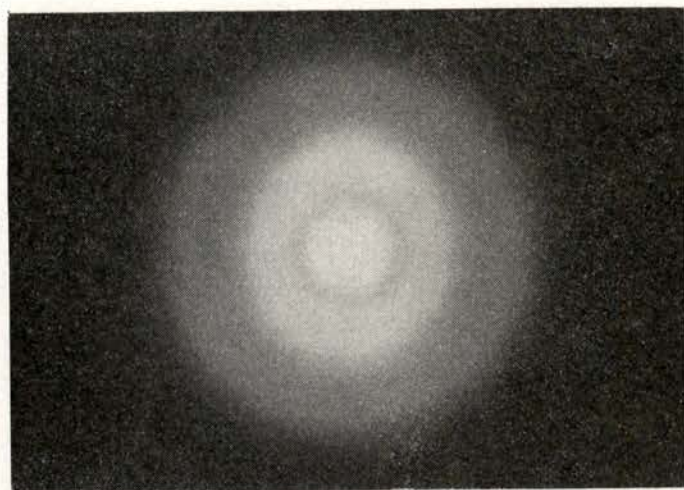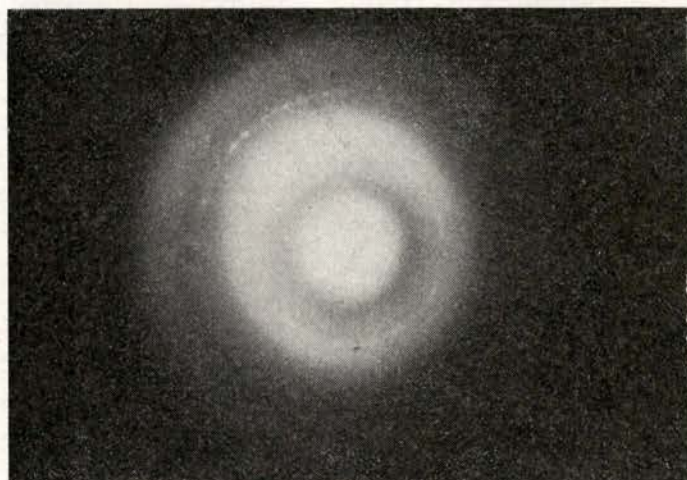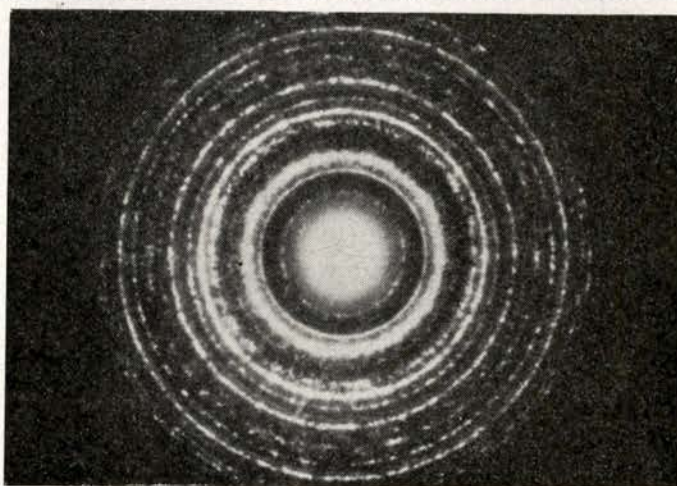
Fig. 3 — Selected area diffraction patterns: a) amorphous film, b) intermediate stage of crystallization process and c) crystallized film.

As observed, the main feature in the ρ vs T curve is an abrupt fall of a few orders of magnitude around 350 K that we associate with the amorphous-crystal transformation. This agrees with the crystallization temperature T$_c \approx$ 360 K [5] determined by calorimetric methods (DSC) for quenched material of the same composition. The irreversible character in the resistivity change is shown clearly in a subsequent cooling process.

3.2 — *Electron microscopy*

The amorphous character of the films has been proved by electron diffraction. The samples were observed in an electron microscope (100 KeV) using a cooling holder and defocussing the incident beam to prevent instantaneous crystallization. Fig. 3 shows electron micrographs and selected area diffraction patterns of three stages of thermal evolution inside the microscope. Fig. 3.a corresponds to the initial stage and reveals the non-crystalline character through the structureless features of the micrograph and the broadened haloes exhibited by the diffraction pattern. Fig. 3.b shows an intermediate stage of amorphous-crystal transformation as indicated by the grain structure in the micrograph and the rings observed in the diffraction pattern; finally, in Fig. 3.c the crystallization process is completed.

From the intensity of the amorphous diffraction pattern, measured with a Joyce microdensitometer, a first approximation to the structure factor (Fig. 4) has been obtained. The method proposed by Nabitovich et al. [6] has been used to eliminate the background intensity and estimate the normalization factor. Features of this structure factor are similar to those reported for amorphous selenium and quantitative differences among them are at first difficult to see.

3.3 — *Optical measurements*

The complex refractive index is defined as $n^* = n - ik$ where the real part is the refractive index and the imaginary part is the extinction coefficient. These constants can be derived [7] from the measured values of Δ and Ψ.
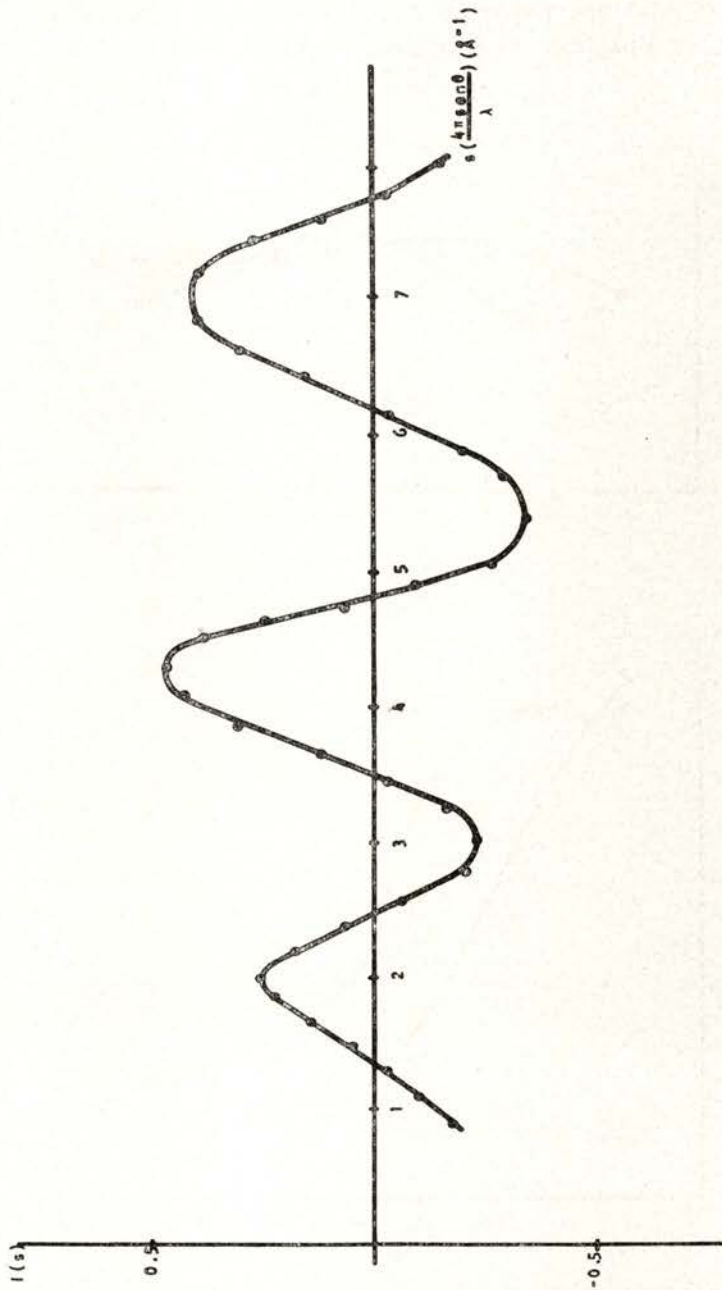
Fig. 4 — A first approximation to the structure factor.

The values of n and k as a function of wavelength of the incident light are shown in Fig. 5 for the amorphous films and after crystallization by annealing at 350 K during 24 h.
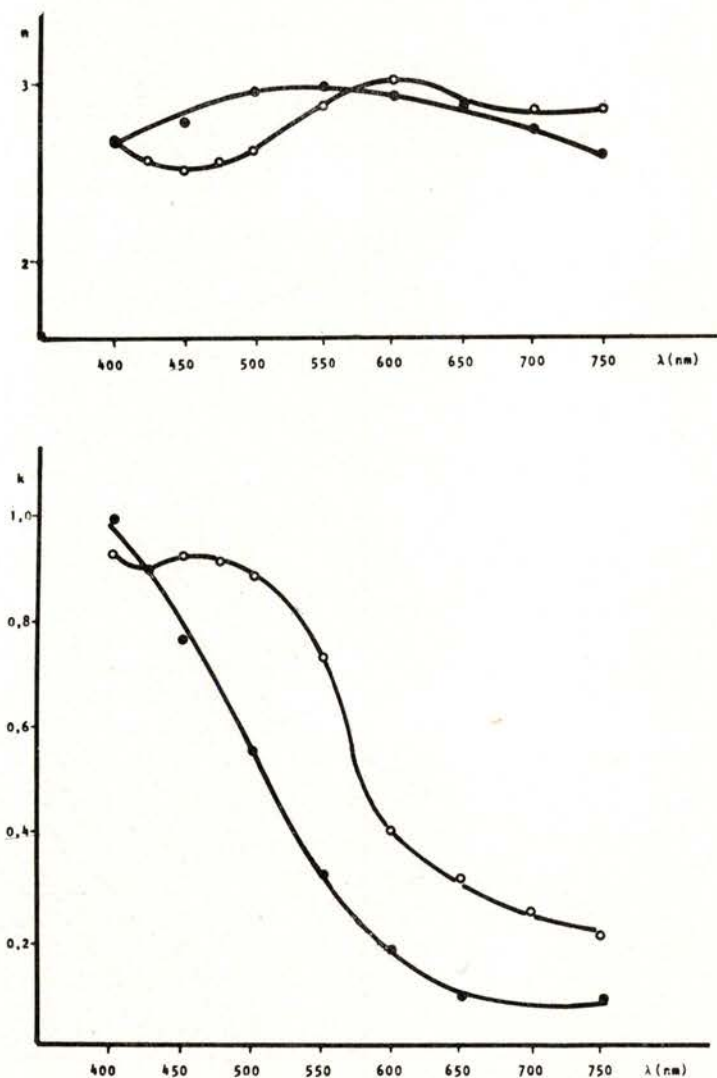
Fig. 5 — Complex refractive index as a function of wavelength for amorphous (•) and crystallized (o) films: a) refractive index, and b) extinction coefficient.

A. Muñoz *et al.* — *Amorphous* $Se_{1-x} Bi_x$ *(x = 0.05 at) coevaporated thin films*

The real part ε' and the imaginary part ε'' of the complex dielectric constant can be calculated from the complex refractive index by

$$\varepsilon' = n^2 - k^2$$
$$\varepsilon'' = 2nk$$

and results derived from the data given in Fig. 5 are shown in Fig. 6. The features observed in the ε'' curves are analogous to
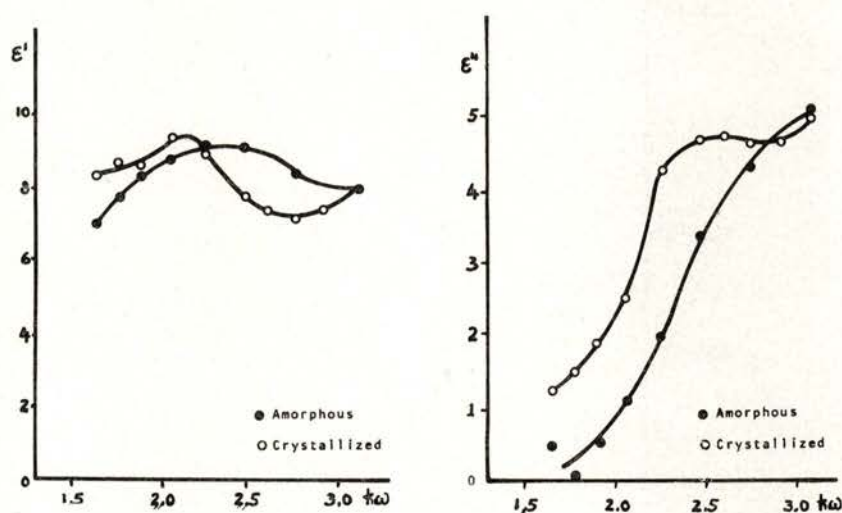
Fig. 6 — Complex dielectric constant as a function of incident photon energy, for amorphous and crystallized films: a) real part, and b) imaginary part.

those reported for amorphous selenium [1] and so the peak at ~ 2.5 eV shown for the crystal films is lost in the amorphous case.

The absorption coefficient α can be related to the extinction coefficient k by

$$\alpha = 4\pi k/\lambda$$

and Fig. 7 shows the values of the absorption coefficient calculated from the data given in Fig. 5.

Portgal. Phys. — Vol. 13, fasc. 1-2, pp. 63-74, 1982

71

For amorphous films, values of the absorption coefficient above the exponential edge fit very well the relation [8]:

$$\alpha \, \hbar \, \omega = A \, (\hbar \, \omega - E_{opt})^2$$
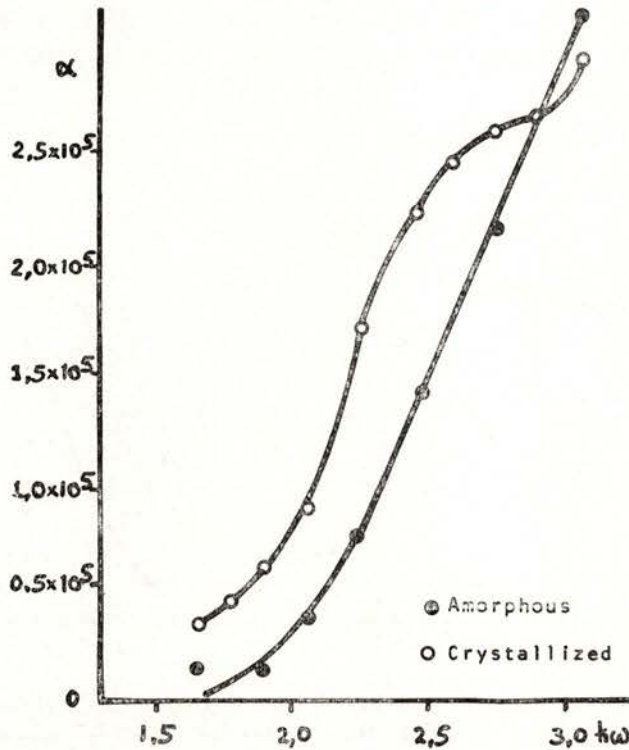
Fig. 7 — Absorption coefficient as a function of exciting photon energy for amorphous and crystallized films.

where E_{opt} is the optical band gap and A is a constant, as can be observed in Fig. 8. Values obtained from a least-squares fit are $E_{opt} = 1.63$ eV and $A = 6.8 \times 10^7$ m^{-1} eV^{-1} (linear regression coefficient $r = 0.999$). The computed value of the A constant is in good agreement with those predicted theoretically [1], [8]. For the crystallized films a worse fit is found: $E_{opt} = 1.41$ eV

A. Muñoz et al. — Amorphous $Se_{1-x} Bi_x$ (x = 0.05 at) coevaporated thin films

and $A = 6.9 \times 10^7$ m^{-1} eV^{-1} (r = 0.892); but a more satisfactory agreement is obtained in this case using the relation

$$\alpha \hbar \omega = A (\hbar \omega - E_{opt})$$

proposed [1] for amorphous selenium. A more detailed study is necessary to ellucidate this point.
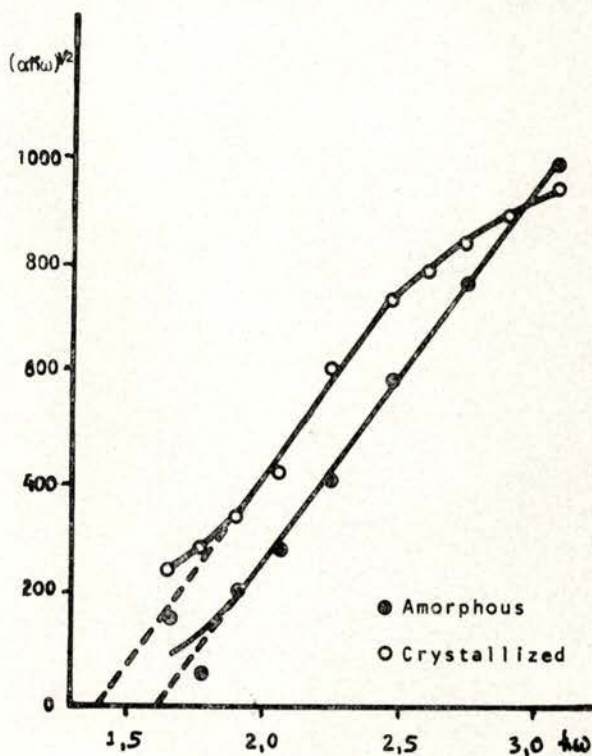
Fig. 8 — Values of $(\alpha \hbar \omega)^{1/2}$ as a function of exciting photon energy for amorphous and crystallized films.

REFERENCES

[1] MOTT, N. F., DAVIS, E. A., Electronic Processes in Non Crystalline Materials (2nd ed.). Clarendon, p. 517 (1979).
[2] HENKELS, H. W., MACZUK, J., Phys. Rev., 24, 1056 (1953).

[3] TOHGE, N., MINAMI, T., TANAKA, M. J. Non Crystal. Solids, **37**, 23 (1980);
     J. Appl. Phys., **51**, 1048 (1980).
[4] ARCHER, R. J. in the *Symposium on the Ellipsometer and its Use in the
     Measurements of Surfaces and Thin Films.* Natl. Bureau Stand.
     Washington D. C. (1963) Miscellaneous Publ., 256.
[5] MIRANDA, H., CUMBRERA, F. L., CONDE, A., MARQUEZ, R., *Portgal. Phys.*,
     13, 53 (1982).
[6] NABITOVICH, I. D., STETSIV, YA. I., VOLOSHCHUK, YA. V., *Sov. Phys. Cryst.*,
     12, 513 (1968).
[7] BORN, M., WOLF, E., *Principles of Optics.* Pergamon Press Inc., p. 617
     (1959).
[8] DAVIS, E. A., MOTT, N. F., *Phil. Mag.*, **22**, 903 (1970).

CRYSTALLIZATION SIZE EFFECTS STUDY OF Fe$_{40}$Ni$_{38}$Mo$_4$B$_{18}$ METALLIC GLASS FROM HIGH VOLTAGE (1 MeV) ELECTRON MICROSCOPY (*)

F. L. Cumbrera, P. Vigier (^{1}), A. Conde and R. Márquez

Departamento de Optica y Sección de Física del Centro Coordinado del C.S.I.C.
Universidad de Sevilla. Spain.

ABSTRACT — A size effect study of the intermediate phases MSI and MSII, on the crystallization of Fe$_{40}$Ni$_{38}$Mo$_4$B$_{18}$ (2826 MB) metallic glass has been carried out. Time evolution of morphological parameters for both grain classes are analysed in the border and inner parts of the wedge-shaped samples observed in a H.V. electron microscope. The transformation rate is accelerated in thinner regions until a saturation is reached.

1 — INTRODUCTION

In the last few years great attention has been paid [1]-[3] to the morphological description of polycrystalline materials and their time evolution. The development of sophisticated automated data systems permitting more reliable results and a better knowledge of physical mechanisms involved in grain growth processes allows the study of some complex problems like textures [4], recrystallization dynamics [5], plastic deformation [6], 'abnormal' grain growth [7], etc. However, to the best of our knowledge, these methods have not been applied to study the nucleation and the grain growth processes during the crystallization of amorphous systems.

Portgal. Phys. — Vol. 13, fasc. 1-2, pp. 75-81, 1982

75

The crystallization process of the metallic glass $Fe_{40}Ni_{38}Mo_4B_{18}$ (2826 MB) [8] takes place in two stages, the second one presenting a close analogy with the recrystallization in cold-rolled metals. In this work the image analysis techniques are applied to elucidate the effects of thickness on the crystallization kinetics of the above metallic glass.

2 — EXPERIMENTAL

Samples prepared as described elsewhere [8] were examined in a high voltage electron microscope (1 MeV) at ONERA (Paris). The samples were heated inside the microscope up to 775 K - above the second stage of the crystallization process - and annealed for 20 minutes at this temperature prior to a dynamic heating to reach the high temperature stable phase.

Images of structural evolution were recorded on a magnetoscopic band. Morphological parameters were measured using a Kontron MOPO2 image analyser. This instrument uses a magnetic cross-grid table with a sensor pen under operator control. By detecting pulses propagating along the X and Y wires and measuring their time of flight to the pen it is possible to determine the x-y coordinates of points on the grain perimeter. These coordinates are fed to a microprocessor which calculates both the perimeter and the area of each grain cross section.

3 — RESULTS

An observed feature on the electron microscope images is that crystallization starts at the border of the wedge-shaped sample, showing a higher nucleation rate than the thicker areas. The crystallite surface density determined in these two areas of the sample are plotted against time in Fig. 1, showing a good linear dependence in both cases. However, it is noteworthy that a saturation of the nucleation mechanism takes place at the border region after about ten minutes.

The nucleation rates calculated by a least-squares fit of data in Fig. 1 are 18.9 s^{-1} and 16.2 s^{-1}, respectively. This observed

difference has been considered significative, from statistical considerations, at a confidence level of 5 %.
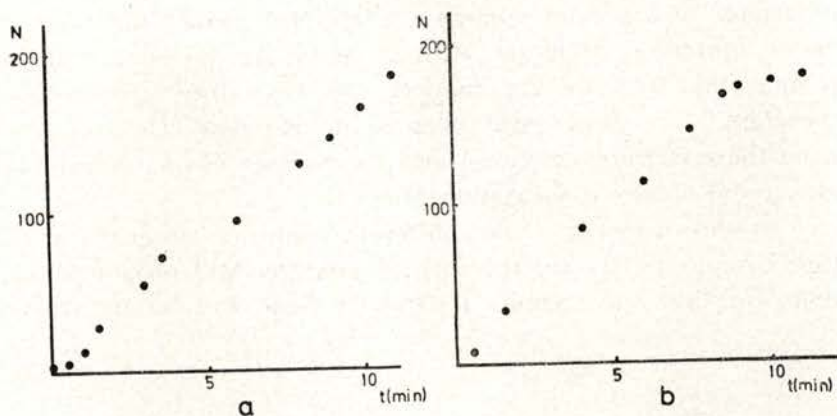
Fig. 1 — Time evolution of nuclei number surface density: a) inside the sample
b) at the border.

Table 1 gives the mean morphological parameters determined for the two sample areas studied. For the grain area a, one defines an equivalent planar diameter $D_a = (4a/\pi)^{1/2}$, and for the perimeter s of the grain, an equivalent planar diameter $D_s = s/\pi$: D_{max} is the maximum diameter of the grain, D_x and D_y are the Feret's diameters [9] and F is a shape factor given by $F = 4\pi a/s^2$.

TABLE 1

	D_a	D_s	D_{max}	D_x	D_y	F
Border	99	115	113	110	103	0.68
Inside	148	180	180	167	156	0.62

Diameters are expressed in nm.

At this stage, two intermediate phases, MSI and MSII, are present in the sample; the first one is formed by small finely

dispersed crystallites and the second one by coarse particles. Data in Table 1 refer to the whole population of the two grain classes.

The higher mean diameter in the thicker region could be associated to a greater volume available for growth, allowing an easier formation of larger MSII crystals. At the border of the sample the free surface hinders the crystallite growth and, therefore, the smaller MSI crystals predominate. On the other hand these steric restrictions limit the number of nucleation sites giving the observed saturation effect.

As shown in Fig. 2, two different zones are observed in the time evolution of D_a for the small crystallite (MSI phase) population. The first one exhibits a parabolic form and can be related
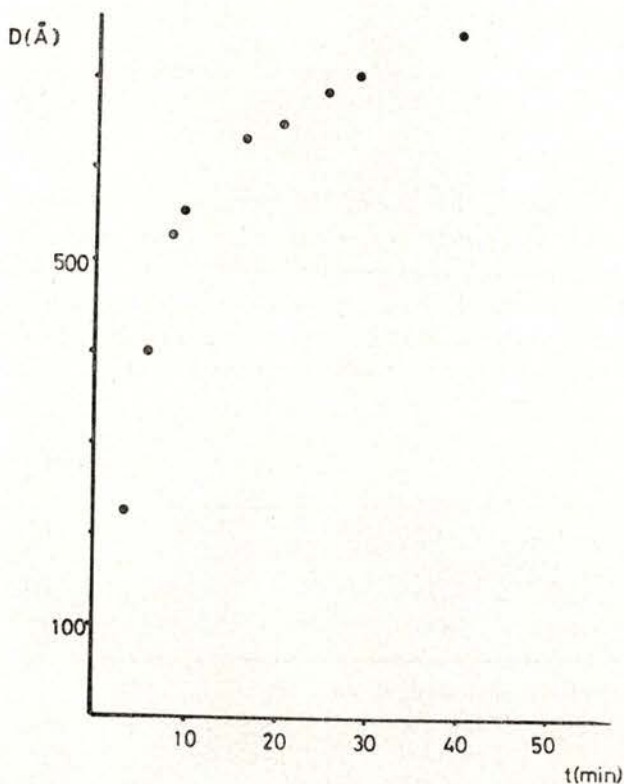
Fig. 2 — Time evolution of equivalent planar diameter for MSI phase grains.

to a diffusion controlled growth (primary nucleation), whereas the second is linear and should correspond to the overlapping of diffusion fields in a saturated situation.
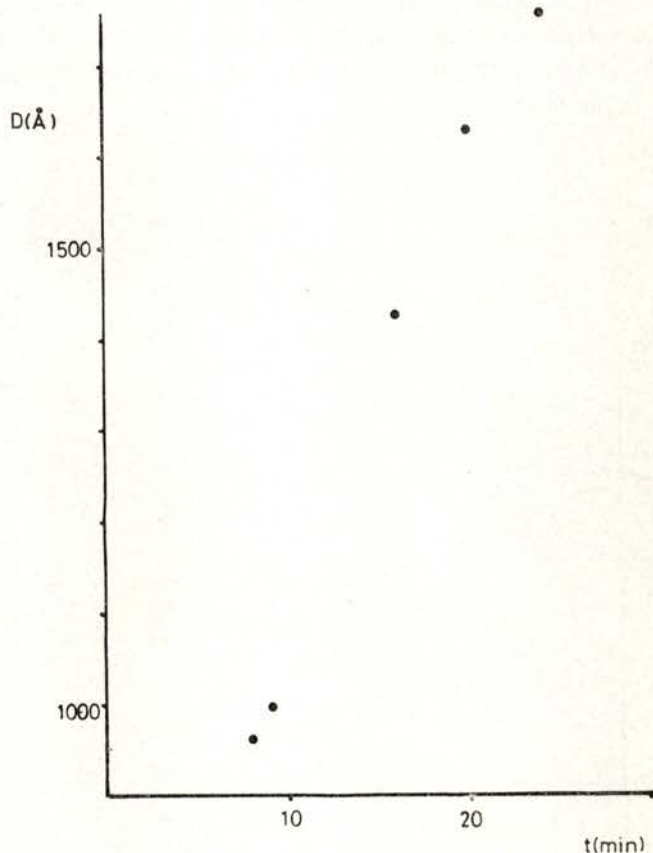
Fig. 3 — Time evolution of equivalent planar diameter for MSII phase grains.

For the other crystallites (MSII phase) the time evolution of D_a (Fig. 3) is linear in all the time range; this behaviour could be assigned to an interfase controlled growth. The growth rate of MSII crystals is higher than the MSI one and, as a consequence, the initial overlapping of the two grain class populations vanishes: MSII phase predominates, exhausting the remaining amorphous matrix.

Standard deviations versus time for lognormal distributions of D_a are show in Fig. 4 for both grain classes. As observed, the standard deviation is higher for MSI crystals and this could be explained from the primary character of crystallization reaction, the time-extended homogeneous nucleation giving a more dispersed distribution. MSII crystals are formed by a peritectic process, therefore the size distribution of crystals is more homogeneous.
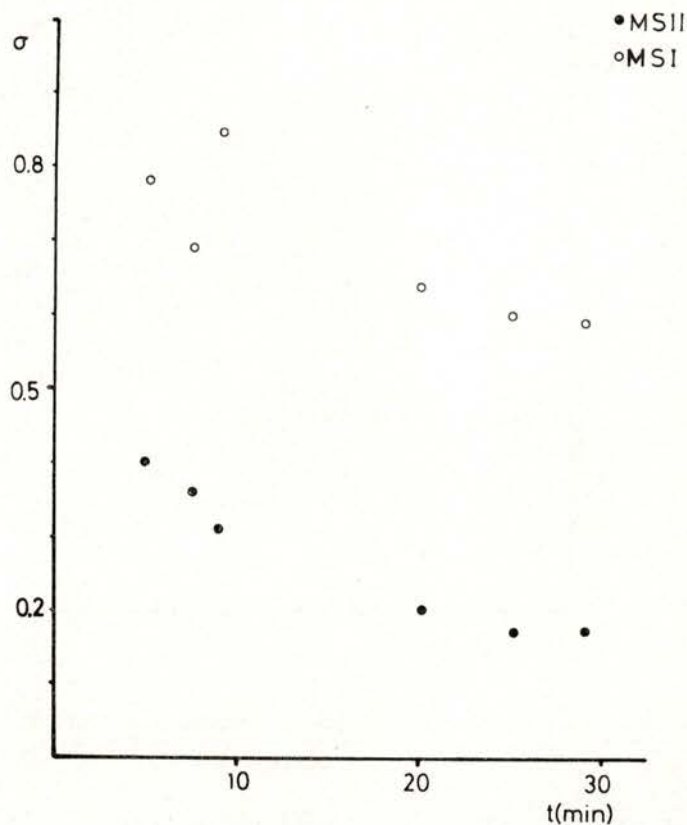
Fig. 4 — Time dependence of standard deviation for both grain populations.

An additional comment to Fig. 4 is relative to the time variation of the standard deviation at the first period of time. In fact, the theory of Kurtz & Carpay [10] predicts that the

standard deviation of equivalent Gaussian distributions of the size parameters for a lognormal population are independent of time. However, this conclusion is based on the hypothesis that no new grains are nucleated during normal grain growth ($\dot{N} \leqslant 0$) and this condition is fullfilled only after the amorphous matrix is exhausted. At this moment the growth of individual grains occurs by the collapse of adjacent grains together with a discontinuous transfer between topological classes.

We can conclude that crystallization has a very local character and the sample thickness may affect significantly the kinetics of crystallization phenomena. Therefore, the sampling for statistic studies must be restricted to small areas in order to obtain homogeneous populations. On the other hand, crystallization begins in the thinnest regions: the onset of the crystallization shows a strong thickness dependence and, thus, this parameter is not suitable for bulk values comparisons or activation energy estimates.

REFERENCES

[1]   Hansen, N., Bay, B., *Acta Met.*, 29, 65 (1981).
[2]   Van Der Biest, O., Thomas, G., *Electron Microsc. Miner.* (ed. by H. R. Wenk), p. 280. Springer (1976).
[3]   Lantuejoul, C. *Prakt. Metallog.*, 8, 40 (1978).
[4]   Novikov, V., *Acta Met.*, 26, 1739 (1978); 27, 1461 (1979).
[5]   Hundery, O., Ryum, N., Westengen, N., *Acta Met.*, 27, 161 (1979).
[6]   Morral, J. E., Ashby, M. F., *Acta Met.*, 22, 567 (1974).
[7]   Sheard, G., Nutting, *J. Met. Technol.*, p. 192 (1980).
[8]   Cumbrera, F. L., Millan, M., Conde, A., Marquez, R., Vigier, P., *J. Mat. Sci.* (In press).
[9]   Allen, T., *Particle size measurement.* chap. 4. Chapman and Hall (1974).
[10] Kurtz, S., Carpay, F., *J. Appl. Phys.*, 51, 5745 (1980).
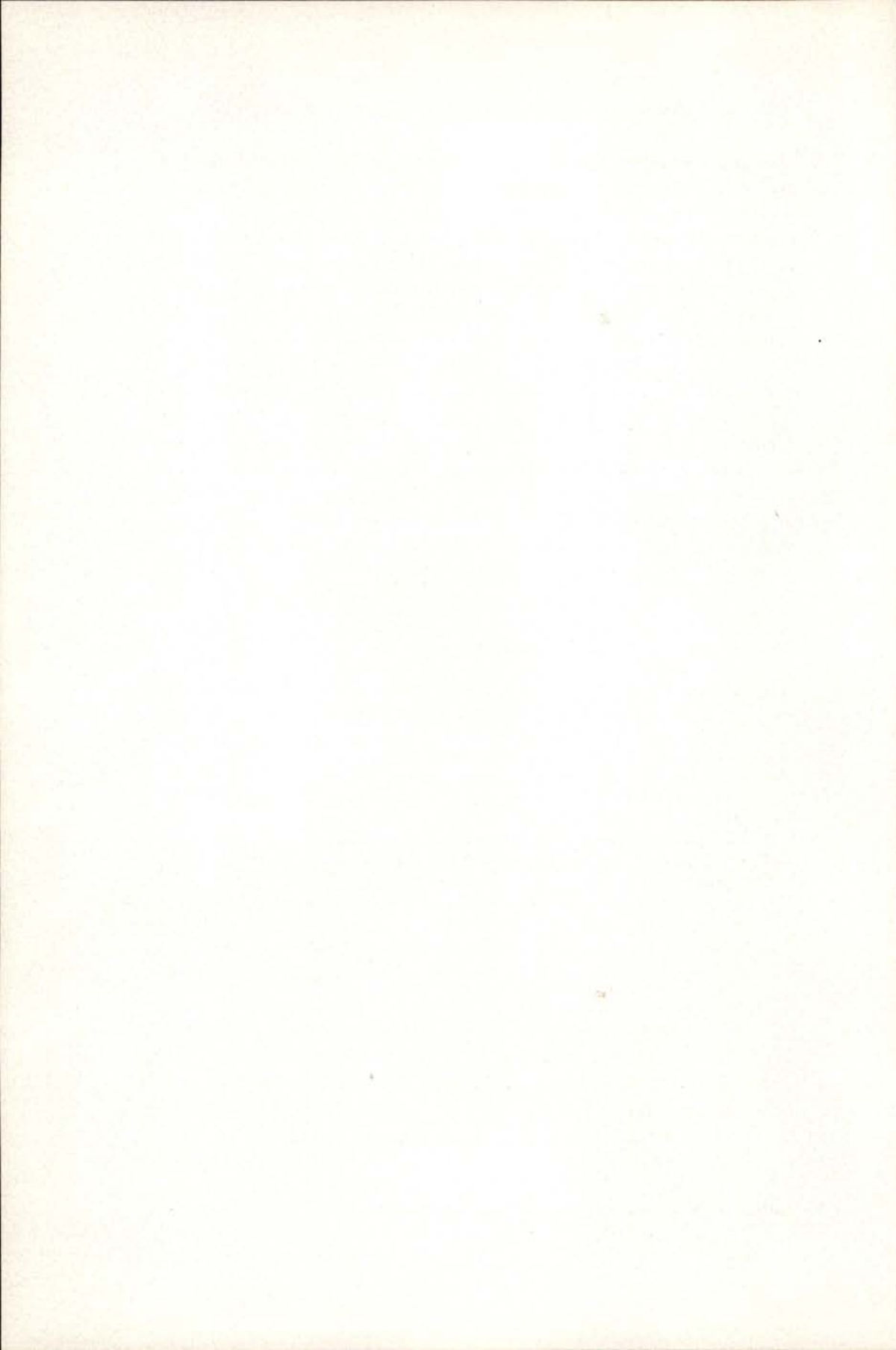
CONFIGURATION SPATIAL DES MOLÉCULES D'EAU D'HYDRATATION DANS LE SULFATE DE LANTHANE ENNÉAHYDRATÉ PAR SPECTROSCOPIE RAMAN (*)

F. RULL, A. GONZALEZ, J. JIMENEZ, A. C. PRIETO
Laboratorio de Física del Estado Sólido, Facultad de Ciencias
Valladolid, Spain.

RÉSUMÉ — A partir de l'étude des modes normaux de vibration des molécules d'eau d'hydratation, par spectroscopie Raman, et de données de diffraction de Rayons-X nous repportons la orientation précise des hydrogènes dans le $La_2(SO_4)_3 \cdot 9 H_2O$.

ABSTRACT — Raman spectroscopy of normal modes of vibration of hydration water molecules and X-ray diffraction data give the precise orientation of hydrogen atoms in $La_2(SO_4)_3 \cdot 9 H_2O$.

1 — INTRODUCTION

Dans l'ensemble d'une étude sur le rôle structural des molécules d'eau dans les cristaux hydratés, nous nous sommes interessés à la série des sulfates hydratés des terres rares.

Nous avons realisé la synthèse, préparation et caractérisation des proprietés physiques de la série $Ln_2(SO_4)_3 \cdot n(X_2O)$ où Ln = La, Ce; n = 9, 8, 5 et x = H, D [1], [2], [3]; et notamment l'étude des proprietés dynamiques par spectroscopie Raman [4], [5].

La considération des données des Rayons-X sur les sulfates de Lanthane et de Cérium avec neuf molécules d'eau montre que, ces deux cristaux sont isomorphes à température ambiante et

---

(*) Presenté au VII Congrès Iberoamericain de Cristallographie (21-26 Septembre 1981, Coimbra, Portugal).

cristallisent dans le système hexagonal avec le groupe spatial C_{6h}^2 ($P6_3/m$) [6], [7].

Néanmoins, les spectres Raman pris dans l'intervalle de températures 15 K - 300 K montrent un comportement très différent, en particulier au dessous de 170 K, où le sulfate de Lanthane présente des modifications de sa symétrie entraînant même la perte du plan de symétrie σ_h de la maille [8].

L'origine de ces anomalies se trouve vraisemblablement associée aux changements des interactions des molécules d'eau avec son environnement.

Puisque ces résultats spectroscopiques ne sont pas suggérés par les données des Rayons-X, notamment à cause de la difficulté à préciser les positions des hydrogènes, nous nous proposons dans cet article d'approfondir le mécanisme de ces anomalies à travers la spectroscopie Raman. Donc, nous allons étudier l'orientation des molécules d'eau d'hydratation dans le monocristal de Sulfate de Lanthane avec neuf molécules d'eau.

2 — CONDITIONS EXPÉRIMENTALES

Les monocristaux de Sulfate de Lanthane utilisés, de bonne qualité optique pour des mesures spectroscopiques, ont été taillés et polis sous forme de parallélépipèdes de dimensions $3 \times 4 \times 4$ mm environ.

Pour obtenir les spectres Raman nous avons utilisé les spectromètres Coderg PHO double monochromateur et Ramanor HGS avec réseaux holographiques, la sensibilité spectrale étant ± 1 cm^{-1}. Les sources de lumière utilisées sont des Laser à Ar$^+$ avec $\lambda = 4.880$ Å et $\lambda = 5.145$ Å et une puissance de 500 à 700 mW.

3 — CONSIDÉRATIONS STRUCTURALES

Les differents rôles structurales qui jouent les molécules d'eau d'hydratation dans les cristaux hydratés viennent définis uniquement par deux sortes fondamentales d'interactions. D'un côté la liaison d'hydrogène, où généralement une molécule d'eau

dans le cristal engage ses deux hydrogènes, et d'autre côté, l'interaction du nuage électronique résiduel avec les possibles cations.

Dans le cas du Sulfate de Lanthane, ces deux types d'interaction déterminent aussi deux types différents de molécules d'eau dans la maille.

L'un est constitué par deux groupes de six molécules d'eau en position générale qu'entourent chacun des cations La^{3+}, avec la distance eau-cation égale à 2.55 Å.

L'autre se trouve formé par six molécules d'eau en site C_s avez ses oxygènes situés sur les plans de symétrie de la maille [6].

Considérons d'abord la molécule H_2O en site C_s.

A partir de sa symétrie de site on déduit que son plan moléculaire, HOH, se trouvera, soit bien sur le plan σ_h, soit perpendiculaire au plan σ_h. En tenant compte que, d'un côté et de l'autre du plan σ_h il y a deux molécules H_2O en position générale à une distance de 2.82 Å et que le plan formé par les trois oxygènes est perpendiculaire au plan σ_h il nous semble raisonnable suposer que cette molécule est située perpendiculairement au plan de symétrie, et formant deux liaisons d'hydrogène avec les molécules H_2O (C_1).

Cette hypothèse se trouve renforcée par la valeur de l'angle O (W2) $-$ O (W1) $-$ O (W2) $= 101°$ (Notation de E. Gebert [6]). Dans ces conditions, la molécule en site C_1 aurait un de ses orbitaux libres acceptant le proton de la molécule H_2O (C_s) et l'autre en interaction de coordination avec le cation. En même temps, elle aurait ses hydrogènes sûrement engagés dans des liaisons d'hydrogène avec les oxygènes voisins.

Cette situation singulière dans la maille nous amène à prendre la molécule d'eau en site C_1 comme centre pour notre étude géométrique.

Avec l'aide d'un programme de calcul sur ordinateur nous avons calculé toutes les distances et angles concernant les atomes compris dans l'environnement immédiat d'une molécule H_2O (C_1) (Tableau I).

Prenons comme hypothèse la géométrie d'une molécule d'eau d'hydratation «moyenne» dans le cristal avec les conditions antérieures [9]. Cette molécule a un angle HÔH $\sim 106°$ et un angle entre orbitaux libres supérieur à 100° [10].

TABLEAU I — Distances et angles entre les atomes qu'entourent la molécule H_2O (C_1) dans le La_2 (SO_4)$_3$. $9 H_2O$. (Notation de E. Gebert [6]).

Atomes			Distances (Å)		Angle $\widehat{BAC}$
A	B	C	A-B	A-C	
O(W1)	O(W2)	O(3)	2.822	2.835	99.7°
O(W1)	O(W2)	La^{3+}_{II}	2.822	2.554	125.8°
O(W1)	O(W2)	O′(W2)	2.822	3.023	110.3°
O(W1)	O(W2)	O(2)	2.822	2.818	169.4°
La(2)	O(W2)	O′(W2)	2.554	3.023	53.5°
La(2)	O(W2)	O(3)	2.554	2.835	131.9°
La(2)	O(W2)	O(2)	2.554	2.818	55.5°
O(3)	O(W2)	O′(W2)	2.835	3.023	100.0°
O(3)	O(W2)	O(2)	2.835	2.818	76.9°
O(3)	O(W2)	O(W1)	2.835	2.822	99.7°
O′(W1)	O(W2)	O(3)	3.190	2.835	90.0°
La(2)	O(W2)	O(W1)	2.554	3.190	49.4°
O(W2)	O(W1)	O″(W2)	2.824	2.824	101.4°

On s'aperçoit sur le Tableau I que uniquement deux possibilités d'orientation pour la molécule H_2O (C_1) semblent satisfaire ces conditions angulaires en gardant les interactions mentionnées auparavant (Fig. 1).

La première serait caracterisée par l'éxistence de deux liaisons d'hydrogène de longueurs trés différentes, l'une dirigée vers l'oxigène O(3) à une distance 2.83 Å et l'autre dirigée vers l'oxigène O(W2) situé à 3.02 Å. Le plan HOH resterait ainsi assez parallèle au plan de symétrie σ_h.

La deuxième aurait aussi deux liaisons d'hydrogène de longueurs différentes dirigées vers l'oxigène O(3), comme dans le cas précédent, et vers l'oxigène O(W1), situé sur le plan σ_h à hauteur $z = 1/4$ et à une distance égale à 3.19 Å. Dans ce cas le plan moléculaire HOH se trouverait incliné d'un angle $\sim 36°$ par rapport au plan σ_h.

Néanmoins, dans les deux cas, l'écart entre les valeurs angulaires calculées et les valeurs nécessaires pour établir les interactions sur les directions optimales pour la molécule d'eau permet de déduire que ces liasisons ne seraient pas linéaires.
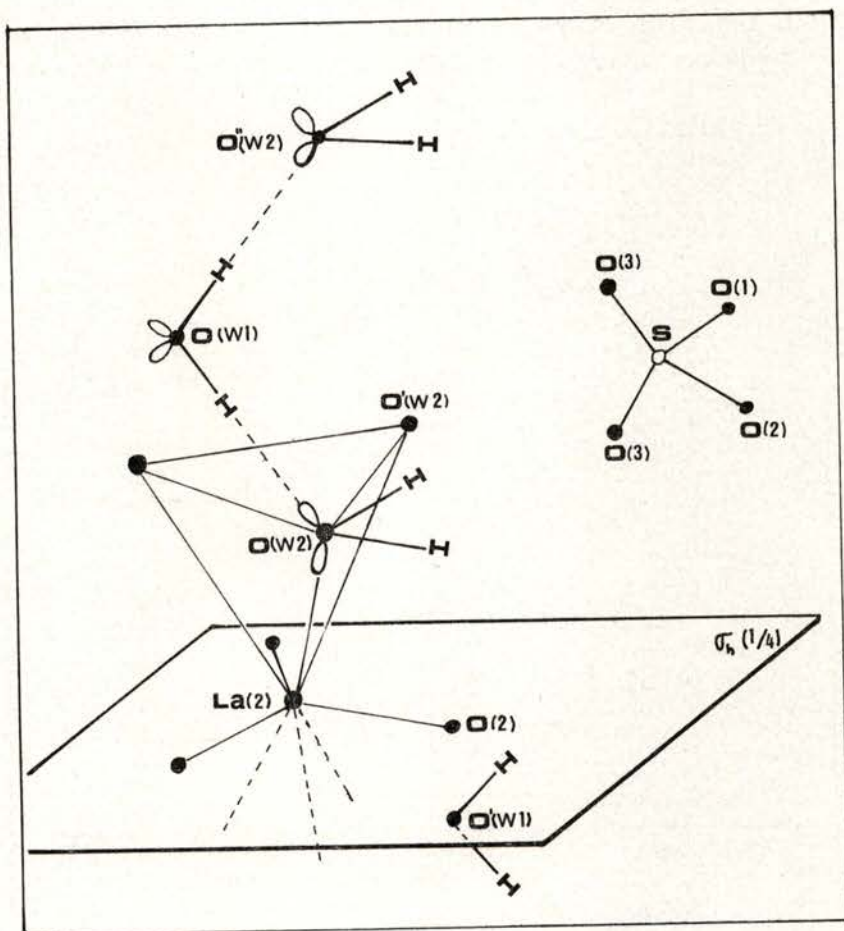
Fig. 1 — Configuration des atomes autour d'une molécule H_2O (C_1) dans le La_2 (SO_4)$_3$. $9 H_2O$ monocristallin.

En particulier pour l'interaction eau — cation, la direction de l'orbital libre s'écarte de la direction H_2O - La^{3+} d'un angle qui varie de 30° à 50°.

4 — RÉSULTATS ET DISCUSSION

Maintenant, si l'on observe les spectres Raman pris à température ambiante dans la région des vibrations ν(O-H) de l'eau, on s'aperçoit de la présence de quatre groupes de bandes s'échalonnant de 3.200 à 3.600 cm^{-1} (Fig. 2). Leurs maxima ont des fréquences à 3.280 cm^{-1}, 3.406 cm^{-1}, 3.520 cm^{-1} et 3.590 cm^{-1}.
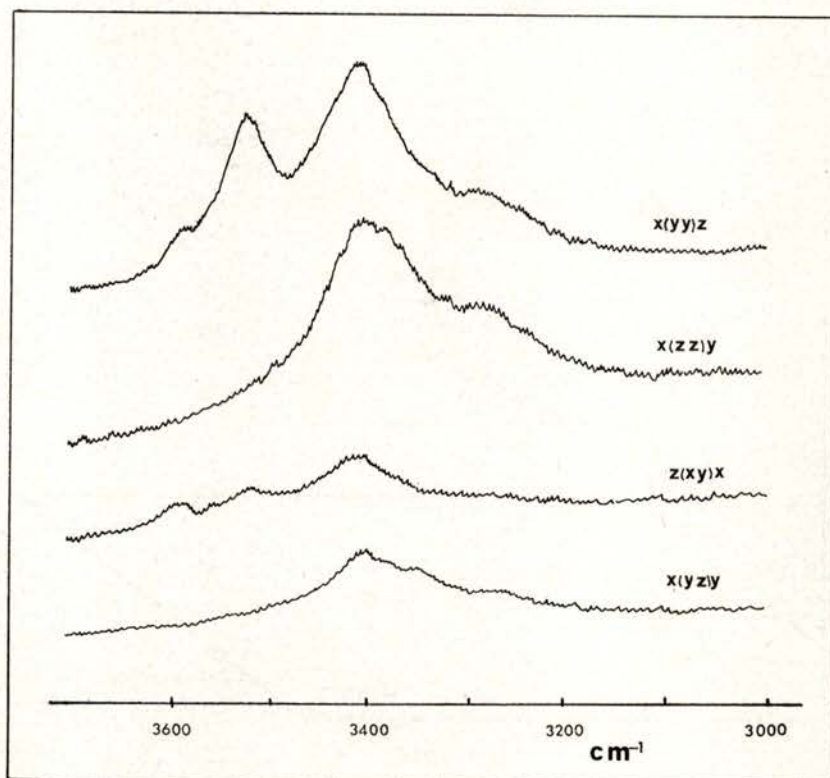
Fig. 2 — Spectres Raman du Sulfate de Lanthane ennéahydraté (température ambiante). Région des vibrations internes des molécules H_2O.

Les deux premières bandes ont déjà été attribuées [4] aux vibrations ν(O-H) de la molécule H_2O(C_s), la bande à 3.280 cm^{-1} étant attribuée à une résonance de Fermi entre 2δ(H_2O) et ν_1(O-H) [11].

Pour l'interprétation des autres deux groupes de bandes nous utilisons d'abord le rapport expérimental entre les valeurs v (O - H) et les distances O - O dans les liaisons d'hydrogène [12]. Ce rapport donne une distance O - O ~ 2.85 Å pour une fréquence de 3.520 cm^{-1} et une distance 3.01 Å pour une fréquence v (O - H) ~ 3.590 cm^{-1}.

Ensuite, l'analyse de l'intensité de ces bandes nous montre que les deux ont des composantes du tenseur de polarisabilité derivé $\varepsilon^2_{xx} = \varepsilon^2_{yy} \neq 0$, $\varepsilon^2_{xy} = \varepsilon^2_{xz} = \varepsilon^2_{yz} = 0$. La bande à 3.520 cm^{-1} a une petite composante ε^2_{zz} qu'on n'observe pas sur la bande à 3.590 cm^{-1}.

Ces résultats nous amènent à conclure que la molécule H$_2$O en position générale a ses hydrogènes dirigés vers les oxygènes O(3) et O(W2), l'angle de la liaison O(W2) - O(3) étant ~ 18° par rapport au plan σ_h et celui de la liaison O(W2) - O(W2) presque parallèle au plan σ_h.

D'autre part, l'angle calculé O'(W2) O(W2) O(3) vaut 100° et l'angle O(W1) O(W2) O(3) vaut 99.7° (Fig. 1).

Pourtant ces liaisons d'hydrogène ne peuvent pas être linéaires, ce qui semble être d'accord avec la fréquence observée à 3.520 cm^{-1}, légèrement supérieure à celle correspondante à une liaison linéaire d'hydrogène de distance O - O = 2.83 Å.

Il nous reste, cependant, l'étude de l'interaction eau-cation.

Sur la base des résultats géometriques précédents, cette interaction se trouverait separée de la direction de l'orbital libre de la molécule H$_2$O (C$_1$) d'un angle compris entre 25° et 35°.

Pour le confirmer on ne peut pas utiliser les spectres Raman pris dans la région de basses fréquences puisque leur attribution n'est pas précise. Cela est dû à un fort couplage entre les différents groupes moléculaires à travers la liaison d'hydrogène.

Ainsi, nous avons utilisé un critère complémentaire: la théorie de Brown sur la valence de liaison [13]. Cette théorie est appliquée à l'étude de l'interaction cation-oxygène où l'expression générale a la forme $S = (R/R_1)^{-N}$ [14], où S est la valence de la liaison, R$_1$ et N sont des paramètres qui dépendent des atomes compris dans l'interaction et R est la distance interatomique. S peut s'exprimer sur la direction qui relie les deux atomes par une valence effective $S' = S \cos \varphi$.

Nous avons calculé les contributions de valence dûes aux oxygènes qu'entourent les deux cations La_I^{3+} et La_{II}^{3+} (voir reference [6]). Les résultats sont presentés sur le Tableau II.

TABLEAU II — Répartition des valences électrostatiques autour des cations La^{3+} (1) et La^{3+} (2) dans le Sulfate de Lanthane ennéahydraté.

	6 O(1)	3 O(2)	6 O(3)	3 O(W1)	6 O(W2)	
La^{3+} (1)	1.87		1.10	0.07		3.04
La^{3+} (2)		1.14			2.08	3.22

On s'aperçoit que la somme des contributions autour du La_{II}^{3+} ne satisfait pas le principe d'electroneutralité de Pauling. La différence de 0.22 u.e.e. provient vraîsemblablement du fait que l'interaction eau-cation ne se fait pas sur la direction reliant l'eau et le cation.

Ou peut calculer l'angle φ et la valeur obtenue est de 26°, en bon accord avec la supposition faite.

5 — CONCLUSIONS

1 — Nous avons fait une étude des modes normaux de vibrations des molécules d'eau d'hydratation dans le $La_2 (SO_4)_3 . 9 H_2O$ par spectroscopie Raman.

2 — En partant des données des Rayons-X, nous avons confirmé l'existence de deux types de molécules d'eau dans la maille avec des rôles structuraux différents.

3 — Ces données des Rayons-X ne permettent pas de déduire une orientation précise des hydrogènes et des orbitaux libres des molécules d'eau en position générale. Néanmoins, l'analyse des spectres Raman nous amène à une configuration qui semble satisfaire les exigences angulaires des quatre possibles interactions affectant la molécule d'eau.

90

Portgal. Phys. — Vol. 13, fasc. 1-2, pp. 83-91, 1982

4 — Cette configuration oblige un des orbitaux libres à se séparer de la direction optimale d'interaction eau-cation. Pour le confirmer nous avons utilisé la théorie de Brown et trouvé un angle d'écart de l'ordre de 26°.

5 — Nous pouvons conclure, à partir de ces résultats, que la molécule d'eau en position générale dans le Sulfate de Lanthane ennéahydraté a une situation structurale assez instable à température ambiante, ce qui peut se trouver à l'origine des anomalies observées sur les spectres Raman quand on varie la température.

6 — On peut remarquer finalement que la spectroscopie Raman représente un outil puissant et complémentaire de la diffraction des Rayons-X dans l'interprétation des modifications affectant la géometrie de la maille cristalline, notamment dans le cas des cristaux hydratés.

BIBLIOGRAPHIE

[1] A. de Saja, J. M. Pastor, F. Rull, J. A. de Saja, *Kristall und Technik*, 12, 1 (1977).

[2] A. de Saja, J. M. Pastor, F. Rull, J. A. de Saja, *Kristall und Technik*, 13, 909 (1978).

[3] A. de Saja, J. M. Pastor, E. Hernandez, F. Rull, J. A. de Saja, *Crystal Res. and Tech.*, 12, 1391 (1981).

[4] M. Abenoza, V. Luu Dang, F. Rull, J. M. Pastor, *J. Raman Spect.*, 6, 26 (1977).

[5] A. Torres, F. Rull, J. A. de Saja, *Spectrochimica Acta* 36A, 425 (1980).

[6] E. Gebert, *J. Solid State Chem.*, 19, 271 (1976).

[7] A. Derigne, G. Pannetier, *Bull. Soc. Chim. France*, 1, 174 (1976).

[8] F. Rull, J. M. Pastor, J. A. de Saja, D. A. Long, *J. Raman Spectr.* (under publication).

[9] R. Chindabaram, A. Sequeira, S. K. Skka, *J. of Chem. Phys.*, 41, 3616 (1964).

[10] G. Ferraris, M. Franchini-Angela, *Acta Cryst.*, B28, 3572 (1972).

[11] F. Rull, Tesis Doctoral. Valladolid 1976.

[12] A. Novak, *Struct. and Bond*, 18, 177 (1974).

[13] I. D. Brown, *Acta Cryst.*, A32, 24 (1976).

[14] I. D. Brown, K. K. Wu, *Acta Cryst.*, A32, 1957 (1976).
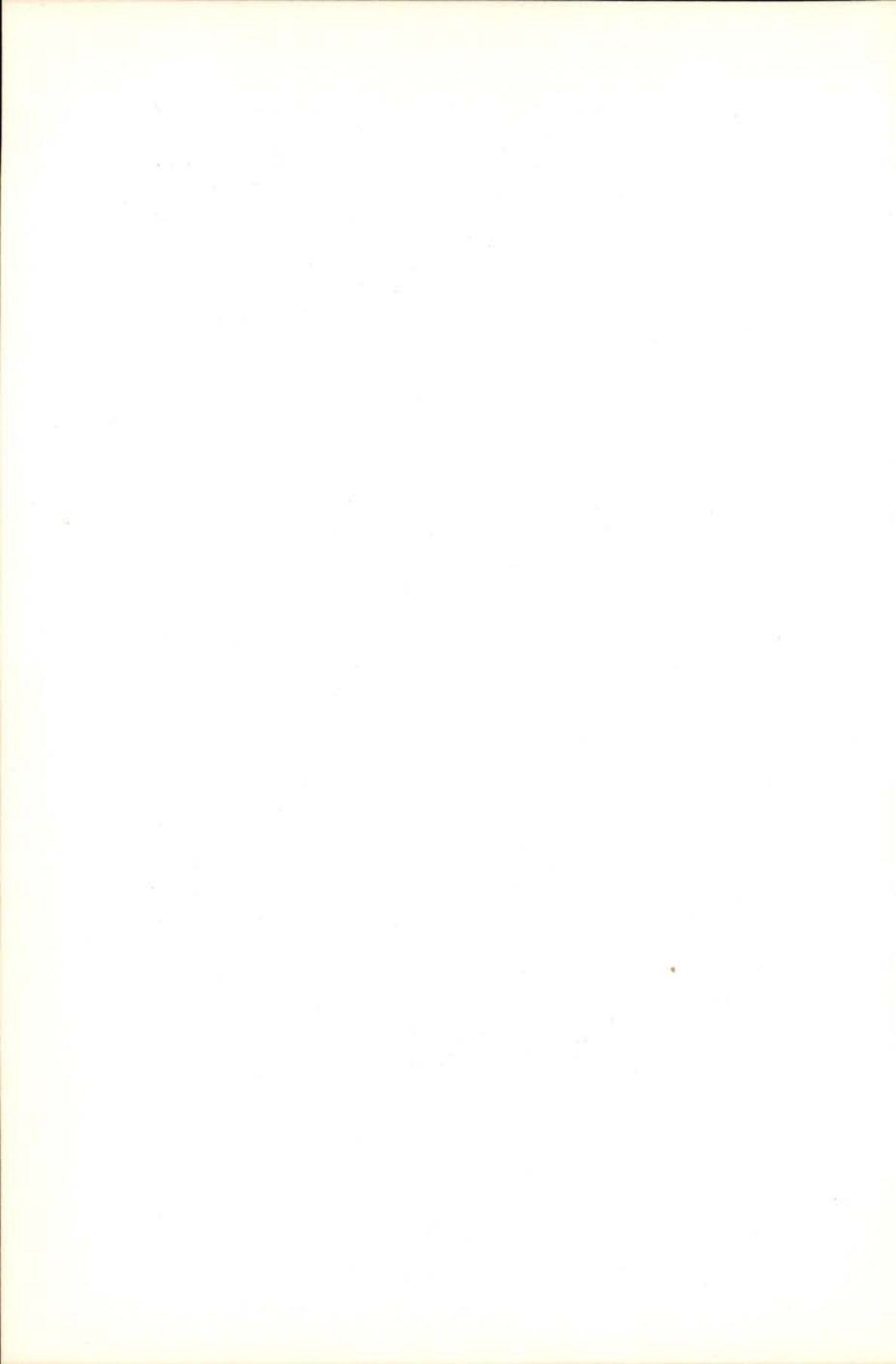
STANDARD REPRESENTATION OF INORGANIC STRUCTURES BASED ON SIMPLE AND ON LOOSE PACKINGS (*)

J. Lima-de-Faria

Junta de Investigações Científicas do Ultramar,
Alameda D. Afonso Henriques, 41-4.o-E, 1000 Lisboa, Portugal

ABSTRACT — The standard representation recently proposed by the author, and applied in detail to structures based on cubic and hexagonal closest packings, has been extended to inorganic structures based on simple and on loose packings. This standard representation clearly shows that these structures have a much simpler atomic organization and are more interrelated than could be imagined using conventional ways of structure representation.

INTRODUCTION

A certain uniformity in the representation of inorganic crystal structures is necessary in order to facilitate their relationship. However, each author represents inorganic structures, even the simplest ones, in several different ways, either considering the linkage between atoms within the unit cell, or the linkage between atomic polyhedra, or the packing of atoms with different sizes, or again the projection of atoms in a certain plane of the unit cell. It is this situation that originated a proposal by the author for a standard representation of layered inorganic structures [1] inspired on the condensed models' technique [2]. The application of this standard method to the representation of crystalline structures based on cubic and on hexagonal closest packings gave rise to very simple descriptions of these structures and of interesting relationships among them [1]. The aim of this work

---

(*) Presented at the VII Iberoamerican Congress of Crystallography (21-26 September 1981, Coimbra, Portugal).

is to extend this standard representation to structures based on other types of close packings, in particular on simple and on loose packings.

STANDARD REPRESENTATION OF INORGANIC STRUCTURES BASED ON SIMPLE AND ON LOOSE PACKINGS

The standard representation of inorganic layered structures consists on the representation of the constructive layers [3], or of their subdivisions, in which the structure can be sliced and the way they stack together. The constructive layers correspond to the transparent sheets of the condensed models and, to represent the kind of layers and their stacking, we only need to consider that part of the condensed model which is included within the unit cell and draw it in perspective (Fig. 1).

Close packed structures, either closest, loose, or simple, normally admit more than one layer description. For instance in the cubic closest packing there are seven possible layer descriptions: four perpendicular to the triad axes, and three perpendicular to the tetrad axes. What is important is to find out the simplest layer description for each structure. This is called the «proper layer description», and the standard representation is the one which corresponds to the proper layer description.

The conventions used in the standard representation are the following. In close packed structures without interstitial atoms the packing atoms are represented by small circles. In structures with interstitial atoms these are represented by small circles and the unoccupied interstices by small squares (a widely used symbol for vacancies); the packing atoms are represented by dots, because it is the configuration of the interstitial atoms i.e., the «distribution pattern» [2] which changes and which it is important to emphasize, the packing being well defined, and identical for a particular group of structures.

The so called loose-packings [4] are less dense close packings and are obtained by stacking closest packed layers not over the holes (as in the densest way) but over valleys, that is, with one atom touching only two atoms of the layer below. These packings are designated by Tb, Tv, Td (T for the triangular closest packed

94

Portgal. Phys. — Vol. 13, fasc. 1-2, pp. 93-99, 1982
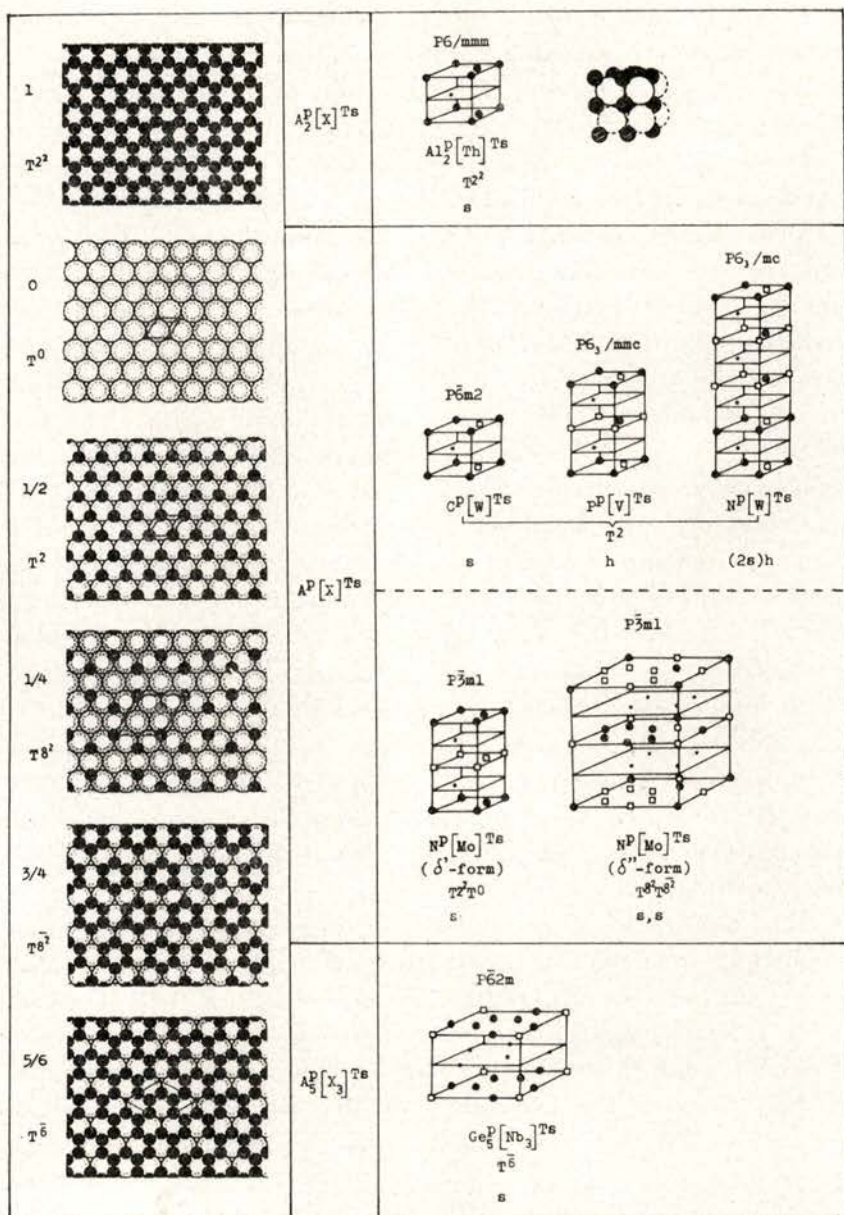
Fig. 1 — Standard representation of inorganic structure types of general formula $A_m^p \left[X_n \right]^{Ts}$ (Ts means simple hexagonal packing, and p triangular prismatic coordination).

layer, and b, v and d for the different kinds of stacking sequences). Similar modes of stacking can be found in structures based on square layers of atoms (Q) and in the body-centered cubic packing, if the rhombic layers (B) parallel to (110) planes are considered. Therefore all these packings are included under the same designation of loose packings [5].

The simple packings are the well known simple hexagonal and the simple cubic packings represented respectively by Ts and Qs (s for the stacking sequence which corresponds to the juxtaposition of the layers with one atom touching only one atom of the layer below).

Before applying the standard representation to the structures based on simple and on loose packings we have determined their proper layer description, and we have restricted our work to structures of binary compounds. The result is shown on Chart I.

The standard representation has then been applied to all these structures, but here only one family is presented (Fig. 1). We have chosen the structures corresponding to the general formula $A_m^p [X_n]^{Ts}$, that is, based on the simple hexagonal packing Ts of the larger atoms X, with interstitial smaller atoms A, having triangular prismatic coordination p. Because the plane of the interstitial atoms does not coincide with the plane of the packing atoms, we have subdivided the constructive layers into two different levels, in order to achieve a more exact representation (Fig. 1).

The distribution pattern of either the packing atoms in minor proportion, or of the interstitial atoms, is symbolized by a capital letter indicating the shape of the plane unit cell of their patterns, using T for hexagonal (triangular net), Q for square (quadrangular net) and R for rectangular or oblique shape. An upper symbol indicates the occupancy of the atoms in the possible sites within this unit cell, for instance T^{8^2} means a proportion of 2/8 (2/8 = 1/4 but the eight expresses the multiplicity of the unit cell); in the particular cases of 1/2, 1/3, 1/4 ... the number one is omitted, for reasons of simplicity, and consenquently T^2, for example, corresponds to a proportion 1/2; T^0 corresponds to zero occupancy. Another simplification is used when a certain distribution pattern is complementary to a simpler one, e.g.,

$[X_mY_n]^{Tb/v/d}$			$A_m^P[X_n]^{Ts}$			$A_m^{P/o}[X_n]^{Tc/h/s}$		
Pr.l.d.	St.	Str. type	Pr.l.d.	St.	Str. type	Pr.l.d.	St.	Str. type
T^1	b	$[Pa]^{Tb}$	T^1	s	$[InSn_3]^{Ts}$	T^2T^0	h	$Cu^P[Ba]^{(2Ts)h}$
T^1	d	$[Fu]^{Td}$	T^{22}	s	$Al^P[Th]^{Ts}$	T^2T^0	c	$Mo^P[S_2]^{(2Ts)c}$
R^2	b,y	$[CuTi]^{Tb}$	T^2	s	$C^P[W]^{Ts}$	T^2T^0	h	$Mo^P[S_2]^{(2Ts)h}$
T^1	b	$[MoSi_2]^{Tb}$	T^2	h	$F^P[V]^{Ts}$	T^2T^0	s	$Nb^P[S_2]^{(2Ts)h}$
T^1	v	$[CrSi_2]^{Tv}$	T^2	(2s)h	$N^P[W]^{Ts}$	T^2T^0	(3h)s	$Nb^P[Se_2]^{(2Ts)ch}$
T^1	d	$[TiSi_2]^{Td}$	$T^{22}T^0$	s	$N^F[Mo]^{Ts}$ (δ'-form)	$T'T^0$	c	$N^0[W_2]^{(2Ts)c}$
R^{tot}	b,y	$[Nb_3Au_2]^{Tb}$	$T^{s2}T^{s2}$	s, s	$N^P[Mo]^{Ts}$ (δ''-form)	T^3T^0	s	$Al^0[(OH)_2]^{(2Ts)h}$ Gibbsite
			$T^{\bar{s}}$	s	$Ge^P_s[Yb_2]^{Ts}$	T^IT^0	s	$Al^0[(OH)_3]^{(4Th)s}$ Nordstrandite
						$T^2T^2T^0$	(2s)h	$N^F_?[W_3]^{(3Ts)h}$

$A_q^{o/t}[X_mY_n]^{Bb}$								
Pr.l.d.	St.	Str. type	Pr.l.d.	St.	Str. type	Pr.l.d.	St.	Str. type
Q^1	f	$[W]^{Bb}$	Q^{s4}	f	$[V_4Zn_5]^{Bb}$	Q^6	b	$D^t[Ta_3]^{Bb}$
Q^2	d	$[NaTl]^{Bb}$	$T^3(4T^0)T^3(3T^0)$	h	$[Pb_3Li_8]^{Bb}$	$\tilde{Q}^{b3}$	fr	$H^t_4[U]^{Bb}$
Q^1Q^0	s	$[LiHg]^{Bb}$	$R^{H3}(110)$	b,y	$[Pb_4Li_7]^{Bb}$	$\tilde{Q}^6Q^4$	s, s	$Ni^t_?[S_4]^{Bb}$
$Q^1Q^1Q^0Q^0$	f	$[CuTi]^{Bb}$	Q^3Q^0	s	$E^0[Ta_3]^{Bb}$	Q^s	d	$Th^t[Cl_4]^{Bb}$
$Q^1Q^0Q^0$	f	$[AlCr_2]^{Bb}$	$Q^{I2}Q^0$	f.	$N^0[Fe_4]^{Bb}$	$R^4R^{Q2}(110)$	f, s	$D^t_?[Ta_4]^{Bb}$
Q^2Q^0	f	$[BiF_3]^{Bb}$						

$A_m^{P/sq}[X_n]^{Qd}$			$A_m^{cb/sq}[X_n]^{Qs}$			$A_q^{P//sq}[X_mY_n]^{Qf/b/s}$		
Pr.l.d.	St.	Str. type	Pr.l.d.	St.	Str. type	Pr.l.d.	St.	Str. type
$\tilde{Q}^{22}$	d	$Si^P_?[Th]^{Qd}$	Q^1	s	$[Po]^{Qs}$	Q^1	(2b)f	$[Ga]^{(2Qb)f}$
Q^1	d	$As^P[Nb]^{Qd}$	Q^2	f	$[KF]^{Qs}$	$Q^2Q^2Q^0$	f	$[AsFe_2]^{(3Qf)s}$
Q^3	d	$F^{sq}[Nb]^{Qd}$	Q^1	s	$Ca^{cb}[Cl_2]^{Qs}$	$Q^2Q^2Q^0$	(2s)f	$[SbLa_2]^{(3Qf)s}$
			Q^2	f	$Ca^{cb}[F_2]^{Qs}$	$Q^1Q^0Q^0$	s	$[CuGa_2]^{(3Qf)s}$
			Q^2	s	$Pt^{cb}[Hg_4]^{Qs}$	$Q^2Q^2Q^0Q^0$	(2f)b	$[AsMn_3]^{(4Qf)s}$
			Q^1Q^0	s	$Fe^{cb}[Si_2]^{Qs}$	Q^1	(2b)f	$Tl^s[I]^{(2Qb)f}$
			$T'T^0T^0$	c	$U^{cb}[O_2]^{Qs}$	$\tilde{Q}^{21}Q^0$	b	$B^P[Ni]^{(2Qb)f}$
			$T'T^0T^0$	h	$Ni^{cb}_?[Al_3]^{Qs}$	$\tilde{Q}^{21}Q^0$	br	$B^P[Mo]^{(2Qb)f}$
			Q^4	f	$Pt^{cb}[Hg_4]^{Qs}$	Q^2Q^0	f	$Pd^{sq}[Cl_2]^{(2Qb)f}$
			Q^c	f	$Pt^{cb}_?[O_2]^{Qs}$	$\tilde{Q}^H\tilde{Q}^2Q^0$	d	$B^P_4[Cr_3]^{(3Qb)f}$
			Q^2	f	$Pt^{sq}[S]^{Qs}$			

Chart I — Proper layer description of structure types of binary compounds based on simple and on loose packings. Notice the simplicity of the layer description of most of these structure types.

instead of T^{3^2} we use $T^{\bar{3}}$, the bar meaning the complementary proportion of 1/3. The sequence of the distribution patterns of either the packing atoms in minor proportion or of interstitial atoms, is indicated by a small letter. When two letters are used, like *br*, this corresponds to a composed operation, that is, a

translation *b* followed by a rotation *r* of 90° [6]. The translations (projected vectors) and/or rotations indicating the sequences of the *T*, *Q* and *R* types of the distribution patterns mentioned in Chart I and on Fig. 1 are shown in Fig. 2.
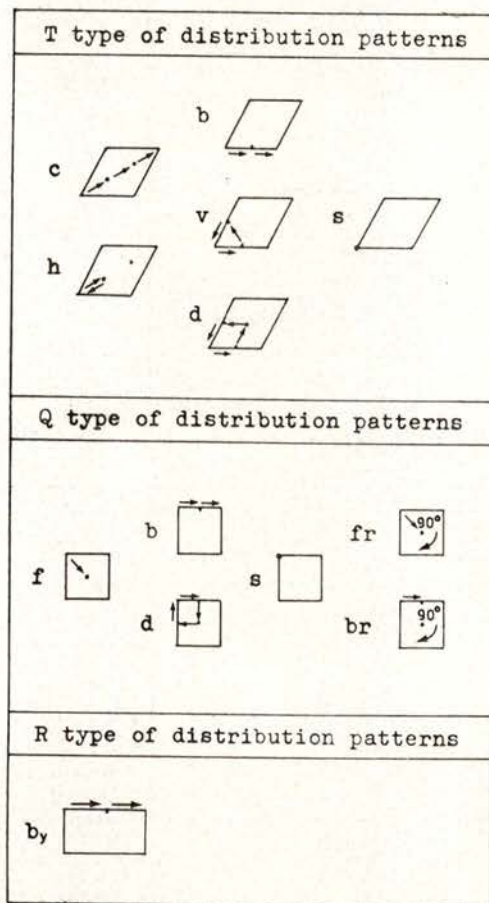
Fig. 2 — Translations (projected vectors) and/or rotations indicating the sequences for the *T*, *Q* or *R* type of distribution patterns mentioned in Fig. 1 and Chart I.

As happened with the closest packed structures [1] we can conclude from Chart I that most of the structures show a very simple proper layer description, based on simple and symmetrical

layers, like T^1, T^0, T^2, Q^1, Q^0, Q^2, ... It is also remarkable that a few types of sequence of the distribution patterns (Fig. 2) are adopted by several different structure types (Chart I) and that these sequences are practically the same as those observed for the structures based on closest packings [1] and for the inorganic structures in general [7]. The standard representation clearly shows that structures have a much simpler atomic organization and are more interrelated than could have been imagined using the conventional ways of structure representation found in the literature.

REFERENCES

[1] Lima-de-Faria, J. (Presented at the 6th European Crystallographic Meeting, Barcelona 1980; in publication).
[2] Lima-de-Faria, J., *Zeitschrift für Kristallographie*, 122, 346 (1965).
[3] Lima-de-Faria, J., *Zeitschrift für Kristallographie*, 148, 1 (1978).
[4] Kripyakevich, P. I., *Kristallografiya*, 18, 730 (1973). (English Translation *Sov. Phys. Cryst.*, 18, 460 (1974)).
[5] Figueiredo, M. O. and Lima-de-Faria, J., *Zeitschrift für Kristallographie*, 148, 7 (1978).
[6] Lima-de-Faria, J. (Presented at the 12th International Congress of Crystallography, Ottawa, 1981).
[7] Lima-de-Faria, J. and Figueiredo, M. O., *J. Solid State Chem.*, 16, 7 (1976).
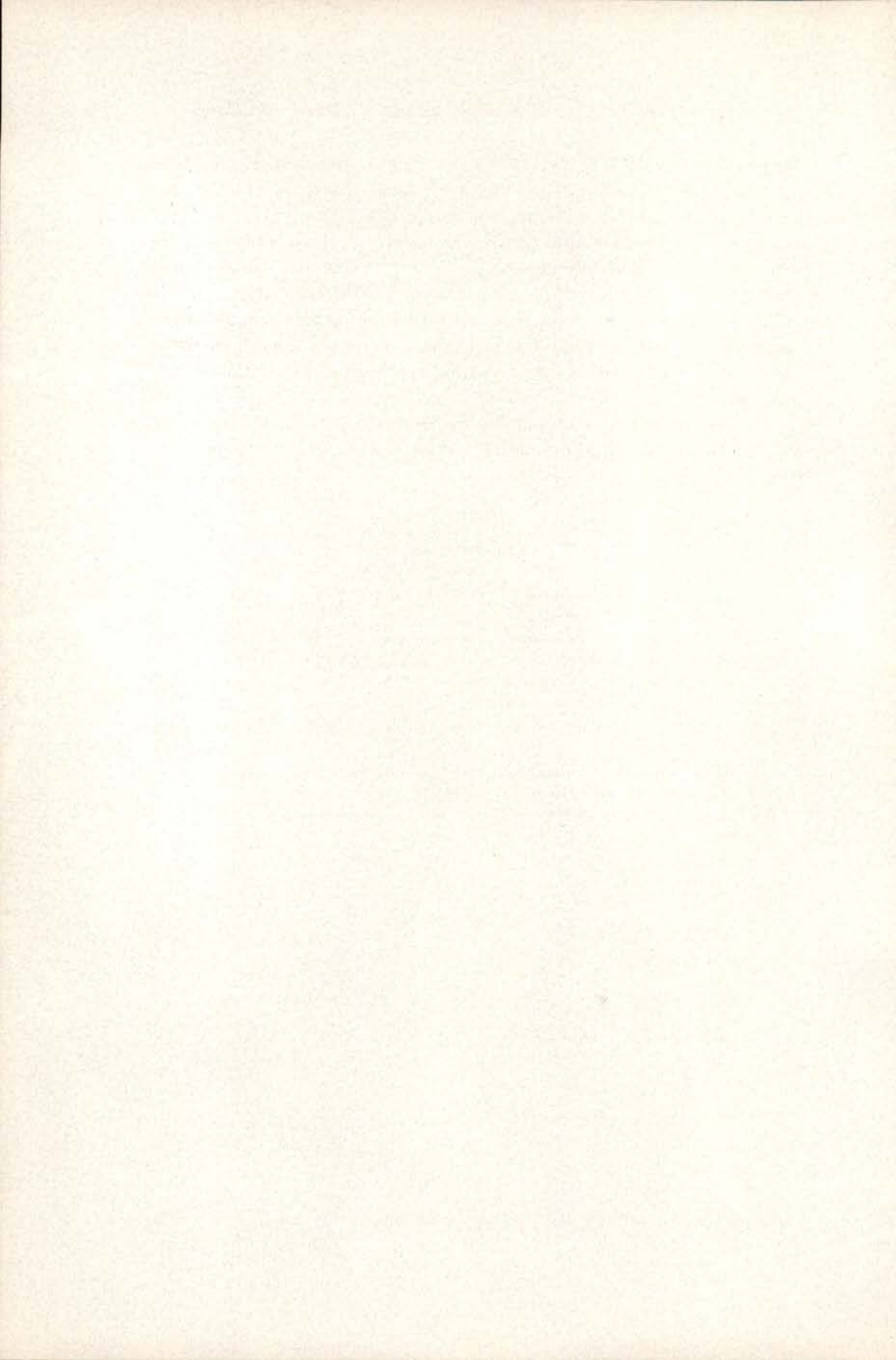
THE CRYSTAL STRUCTURE OF VANADIUM DIFLUORIDE: RELIABILITY TEST OF HYPOTHETICAL INTENSITY VARIANCES BASED ON x^2 DISTRIBUTIONS (*)

M. J. M. DE ALMEIDA, M. M. R. R. COSTA, W. GONSCHOREK [1]

Centro FC1, INIC — Departamento de Física, Universidade de Coimbra
3000 Coimbra, Portugal

ABSTRACT — X-ray integrated intensities from two different crystals of VF_2 have been collected using a CAD4 diffractometer.

Statistical tests of the experimental results were performed: a better agreement with the theoretical χ^2-distribution was found when the Poisson variances, σ^2_p, were multiplied by a parameter, v , which was subsequently refined.

A least-squares refinement yielded the values of the positional parameter, x , of the fluoride atom, as well as the anisotropic temperature parameters for both vanadium and fuorine atoms. The results are discussed in terms of the reliability (R-) factors and goodness-of-fit (g.o.f.) parameters obtained.

1 — INTRODUCTION

Vanadium difluoride (VF_2) has a rutile type structure with space group $P4_2/mnm$. The heat capacity, magnetic ordering and

---

crystal structure of this compound were investigated by Stout and Boo [1]. Using a needle shaped crystal these authors determined the lattice parameters as

$$a = b = 4.804 \pm 0.005 \text{ Å} \quad \text{and} \quad c = 3.237 \pm 0.005 \text{ Å}$$

From a set of visually estimated intensities difracted by a polycrystalline sample, they obtained the position parameter of the fluorine atom in the unit cell, $x = 0.306 \pm 0.005$, and the isotropic temperature factors for the constituent atoms, namely, $B_V = 0.37 \text{ Å}^2$ and $B_F = 0.70 \text{ Å}^2$.

The present work on VF_2 was undertaken as part of a program of electron density determination in several rutile type compounds.

2 — DATA COLLECTION

Two single crystals (A and B), used in the intensity measurements which will be described, were obtained from a large single crystal of VF_2 grown by B. J. Garrard [2], Clarendon Laboratory, Oxford, England.

Since the material is highly opaque, optical tests with polarized light were not possible and the choice of crystals was based on the observation of their shape and size only.

Crystals A and B, although rather irregular in shape, could be described as small blocks of dimensions $(0.05 \times 0.06 \times 0.13)$ mm and $(0.04 \times 0.05 \times 0.10)$ mm, respectively.

The reflection intensities were collected on an automatic X-ray single crystal diffractometer, CAD4, using AgKα radiation and a graphite monochromator. The experiment was carried out at a constant temperature of 20°C stabilized to $\pm$ 1°C.

The intensity distribution over a cross-section of the primary beam was checked. The region of maximum intensity was found to be an ellipse having the smaller axis perpendicular to the equatorial plane. Maximum intensity fluctuations of $\pm$ 7 % and

$\pm 14\%$ were observed along the normal to that plane within 0.1 mm and 0.14 mm respectively.

Using the standard technique developed for the CAD4 diffractometer the lattice parameters were determined as:

$$a = b = 4.808 \pm 0.002 \text{ Å} \quad \text{and} \quad c = 3.239 \pm 0.003 \text{ Å}$$

The integrated intensities of all reflections out to $(\sin \theta)/\lambda = 0.9 \text{ Å}^{-1}$ were collected during $\omega - 2\theta$ scans.

Several independent measurements of a number of integrated intensities were carried out for both crystals. These will be referred to, hereafter, as «repeatedly measured intensities».

3 — STATISTICAL TREATMENT

Intensities of Bragg reflections with an asymmetric background were rejected; the remaining 997 integrated intensities from crystal A and 696 from crystal B were used in subsequent statistical tests.

The distribution function of twice measured intensities from both crystals, $F_0(\chi_0^2, \nu)$, was compared with the theoretical distribution function, $F(\chi^2, \nu)$, where $\nu = n - 1$, n being the number of degrees of freedom (n = 2, in the present case). For this comparison, several values of $\chi_0^2 = (n_j - 1)s_j^2/\sigma_0^2 (I_j)$ were chosen, which will be denoted by χ_{0i}^2; the corresponding $F_0(\chi_{0i}^2, \nu)$ were calculated and compared to $F(\chi_i^2, \nu)$. The differences

$$y_i = F(\chi_i^2, \nu) - F_0(\chi_{0i}^2, \nu) \qquad \text{with } i = 1, 2, \ldots m$$

were used to compute the statistical R-factors

$$R = (m^{-1} \sum_{i=1}^{m} y_i^2)^{1/2}$$

These are a measure of the agreement between the observed and the theoretical χ^2-distribution.

In the present work, the Poisson variances σ_ρ^2 were replaced by $\nu \sigma_\rho^2$ and the parameter v was refined as suggested by Gonschorek [3].

The experimental data have been compared with both the theoretical and the asymptotic χ^2-distribution. The corresponding R-factors, R and R_{asympt}, respectively, are shown in Table 1. This table summarizes the results of the statistical treatment which has just been outlined; γ is a parameter which defines the time

TABLE 1

		Crystal A	Crystal B
Total number of reflections		997	696
$\gamma > \sigma_p(I_{ji})/I_{ji}$		0.1	0.005
Twice	Number of reflections	154	54
measured	v	1.20	1.54
reflections	R	0.023	0.031
Symmetry	Number of reflections	99	82
equivalent	$R_{asympt.}$ (without abs. corr.)	0.034	0.031
reflections	$R_{asympt.}$ { with abs. corr. $0.82 \leqslant A \leqslant 0.88$	0.025	—

spent in the measurement of each reflection; this is chosen so that $\sigma_p(I)/I < \gamma$, $\sigma_p(I)$ being the square root of the Poisson variance of the measured integrated intensity, I.

In Table 2, data obtained for both crystals are compared on the basis of the asymptotical χ^2-distribution proposed by Gonschorek [3] and of the theoretical χ^2-distribution. The number of groups having the same number, n_s, of symmetry equivalent reflections is denoted by $K(n_s)$.

TABLE 2

	Crystal A + Crystal B
Number of common reflections	72
R [n = 2; K(2) = 72]	0.12
Number of rejected reflections (χ^2-test; $\alpha = 0.1$)	11
$R_{asympt.}$	0.07
R [n = 2; K(2) = 61]	0.07

4 — DATA REDUCTION

The two sets of intensities from crystals A and B, respectively, were corrected in the usual way for Lorentz and polarization factors; for the latter correction the monochromator was assumed to be 50 % ideally perfect and 50 % ideally imperfect and set at a Bragg angle, $\sigma_M = 4.55°$.

Absorption factors for each reflection were computed using the Gaussian quadrature program of the CAD4 diffractometer and the absorption coefficients listed for the vanadium and fluorine atoms in «International Tables for X-Ray Crystallography», vol. IV. For crystal A the absorption correction was found to improve the statistical agreement between symmetry equivalent reflections.

For crystal B, the asymptotic R-factor for symmetry equivalent reflections is the same as the theoretical R value for twice measured reflections. This has been taken as an indication that the absorption correction would not improve the data.

The intensities were corrected for anisotropic atomic vibrations; the refined values of the temperature parameters are shown in Table 3.

Atomic scattering factors for the spherical neutral atoms were used in the calculation of structure factors; these and the real and imaginary parts of the anomalous dispersion corrections were calculated using data given in «International Tables for X-ray Crystallography».

Extinction is likely to affect X-ray integrated intensities, particularly those corresponding to the largest observed structure amplitudes, usually occurring at small $(\sin \theta)/\lambda$ values. Several corrections have been proposed to account for this effect; instead of using one of them, at this stage of the present work an attempt was made to avoid or at least to minimize the extinction effects, by selecting a variety of crystals of different sizes and using the shortest possible wavelength $(\lambda_{AgK_\alpha} = 0.5609 \text{ Å})$.

TABLE 3

	V	F
μ_{11} (Å)	0.0073(1)	0.0129(3)
μ_{33}	0.0063(2)	0.0085(3)
μ_{12}	−0.0006(2)	0.0056(3)
x	—	0.3053(2)
μ^2_{110} (Å^2)	0.0067(3)	0.0073(6)
$\mu^2_{1\bar{1}0}$	0.0079(3)	0.0185(6)
μ^2_{001}	0.0063(2)	0.0085(3)
μ^2	0.0070	0.0114

In order to decide whether or not the integrated intensities are affected by extinction, a few arguments can be used. One of them is based on the statistical treatment that has been described. Extinction is most probably anisotropic in an irregularly shaped crystal; therefore, symmetry equivalent reflection intensities are affected differently.

This should lead to an enhancement of the corresponding χ^2 value taken over symmetry equivalent intensities. Hence, the χ^2 test itself should make a preliminary selection of those reflections which are less seriously affected by extinction.

A further argument can be given which is based on the independent refinement of both crystal data sets. A scale factor, S, was refined using all reflections with $|F_{calc}| < E$, for different

106

Portgal. Phys. — Vol. 13, fasc. 1-2, pp. 101-109, 1982

values of E. Table 4 shows the results obtained for both crystals, as far as the variation of S is concerned. If extinction is present, the scale factor should decrease with decreasing E, since stronger reflections are more seriously affected by extinction.

TABLE 4

	Number of reflections	Scale factor	E
Crystal A	100	2.215(9)	40.0
	98	2.213(10)	30.0
	95	2.201(10)	25.0
	91	2.204(11)	20.0
Crystal B	101	2.980(7)	40.0
	99	2.971(8)	30.0
	96	2.972(9)	25.0
	93	2.975(10)	20.0

Based on the latter argument and on the results shown in Table 4, five reflections from crystal A with $|F_{calc}| > 25$ and four reflections from crystal B with $|F_{calc}| > 26$ were excluded from the final cycles of the refinement.

A Fourier refinement was carried out based on the observed structure factors wheighed according to the inverse of the corresponding Poisson variance, $\sigma_F^2 = (\sigma_I/2F)^2$.

The data sets for both crystals were finally scaled together, using the appropriate scale factors obtained in the last cycle of the structure refinement.

5 — DISCUSSION

The above results show that the 154 independent reflection intensities from crystal A do not deviate significantly from a Poisson distribution with $v = 1.20$ and $R = 0.023$ (Table 1). However, similar data from crystal B, significantly deviate from this distribution, as evidenced by the larger value of $v = 1.54$; the large R-factor, $R = 0.031$, obtained from this data set is probably due to the smaller sample size, since only 54 independent observations were available in this case.

The above deviation from Poisson statistics can be understood taking into account the much smaller value of γ used for the data collection from crystal B (Table 1). Intensities from this crystal were measured for a very long time; as a consequence, the corresponding Poisson variances become unrealistically smaller than typical instrumental variances, such as time drifts and inhomogeneity of the primary beam. Therefore, the question of increasing the reliability of the data by spending more time measuring the integrated intensities arises and should be discussed. This will be postponed until more experience is gained concerning such long time measurements.

As far as the crystallographic R-factors are concerned (see Table 5) it appears in the present work that the quality of the data improves as the time spent in each measurement is increased.

TABLE 5

Crystal	N.º of independent reflections	N.º of parameters refined	Crystallographic R – factors		Goodness of fit
			R-weighed	R	
A	95	8	0.020	0.023	2.3
B	96	8	0.012	0.021	2.7
A + B	191	9	0.014	0.021	2.6

The goodness of fit (g.o.f.) parameters shown in Table 5 for both crystals are significantly different from unity. There is evidence that this is not caused by inaccuracy of the data or improper standard deviations: out of the reflections which are common to both crystals, there are eleven from crystal A which have $|F_{obs}-F_{calc}| > 2\sigma_F$; of these, only in four cases does the above difference change sign when taken for crystal B. Similarly, taking the nineteen reflections common to both crystals which, for crystal B, yield $|F_{obs}-F_{calc}| > 2\sigma_F$, only five behave as mentioned above.

The values obtained for the above parameters indicate that the model assumed in the course of the present refinement deviates

108

Portgal. Phys. — Vol. 13, fasc. 1-2, pp. 101-109, 1982

from the observed one. Such deviation may be due to the fact that neither thermal diffuse scattering, nor anharmonic motion have been taken into account; but the most significant deviation probably arises from the fact that the electron density in this compound is not spherically symmetric, as was assumed for the calculation of structure factors.

The work on this compound is to be continued with the aim of investigating the electron density distribution.

REFERENCES

[1] STOUT, J. W. and BOO, W. O., *J. Chem. Phys.*, **71**, 1 (1979).
[2] WANKLYN, B. M., GARRARD, B. J. and WONDRE, F., *Journal of Crystal Growth*, **33**, 165 (1976).
[3] GONSCHOREK, W., Intensitätsvarianzen und -verteilungen, accepted for publication in *Z. Krist.*

CONTRIBUTION TO THE STUDY OF THE ORDERING
OF THE SIGMA PHASES (*)

A. Matos Beja and L. Alte da Veiga

Grupo de Estruturas dos Materiais, FC1 INIC, Departamento de Física
3000 Coimbra, Portugal

ABSTRACT — Polyhedra around the atomic sites of the sigma phase structure were defined in a way similar to Wigner-Seitz cell and computer programs for the calculation of their volumes were written; the apllication to the sigma phase Mo_3Co_2 shows that again the J-sites exhibit a peculiar behaviour.

The ordering of sigma phases has been discussed in terms of two determining factors: electronic configuration, and size of constituent atoms [1], [2]. Recent work [3] shows that a sphere-packing model is not appropriate and it appears that the occupancy of the J-sites is determined by the electronic factor [4]. As an attempt to obtain more information it was decided to calculate the volume of the polyhedron, around each site, defined in a way similar to the Wigner-Seitz cell.

For the calculation of the volumes of the polyhedra computer programs were written, having the following main steps:

1. Determination of the polyhedra corners.
2. Determination of the intersections of the polyhedra with parallel planes.
3. Calculation of the volumes of the slabs defined by the parallel planes and, from these, the volume of the corresponding polyhedron.

The results obtained for the sigma phase Mo_3Co_2 are listed in Table I.

(*) Presented at the VII Iberoamerican Congress of Crystallography (21-26 September 1981, Coimbra, Portugal).

The volume of the unit cell calculated by adding the volumes of its 30 polyhedra is 410.4 Å^3, whereas the volume given by unit cell parameters is 411.10 Å^3, which shows an agreement of the order of 0.2 %. Similar calculations will be carried out for other sigma phases and the results will be compared.

TABLE I — Volumes of the polyhedra for the sigma phase Mo$_3$Co$_2$

Site	Multiplicity	Occupancy	Coordination number	Polyhedron volume
A	2	2 Co	12	12.38 Å^3
I$_1$	8	8 Co	12	12.94 Å^3
I$_2$	8	7 Mo + 1 Co	14	14.42 Å^3
J	8	7 Mo + 1 Co	14	13.53 Å^3
G	4	4 Mo	15	14.63 Å^3

Table I shows that the volume corresponding to the J-site is significantly smaller than that corresponding to I$_2$, although both have the same coordination number and occupancy. However, J-sites are special sites in the structure, forming linear chains with abnormally short interatomic distances.

REFERENCES

[1] Hansen, R. C., Raman, A., *Z. Metallkd.*, **61**, 115 (1970).
[2] Wilson, C. G., Spooner, F. J., *Acta Cryst.*, **A29**, 342 (1973).
[3] Alte da Veiga, L. M., Costa, M. M. R. R., de Almeida, M. J. M., Andrade, L. R., Matos Beja, A., *Acta Cryst.*, **A37**, 197 (1981).
[4] Alte da Veiga, L. M., Costa, M. M. R. R., de Almeida, M. J. M., Andrade, L. R., Matos Beja, A., *Acta Cryst.*, **B36**, 1750 (1980).

112

Portgal. Phys. — Vol. 13, fasc. 1-2, pp. 111-112, 1982

THE ORDERING OF THE SIGMA PHASE V$_{62}$Co$_{38}$ (*)

J. M. DE FREITAS, L. M. ALTE DA VEIGA and W. GONSCHOREK ([1])

Grupo de Estruturas dos Materiais, FC1 INIC, Departamento de Física
3000 COIMBRA, Portugal

ABSTRACT — The σ-phase structure V$_{62}$Co$_{38}$ has been studied using an X-ray single-crystal diffractometer. Both size and electronic factors appear to account for a complete ordering of this phase which is approximately stoichiometric. However a significant departure from complete ordering has been detected. [Crystal data: space group P4$_2$/mmm, a = b = 8.834 $\pm$ 0.004, c = 4.586$_5$ $\pm$ 0.002 Å].

1 — INTRODUCTION

The σ-phase structure has thirty atoms per unit cell distributed amongst sites (2 A + 8 I$_1$ + 8 I$_2$ + 8 J + 4 G) of coordination numbers 12 (A , I$_1$), 14 (I$_2$, J) and 15 (G). The occupancies of the different atomic positions have been attributed to the following two factors: the electron concentration and the sizes of the constituent atoms. A review of previous works and a detailed description of ordering schemes is given in a recent paper [1].

The study of the σ-phase in the (V, Co) system is of interest owing to the wide composition range, 45 to 66 at % V [2], thus enabling a study of composition influence on ordering. The present work is concerned with the study of the ordering of an alloy at the V-rich end of the composition range.

---

2 — EXPERIMENTAL

A single crystal was taken from an ingot of $V_{62}Co_{38}$, kindly supplied by Dr. J. M. Welter, from IFF/KFA, Julich, West Germany. A CAD4 diffractometer (Ag radiation) was used to measure the intensities. The lattice parameters were calculated using the least-squares method developed for the CAD4, as:

$$a = b = 8.834 \pm 0.004 \quad , \quad c = 4.586_5 \pm 0.002 \text{ Å}$$

3 — REFINEMENT

A statistical method developed by Gonschorek [3] was applied to select the 128 independent reflections used in the refinement. The selected reflections were corrected for Lorentz and polarization factors; these data were processed using the SDP CAD4 facilities. An isotropic temperature factor of 0.4 was used and no evidence of extinction was detected; no absorption correction was applied since this effect is likely to be small owing to the shape and small size of the crystal and to the radiation used.

The position parameters (Table 1) were refined from an initial set obtained with a different crystal of the same ingot in a preliminary investigation of the [001] projection, using data obtained with Weissenberg photographs.

The refinement was carried out, firstly by least-squares, and subsequently based on difference Fourier syntheses. The R-factors for the ordered, totally disordered and observed structures are listed in Table I. Figures 1 to 4 show the Fourier maps (direct and difference) for the three ordering arrangements tested.

Fig. 1 (next page) — F_o Fourier sections for the observed structure. Contours are at arbitrary equal intervals. Dashed lines represent negative contours. A), B) and C) show sections at $c = 0$, $c = 0.25$, $c = 0.5$ respectively.

Fig. 2 (next page) — $(F_o - F_c)$ Fourier sections for the observed structure. Countours are at 1/10 those of F_o in fig. 1. Dots mark the atomic sites. A), B) and C) as in fig. 1.
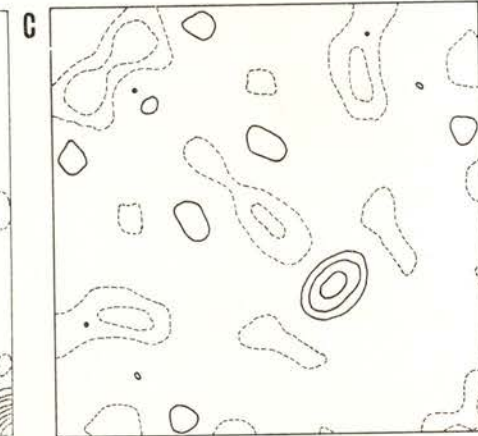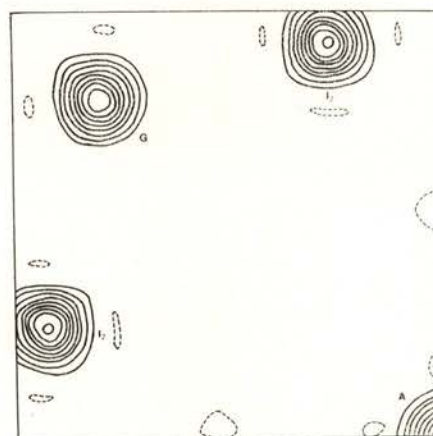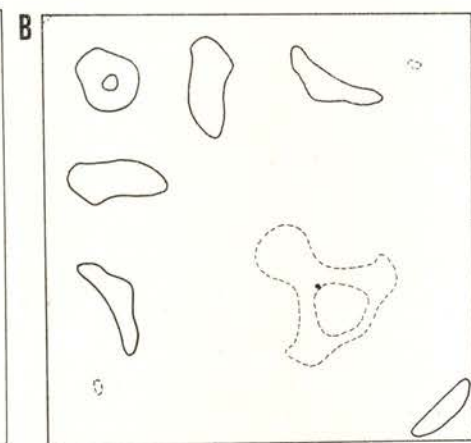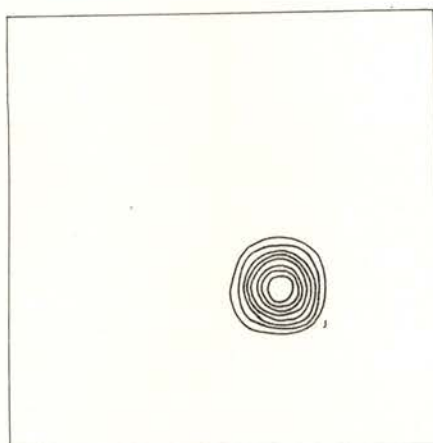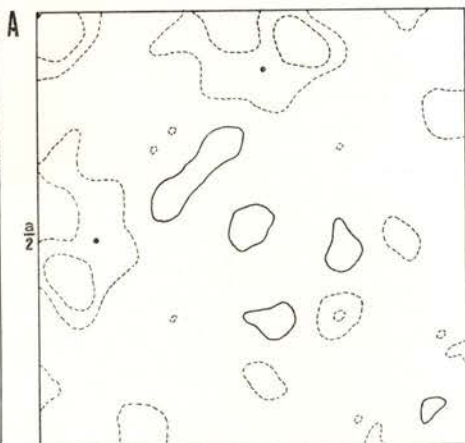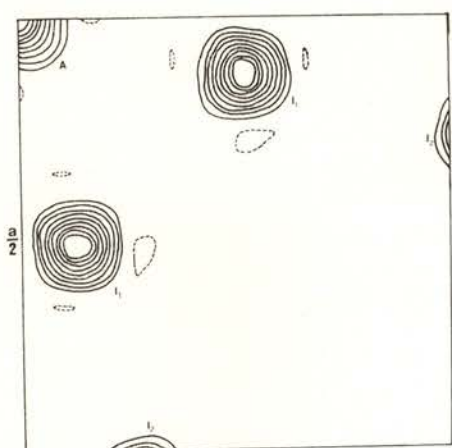
Fig. 1

Fig. 2

V and Co (Z = 23 and Z = 27) are very close in the periodic table which is a disadvantage for the study of the ordering by an X-ray technique. However, the method used by Alte da Veiga et al. [1] for the estimation of the errors (Fig. 5) shows that the ordering observed departs significantly from complete ordering.

TABLE I — Atomic parameters and possible ordering arrangements in σ-VCo

Type	Site	Parameter	Occupancy (No. At. Co)		
			Ordered	Disordered	Observed
2 (a) (0, 0, 0)	A	—	2	0.76	1.3
8 (i) ($x_1, y_1, 0$)	I_1	$x_1 = 0.0664$ $y_1 = 0.2616$	8	3.04	6.8
8 (i) ($x_2, y_2, 0$)	I_2	$x_2 = 0.5369$ $y_2 = 0.1310$	0	3.04	1.25
4 (g) ($x_3, \overline{x}_3, 0$)	G	$x_3 = 0.4001$	0	1.52	0.05
8 (j) (x_4, x_4, z_4)	J	$x_4 = 0.3176$ $z_4 = 0.2479$	0	3.04	2.0
R-factors			7.88	9.04	6.86

4 — DISCUSSION

The ordering of the σ-phases has been discussed in terms of two factors: electronic and size of the constituent atoms. In the σ-phase of the sistem (V, Co) both factors are cooperative and it would be expected that, owing to its almost stoichiometric

---

Fig. 3 (next page) — (F_o - F_c) Fourier sections for the ordered structure. Contours are at 1/10 those of F_o in fig. 1. A), B) and C) as in fig. 1.

Fig. 4 (next page) — (F_o - F_c) Fourier sections for the totally disordered structure. Contours are at 1/10 those of F_o in fig. 1. A), B) and C) as in fig. 1.
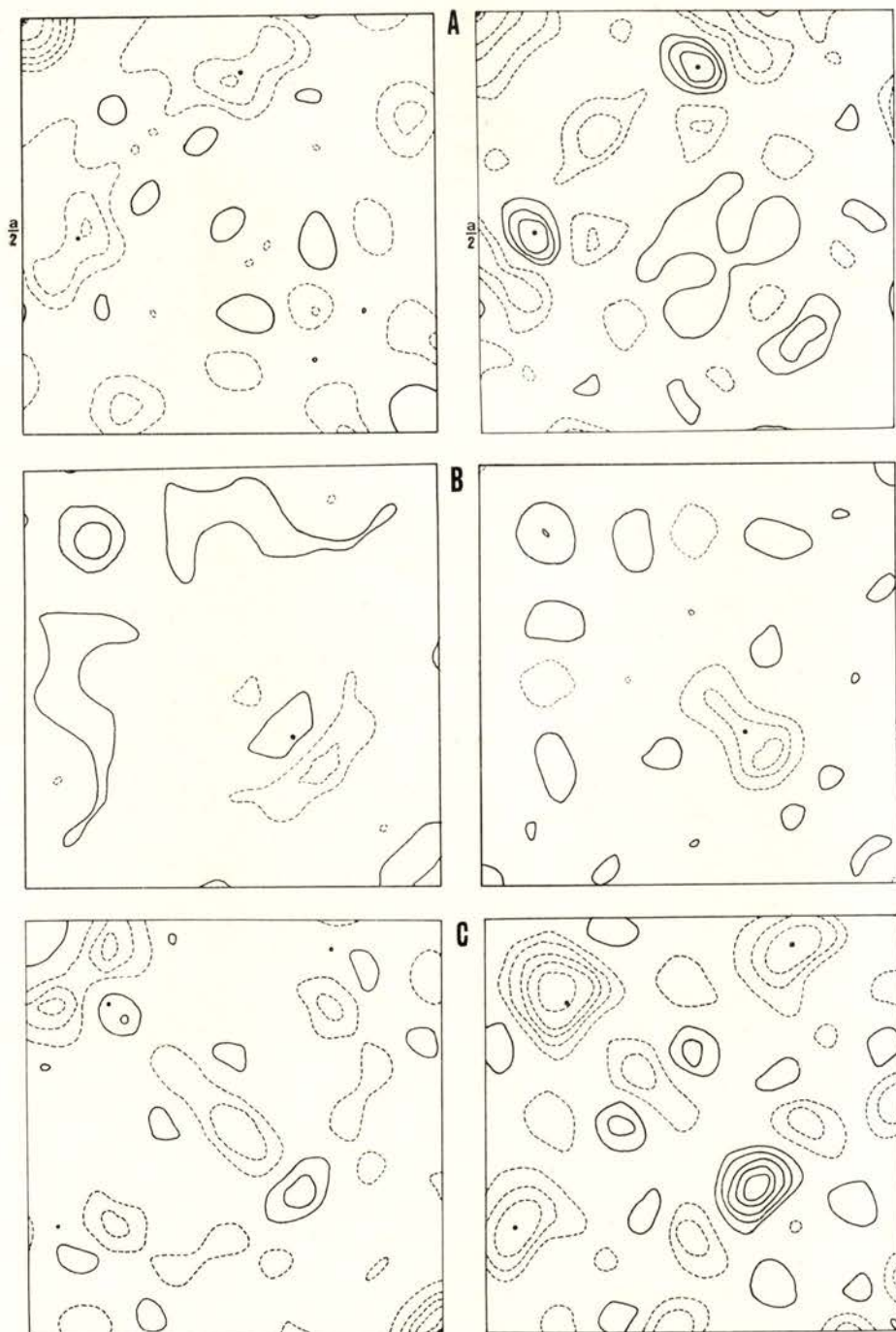
Fig. 3

Fig. 4

composition, the structure would be completely ordered; however, this is not observed. No attempt to interpret this result is made until the study of the ordering in a phase with a different composition is completed. The dependence of ordering on composition will be studied in order to investigate preferential occupation of the atomic sites as observed in the σ-phases $Cr_2 Ru$ and $Cr_2 Os$ [1].
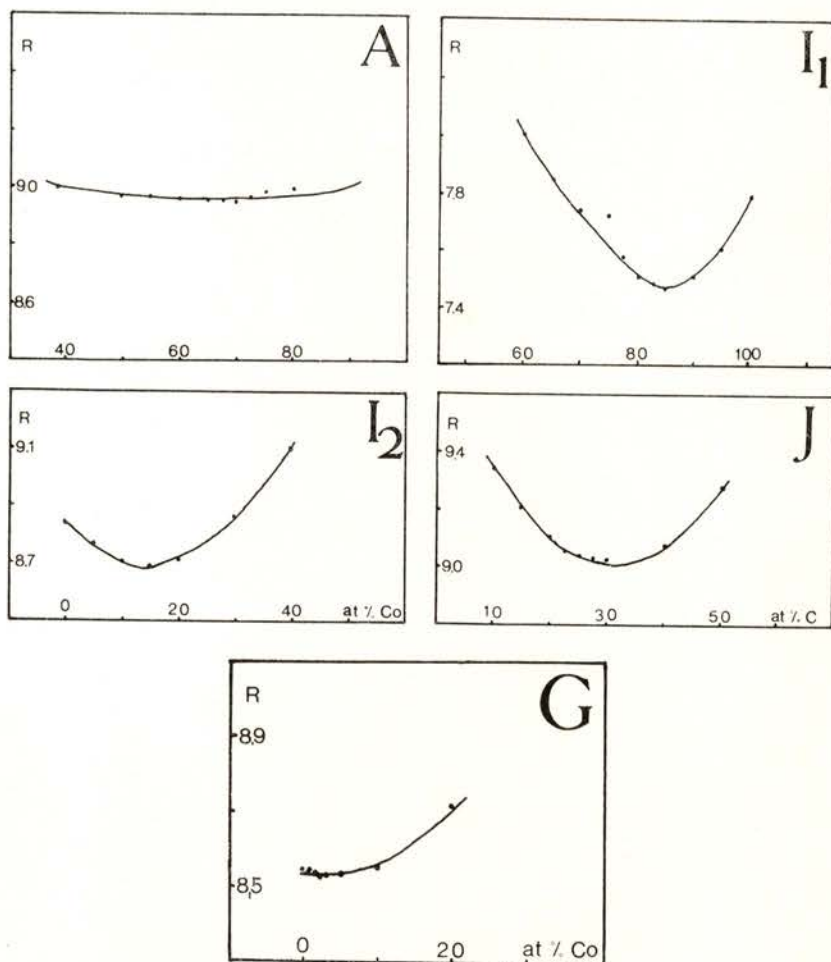
Fig. 5 — Plot of the R-factors against occupancies for each atomic site. Whilst the occupancy for each atomic site was varied, all the remaining sites were assumed to be occupied by the same type of «compound» atom, as required by the composition of the alloy.

REFERENCES

[1] ALTE DA VEIGA, L. M., COSTA, M. M. R. R., DE ALMEIDA, M. J. M., ANDRADE, L. R. and MATOS BEJA, A., *Acta Cryst.*, **B36**, 1750 (1980).

[2] PEARSON, W. B., A Handbook of Lattice Spacings and Structures of Metals and Alloys, edited by W. B. PEARSON, Vols. 1, 2. London: Pergamon Press (1958, 1967).

[3] GONSCHOREK, W., *Portgal. Phys.*, **12**, 49 (1981).

PORTUGALIAE PHYSICA

VOL. 13 · NUMB 1/2 · 1982

CONTENTS

PORTUGALIAE PHYSICA

PORTUGALIAE PHYSICA

PORTUGALIAE PHYSICA

PHYSICA

MANUEL VALADARES

1904 - 1982

Few Portuguese names stand out, in the field of Atomic and Nuclear Physics, as brightly as that of Manuel Valadares.

Born in Lisbon, on February 26th, 1904, Manuel José Nogueira Valadares studied Physics in the Faculty of Science, University of Lisbon, where he later became a lecturer, after post-graduate studies in France.

He received his fundamental research training at the "Laboratoire Curie", Paris, obtaining his PhD in 1933, under Mme Pierre Curie; he was awarded the mention "très honorable" for his thesis "Contribution à la spectrographie, par diffraction cristalline, du rayonnement gamma". During his stay in France he worked also with Dr. S. Rosenblum in the "Laboratoire de l'Aimant Permanent", Bellevue.

In 1940 he moved to Italy, where he carried out research in the "Istituto di Volta" and in the "Laboratorio di Fisica dell'Istituto di Sanità Pubblica".

Having returned to Portugal in 1941, he played a fundamental role in starting Atomic and Nuclear research at the "Laboratório de Física" of the Faculty of Science, Lisbon. Some graduate students obtained their PhD under his supervision and profited by his helpful advice and instructive criticism.

In June 1947 he was dismissed due to increasingly oppressive government measures and, invited by Mme Joliot-Curie, went to France, where he held several academic positions with great success.

Manuel Valadares soon became "Maître de Recherches" and, in 1957, was appointed "Directeur de Recherches". He was "Directeur du Centre de Spéctrométrie Nucléaire et de Spéctrométrie de Masse", Orsay, until 1968, when he wrote a letter of resignation to the "Directeur du C.N.R.S.".

He worked with S. Rosenblum on the development of a technique of magnetic alpha spectrometry and proposed, with him, disintegration schemes for some nuclides.

X-Ray spectroscopy techniques were used by him for the study of L satellites on heavy elements and L radiation intensities.

Manuel Valadares published, often in collaboration with his colleagues or students, over 70 papers, concerned mostly with his research in experimental Atomic and Nuclear Physics; but he was also concerned with problems of history of physics, science policy, application of physics to the study of works of art, etc.

He was widely respected for his modesty and probity and had profound influence on many scientists, who benefited both from his sound advice and his personal prestige.

He was awarded many honours:

"Prémio Artur Malheiros" from the "Academia de Ciências de Lisboa" (1930) for his work "Análise, por espectrografia de Raios X, de transmutações naturais e provocadas";

"Prix La Caze" from the "Académie des Sciences de Paris" (1966), in recognition for his research in alpha radiation spectrometry;

Degree "Doctor Honoris Causa" from the University of Lisbon (1981);

He was appointed, in 1969, by the "Directoire du C.N.R.S.", "Directeur Honoraire du Centre de Spéctrométrie Nucléaire et de Spéctrométrie de Masse".

He was elected honorary member of the Portuguese Physical Society on the occasion of its First National Conference (1978).

The Portuguese government conferred on Prof. Manuel Valadares, in 1979, the "Grau de Grande Oficial da Ordem Militar de Sant'Iago da Espada"; this honour was bestowed upon him in recognition of services rendered to his country.

Manuel Valadares died on the 31st of October, 1982, at the age of 78, in Paris. His contribution to Atomic and Nuclear Physics was highly regarded and his role as a scientist was, in many instances, of the highest importance; Manuel Valadares was one of the founders of *Portugaliae Physica*.

LIST OF PUBLICATIONS

RESEARCH IN ATOMIC AND NUCLEAR PHYSICS

L'antagonisme des radiations dans leurs effets sur la plaque
photographique
(with E. Wassmer and M. Patry)
Helv. Phys. Acta **3** (1930) 391; and Arquivo de Patologia **3** (1931) 41

Figures de distribution du dépôt actif sur les électrodes
(with S. Rosenblum)
C. R. Acad. Sc. Paris **192** (1931) 939

Sur la structure fine des rayons alpha du ThC
(with S. Rosenblum)
C. R. Acad. Sc. Paris **194** (1932) 967

Spectrographie, par diffraction cristalline, des rayons gamma
et X de la famille du Thorium
C. R. Acad. Sc. Paris **196** (1933) 856

Spectrographie, par diffraction cristalline, des rayons gamma
et X de la famille du Radium
C. R. Acad. Sc. Paris **197** (1933) 144

Contribution à la spectrographie, par diffraction cristalline, du
rayonnement gamma
Thèse, Paris, 1933; and Annales de Physique **2** (1934) 197

Étude des satellites $L\alpha$ de l'élement 82 (Pb)
(with F. Mendes)
C. R. Acad. Sc. Paris **206** (1938) 744

Studio dei satelliti delle righe α dello spectro L del piombo
La Ricerca Scientifica **11** (1940) 270

Contributo allo studio degli spettri γ e X molli dei prodotti di
disintegrazione del radon
Rend. R. Accad. d'Italia **2** (1940) 351; and Rend. Ist. Sanità Pub. **3**
(1941) 953

Gli spettri γ e X dei derivati del radon nella regione 700 à 1300 U.X.

Rend. R. Accad. d'Italia **2** (1941) 1049; and Rend. Ist. Sanità Pub. **4** (1941) 713

La loi photoélectrique d'Einstein et le phénomène de conversion interne

Portgal. Phys. **1** (1943) 35

Le spectre L des rayons X du radium D

Portgal. Phys. **1** (1943) 73

O núcleo atómico e os espectros de riscas dos raios X

Lisboa (1944)

Influence de la tension d'excitation sur les satellites des raies $L\alpha$ de l'or

(with F. Mendes)

C. R. Acad. Sc. Paris **226** (1948) 1185

Structure fine du spectre magnétique des rayons α de l'ionium

(with S. Rosenblum and J. Vial)

C. R. Acad. Sc. Paris **227** (1948) 1088

Le spectre du rayonnement alpha émis par RTh + ThX

(with S. Rosenblum and M. Perey)

C. R. Acad. Sc. Paris **228** (1949) 385

Les spectres L et gamma émis par la transmutation RaD → RaE

(with L. Salgueiro)

Portgal. Phys. **3** (1949) 21

Structure fine du spectre magnétique alpha du thorium X

(with S. Rosenblum, M. Perey and J. Vial)

C. R. Acad. Sc. Paris **229** (1949) 1009

Nouvelle détermination de quelques rayons des noyaux radioactifs lourds

(with S. Rosenblum)

C. R. Acad. Sc. Paris **230** (1950) 384

Structure fine du spectre magnétique alpha du plutonium 239

(with S. Rosenblum and B. Goldschmidt)

C. R. Acad. Sc. Paris **230** (1950) 638

Spectrographie par diffraction cristalline du rayonnement electro-magnétique du RaD

(with M. Frilley and B. G. Gokhale)

C. R. Acad. Sc. Paris **232** (1951) 50

Spectre L émis dans la transmutation RaD → RaE
    (with M. Frilley and B. G. Gokhale)
        C. R. Acad. Sc. Paris **232** (1951) 157

Le spectre beta de conversion interne émis dans la transmutation
    ionium → radium
    (with S. Rosenblum)
        C. R. Acad. Sc. Paris **232** (1951) 501

Sur l'influence du moment magnétique nucléaire sur la largeur
    des raies dans les spectres de rayons X
    (with M. Frilley and B. G. Gokhale)
        C. R. Acad. Sc. Paris **233** (1951) 1183

Spectre β de conversion interne émis dans la transmutation
    thorium X → thoron
    (with S. Rosenblum and M. Guillot)
        C. R. Acad. Sc. Paris **234** (1952) 1767

Les spins des niveaux des noyaux pairs-pairs et la théorie de
    l'émission α
    (with S. Rosenblum)
        C. R. Acad. Sc. Paris **234** (1952) 2359

Spectre d'électrons de conversion interne émis dans la trans-
    mutation radiothorium → thorium X
    (with S. Rosenblum and M. Guillot)
        C. R. Acad. Sc. Paris **235** (1952) 238

Sur les niveaux nucléaires (premiers états excités)
    (with S. Rosenblum)
        C. R. Acad. Sc. Paris **235** (1952) 711

Classification des "rayons" des noyaux émetteurs α en fonction
    de l'excès neutronique
    (with S. Rosenblum)
        C. R. Acad. Sc. Paris **236** (1953) 196

Sur les rayonnements émis au cours de la transmutation
    RaAc → AcX (I)
    (with M. Frilley and S. Rosenblum)
        J. de Phys. et Rad. **15** (1954) 45

Sur la structure fine α de l'ionium
    (with S. Rosenblum, J. Blandin-Vial and R. Bernas)
        C. R. Acad. Sc. Paris **238** (1954) 1496

Sur le spectre d'électrons de conversion émis par ^{241}Am → ^{237}Np
(with J. Milsted and S. Rosenblum)
C. R. Acad. Sc. Paris **239** (1954) 259

Sur le schéma de niveaux du ^{237}Np
(with J. Milsted and S. Rosenblum)
C. R. Acad. Sc. Paris **239** (1954) 700

Les spectres d'électrons de conversion émis dans les transmutations radiothorium → thorium X → thoron
(with S. Rosenblum and M. Guillot)
J. de Phys. et Rad. **15** (1954) 129

Le spectre d'électrons de conversion émis dans la transmutation ionium → radium
(with S. Rosenblum and R. Bernas)
C. R. Acad. Sc. Paris **239** (1954) 759

Sur les rayonnements émis au cours de la transmutation RaAc → AcX (II)
(with M. Frilley, S. Rosenblum and G. Bouissières)
J. de Phys. et Rad. **16** (1955) 378

Sur la largeur propre des raies d'électrons de conversion
J. de Phys. et Rad. **16** (1955) 542

Spectrographe magnétique avec pré-accélération pour l'étude d'électrons de faible énergie
(with S. Rosenblum and J. Sant'Ana Dionísio)
J. de Phys. et Rad. **17** (1956) 112

Sur le rayonnement γ émis au cours de la transmutation RaD → RaE
(with M. Frilley)
J. de Phys. et Rad. **18** (1957) 468

Etudes sur la transmutation ^{241}Am → ^{237}Np
(with S. Rosenblum and J. Milsted)
J. de Phys. et Rad. **18** (1957) 609

Coefficients de conversion interne dans les niveaux L_I, L_{II}, L_{III}
(with M. Frilley)
J. de Phys. et Rad. **20** (1959) 60

Le spectre d'électrons de conversion émis au cours de la transmutation ^{233}Pa → ^{233}U
(with G. Albouy)
J. de Phys. et Rad. **20** (1959) 816

Le spectre d'électrons de conversion (faibles énergies) et les spectres Auger (L, M, N) émis au cours de la transmutation β du protactinium 233
(with G. Albouy)
C. R. Acad. Sc. Paris **250** (1960) 2877

Sur le rayonnement γ émis au cours de la transmutation thorium 234 (uranium X_1) $\rightarrow$ protactinium 234 métastable (uranium X_2)
(with R. Foucher, J. Merinis and A. de Pinho)
C. R. Acad. Sc. Paris **255** (1962) 882

Schéma des niveaux excités du protactinium 234
(with R. Foucher, J. Merinis and A. de Pinho)
C. R. Acad. Sc. Paris **255** (1962) 1916

Interprétation du schéma de niveaux du ^{234}Pa, noyau impair-impair
(with R. Foucher, J. Merinis and A. de Pinho)
Journal de Physique **24** (1963) 203

Quelques résultats nouveaux sur la désintegration ^{231}Pa $\rightarrow$ ^{227}Ac
(with H. Abou-Leila, R. Foucher, A. de Pinho and N. Perrin)
Journal de Physique **24** (1963) 857

Sur l'existence de bandes satellites dans les spectres d'électrons de conversion interne
(with R. J. Walen and Ch. Briançon)
C. R. Acad. Sc. Paris **263** (1966) 313

Sur le spectre d'électrons de conversion interne émis par des atoms en vol: cas de la désintégration α de l'américium 241
(with Ch. Briançon and R. J. Walen)
C. R. Acad. Sc. Paris **265** (1967) 1496

Effets du recul alpha en conversion interne
Journal de Physique **29** Cl (1968) 103

Mise en evidence d'excitations multiples des couches electroniques profondes dans le spectre de conversion interne de la transition nucléaire isomérique de ^{109}Ag
(with Ch. Briançon and R. J. Walen)
Physics Letters **34B** (1971) 599

Bandes satellites des raies d'électrons de conversion interne
(with R. J. Walen and Ch. Briançon)
Journal de Physique **32** C4 (1971) 145

Internal conversion electrons: Energy shift and nuclear half-life in ionized atoms — multiple deep vacancy production through second order effects
(with R. J. Walen and Ch. Briançon)
International Conference on Inner Shell Ionization Phenomena, Atlanta, Georgia (1972) 1906.

BOOKS AND SOME OTHER PUBLICATIONS

Absorção da radiação beta na passagem através lâminas metálicas (contribuição para beta-terapia superficial)
Arquivo de Patologia 2 (1930) 238

Colheita e preparação do radão (instalação e técnica)
Arquivo de Patologia 2 (1930) 247

Propriedades físicas dos óleos fixos
(with H. A. Ferreira, V. Paraíso, F. Mendes)
Publ. do Lab. Física da Univ. de Lisboa 1 (1932) 63

Mecanismo de emissão da radiação gama
Revista de Química Pura e Aplicada 9 (1934) 3

Madame Curie
Técnica, no. 64 (1935) 51; and Gazeta de Física 1 (1948) 272

Transmutation des éléments par des particules accélérées artificiellement
Ed. Hermann et Cie, Paris (1935)

A Salomé de L. Cranach, o Velho
(with J. Couto)
Boletim da Acad. Nac. de Belas-Artes 4 (1938) 39

Laboratório para o exame de obras de arte
Boletim dos Museus Nacionais de Arte Antiga 1 (1939) 32

Estudo comparativo, ao Raio X, da obra dos Cranach
(with O. Trigo de Sousa)
Boletim dos Museus Nacionais de Arte Antiga 8 (1943) 187

A obra científica de Jean Perrin
Publ. Instituto Francês em Portugal (1944)

Exame, ao raio X, do quadro "Cristo descido da Cruz" (autor desconhecido)

Boletim dos Museus Nacionais de Arte Antiga **9/10** (1944) 39

Observação com raios X de diamantes inclusos em massas de cera (with F. Mendes)

Boletim no. 14 do Museu Min. e Geol. da Univ. de Lisboa (1946) 179

Elementos de Física Atómica

Sá da Costa Ed., Lisboa (1947)

Recordações de Paul Langevin

Gazeta de Física **1** (1947) 103

O Laboratório de Física da Fac. Ciênc. de Lisboa sob a direcção do Prof. Dr. A. Cyrillo Soares (1930-47) e a investigação científica

Gazeta de Física **2** (1950) 93

Transmutação por captura electrónica

Gazeta de Física **3** (1954) 1

A importância da energia nuclear para o nosso país

Seara Nova 1331-6 (1957) 77

A obra científica de Frederic Joliot

Gazeta de Física **3** (1959) 188

A reforma das Faculdades de Ciências

Repùblica, 15 Junho 1959, 24 Julho 1959, 25 Agosto 1959

Salomon Rosenblum

Nuclear Physics **15** (1960) 189; and Journal des Recherches du CNRS (1960)

NON-COLLINEAR BREAKING OF COLLINEAR SYMMETRIES
AT FINITE MOMENTUM TRANSFER

J. Pulido (*)

Department of Mathematical Physics. University of Birmingham, U. K.

ABSTRACT — The breaking of the $SU(2)_w$ collinear symmetry arising when leaving the forward direction in scattering processes is studied. The starting point is the null-plane hydrogen atom Hamiltonian of Bell and Ruegg which exhibits this $SU(2)_w$ symmetry in an approximate form. Introducing an electromagnetic interaction with non-zero momentum transfer photons, it is found that breaking is mainly due to transversely polarized photons. Application to hadron-hadron scattering can only be realistic in the low q^2 exchange sector.

1 — INTRODUCTION

The null plane dynamics of hydrogen-like atoms was studied by Bell and Ruegg (BR) [1] in an approximation depending on c, the velocity of light, being large. Their ground state Hamiltonian exhibits an approximate $SU(2)_w$ symmetry which arises upon neglecting third order and higher terms in c^{-1} and which we will use as our starting point (1). They implicitly assume the interaction with $q = 0$ photons in their calculation of the magnetic moment. In this paper we examine the breaking process of a collinear symmetry like $SU(2)_w$ by calculating the interaction with non-zero momentum transfer ($t = q^2 \neq 0$) photons.

To this end we split the Hamiltonian into two terms

$$H_0 + H_I \tag{1.1}$$

(*) Present Address: Centro de Física da Matéria Condensada, Av. Prof. Gama Pinto 2, 1699 Lisboa Codex, Portugal.

(1) Either expression (17) or (26) of [1].

where H_0, the free part, given by BR, is supposed to be symmetry conserving and H_I, depending explicitly on q^2 through the form factors, will be symmetry breaking. The basis for the analysis of the symmetry breaking will be to compare the order of magnitude of the q^2 dependent terms involving spin in H_I with the terms of H_0.

The plan of the paper is as follows: in part 2 the calculation of the form factors of the hydrogen atom is outlined. In part 3 the $SU(2)_w$ symmetry breaking is analyzed in order to determine the minimum value of q^2 which breaks the symmetry. The result is valid for the long range sector of the potential.

2 — THE FORM FACTORS OF THE HYDROGEN ATOM

The model we use for the hydrogen atom is that of a bound state in a Coulomb-like potential. Thus the proton is just a force centre and the interacting external photon only «sees» the electron spin and electron charge. The hydrogen atom is therefore considered as a charged spin $1/2$ particle with structure. The electromagnetic interaction of a non-point-like spin $1/2$ particle is given by the usual expression [2, 3]:

$$\bar{\psi} \, [\, i \, \gamma_\mu \, e_\mu \, F_1(q^2) + \sigma_{\mu\nu} \, q_\nu \, e_\mu \, F_2(q^2) \,] \, \psi \qquad (2.1)$$

to which corresponds the diagram of Fig. 1
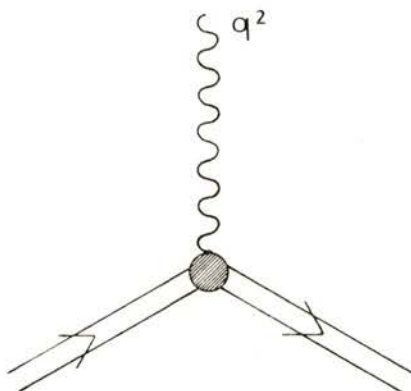
Fig. 1 — Photon-hydrogen atom interaction with a structure described by the form factors.

Here $F_1(q^2)$, $F_2(q^2)$ are the form factors of the hydrogen atom (electric and magnetic, respectively), q_ν is the photon four-momentum, e_μ is the polarization four-vector of the photon, $\sigma_{\mu\nu} = [\gamma_\mu, \gamma_\nu]$; the Dirac matrices are [1]

$$\vec{\gamma} = \begin{bmatrix} 0 & -i\vec{\sigma} \\ i\vec{\sigma} & 0 \end{bmatrix} \qquad \gamma_4 = \begin{bmatrix} 1 & \\ & -1 \end{bmatrix} \qquad (2.2)$$

and $\bar{\psi} = \psi^+ \gamma_4$. Expression (2.1) is to be calculated between initial and final states which are just described by solutions of the free particle Dirac equation.

Here the information on the structure of the system is all contained in the form factors. In order to evaluate these, we equate the above description (2.1) for the interaction to the one within the impulse approximation in which the structure of the system is all contained in the initial and final wave functions and to which corresponds the diagram of Fig. 2.
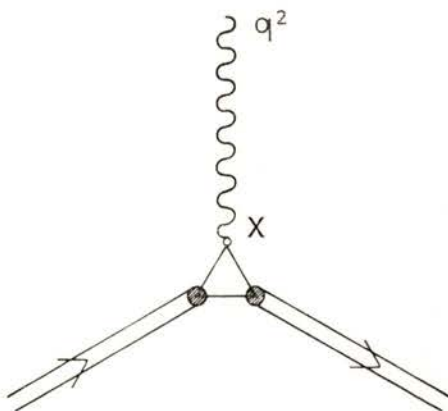
Fig. 2 — The same process considered as a point-like interaction. Here the structure lies in the wave functions of the hydrogen atom.

Here, contrarily to Fig. 1, we have now a point-like interaction at x of the usual form: $ie\gamma_\mu e_\mu$.

In the case of deuteron scattering, the amplitude for the diagram of Fig. 2 was written by Abers, Burkhardt, Teplitz and

---

[1]   At this stage we use the conventional «low energy» Dirac notation.

Wilkin (ABTW) [4] (¹) and becomes in our case after some manipulation [5] in which the convolution theorem was used:

$$\int d^3r \, \bar{\psi}_f(\vec{r}) \, ie\gamma_\mu \, e_\mu \, \psi_i(\vec{r}) \, \exp(i\vec{q}\cdot\vec{r}/2) \qquad (2.3)$$

where the ψ's are now electron spin wave functions within the hydrogen atom (see for instance [6]), $\vec{q}$ is the 3-momentum transfer carried by the photon and $\vec{r}$ is the distance of the electron from the proton.

In equating the two descriptions (2.1) and (2.3), care must be taken of the motion of the final state relative to the initial one. In the case of (2.1) this is explicitly included in the form of the spinor $\bar{\psi}$. As for (2.3), and assuming the initial state at rest we apply a Lorentz boost along the z-axis to the final wave function, in order to bring it to rest. This is given by [7]

$$S_3 = \exp(-\omega \, \sigma_{03}/2) \qquad (2.4)$$

where ω, the rapidity of the transformation, is:

$$\text{ch } \omega = (1 - \beta^2)^{-\frac{1}{2}}$$

where $\beta = Q/E_2$ is the velocity. Q is the z-component of the 3 momentum of the final state (assumed to be along the z-axis, $q = (v, 0, 0, Q)$), M its mass, and E_2 its energy [5]:

$$E_2 = (2M^2 - q^2)/2M^2 \,, \, Q = (q^4 - 4M^2q^2)^{\frac{1}{2}}/2M \,, \, v = q^2/2M \qquad (2.5)$$

Separating transverse components (spin-flip) and longitudinal and time-like components (non-flip), we obtain the following two equations:

Transverse

$$\int d^3r \, \bar{\bar{\psi}}_f(\vec{r}) \, ie \, \vec{\gamma}_\perp \cdot \vec{e}_\perp \, e^{i(\vec{q}/2)\cdot\vec{r}} \, \psi_i(\vec{r})$$

$$= [0, 1, 0, Q/(E_2 + M)] \cdot \{\vec{\gamma}_\perp \cdot \vec{e}_\perp \, F_1 + \sigma_{\perp v} q_v e_\perp F_2\} \cdot \begin{bmatrix} 1 \\ 0 \\ 0 \\ 0 \end{bmatrix}$$

(¹) Equation (2.18) of ABTW.

Longitudinal and time-like

$$\int d^3r \; \bar{\tilde{\psi}}_f (\vec{r}) \; ie \; (\gamma_0 \; e_0 - \gamma_3 \; e_3) \; e^{i \, (\vec{q}/2) \cdot \vec{r}} \; \psi_i (\vec{r})$$
$$= [1, \, 0, \, Q/(E_2 + M), \, 0] \cdot \{ i \, (\gamma_0 \, e_0 - \gamma_3 \, e_3) \, F_1 \begin{bmatrix} 1 \\ 0 \\ 0 \\ 0 \end{bmatrix}$$
$$+ (\sigma_{\nu_0} \, q_\nu \, e_0 - \sigma_{3\nu} \, q_\nu \, e_3) F_2 \}$$

where the twiddles over the final wave functions represent the Lorentz boost given by (2.4): $\tilde{\psi}_F = S_3 \, \psi_f$.

Solving this system of equations, we obtain for the hydrogen atom form factors the following expressions:

$$F_1 (q^2) = (q^2/2M) \; F_2 (q^2) + (e/2M) \; z \; (1 + y^2)^{-2} \quad (2.6)$$

$$F_2 (q^2) = e \; z^{-1} \; (1 + y^2)^{-2} + e/(\mu^2 + 1) \cdot z^{-1} \; (1 + y^2)^{-2}$$
$$+ \mu e a z / 4M \; (\mu^2 + 1) \cdot (1 + y^2)^{-2} \quad (2.7)$$
$$- \mu^2 \, e/(\mu^2 + 1) \; z^{-1} \; [(2 + y^{-2}) \, (1 + y^2)^{-2} - y^{-3} \, \text{ang tg y}]$$

where

$z = (4M^2 - q^2)^{\frac{1}{2}}$, $y^2 = (a/8M)^2 \; (q^4 - 4M^2q^2)$, $\mu^2 = (mc - E)/(mc + E)$, $e = 1/\sqrt{137}$ is the electron charge and a the typical electron orbit radius.

Therefore

$$F_1 (0) = e \; , \; F_2 (0) = e \, (2 - \mu^2 + a\mu M)/2M \, (\mu^2 + 1) \simeq e/4 \quad (2.8)$$

$$F'_1 (0) = (1/2M) \; F_2 (0) + e \, (M^2a^2 - 1)/8M^2 \simeq ea^2/8 \quad (2.9)$$

$$F'_2 (0) = e \, (1 + M^2a^2)/16 \, M^3 \cdot [1 + 1/(\mu^2 + 1)]$$
$$+ \mu e a \, (a^2M^2 - 1) / 16 \, M^2 \, (\mu^2 + 1) \quad (2.10)$$
$$+ \mu^2 e / 160M^3 \, (\mu^2 + 1) \cdot (9a^2M^2 - 20) \simeq a^3 \mu e / 16 \, (\mu^2 + 1)$$

These form factors are smoothly decreasing functions of q^2 behaving as $(q^2)^{-2}$ for large q^2. It is easy to check that $F_1 (0) = e$

as expected, since the hydrogen atom in this model is a charged particle with charge e. This model also gives a reasonable prediction for the mean square radii of the spatial distributions [2, 5].

3 — THE ANALYSIS OF THE SYMMETRY BREAKING

Expanding the form factors in series of q^2, (2.1) can be converted into $(F_2(0) = \mu_M = $ magnetic moment):

$$\bar{u} [\gamma_\mu e_\mu (e + q^2 F'(0) + ...) + \sigma_{\mu\nu} q_\nu e_\mu (\mu_{\perp} + q^2 F_2'(0))] u \qquad (3.1)$$

This is of course a transition matrix element which, since we are treating the interaction in perturbation theory, is directly related to the Hamiltonian. However, it can only provide a quantitative measure of BR symmetry breaking if we use the usual «high energy» Dirac notation as in [1],

$$\vec{\gamma}_\perp = \begin{bmatrix} -\sigma_3 \vec{\sigma}_\perp & 0 \\ 0 & -\sigma_3 \vec{\sigma}_\perp \end{bmatrix} , \quad \gamma_3 = \begin{bmatrix} 0 & -\sigma_3 \\ \sigma_3 & 0 \end{bmatrix} , \quad \gamma_0 = \begin{bmatrix} 0 & \sigma_3 \\ \sigma_3 & 0 \end{bmatrix}$$

$$\bar{u} = u^+ \gamma_0 \quad , \quad \sigma_{\mu\nu} = i/2 [\gamma_\mu, \gamma_\nu] \quad , \quad S_3 = \exp(-i\omega\sigma_{03}/2)$$

to which correspond the following solutions for the free Dirac equation

$$\frac{1}{\sqrt{2}} \begin{bmatrix} 1 \\ 0 \\ 1 \\ 0 \end{bmatrix} \quad , \quad \frac{1}{\sqrt{2}} \begin{bmatrix} 0 \\ 1 \\ 0 \\ -1 \end{bmatrix}$$

for spin + and − respectively.

As we said previously we will now compare the order of magnitude of the spin dependent terms arising in (3.1) with the

128

Portgal. Phys. — Vol. 13, fasc. 3-4, pp. 123-136, 1982

spin dependent terms of BR's free Hamiltonian for the ground state hydrogen atom in the null-plane, which is repeated here [1]:

$$\hat{h} = 1/2\ (\eta + \eta^{-1})$$
$$+\ 1/2\ p^2_\perp\ \eta^{-1} + 1/2\ v + 1/2\ \eta^{-1}\ v\ \eta^{-1}$$
$$+\ 1/2\ \eta^{-1}\ [\sigma_3\vec{\sigma}_\perp \cdot \vec{p}_\perp\ ,\ v]\,\eta^{-1}$$
$$+\ 1/2\ \eta^{-1}\ \vec{\sigma}_\perp \cdot \vec{p}_\perp\ v\ \vec{\sigma}_\perp \cdot \vec{p}_\perp\ \eta^{-1} + 1/2\ \eta^{-1}\ v\ \eta^{-1}\ v\ \eta^{-1} \qquad (3.2)$$
$$+\ ...$$

where p is the momentum of the hydrogen atom electron, supposed to be a first order small quantity, v the binding Coulomb potential and η denotes the z-differentiation in the null-plane. We note that the terms up to second order in small quantities are spin independent. Introducing $q^2 \neq 0$ photons via (3.1), the appearance of any spin dependent terms of order of magnitude equal or greater than p^2 will therefore break BR symmetry [2]. To state it more precisely, a term like $(\vec{\sigma} \cdot \vec{p})\,p$ will be responsible for a symmetry breaking as well as something like $(\vec{\sigma} \cdot \vec{p})$ (even stronger effect), but $(\vec{\sigma} \cdot \vec{p})\,p^2$, for instance, will not.

We need to adopt units as BR, that is, $\hbar = c = m = 1$. Thus the Compton wavelength of the electron is our unit of length: $\hbar/mc = 1$.

From ref. [6], $a = 137$ (in units of $\hbar/mc$) and making use of the uncertainty principle:

$$p = 1/a = 7.3 \times 10^{-3}\ ,\ p^2 = 5.3 \times 10^{-5} \qquad (3.3)$$

Corresponding to the two amplitudes considered before, there are two types of symmetry breaking to consider: one for transverse photons and the other for longitudinal and time-like ones.

---

[1] Expression (17) of [1].

[2] $p^2 = \vec{p} \cdot \vec{p}$.

3.1 — *Symmetry breaking for transverse photons*

The interaction Hamiltonian assumes in this case the form

$$
\left.\overline{S_3\, u_f}\right\} A
\begin{bmatrix}
0 & -\sqrt{2}\,e_- & 0 & 0 \\
\sqrt{2}\,e_+ & 0 & 0 & 0 \\
0 & 0 & 0 & -\sqrt{2}\,e_- \\
0 & 0 & \sqrt{2}\,e_+ & 0
\end{bmatrix}
\tag{3.4}
$$

$$
+
\begin{bmatrix}
0 & 0 & 0 & -\sqrt{2}\,e_- \\
0 & 0 & -\sqrt{2}\,e_+ & 0 \\
0 & \sqrt{2}\,e_- & 0 & 0 \\
\sqrt{2}\,e_+ & 0 & 0 & 0
\end{bmatrix}
B\,Q -
\begin{bmatrix}
0 & 0 & 0 & \sqrt{2}\,e_- \\
0 & 0 & \sqrt{2}\,e_+ & 0 \\
0 & \sqrt{2}\,e_- & 0 & 0 \\
\sqrt{2}\,e_+ & 0 & 0 & 0
\end{bmatrix}
B_V \Big\} u_i
$$

where $A = (e + q^2\, F_1'(0) + \ldots)$; $B = (\mu_M + q^2\, F_2'(0) + \ldots)$ and $e_\pm = (1/\sqrt{2})\,(e_1 \pm ie_2)$ are the polarization vectors.

For $q^2 = 0$ the electric charge term e in the electric form factor expansion is still present while all the others vanish. Since the symmetry is defined at $q^2 = 0$, this term cannot represent any symmetry breaking effect and must therefore be excluded from the analysis [1].

As a starting point we may choose a value for q^2 of the order of p^2 ($q^2 = -p^2$, since $q^2 < 0$). Then, using the solutions of the free particle Dirac equation for $\bar{u}$ and u and equations (2.5), (2.9), we have for the electric term in (3.4)

zero order
$$
-\sqrt{2}\ e\ (-q^2)^{1/2}\,/\,2M = -2.4 \times 10^{-7}
\tag{3.5}
$$
first order
$$
-\sqrt{2}\ (-q^2)^{1/2}\,/\,2M \,.\, q^2\, F_1'(0) = 3 \times 10^{-8}
\tag{3.5a}
$$

which does not produce any symmetry breaking, as we realize upon comparison with p^2 (3.3).

---

[1] In fact one easily sees that it gives zero.

Turning to the magnetic terms in (3.4), we have similarly, using (2.5), (2.8), (2.10).

zero order

$$\sqrt{2} \; (q^2 / 2M) \; \mu_M \; (-q^2)^{1/2} / 2M \simeq -8.7 \times 10^{-16} \qquad (3.6)$$

first order

$$\sqrt{2} \; (q^2 / 2M) \; (-q^2)^{1/2} / 2M \cdot q^2 \, F'_2 \, (0) \simeq 1.08 \times 10^{-16} \qquad (3.6a)$$

for the v terms in (3.4) and

zero order

$$-\sqrt{2} \; [1 - q^2 / 4M^2]^{1/2} \; (-q^2)^{1/2} \; (4M^2 - q^2)^{1/2} \; \mu_M / 2M$$
$$\simeq -2.2 \times 10^{-4} \qquad (3.7)$$

first order

$$-\sqrt{2} \; [1 - q^2 / 4M^2]^{1/2} \; (-q^2)^{1/2} \; (4M^2 - q^2)^{1/2} \; q^2 \, F'_2 \, (0) / 2M$$
$$\simeq -2.8 \times 10^{-5} \qquad (3.7a)$$

for the Q terms in (3.4).

Symmetry breaking is apparent here when we compare (3.7) with p^2 (3.3). Convergence of the series implies smaller values for higher order terms, therefore making it unnecessary to calculate further form factor derivatives.

Therefore, for transverse photons the symmetry breaking effect occurs overwhelmingly in the magnetic part of the amplitude. The smallest photon four-momentum able to produce it is easily determined from (3.7) being of the order of $p^2/16$. At this order of magnitude the contribution of all the other terms from the electric and magnetic part is negligible. In fact, substituting $q^2 = -p^2/16$ in (3.7), we have:

$$\sqrt{2} \; q^2 \, \mu_M = -5.5 \times 10^{-5} \qquad (3.8)$$

which is just over p^2 (3.3).

These results are summarized in Table I.

3.2 — Symmetry breaking for longitudinal and time-like photons

The interaction Hamiltonian is in this case:

$$\overline{S_3\, u_f} \left\{ \begin{bmatrix} 0 & 0 & (1+v/Q) & 0 \\ 0 & 0 & 0 & -(1+v/Q) \\ (1-v/Q) & 0 & 0 & 0 \\ 0 & (v/Q-1) & 0 & 0 \end{bmatrix} e_0 \right.$$

$$\left. + \begin{bmatrix} -q^2/Q & 0 & 0 & 0 \\ 0 & -q^2/Q & 0 & 0 \\ 0 & 0 & q^2/Q & 0 \\ 0 & 0 & 0 & q^2/Q \end{bmatrix} e_0 \right\} u_i \qquad (3.9)$$

Whereas in the previous case the Lorentz condition $q_\mu\, e_\mu = 0$ did not provide any information, here it is essential for expressing e_0, e_3 in terms of kinematical quantities.

Expanding (3.9) and using equations (2.5) for v and Q we obtain

$$\left[\left(1 - \frac{q^2}{4M^2}\right)^{1/2} - \frac{q^2}{2M\,(4M^2 - q^2)^{1/2}} \right] \left(e + \frac{q^2\, a^2}{8}\, e \right)$$

$$+ \frac{q^2}{(4M^2 - q^2)^{1/2}} \left(\frac{e}{4} + q^2\, \frac{a^3\, \mu}{16\,(\mu^2 + 1)}\, e \right) \qquad (3.10)$$

Proceeding now with the symmetry breaking analysis, we first note that, as regards the electric form factor, the first term cannot be accounted for, since it produces its largest contribution at $q^2 = 0$ and therefore does not represent a measure of the symmetry breaking effect for small q^2. Starting by choosing $q^2 = p^2$ as before, we have, for the electric part of the amplitude, using (2.9),

zero order

$$- e\,(q^2/2M)\,(4M^2 - q^2)^{-1/2} \simeq 3.36 \times 10^{-13} \qquad (3.11)$$

first order

$$- (q^2/2M)\,(4M^2 - q^2)^{-1/2}\, q^2\, F_1'(0) \simeq - 4.2 \times 10^{-14} \qquad (3.11a)$$

Comparing these values with p^2 (3.3) there is obviously no symmetry breaking in this case.

For the magnetic part, using (2.8), (2.10):

zero order

$$q^2 (4M^2 - q^2)^{-1/2} \cdot (e / 4) \simeq - 3 \times 10^{-10} \qquad (3.12)$$

first order

$$q^2 (4M^2 - q^2)^{-1/2} \cdot q^2 F_2' (0) \simeq 3.9 \times 10^{-11} \qquad (3.12a)$$

which does not give rise to any symmetry breaking as well. The smallest q^2 which is able to produce it, is, from (3.12a), of the order of 7p since in this case

$$(3.12a) \rightarrow 3.5 \times 10^{-5}$$

which is of the order of p^2 (3.3). The contribution from the other terms is again negligible. Therefore, for longitudinal and time-like photons, the symmetry breaking is much less drastic than for transverse ones and also determined by the magnetic part of the amplitude.

These results are summarized in Table II.

3.3 — *Discussion*

As we have seen the minimum photon momentum which is responsible for symmetry breaking is about 1.5×10^4 times greater for longitudinal and time-like photons than for transverse ones. It is worth noting that since, in the usual natural units system ($\hbar = c = 1$) the electron mass is m = 0.511 MeV, its Compton wavelength will be $\hbar / mc = (0,511 \text{ MeV})^{-1}$ resulting p = 1 / a = 3.72 keV. Therefore the limit for transverse photons for instance is: $q^2 \sim p^2 / 16 = 0.86 \text{ keV}^2$.

Equations (3.5) to (3.7a) and (3.11) to (3.12a) give us the information we require on the symmetry breaking. Higher than linear terms in q^2 are negligible provided this is kept small. The

TABLE I — For transverse photons breaking is determined by the magnetic part of the amplitude and always thereby dominated (p = 1/a).

	F$_1$				F$_2$					
q^2→	0	p^2	Limit p	p^0	0	p^3	Limit p^2/16	p^2	p	p^0
p^{-1}										B
p^0										
p				B					B	
p^2			B				B	B		
p^3	[B]	B			[B]	B				

results are summarized in Tables I, II where horizontally we plot q^2 values and vertically the order of magnitude of the corresponding terms in the Hamiltonian. The letter B denotes breaking at the corresponding order of magnitude. Thus BR symmetry breaking occurs everywhere above the row for p^3.

TABLE II — For longitudinal and time-like photons breaking is likewise determined and dominated by the magnetic part of the amplitude but much less drastic.

	F$_1$					F$_2$				
q^2→	0	p^2	p	p^0	Limit 2p^2	0	p^2	p	Limit 7p	p^0
p										B
p^2					B				B	
p^3	[B]	B	B	B		[B]	B	B		

One important remark should be made here concerning the $q^2 = 0$ limit: it is an assumption that at $q^2 = 0$ there is a residual symmetry breaking which is precisely BR's one (see equation (3.2)) and which is therefore always present. This residual breaking is denoted by the boxes enclosing the letter B in Tables I, II. It cannot be given by our model (which gives zero at $q^2 = 0$) and must therefore be taken as a starting point.

Finally, if one shifts the analysis to the final state rest frame by reversing the sign of ω in the boost matrix S_3 and boosting the initial state instead, it is easily seen that the results are quite insensitive to the shift for all the orders of q^2 considered in the tables.

3.4 — *Summary and conclusion*

Bell and Ruegg have defined an approximate symmetry which is broken by third order small terms at $q^2 = 0$ momentum transfer. This can be considered as a sort of residual breaking, always present, and denoted by the squares in Tables I, II. We investigated the effects of introducing $q^2 \neq 0$ carried by photons on the breaking of this approximate symmetry. The photon 4-momentum was compared to the internal momentum p of the constituents of the system (the hydrogen atom was taken as the working model). It appears that breaking is more drastic for transverse photons than for longitudinal and time-like ones. Thus, whereas these produce a limit $q^2 \sim 7\,p$, the limit for the transverse ones is $q^2 \sim p^2 / 16$, about 1.5×10^4 smaller.

These results are of course applicable to hadron-hadron scattering in the small q^2 sector. Here the quark-quark interaction can obviously not be treated in the one gluon exchange approximation and some further work is required so as to apply it in a realistic way to the confining-like sector of the interaction.

REFERENCES

[1] BELL, J. S. and H. RUEGG, *Nucl. Phys.* **B93** (1975), 12.

[2] DRELL, S. D. and F. ZACHARIASEN, «*Electromagnetic Structure of Nucleons*», Oxford University Press, 1961.

[3] LURIÉ, D., «*Particles and Fields*», John Wiley, 1968.

[4] ABERS, E. S., H. BURKHARDT, V. L. TEPLITZ, C. WILKIN, *Nuovo Cimento*, **42** (1966), 305.

[5] PULIDO, J., Ph. D. Thesis, University of Birmingham, 1978.

[6] FLUGGE, S., «*Practical Quantum Mechanics*», Springer-Verlag, 1974.

[7] BJORKEN, J. D. and S. D. DRELL., «*Relativistic Quantum Mechanics*», McGraw Hill, 1964.

HIGH ACCURACY MEASUREMENT OF THE HALL EFFECT IN MAGNETIC MATERIALS WITH AN A.C. LOCK'IN TECHNIQUE

J. B. Sousa, J. M. Moreira

Centro de Física da Universidade do Porto
4000 Porto, Portugal

ABSTRACT — A very sensitive a. c. method is described for the measurement of the Hall effect in metals. It uses a high quality lock'in amplifier with the oscillator incorporated, an operational power supply, and a low noise step-up transformer to rise the signal level. Special precautions have been taken in the design of the experimental chamber and measuring circuit. Voltage resolutions down to 1 nV are currently achieved, enabling the Hall coefficient of most magnetic metals to be measured within 1 part in 10^3.

A summary on the general transport equations and the correct definitions regarding the Hall effect in magnetic systems is presented. High accuracy data are given on the temperature dependence of the Hall resistivity (ρ_H) in a single crystal of Gadolinium, with the magnetic field in the basal plane. For the first time, we believe, experimental data have been obtained on the temperature derivative $d\rho_H/dT$. As shown here, this coefficient reveals clearly the critical behaviour associated with the ferro-paramagnetic transition point in Gadolinium. A preliminary analysis on the critical behaviour is given, with specific suggestions for further developments.

1 — INTRODUCTION

The investigation of the critical behaviour of transport properties in magnetic systems received considerable attention in the past, both in theory and experiment. The behaviour of the electrical resistivity is now satisfactorily understood [1], [2], followed by the case of the thermoeletric power [3]-[5] and, to a lesser extent, the thermal conductivity [3], [6]-[8]. The study of magnetic field effects on these transport coefficients near

a magnetic phase transition is also receiving increasing atten-
tion [9], [10].

The knowledge on higher-order transport phenomena, such
as the thermo-magneto-galvanic effects, is rather scarce indeed [11].
The Hall effect stands however as a promising candidate for
significant progress in the future [12].

For this reason we decided to implement a very sensitive
and accurate method for the a.c. measurement of the Hall
coefficient in metals, using a lock'in technique. The method
described here also provides direct information on the transverse
magnetoresistance coefficient. The voltage resolution is currently
of the order of 10^{-9} V, enabling the Hall coefficient of most
magnetic metals to be measured with a relative resolution better
than $1:10^3$. The data reproducibility in different experimental runs
is of the order of 1 part in 10^3.

In section 2 we summarize the general transport equations
and give the correct definitions regarding the Hall effect and
the magnetoresistance in magnetic systems, in order to set the
precise experimental requirements. In section 3 the experimental
method is described, with a brief reference to the errors and
corresponding minimization procedures. In section 4 we report
some representative data obtained with a characteristic ferromag-
net (Gd single crystal; $T_c = 293$ K). Finally, a brief analysis of
the main features present in the experimental curves for ferromag-
nets is given in section 5.

2 — THEORY

2.1 — Transport coefficients in a magnetic field

Usually, the electrical fields causing transport phenomena
are sufficiently weak to be valid a linear approximation,

$$E_i = \rho_{ik} \, j_k \qquad (1)$$

between the components E_i of the electrical field (E) and the
components j_k of the electrical current density (j). The quanti-
ties ρ_{ik} define the electrical resistivity tensor for the material

138

under consideration. Isothermic conditions are assumed here and repetition of the k-index indicates a sum over all k-values (1, 2, 3).

In the presence of an internal magnetic induction ($\mathbf{B}$) the transport coefficients ρ_{ik} obey the Onsager relations [13]:

$$\rho_{ik}(\mathbf{B}) = \rho_{ki}(-\mathbf{B}) \tag{2}$$

One can separate ρ_{ik} into a symmetrical (s_{ik}) and an antisymmetrical part (a_{ik}):

$$\rho_{ik}(\mathbf{B}) = s_{ik}(\mathbf{B}) + a_{ik}(\mathbf{B}) \tag{3}$$

where

$$s_{ik}(\mathbf{B}) = s_{ki}(\mathbf{B}) = (1/2)[\rho_{ik}(\mathbf{B}) + \rho_{ki}(\mathbf{B})] \tag{4}$$

$$a_{ik}(\mathbf{B}) = -a_{ki}(\mathbf{B}) = (1/2)[\rho_{ik}(\mathbf{B}) - \rho_{ki}\mathbf{B})] \tag{5}$$

The Onsager relations (2) imply the following symmetry for s_{ik} and a_{ik}:

$$s_{ik}(\mathbf{B}) = s_{ik}(-\mathbf{B}) \tag{6}$$

$$a_{ik}(\mathbf{B}) = -a_{ik}(-\mathbf{B}) \tag{7}$$

Substituting the decomposition (3) into (1) one gets:

$$E_i(\mathbf{B}) = s_{ik}(\mathbf{B}) j_k + a_{ik}(\mathbf{B}) j_k \tag{8}$$

Since the diagonal elements of a_{ik} are zero, this relation can be be written in the equivalent form:

$$E_i(\mathbf{B}) = s_{ik}(\mathbf{B}) j_k + (j \wedge \mathbf{A})_i \tag{9}$$

with

$$\mathbf{A} = (a_{23}, -a_{13}, a_{12}) \tag{10}$$

Or, in a more compact notation,

$$E_i = s_{ik} j_k + \varepsilon_{ikl} j_k A_l \tag{11}$$

where $\varepsilon_{ikl} = +1$ for i, k, l = 1, 2, 3 (or any even permutation), $\varepsilon_{ikl} = -1$ for odd permutations and zero otherwise.
Now the effects of the magnetic field are usually small, which justifies an expansion of the resistivity tensor components (s_{ik}, a_{ik}) in powers of B_i. Since a_{ik} is an odd function of the magnetic induction, $\mathbf{A}$ is odd in $\mathbf{B}$. Therefore, the expansion of

the corresponding components involves only odd powers in B [13], [14]. Restricting the expansion to linear terms we have:

$$A_l = \alpha_{lm} B_m \tag{12}$$

The expansion of the even functions $s_{ik}(B)$ will involve only even powers, so that to second order we have:

$$s_{ik}(B) = s_{ik}(0) + \beta_{iklm} B_l B_m \tag{13}$$

The tensor β_{iklm} is symmetrical with respect to (i, k) and (1, m). Substituting (12) and (13) into (11) we obtain, disregarding terms of the order $\mathcal{O}(B^3)$ or above:

$$E_i(B) = E_i(0) + \varepsilon_{ikl} j_k \alpha_{lm} B_m + \beta_{iklm} j_k B_l B_m \tag{14}$$

2.2 — Hall effect

As shown below, the Hall effect is related to the odd part of $E_i(B)$, whereas the magnetoresistance coefficients are related to the even part. Let us write:

$$E_i^{odd} = \varepsilon_{ikl} j_k \alpha_{lm} B_m \tag{15}$$

Performing formally the sum in 1 we can write:

$$E_i^{odd} = (\varepsilon_{ikl} \alpha_{lm}) j_k B_m = R_{ik}(m) j_k B_m \tag{16}$$

where $R_{ik}(m)$ is a generalized transport tensor corresponding to the B_m component of the magnetic induction,

$$R_{ik}(m) = \varepsilon_{ikl} \alpha_{lm} \tag{17}$$

As shown below it contains the usual Hall effect coefficient as one of its components. Since $\varepsilon_{ikl} = 0$ when two of the indices are equal, it follows that (for any i)

$$R_{ii}(m) = 0 \tag{18}$$

Also, since $\varepsilon_{ikl} = -\varepsilon_{kil}$, we have:

$$R_{ik}(m) = -R_{ki}(m) \tag{19}$$

Thus, the general form of the tensor $R_{ik}(m)$ involves only three distinct components

$$[R_{ik}(m)] = \begin{bmatrix} 0 & R_{xy}(m) & R_{xz}(m) \\ -R_{xy}(m) & 0 & R_{yz}(m) \\ -R_{xz}(m) & -R_{yz}(m) & 0 \end{bmatrix} \qquad (20)$$

From eq. (17) it is clear that the crystal symmetry of the sample (contained implicitly in α_{lm}) can lead to simplifications in the components $R_{ik}(m)$. For example, in isotropic media we have $R_{xz}(z) = R_{yz}(z) = 0$, so that:

$$[R_{ik}] = \begin{bmatrix} 0 & R & 0 \\ -R & 0 & 0 \\ 0 & 0 & 0 \end{bmatrix} \qquad (21)$$

with $R = R_{xy}(z)$.

The odd components of the electrical field (E_i^{odd}) can be experimentally obtained from the components of the total field E_i measured for two opposite values of the magnetic field (H):

$$E_i^{odd} = 1/2 [E_i(H) - E_i(-H)] \qquad (22)$$

For the geometry shown in Fig. 1 several distinct experiments may be considered:

(i) We can measure the odd component of the electric field in a direction normal to j and H, obtaining from eq. (16):

$$E_y^{odd} = E_y^{Hall} = R_{yx}(z) j_x B_z \qquad (23)$$
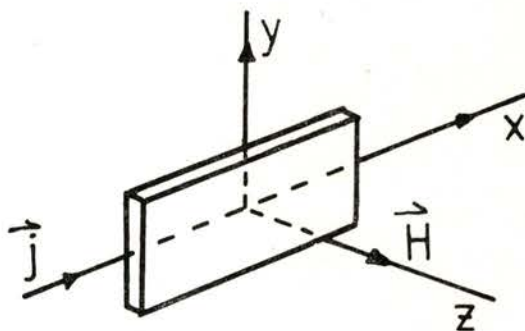
Fig. 1 — Geometry for the measurement of the Hall effect.

This corresponds to the usual Hall effect measurement, the component $R_{xy}(z)$ being precisely the Hall coefficient.

(ii) One can measure E^{odd} along the z-direction (parallel to H); eq. (16) then gives:

$$E_z^{odd} = R_{zx}(z) j_x B_z \qquad (24)$$

which enables the coefficient $R_{zx}(z)$ to be experimentally determined.

(iii) Along the j-direction (x-axis), no odd electric field exists, since we have:

$$E_x^{odd} = R_{xx}(z) j_x B_z = 0 \qquad (25)$$

If we want to know the coefficient $R_{zy}(z)$ we apply j along the y-axis, measuring the odd component of the field along the z-axis:

$$E_z^{odd} = R_{zy}(z) j_y B_z \qquad (26)$$

2.3 — Magnetoresistance

Let us consider the even part of the electric field:

$$E_i^{even} = E_i(0) + \beta_{iklm} j_k B_l B_m = [\rho_{ik}(0) + \beta_{iklm} B_l B_m] j_k \qquad (27)$$

We can define a magnetoresistivity tensor

$$\rho_{ik}^m(B) = \rho_{ik}(0) + \beta_{iklm} B_l B_m \qquad (28)$$

which is an even function of B, so that:

$$E_i^{even} = \rho_{ik}^m(B) j_k \qquad (29)$$

Experimentally one obtains E_i^{even} from the total electric field components $E_i(B)$, measured for two opposite values of the magnetic field applied externally (H_a):

$$E_i^{even} = (1/2) [E_i(H_a) + E_i(-H_a)] \qquad (30)$$

142

Portgal. Phys. — Vol. 13, fasc. 3-4, pp. 137-172, 1982

Reassembling the results obtained in 2.2 and 2.3, we can write a general expression for the full electrical resistivity tensor (defined by eq. 1):

$$\rho_{ik}(\mathbf{B}) = \rho_{ik}(0) + R_{ik}(m) B_m + \beta_{iklm} B_l B_m \qquad (31)$$

The quantities $R_{ik}(m), \beta_{iklm},\dots$ are the so called galvanomagnetic coefficients.

2.4 — Hall effect in ferromagnetic materials

Assuming for simplicity an isotropic or cubic system with the geometry of Fig. 1, one gets for the Hall resistivity coefficient (eqs. 21, 31):

$$\rho_H = E_H/j = R_o B \qquad (32)$$

where $R_o = R_{yx}(z)$, $B = B_z$, $E_H = E_y^{odd}$, $j = j_x$.

In a normal metal $\mathbf{B}$ is simply given by $\mathbf{B} = \mu_o \mathbf{H_a}$, where $\mathbf{H_a}$ is the external magnetic field and μ_o is the magnetic permeability of the medium (taken here equal to the vacuum permeability). However, for a magnetic material there are two additional contributions to $\mathbf{B}$, one from the internal magnetization $\mathbf{M}$ and the other due to the demagnetisation field $\mathbf{H_d}$ created by the discontinuity in $\mathbf{M}$ at the surface of the medium. Then we have:

$$\mathbf{B} = \mu_o \mathbf{H_a} + \mu_o \mathbf{M} + \mu_o \mathbf{H_d} \qquad (33)$$

Assuming that the sample geometry can be approximately described by an equivalent ellipsoid, $\mathbf{H_d}$ is related to the magnetization by the simple formula $\mathbf{H_d} = -D\mathbf{M}$, where D is the demagnetization factor of the equivalent ellipsoid. Then we obtain:

$$\mathbf{B} = \mu_o \mathbf{H_a} + \mu_o \mathbf{M} - \mu_o D \mathbf{M} \qquad (34)$$

This result should be inserted in eq. (32) to analyze the Hall effect. However, experiment shows that such a simple formula (eq. 32) does not work in magnetic materials.

The reason for this was the assumption that the transport coefficients were functions only of the magnetic induction $\mathbf{B}$

inside the medium. This induction **B** is in fact responsible for the existence of a Lorentz force on the charge carriers which changes the corresponding trajectories, and then affects the transport coefficients.

However, in magnetic materials, besides the effects of **B** on the electron trajectories between scattering centers, we must consider the possibility that the scattering events might themselves change the trajectories in a *preferential* way so as to give a net contribution for the Hall voltage. Of course, those scattering processes which give the same probability for electron deflections to the «right» or «left» of the initial **k**-direction of the electron do not contribute to the Hall effect.

A careful analysis of the electron interaction with the ionic spins **S**$_i$ in a crystal lattice indeed shows that several processes exist which produce an asymmetric scattering [15], [16]. For example, the coupling of an ionic spin **S**$_i$ with the orbital momentum **L** of an electron travelling in its vicinity does distinguish between right and left deflections, through the interaction term **S**$_i \cdot$ **L**$/r^3$ (see Fig. 2). This term is independent of the electron
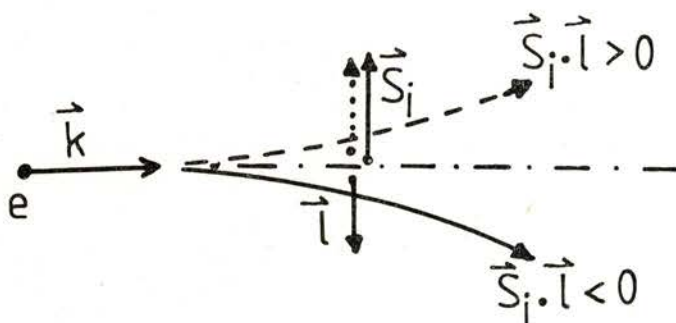
Fig. 2 — Asymmetric scattering resulting from the coupling of an ionic spin **S**$_i$ with the electron orbital momentum **L**

spin, which means that spin up and spin down electrons are deflected in the same way. This is not sufficient to produce an Hall voltage. We need a *preferential* alignement of the spins **S**$_i$ in order to obtain a non-zero effect from scattering by different ions, i.e. there should exist a magnetization **M** inside the sample. Thus, extra contributions to the Hall effect in magnetic materials are

expected below their magnetic ordering temperatures ($T < T_c$) [17]. Generally, these extra contributions first increase as T decreases (M is enhanced) but as $T \rightarrow 0\,K$ full magnetic order takes place in the crystal and coherence effects on the electron wave function indeed suppress the scattering events. The Hall voltage thus vanishes as $T \rightarrow 0\,K$.

Whereas for the Hall effect *both* the asymmetry of the scattering and the preferential magnetic alignment (M) are simultaneously needed for its very existence, for most other transport coefficients important effects arise simply from the magnetic order in the system (M). We can then write:

$$\rho_{ik} = \rho_{ik}(\mathbf{B}, \mathbf{M}) \tag{35}$$

and the Onsager relations can now be generalized:

$$\rho_{ik}(\mathbf{B}, \mathbf{M}) = \rho_{ki}(-\mathbf{B}, -\mathbf{M}) \tag{36}$$

Separating ρ_{ik} into a symmetrical and an antisymmetrical part, and developing the corresponding tensors in increasing powers of the components of **B** and **M**, one obtains for the odd part of the electric field components (in first order):

$$E_i^{odd} = R_{ik}^o(m)\,j_k\,B_m + R_{ik}^s(m)\,j_k\,\mu_0\,M_m \tag{37}$$

where $R_{ik}^o(m)$ and $R_{ik}^s(m)$ are respectively the ordinary and the extraordinary Hall effect tensor components, when the external magnetic field is applied along the m-axis. For the geometry of Fig. 1 and in isotropic (or cubic) magnetic media, we have now the appropriate generalization of eq. (32):

$$\rho_H = R_o\,B + R_s\,\mu_0\,M \tag{38}$$

In the results (35)-(38) we are neglecting correlation effects between ionic spins; for example, ρ_{ik} might also depend on fluctuations of the form $< S_i \cdot S_j > - < S_i > \cdot < S_j >$. These terms are certainly very important in the vicinity of a magnetic phase transition [18]. Unfortunately, the theory of the Hall effect is not yet fully developed to give an appropriate account of these effects.

3 — EXPERIMENTAL METHOD

3.1 — *Principle of the method*

A simple geometry for the Hall effect measurement is that of Fig. 1, with the Hall voltage (V_H, odd part) measured across the sample, in a direction normal both to **j** and **B**. From eq. (23) we readily obtain:

$$V_H = (R_H I B)/d \qquad (39)$$

with $R_H = R_{yx}(z)$, $B = B_z$; I is the total electrical current (x-axis) and d is the thickness of the sample.

In normal metals, the fairly high values of the free-electron concentration leads to small values of the Hall coefficient ($R_H \lesssim 10^{-10} \Omega.m.T^{-1}$). In order to increase V_H the samples then need to be as thin as possible, and usually we have $d \lesssim 1$ mm for bulk samples. Even under these favourable conditions, the use of $B \sim 1$ T and $I \sim 1$ A produces Hall voltages of only 0.1 μV. In order to achieve 1 % resolution in the corresponding measurement, we must then have at least 1 nV voltage sensitivity.

In magnetic materials the Hall coefficient can be considerably higher in the cooperative phase ($R_H \sim 10^{-9} \Omega.m.T^{-1}$) and then a resolution of 1 part in 10^3 becomes possible within 1 nV resolution in the voltage measurements. Of course, the voltage stability must be maintained at this level when reversing the magnetic induction from $+$ **B** to $-$ **B**.

In order to achieve such high degree of voltage resolution and stability one is forced, almost invariably, to rule out d.c. methods. Even if we had solved all the noise problems and maintained the required stability of the measuring equipment, unavoidable parasitic d.c. thermal emf's would appear in the sample or along the leads in the cryostat, including those produced by the inversion of **B** [13]. For these reasons we adopted an a.c. method, and in order to minimize noise problems we used a lock'in technique.

Fig. 3 shows a schematic diagram of the experimental set up. A high stability oscillator, with frequency adjustable from 0.5 Hz to 100 KHz, provides both the reference signal for the lock'in

amplifier (Ortec 9501D) and the input signal for the operational power supply providing the current I for the sample (Kepko BOP50-2M; 0-3A). The sample had the shape of a thin slab with three Pt (or Cu) contacts spotwelded in the opposite edges of the middle portion (two on one side, about a fraction of a mm apart). These electrical contacts enabled the transverse voltage to be measured and also the «zero» adjustment at $B = 0$, through a 10 Ω, 20 turns potentiometer shown in Fig. 3.
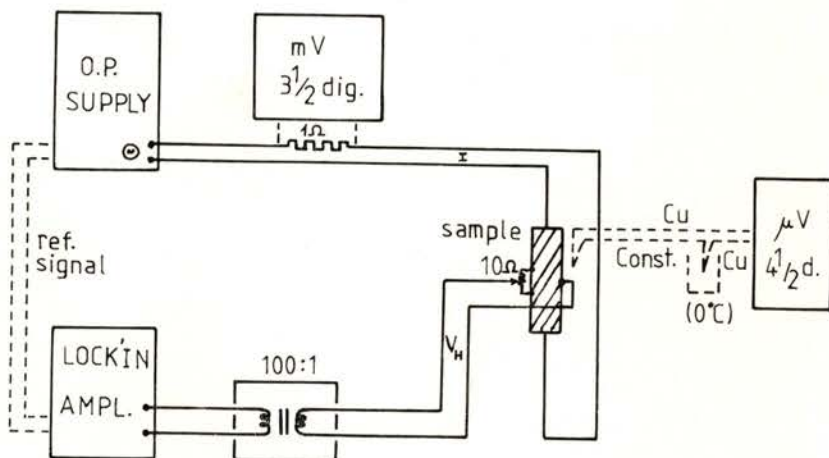
Fig. 3 — Block diagram of the experimental set up for the Hall effect measurement.

The transverse (Hall) voltage was amplified just at the top of the cryostat by a low noise, high quality step up signal transformer (1:100; Ortec 9433). This ensured a proper level of the signal outside the cryostat ($\gtrsim 1$ μV), just when the measuring circuit is more exposed to noise and pick-up signals from external sources. The output of the transformer was fed into the lock'in phase sensitive detector, where it was amplified again. This detector provided a digital display (3 1/2 digits) up to a resolution of 1 nV.

The current I through the sample was measured to within 1 part in 10^3 on a digital voltmeter (Philips PM 2421), using the voltage drop produced in a stable 1 Ω resistor.

3.2 — *Auxiliary equipment and experimental details*

In order to measure the Hall effect over a wide range of temperature (77-340 K) a standard metallic cryostat was used (Fig. 4), with a tail in the lower part to fit the 6 cm pole gap of a conventional electromagnet (Newport; 0-15 KOe). A high stability d.c. current power supply (± 1 in 10^5) provided an adjustable current up to 30 A for the electromagnet. A sweep unit enabled a wide range of energization rates to be used for the electromagnet. A servo-unit enabled the remote control of the eletromagnet (on-off, reverse, and sweep modes).

The magnetic field was measured with a calibrated transverse Hall probe (Phillips RHY17; see Fig. 5a), placed within the pole gap of the electromagnet, with a sensitivity of the order of 10^3 $\mu V/KG$ per mA. Using a Hall-probe current of 5 mA and having voltage resolutions of 10 μV (read in a 3 1/2 digit voltmeter), a field resolution of 2 G was possible.

The temperature was measured with a copper-constantan thermocouple, with one of its juctions in an ice-water bath and the other in good thermal contact with the sample. The sample was mounted on a thick copper block (glued with varnish) and surrounded by a metallic shield to homogenize the temperature in the experimental chamber. The temperature could be raised from 77 K to room temperature at a fairly small rate (as low as a few mK per min) by the combined action of Joule heating in a small heater in the experimental chamber and the adjustment of the vacuum conditions in the dewar. The emf of the thermo-couple was measured directly on a 5 1/2 digit voltmeter (0.1 μV resolution), so that temperature resolutions of the order of a few mK were easily achieved.

The electrical contacts were made with thin wires of Pt or Cu ($\varnothing = 0.05$-0.1 mm) directly spotwelded into the sample using a capacitive discharge unit locally constructed [19]. In an earlier stage we tried pressure contacts, made of elastic copper-berilium wires, but the differences in thermal expansion coefficients of the different materials produced minute relative displacements between sample and contacts as the temperature changed in the
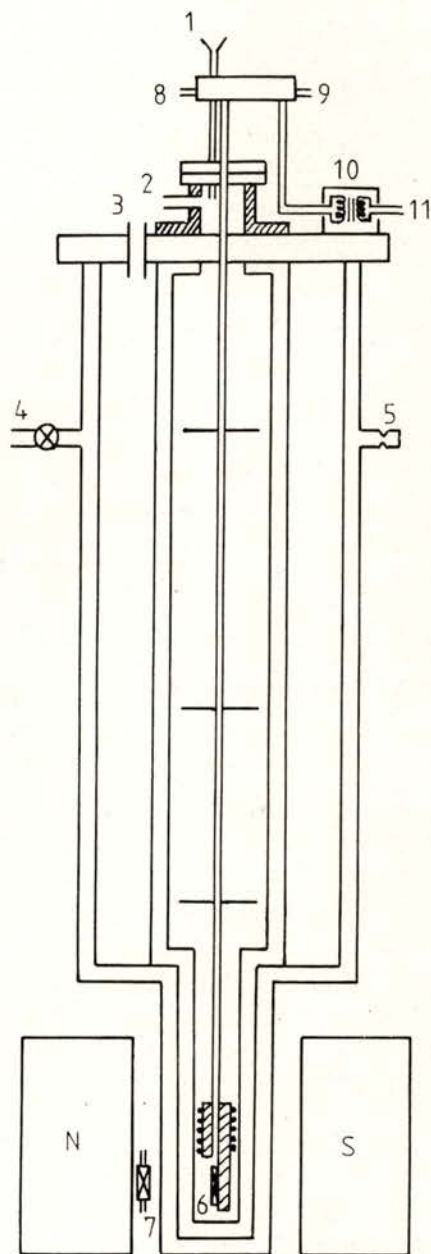
Fig. 4 — Cryostat and auxiliary equipment: 1 — filling tube (N_2 or He); 2 — pumping line (bath); 3 — nitrogen tube; 4 — vacum (to pump); 5 — safety valve; 6 — sample; 7 — Hall probe; 8 — current to the sample; 9 — thermocouple voltage; 10 — step up transformer (1:100); 11 — Hall voltage (x 100).

cryostat. This produced a significant and erratic increase in the scatter of the experimental points, and also in the «zero» drift. Besides the measurement of the Hall coefficient as a function of temperature under a constant applied magnetic field (H_a) we could also measure the field dependence of the Hall voltage at constant temperature. For this we used an automatic data acquisition system locally constructed which could measure simulta-
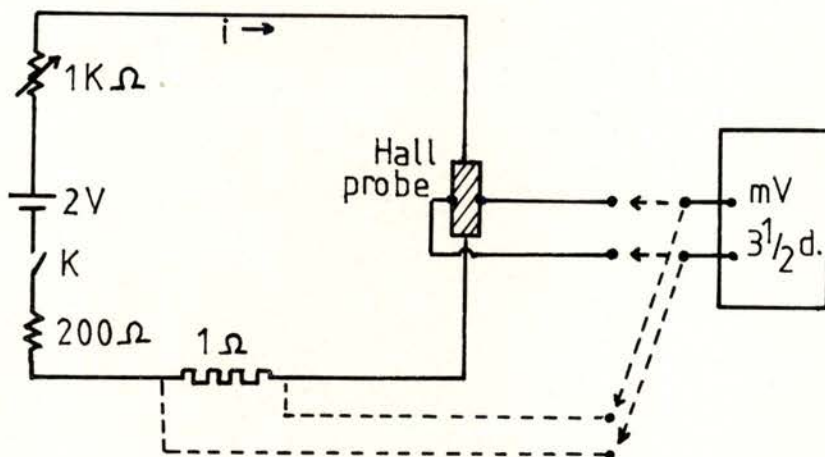
Fig. 5-a — Circuit for the measurement of the applied magnetic field.

neously, and every 3 s (adjustable for longer periods), the Hall voltage V_H and the field H_a, performing automatically the derivative dV_H/dH_a over an adjustable period of time, typically of the order of 1 min. A slow sweep of the field H_a (e.g. over 10 min) enabled a fairly detailed knowledge of the field dependence $V_H = V_H(H_a)$ at constant temperature.

The experimental resolution of the Hall data as a function of temperature was sufficiently good to enable an accurate knowledge of the temperature derivative dV_H/dT at any particular temperature. This was done with the so called «sliding rule» method, using always a set of 3 (or 5) experimental points (V_H, T) to compute the corresponding derivative within such interval. This process was repeated along the whole set of experimental data points in order to obtain the complete curve dV_H/dT as a function of temperature.

3.3 — *Experimental errors*

3.3.1 — Spurious voltages in the measuring circuit

a) In order to minimize the Johnson noise, the electrical resistance of the measuring circuit was kept as low as possible, the major resistive component being the potentiometer for the zero adjustment. As a compromise between its resistance and resolution, we used a 20 turns, 10 Ohm helipot. This gives a thermal noise of about $0.5nV/\sqrt{Hz}$ at room temperature, which is negligible for our purposes.

In order to analyze other errors, it is convenient to use the equivalent circuit of Fig. 5b, introducing the current I and the
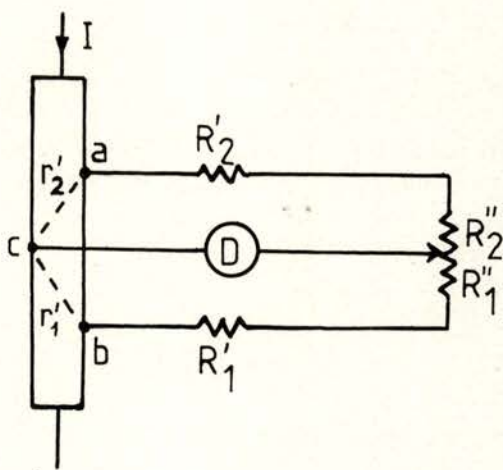
Fig. 5-b — Equivalent circuit of sample + leads + potentiometer resistances, for the analysis of errors; $R_1 = R_1' + R_1''$, $R_2 = R_2' + R_2''$.

resistances of each lead + corresponding branch in the potentiometer (R_1, R_2; see Fig. 5b), and the sample resistance on both sides of the central electrical contact (r_1, r_2). In principle the parameters R_1, R_2, r_1, r_2 and I should be constant, but this never happens exactly in practice and so a spurious voltage (δv) appears

in the measuring circuit. For small changes in the above parameters one can show that:

$$\delta v = v_H \, \frac{\delta I}{I} + V \delta \left(\frac{R_1}{R_1 + R_2} \right) - V \delta \left(\frac{r_1}{r_1 + r_2} \right) \tag{40}$$

where $V = (r_1 + r_2) \, I$. In our case, $I = 0.5$ A, $V \sim 10^3 \, \mu V$, $v_H \sim \mu V$, $R_1 + R_2 \sim 10 \, \Omega$, $r_1 + r_2 \sim m \, \Omega$.

b) The drift voltage associated with the current $[v_H (\delta I/I)]$ is usually negligible. For example, with a (poor) current stability of $1:10^3$ such voltage is only of 1 nV, since v_H is itself fairly small ($\sim \mu V$).

The errors due to the relative changes in the resistances produced by changes of temperature demand far greater care, since they appear multiplied by the longitudinal voltage in the sample, $V \sim 10^3 \times v_H$.

c) Let us consider first the term which involves the changes of the leads and potentiometer resistances with temperature. Since the potentiometer is at room temperature and outside the cryostat, it is not difficult to have proper thermal insulation so as to eliminate virtually the changes in its resistance during the measurements. The above expression then leads to:

$$V \delta \left(\frac{R_1}{R_1 + R_2} \right) \simeq \frac{R_1 R_2}{(R_1 + R_2)^2} \left[\frac{\delta R_1'}{R_1} - \frac{\delta R_2'}{R_2} \right] V \tag{41}$$

where $\delta R_1'$, $\delta R_2'$ are the changes in the leads resistances due to changes in temperature. In practice we can easily set the conditions to have the balance of the potentiometer close to its middle point ($R_1 \simeq R_2$), so that:

$$V \delta \left(\frac{R_1}{R_1 + R_2} \right) \simeq \frac{1}{4 R_1} \, (\delta R_1' - \delta R_2') \, V \tag{42}$$

One way to minimize this error is to use leads closely matched in diameter and length, and following the same path along the cryostat in order to ensure the same thermal effects ($\delta R_1' \simeq \delta R_2'$).

d) With regard to the temperature effects in the sample, the corresponding error can be written as:

$$V \, \delta \left(\frac{r_1}{r_1 + r_2} \right) \simeq V \left[\frac{1}{\rho} \frac{d\rho}{dT} - \alpha \right] \delta T \tag{43}$$

where ρ is the sample resistivity, α the linear expansion coefficient, and δT is the difference of temperature between the voltage contacts (a, b in Fig. 5b). With a careful mounting of the sample (in good thermal contact with a copper basis) one can easily ensure that $\delta T \lesssim 10^{-2}$ K. Since $\alpha \sim 10^{-5}$ K^{-1} and $(1/\rho)(d\rho/dT)$ $\sim 10^{-3}$ K^{-1}, we get a non-negligible voltage of the order of 10 nV. For a given difference of temperature δT in the sample this originates a systematic error in the measurement (see 3.3.2).

3.3.2 — Elimination of systematic errors

a) In order to eliminate spurious voltages which are even functions of the magnetic field we invert H and take half of the difference between the corresponding voltage readings (see eq. 30). This procedure also eliminates the thermal gradient effects which are independent of H, when the operation $(H) \rightarrow (-H)$ is sufficiently quick, so as to keep the thermal gradients practically the same during the switching operation.

b) The use of an alternating technique completely eliminates the effect of all parasitic d.c. voltages in the measuring circuit, and of the effects which are even functions of the electrical current I. This includes all the thermal gradient effects independent of the sense of I, which would produce spurious voltages, e.g. through the Nernst effect: a longitudinal temperature gradient originates a transverse voltage under H [11].

c) There are, however, thermal gradients associated with the *sense* of the electrical current (e.g. Peltier heating or cooling: odd parity in I) and so not eliminated through the current reversal procedure. However, using an a.c. current of sufficient frequency (e.g. above ~ 20 Hz) one can severely reduce the building up of thermal gradients in either sense during the correspondingly small period used. This is particularly useful to reduce the Ettinghausen

effect, which has exactly the same parity as the Hall effect with respect to I and H (a longitudinal current I produces a transverse gradient under H). Other considerations on the Hall effect measurement can be found in the literature [13], [20]-[22].

3.3.3 An experimental check on stability and reproducibility.

After completion of the several stages of implementation of our experimental method, a thorough check was made on the stability and reproducibility of the equipment under realistic working conditions. For such purpose we mounted a Gd single crystal in the cryostat under an applied magnetic field of 7.7×10^5 A.m^{-1} (9.7 KOe), and measured the corresponding Hall voltage from 77 up to 273 K in two different runs, performed in different days. The table below shows that the Hall voltages measured in each run (V_1, V_2) could be reproduced to within a few nV. Since each run takes an average of 24 hrs, we can also claim a comparable degree of stability of the measuring equipment over such a period of time.

T (K)	V_1 (μV)	V_2 (μV)
77.231	1.959	1.957
92.594	2.530	2.534
102.779	2.854	2.855
121.685	3.446	3.443
130.536	3.700	3.703
143.192	4.135	4.130
155.210	4.602	4.597
166.679	5.113	5.108
177.673	5.876	5.867
188.248	6.810	6.812
198.452	7.989	7.984
211.544	9.748	9.740
224.118	11.749	11.741
236.235	13.985	13.972
250.812	16.647	16.621
262.067	18.370	18.347
272.999	19.016	19.012

154

Portgal. Phys. — Vol. 13, fasc. 3-4, pp. 137-172, 1982

4 — EXPERIMENTAL RESULTS

Fig. 6 shows the temperature dependence of the Hall resis-
tivity ρ_H, from 77 K up to 330 K, measured in a single crystal
of gadolinium with dimensions of 12.5 mm $\times$ 2.20 mm $\times$ 0.455 mm.
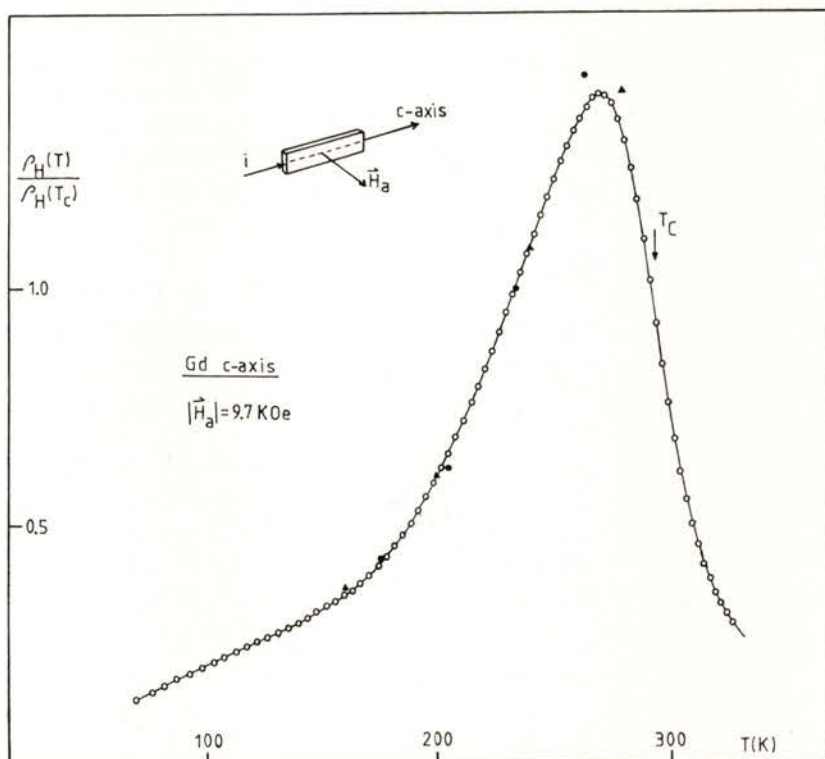
Fig. 6 — Temperature dependence of the Hall electrical resistivity (ρ_H) in a
single crystal of Gd, normalized by a factor $\rho_H(T_c)$, with $T_c = 293$ K.
($\bullet$) data from ref. [18] ($\blacktriangle$) data from ref. [30] (see text).

For convenience, we present our data normalized by a factor
$\rho_H(T_c)$, with $T_c = 293$ K as shown below. The electrical current
flows along the c-axis, which is the major dimension of the
sample. The external magnetic field (H_a) was always perpen-
dicular to the flat face of the crystal, thus having a basal

direction. For the data of Fig. 6 we used $H_a = 7.7 \times 10^5$ A.m^{-1} (9.7 KOe).

The experimental curve exhibits all the qualitative features predicted by theory: (i) at low temperatures the Hall effect decreases noticeably with T, due to the reduction in the electron scattering as the sample orders magnetically; (ii) at higher temperatures (T ≳ 150 K), there is a noticeable increase in the Hall resistivity, associated with the production of magnetic disorder in the system; (iii) with the approach of T_c, and in spite of the increasing magnetic disorder, ρ_H decreases sharply due to the vanishing of the spontaneous magnetization in the sample; (iv) however, the decrease of ρ_H still continues in the paramagnetic phase, due to the persistence of an induced magnetization under the applied field; it naturally decreases with the increase of T, as the magnetic susceptibility falls off in the paramagnetic phase.

A better insight into the reduction of the Hall effect near the Curie point can be obtained from the temperature derivative curve d ρ_H/dT as a function of T. This quantity was calculated by numerical differentiation of ρ_H (T), using groups of five consecutive experimental points, slided along the ρ_H (T) curve. The results are shown in Fig. 7, normalized by the quantity ρ_H (T_c).

There is a deep minimum in the derivative d ρ_H/dT at the critical region, with the lowest point at 293 K approximately. This temperature has been identified with the Curie point of our Gd sample. It is in fact consistent with corresponding data available in the literature [23], [24]. The [$1/\rho_H$ (T_c)] (d ρ_H/dT) curve exhibits an approximately constant value for temperatures below ~ 150 K, which means an approximately linear dependence of ρ_H with T at these temperatures. A change in regime occurs for T ≳ 150 K, as evidenced by the pronounced rise in [$1/\rho_H$ (T_c)] (d ρ_H/dT) towards a broad maximum around 230-240 K. It should be recognized that Gd has a spin-reorientation transition in zero field at temperatures close to these values [25], [26]. The spontaneous magnetization in Gd then turns rapidly from a cone easy axis towards the c-direction. We indeed found that this transition produces a striking anomaly in the even-part of the transverse voltage, an observation which appears not to be referred previously in the literature. These results will be the object of a forthcoming publication.
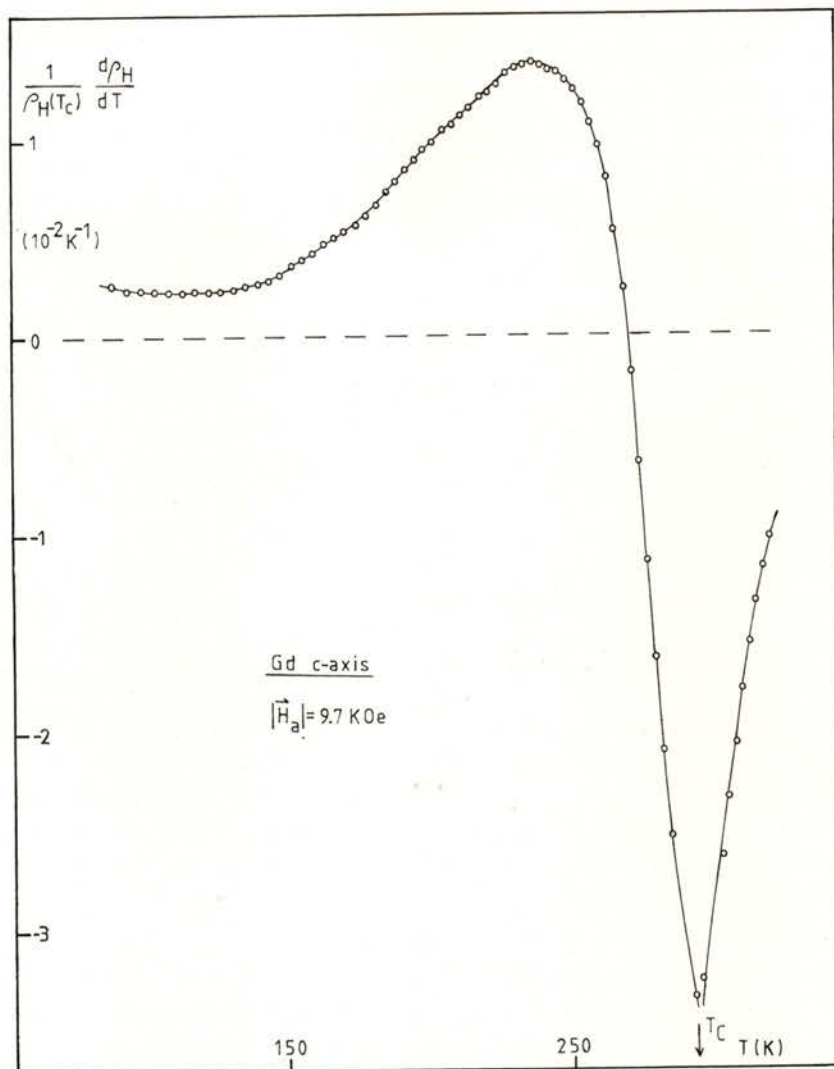
Fig. 7 — Temperature derivative of the normalized Hall electrical resistivity as a function of temperature.

5 — ANALYSIS AND DISCUSSION

5.1 — *Ferromagnetic phase*

a) $T \lesssim 270$ K:

Due to the high demagnetization factor of the sample under the conditions of measurement ($D \simeq 1$), and the use of a moderate

value for H_a ($\lesssim 10$ KOe; in Gd the saturation field at low temperatures exceeds 26 KOe [27]), magnetic field penetration is not expected at these temperatures (see 5.1.b). In good quality samples we then expect that the magnetic domain structure inside the sample adjusts itself at each temperature so as to keep a vanishing internal magnetic field. Since $H_i = H_a - D M$, this produces a temperature independent bulk magnetization in the sample:

$$M = (1/D)\ H_a \simeq H_a \tag{44}$$

This magnetization represents a coarse average over many magnetic domains, and should not be confused with the spontaneous magnetization inside each domain, $M_s(T)$; we have in fact $M \leq M_s$. The average magnetic induction in the sample is then:

$$B = \mu_0 (H_i + M) \simeq \mu_0 M \simeq \mu_0 H_a \tag{45}$$

and we obtain for the Hall resistivity:

$$\rho_H = R_0 B + R_s \mu_0 M \simeq (R_0 + R_s) \mu_0 H_a \tag{46}$$

At constant H_a, the temperature dependence of ρ_H essentially reflects the corresponding dependence of $(R_0 + R_s)$. Since in Gd the coefficient R_0 is approximately two orders of magnitude smaller than R_s [18], [28], [29], our Hall resistivity at T sufficiently below T_c ($H_i \simeq 0$) essentially gives the behaviour of the extraordinary Hall coefficient:

$$\rho_H(T) \simeq \mu_0 H_a R_s(T) \tag{47}$$

In order to check this, a direct comparison was made between the normalized $\rho_H(T)$ data of Fig. 6 and $R_s(T)$ values published in the literature for Gd single crystals, with H_a along a basal direction [18], [30]. As shown by the full circles and the triangular symbols in Fig. 6, fairly good agreement is indeed obtained, with a normalization constant chosen to match all the data at T=237 K.

b) $270 \lesssim T < T_c$:

The condition $H_i \simeq 0$ used above is expected to break down when the spontaneous magnetization decreases sufficiently (as $T \to T_c$) so as to be no longer able to prevent field penetration.

As shown below, this originates the appearance of a maximum in the $\rho_H(T)$ curve of Fig. 6 ($H_a = 9.7$ KOe). Such maximum is not a characteristic feature of the extraordinary Hall coefficient $R_s(T)$ (monotonic increasing function of T), but a consequence of the fact that $\rho_H(T)$ contains the product $R_s(T)\, M(T)$.

Whereas no field penetration occurs at low temperatures ($H_i \simeq 0$; M=constant=H_a/D), the situation changes as we approach a temperature T^* for which the spontaneous magnetization $M_s(T)$ gets smaller than H_a/D. We then expect $M \simeq M_s(T)$ and a single domain situation. Using $D = 1$, $H_a = 9.7$ KOe, and calculating $M_s(T)$ within a mean field approximation (see 5.2) we arrive at $T^* = 270.1$ K, which is indeed remarkably close to the temperature at which ρ_H is maximum ($T = 270 \pm 1$ K).

As the spontaneous magnetization is a decreasing function of T, the condition:

$$D\, M_s(T^*) = H_a \tag{48}$$

predicts the gradual shift of the maximum in ρ_H to the right, as the field H_a decreases. This is clearly shown in Fig. 8, for $H_a = 7.7 \times 10^5$, 3.87×10^5 and 2.0×10^5 A.m^{-1} (9.7, 4.87 and 2.52 KOe, respectively).

c)   Theoretical considerations.

The general features of ρ_H in the ferromagnetic phase of Gd are: (i) a gradual increase of ρ_H from low temperatures upwards ($\sim T^2$ dependence [31]) and (ii) a well defined maximum at high temperatures, just preceding the rapid decrease of ρ_H as T approaches the Curie point. Since $R_0 \ll R_s$ in gadolinium [29], we have $\rho_H(T) \simeq R_s(T)\, M(T)$.

The observed temperature dependence of ρ_H in gadolinium has been successfully described by the theory of Maranzana [32], based on the asymmetric scattering of electrons by thermal spin disorder through the coupling between the orbital angular momentum of the conduction electrons and the localized magnetic moments. Maranzana uses a mean field approximation and assumes a single domain in the sample ($M(T) = M_s(T)$), giving an explicit expression for the extraordinary Hall resistivity:

$$R_s(T)\, M_s(T) = A < (S_z - <S_z>)^3 > \tag{49}$$

A is a constant independent of the temperature, S_z is the z-com-
ponent of an ionic spin, and $< ... >$ represents a thermal average
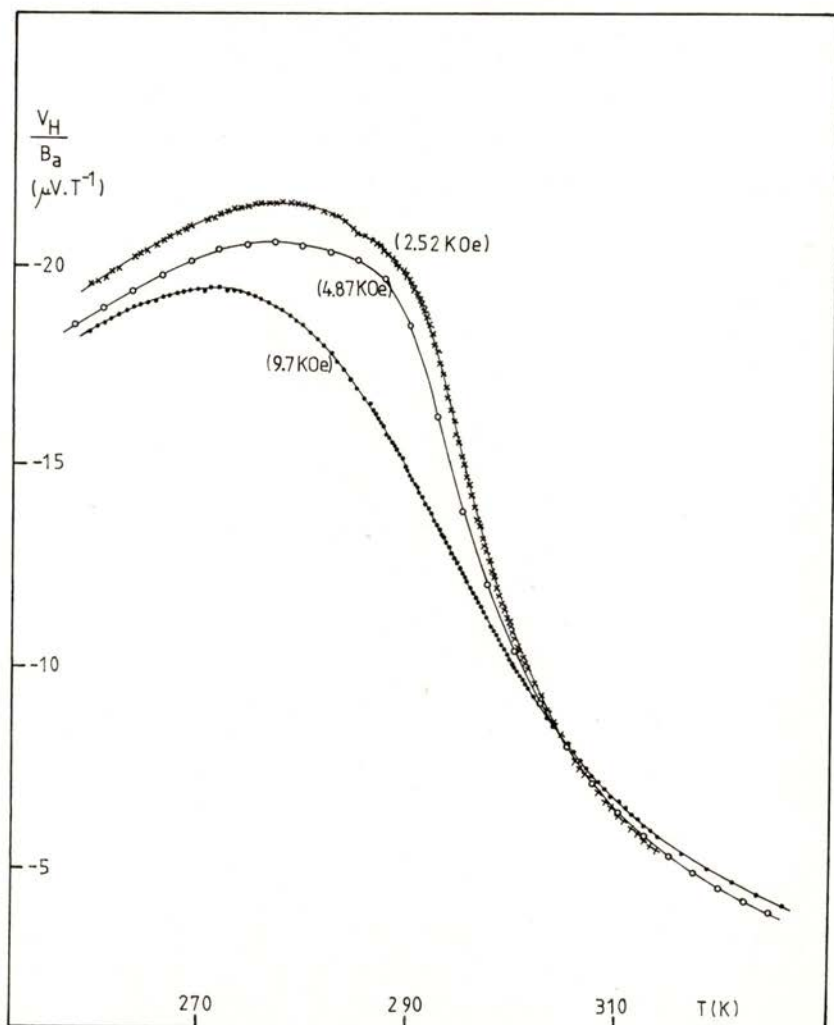
Fig. 8 — Temperature dependence of the Hall voltage (v_H), normalized
by $B_a = \mu_o H_a$, at several values of B_a: 0.97, 0.487 and 0.252 T.

over all possible values of the z-component of a spin at a single
lattice. As a mean field model, Maranzana's theory cannot be valid

160

very near T_c, where fluctuations dominate. If we work out the $< ... >$ factor in expression (49) we can show that:

$$<(S_z - <S_z>)^3> = [<S_z^3> - <S_z>^3] - 3<S_z>[<S_z^2> - <S_z>^2]$$
$$= [-2<S_z> + \coth(\alpha/2)][<S_z^2> - <S_z>^2] + 1/2<S_z>\operatorname{sech}^2(\alpha/2)$$

$$(50)$$

where $\alpha = 3 S/(S+1) < S_z > (T_c/T)$. For temperatures reasonably below T_c and for systems with $S \gg 1/2$ ($S = 7/2$ in Gd), the second and third terms on the right hand side of (50) are considerably smaller than the first, and we can write approximately [33]:

$$\rho_H \sim <(S_z - <S_z>)^3> \simeq -2<S_z>[<(S_z^2> - <S_z>^2] \quad (51)$$

This expression has a very simple physical meaning: the extraordinary Hall effect requires the existence of electron scattering $[<S_z^2> - <S_z>^2]$ *and* the existence of a finite magnetization in the sample, $<S_z>$. One can now understand the general trend of $\rho_H(T)$ in gadolinium, as a result of two factors: a monotonically increasing function of temperature, $[<S_z^2> - <S_z>^2]$ (responsible for the initial rise of ρ_H with T), multiplied by a monotonically decreasing function of T, $<S_z>$ (responsible for the sharp decrease of ρ_H near T_c). A maximum in ρ_H thus occurs due to the competing effect of both factors. It occurs rather close to T_c because at low temperatures $<S_z>$ has a rather weak temperature dependence, which cannot prevent the increase in ρ_H caused by the other factor.

Unfortunately, Maranzana's theory is unable to justify the large magnitude of R_s in Gd, although it appears quite satisfactory to explain the temperature dependence of $R_s(T)$ [28], [34]. An alternative theory, based on the side jump mechanism for the collisions between electrons and the (thermally disordered) localized spins, has been worked out by Fert [35]. This theory can also explain rather well the temperature dependence of ρ_H in Gd and, for quantitative purposes, it requires more reasonable values for some adjustable parameters than in the case of Maranzana's theory. We feel, however, that more experimental and theoretical work is needed to clarify definitely this interesting question related to the scattering mechanism ultimately responsible for the magnitude of ρ_H in Gd [39].

5.2 — *Paramagnetic phase*

a) Our experimental data show a progressive decrease of $\rho_H(T)$ in the paramagnetic phase, essentially reflecting the decrease of the induced magnetization $M(T)$ inside the sample; of course, no spontaneous magnetization $M_s(T)$ exists above T_c. From expression (38) we can write:

$$\rho_H = R_0 B + R_s \mu_0 M = R_0 \mu_0 (H_i + M) + R_s \mu_0 M$$
$$= R_0 \mu_0 H_a + \mu_0 [R_s + (1 - D) R_0] M \qquad (52)$$

Since $D = 1$ in our case, $\rho_H(T)$ in the paramagnetic phase can be approximated by the simpler expression:

$$\rho_H(T) = \mu_0 R_0 H_a + \mu_0 R_s M(T) \qquad (53)$$

Excluding the immediate vicinity of T_c, the theory predicts that R_s becomes constant in the paramagnetic phase [28], [33]. Since $R_0 \ll R_s$, this means that the temperature dependence of the measured Hall resistivity in the paramagnetic phase should essentially reproduce the T-dependence of the induced magnetization $M(T)$. One can calculate this quantity within a mean field approximation, using the standard expression [36]:

$$M(T)/M(0) = B_s[\mu_0 g \; \mu_B SH_i/(KT_c) \cdot (T_c/T) +$$
$$+ 3 S/(S+1) \cdot M(T)/M(0) \; (T_c/T)] \qquad (54)$$

where B_s is the Brillouin function,

$$B_s(x) = (2S+1)/S \cdot \coth x (2S+1)/S - (1/2S) \coth x/2S \qquad (55)$$

H_i is the internal magnetic field, $H_i = H_a - DM$, g is the Landé factor and μ_B is the Bohr magneton. Introducing $M(T)$ calculated in this way into expression (53), we can separate R_0 and R_s from a fit to the experimental data on $\rho_H(T)$.

The simpler approach generally adopted is to go into the asymptotic form of $M(T)$ at temperatures sufficiently above T_c, where a simple Curie-Weiss behaviour is expected:

$$M(T) = C/(T - \Theta) \cdot H_i = \chi(T) \cdot H_i \qquad (56)$$

with C = constant, Θ = paramagnetic Curie temperature. Experiment gives $\Theta = 317$ K and C = 0.05 K for Gd [27]. Introducing $H_i = H_a - DM$ in this expression we obtain:

$$M(T) = x/(1+xD) H_a \simeq x/(1+x) H_a = C/(T - T_c^*) \tag{57}$$

where $T_c^* = \Theta - C$.

However, experiment shows that the Curie-Weiss behaviour in Gd is only valid for $T \gtrsim 400$ K, which is well outside the temperature range covered by our data. We must therefore use the full mean field expression (54) to obtain $M(T)$ values in the paramagnetic range order to analyze our data.

b) For Gd we used S = 7/2, $M(0) = 2.10 \times 10^6$ A.m^{-1} (26.4 KOe) [27], $T_c = 293$ K, and D = 1 under our experimental conditions. The field H_a was allowed to take the three distinct values used in our experiments: $H_a = 2.0 \times 10^5$ A.m^{-1} (2.52 KOe), 3.87×10^5 A.m^{-1} (4.87 KOe) and 7.7×10^5 A.m^{-1} (9.7 KOe). The calculations were performed with a Texas 59 calculator, producing for each H_a the dependence of M with T. Fig. 9 gives the three curves obtained, ploted in a reduced scale, $M(t)/M(0)$ versus $t = T/T_c$.

We can check whether $\rho_H(T)$ satisfies eq. (53), or its equivalent form:

$$\rho_H/(\mu_0 H_a) = R_0 + R_s(M/H_a) \tag{58}$$

Since R_0 and R_s are practically constant sufficiently above T_c ($T \gtrsim 319$ K; see 5.3) we should obtain there a linear plot between ($\rho_H/\mu_0 H_a$) and (M/H_a), the corresponding slope and intercept giving R_s and R_0 respectively. Moreover, we should obtain the same straight line irrespective of the particular H_a value used in each experimental run. As shown in Fig. 10, these features are indeed present in our results for the paramagnetic phase. At lower temperatures, considerable deviations from the linear behaviour do appear, more and more important as $T \to T_c$, and also when H_a is smaller. This is certainly due to the increasing role played by the critical fluctuations, which are not appropriately accounted for with the assumption $R_0, R_s =$ constant (see 5.3). From the linear plot of Fig. 10 we obtain for R_s:

$$R_s = -2.38 \times 10^{-8} \ \Omega.m.T^{-1}$$
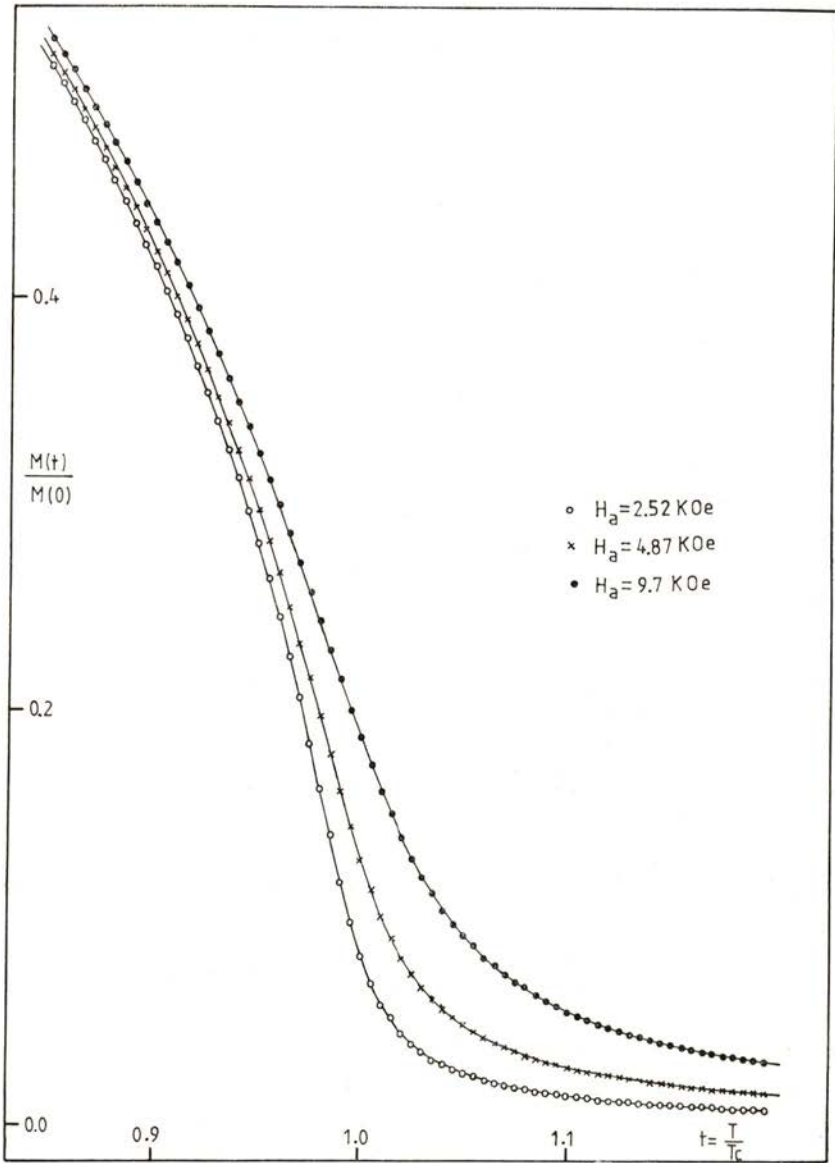
Fig. 9 — Reduced magnetization $M(t)/M(0)$ as a function of reduced tempe-
rature $t = T/T_c$; for $H_a = 9.7$ KOe (•), 4.87 KOe (x) and 2.52 KOe (o), cal-
culated from eq. (54) with $D = 1$.

This value is fairly close to the R_s value obtained by Volkenshtein et al [30] in a Gd single crystal, $R_s = -2.57 \times 10^{-8}$ $\Omega.m.T^{-1}$. Both values differ considerably from the value previously quoted by
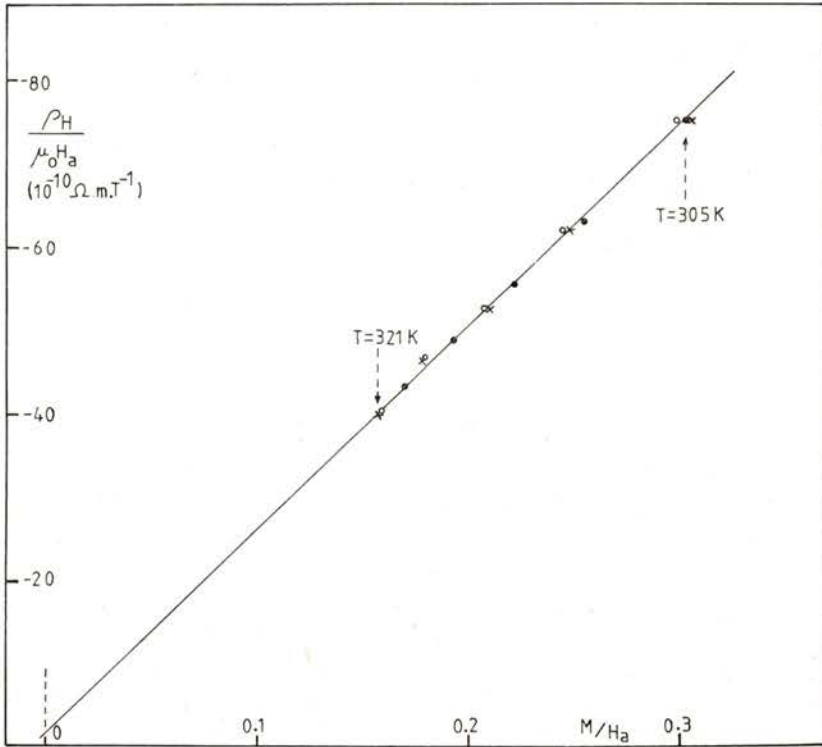
Fig. 10 — In the paramagnetic phase at temperatures sufficiently above T_c, a linear relation occurs between $\rho_H/\mu_o H_a$ and M/H_a (see eq. 58).

Rhyne [37], $R_s = -1.22 \times 10^{-8}$ $\Omega.m.T^{-1}$. We notice however that in a later work this author and Cullen [18] obtained R_s values of the order of -2×10^{-8} $\Omega.m.T^{-1}$ (at $T \lesssim T_c$), which are considerably closer to our results than his previous value. From the intercept of the straight line in Fig. 10 we obtain:

$$R_o = -1.92 \times 10^{-10} \ \Omega.m.T^{-1}$$

Portgal. Phys. — Vol. 13, fasc. 3-4, pp. 137-172, 1982

165

This value is considerably higher than the values obtained by Rhyne and Cullen [18] at temperatures near T_c ($-R_0 \gtrsim 0.65 \times 10^{-10}$ $\Omega.m.T^{-1}$) and the values quoted by Vedernikov et al [29] from a study of the Hall effect at fairly high temperatures (410 K-800 K; $R_0 = -1.2 \times 10^{-10}$ $\Omega.m.T^{-1}$). We must, however, recognize that the limited range of temperatures available in our case above T_c for the extraction of R_0 from extrapolation of a straight line (319 K-335 K) precludes high accuracy in the corresponding numerical determination.

The calculations of $M(T)/M(0)$ have been repeated with $D = 0.9$ instead of $D = 1$. Only minor changes occur in the results, the new R_0 and R_s values differing by less than 5 % from the values quoted above.

5.3 — *Critical region*

We have seen that the temperature dependence of the spontaneous magnetization explains the rapid decrease of ρ_H as T approaches the Curie point. A convenient location of T_c can be obtained from the sharp minimum in the $d\rho_H/dT$ curve. We obtain $T_c = 293 \pm 0.5$ K, in fair agreement with representative data for Gd [23], [24]. Of course, due to the field penetration in the critical region (both above and below T_c), different $1/\rho_H(T_c) \cdot d\rho_H/dT$ curves are obtained with different applied fields H_a, as shown in Fig. 11. However, the minimum in $d\rho_H/dT$ takes place approximately at the same temperature T_c.

Since the magnetic energy of a spin under the applied external fields used in this work is always much smaller than kT_c the shifts in T_c produced by H_a should be fairly small, and so the singularity in $d\rho_H/dT$ indeed occurs at approximately the same temperature.

For the first time, we believe, an attempt is made here to display directly the critical behaviour of the temperature derivative dR_s/dT. For this purpose we took the log-derivative of both members of the relation $\rho_H \simeq R_s(T) M(T)$, so as to obtain:

$$\frac{1}{R_s}\frac{dR_s}{dT} = \frac{1}{\rho_H}\frac{d\rho_H}{dT} - \frac{1}{M}\frac{dM}{dT} \qquad (59)$$

166

Portgal. Phys. — Vol. 13, fasc. 3-4, pp. 137-172, 1982

This relation enables us to extract $(1/R_s)(dR_s/dT)$ directly from the difference between the measured quantity $(1/\rho_H)(d\rho_H/dT)$
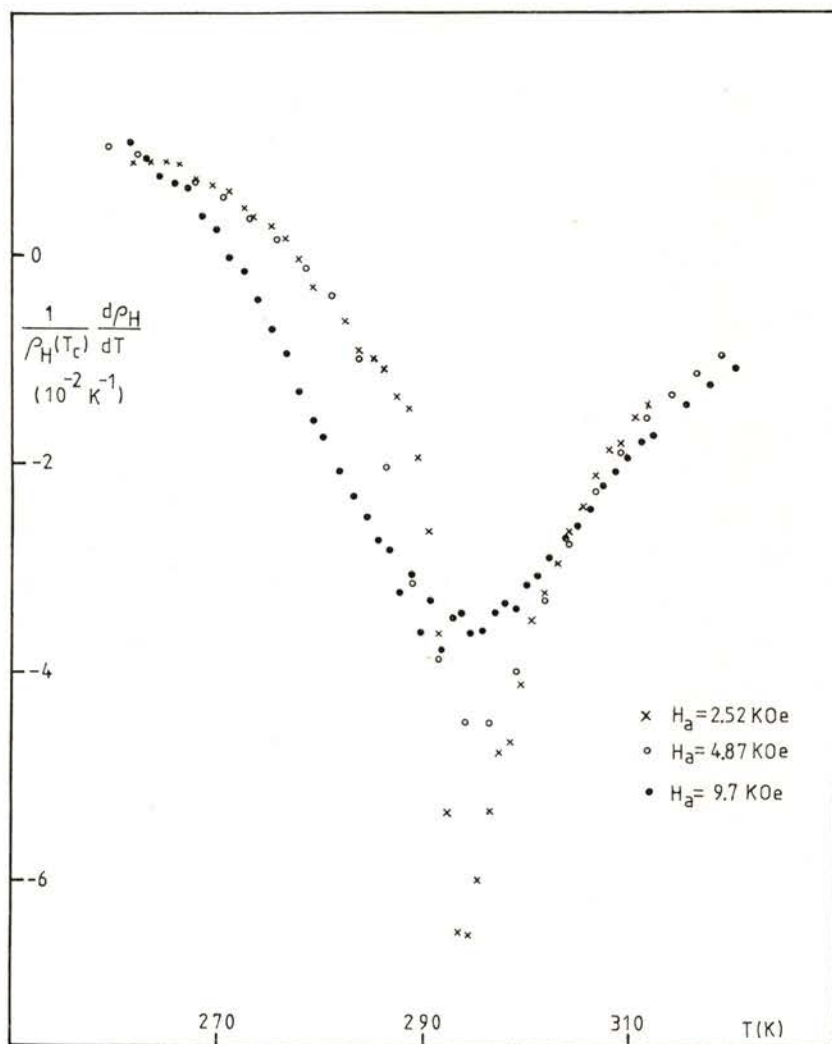
Fig. 11 — Normalized temperature derivative of the Hall resistivity as a function of T, for $H_a = 2.52$ (x), 4.87 (o) and 9.7 KOe (•).

and the calculated magnetization term (from $M(T, H_a)$ given in Fig. 9.). The quantities $(1/\rho_H)(d\rho_H/dT)$ and $(1/M)(dM/dT)$

Portgal. Phys. — Vol. 13, fasc. 3-4, pp. 137-172, 1982

167
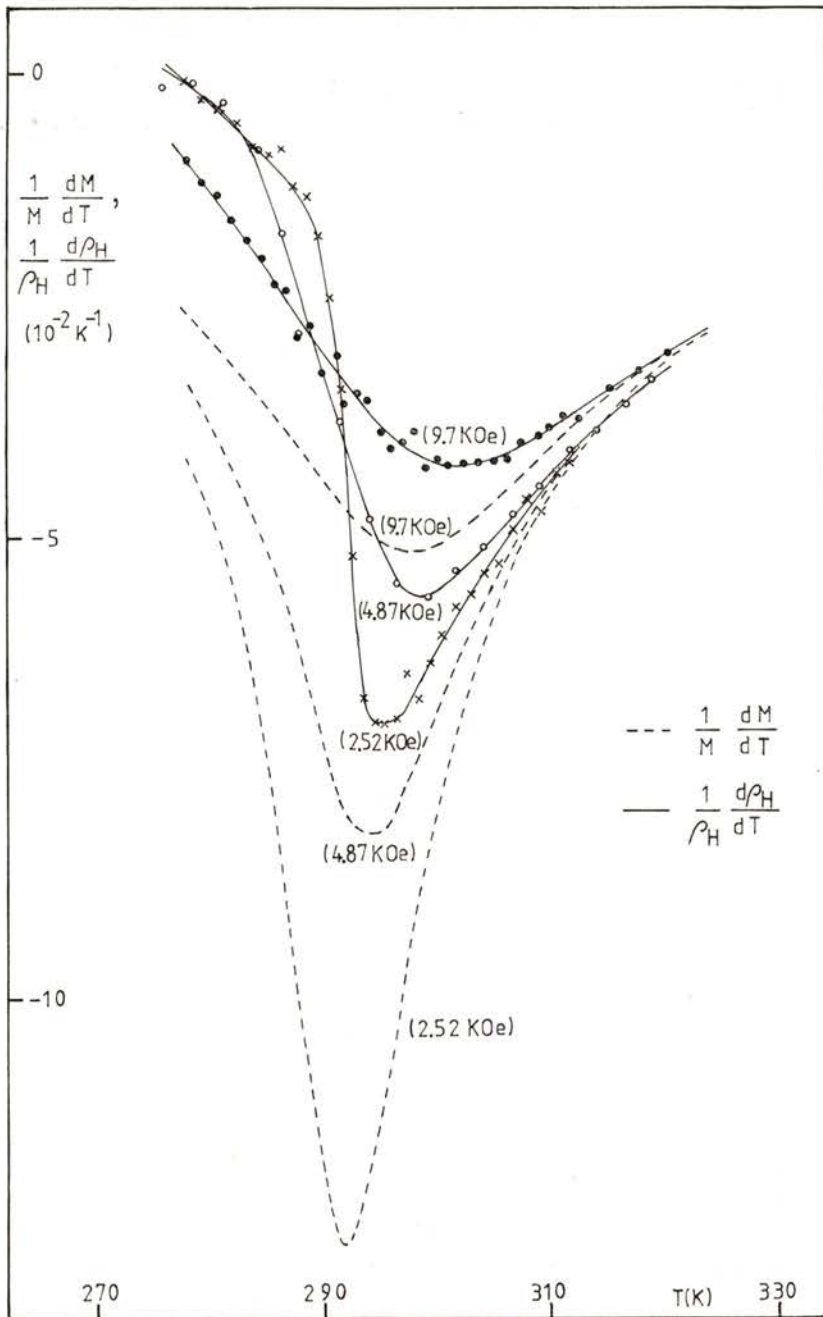
Fig. 12—Temperature dependence of the normalized derivatives (1/M) (dM/dT) and $(1/\rho_H)$ $(d\rho_H/dT)$ near the Curie point of Gadolinium.

for $H_a = 2.52$, 4.87 and 9.7 KOe are displayed in Fig. 12, from which the corresponding coefficients $(1/R_s)$ (dR_s/dT) can be extracted. As showr in Fig. 13, dR_s/dT vanishes at sufficiently
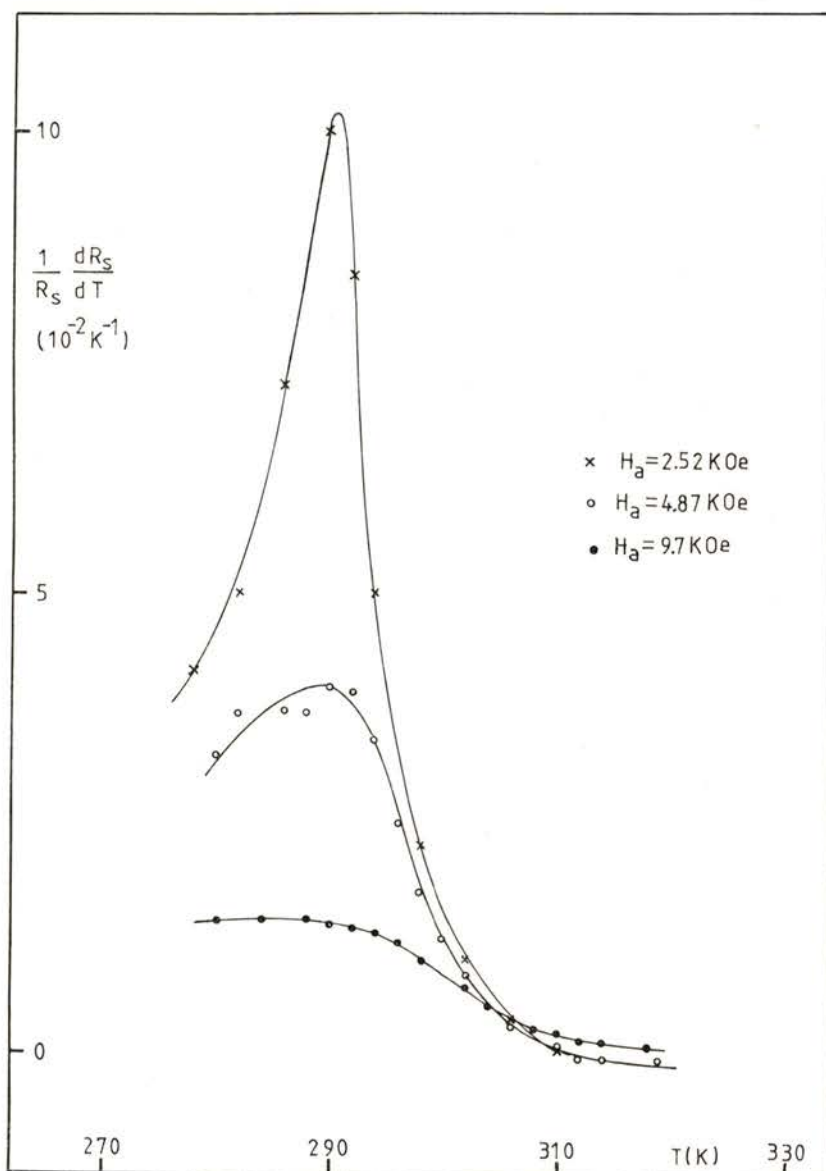
Fig. 13 — Critical behaviour exhibited by the normalized temperature derivative of the extraordinary Hall coefficient R_s, at constant applied field.

high temperatures, where R_s becomes constant. However, as we approach T_c there is a steady increase in R_s, due to the effect of critical fluctuations. This is clearly shown by the curve for the lower field, where dR_s/dT exhibits a sharp peak near T_c, in a manner characteristic of a critical phenomenon [38].

Our results also show an evident slowing down in the «critical features» of dR_s/dT as H_a increases. This is due to the gradual suppression of the spin fluctuations by the applied magnetic field.

Encouraged by these promising preliminary results on the observation of critical features in the temperature derivative of the extraordinary Hall coefficient of Gd, further work is now in progress to investigate ρ_H at lower fields, and to improve, in a first stage, the calculation of the dM/dT derivatives in the paramagnetic phase. At a later stage we aim at the direct measurement of the derivative dM/dT, simultaneously with the ρ_H measurements. Another pertinent question for the future work is the following: which parameter (ρ_H or R_s) is intrinsically more relevant to study the critical behaviour of the Hall effect?

REFERENCES

[1]   S. ALEXANDER, J. S. HELMAN, I. BALBERG, Phys. Rev., **B13**, 304 (1976).

[2]   T. G. RICHARD, D. J. W. GELDART, Phys. Rev., **B15**, 1502 (1977).

[3]   T. KASUYA, Progr. Theor. Phys., 22, 227 (1959).

[4]   S. H. TANG, T. A. KITCHENS, F. J. CADIEU, P. P. CRAIG, Proc. Conf. Low Temp. Phys., **LT13**, Boulder; Plenum, N. Y., p. 385 (1972).

[5]   J. B. SOUSA, R. P. PINTO, M. M. AMADO, J. M. MOREIRA, M. E. BRAGA, M. AUSLOOS, I. BALBERG, Solid State Communic., 31, 209 (1979).

[6]   Y. SUEZAKI, H. MORI, Progr. Theor. Phys., 41, 1177 (1969).

[7]   K. KAWASAKI, Progr. Theor. Phys., 29, 801 (1963).

[8] K. V. Rao, S. Arajs, D. Abukay, in *Thermal Conductivity* 14, ed. P. G. Klemens and T. K. Chu, Plenum Press, p. 57 (1976).

[9] I. Balberg, *Physica,* **91B**, 71 (1977).

[10] I. Balberg, J. S. Helman, *Phys. Rev.,* **B18**, 303 (1978).

[11] I. A. Campbell, *J. Mag. and Mag. Mat.,* **12**, 31 (1979).

[12] See, e. g., *The Hall effect and its Applications,* ed. C. L. Chien and C. R. Westgate, Plenum Press, N. Y. (1980).

[13] J. P. Jan, in *Solid State Physics,* ed. F. Seitz, D. Turnbull; Academic Press, N. Y., vol. 5, p. 17 (1957).

[14] L. Landau, E. Lifshitz, *Electrodynamique des Millieux Continus,* ed. Mir, Moscou, p. 132 (1969).

[15] J. Smit, *Physica,* **24**, 39 (1958); J. Kondo, *Progr. Theor. Phys.,* **25**, 722 (1962); A. Friederich, A. Fert, *Phys. Rev.,* **B9**, 1214 (1974).

[16] L. Berger, *Phys. Rev.,* **B2**, 4559 (1970).

[17] F. E. Maranzana, *Phys. Rev.,* **160**, 421 (1967).

[18] J. J. Rhyne, J. R. Cullen, *Journal de Physique* (Paris) Coll., **C1**, Tome **32**, 246 (1971).

[19] J. B. Sousa, C. L. Serpa Rosa, P. A. Oliveira Lopes, A. J. Rodrigues Pinto, *Anais da Faculdade de Ciências do Porto* (in press).

[20] J. P. Jan, *Helvetica Physica Acta,* **25**, 677 (1952).

[21] A. Beer; in *Solid State Physics,* ed. F. Seitz, D. Turnbull, Academic Press, N. Y., supl. 4, p. 50 (1963).

[22] C. M. Hurd, *Hall Effect in Metals and Alloys,* Plenum Press, N. Y., ch. 6 (1972).

[23] S. Legvold; in *Magnetic Properties of Rare Earth Metals,* ed. R. J. Elliott, Plenum, N. Y., p. 346 (1972).

[24] S. R. Lee, S. Legvold, *Phys. Rev.,* **162**, 431 (1967).

[25] M. B. Salamon, D. S. Simons, *Phys. Rev.,* **B7**, 229 (1973).

[26] J. B. Sousa, M. M. Amado, R. P. Pinto, M. F. Pinheiro, J. M. Moreira, M. E. Braga, M. Ausloos, P. Clippe, D. Hukin, G. Garton, P. Walker; in *Recent Advances in Condensed Matter Physics,* ed. J. T. Devreese, L. F. Lemmens, V. E. Van Doren, J. Van Rayen, Plenum, N. Y., vol. 4, p. 115 (1981).

[27] H. E. Nigh, S. Legvold, F. H. Spedding, *Phys. Rev.,* **132**, 1092 (1963).

[28] B. Coqblin; in *The Electronic Structure of Rare Earth Metals and Alloys,* The Magnetic Heavy Rare Earths, Academic Press, ch. 9 (1978).

[29] M. V. Vedernikov, V. G. Dvunitkin, N. I. Moreva, *Journal de Physique* (Paris), Coll. **C5**, tome **40**, 46 (1979).

[30] N. V. Volkenshtein, I. K. Grigorova, G. V. Fedorov, *Soviet Physics JETP,* **23**, 1003 (1966).

[31] N. A. Babushkina, *Soviet Physics-Solid State,* **7**, 2450 (1966).

[32] F. MARANZANA, *Phys. Rev.*, **160**, 421 (1967); see also J. KONDO, *Progr. Theor. Phys.*, **27**, 772 (1962), B. GIOVANNINI, *Phys. Lett.*, **36A**, 381 (1971).

[33] YU. P. IRKHIN, SH. SH. ABEL'SKII, *Soviet Physics-Solid State*, **6**, 1283 (1964).

[34] L. BERGER, G. BERGMAN; in *The Hall Effect and its Applications*, ed. C. L. Chien and C. R. Westgate, Plenum, N. Y., p. 55 (1980).

[35] A. FERT, *Journal de Physique Lettres* (Paris), **35**, L107 (1974); see also ref. 28.

[36] D. H. MARTIN; in *Magnetism*, Iliffe Books (1967).

[37] J. J. RHYNE, *Coll. Int. CNRS n.° 180*, Grenoble, p. 521 (1969).

[38] H. E. STANLEY, *Introduction to Phase Transitions and Critical Phenomena*, Clarendon Press, Oxford (1971).

[39] Added in proof: R. ASOMOZA, A. FERT, R. REICH (in press) have developed a theory (based on the predominance of the side-jump mechanism) which accounts for the experimental value of R_s in Gd.

FLUCTUATIONS OF COMPOSITION AND PHASE TRANSITION IN FERROELECTRIC Sb Se$_{0.40}$S$_{0.60}$I (*)

M. Helena Amaral and M. Renata Chaves
Laboratório de Física, Universidade do Porto, 4000 Porto, Portugal

A. Levelut and S. Ziolkiewicz
Laboratoire d'Ultrasons (¹) de l'Université Pierre et Marie Curie
75230 Paris Cedex France

ABSTRACT — Pyroelectric coefficient (λ) was investigated in crystals of Sb Se$_x$S$_{1-x}$I and a notorious broadening of the transition when x increases is verified. Spontaneous polarization (P$_s$) for Sb Se$_{0.40}$S$_{0.60}$I is deduced from λ and the broadening of the transition is analised by assuming a non-homogeneous distribution of Se atoms through the sample.

1 — INTRODUCTION

SbSI exhibits a very sharp ferro-paraelectric phase transition of displacive type around 293 K under atmospheric pressure [1]-[4]. On substituting sulfur atoms by selenium, the order of the transition changes from first to second order for a selenium concentration larger than 0.33 ± 0.03, and the Curie temperature decreases almost linearly with Se concentration, with a large slope, $dT_C/dx \simeq - 330$ K [5], [6]. It will then be expected that even small variations of x around a mean value will have a strong effect on the broadening of the phase transition on mixed compounds Sb Se$_x$S$_{1-x}$I.

2 — EXPERIMENTAL RESULTS

We studied the pyroelectric effect on vapour grown samples of Sb Se$_x$S$_{1-x}$I by measuring the potential difference originated

---

across a known short-circuiting resistance as the samples were heated at constant rates (dT/dt) from about 40 K below the respective Curie temperatures (T$_C$) up to some degrees above it. The samples were previously polarized along the c-axis while being cooled down and the electric field was removed when actually measuring the pyroelectric effect. The short-circuiting resistance was kept at a constant temperature thus allowing the determination of the discharging current (I) arising from the changes in the spontaneous polarization (P$_s$) of the samples on heating. An increase in the temperature of a ferroelectric crystal of cross section S will cause a diminution of P$_s$ related to the current flowing in the external circuit by

$$ I = S \left| \frac{dP_s}{dT} \right| \cdot \frac{dT}{dt} $$

The pyroelectric coefficient $\lambda = |dP_s/dT|$ may be evaluated from this relation. The results for various samples of Sb Se$_x$S$_{1-x}$I are displayed in Fig. 1, and show that, as x increases, there is a remarkable broadening of the transition. This behaviour has been often associated with a diffuse phase transition and may be due to
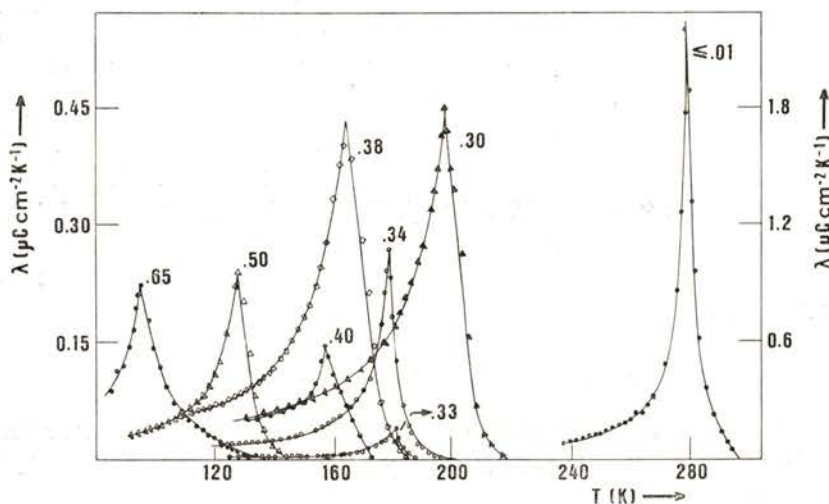
Fig. 1 — Temperature dependence of pyroelectric coefficient $\lambda = |dP_s/dT|$ for Sb Se$_x$S$_{1-x}$I (x $\leqslant$ 0.01, x = 0.30, x = 0.33, x = 0.34, x = 0.38, x = 0.40, x = 0.50, x = 0.65). The right hand side scale applies to the x $\leqslant$ 0.01 curve.

structural disorder, internal stresses, thermal and composition fluctuations. By means of a simple model we have tried to study the effect of composition fluctuations on the broadening of the transition and we applied these results to Sb Se$_{0.40}$S$_{0.60}$I.

Spontaneous polarization may be deduced from the pyroelectric coefficient by

$$P_s(T) = \int_\tau^T \lambda(T) \, dT$$

where $\lambda(\tau) = 0$. The resulting temperature dependence of spontaneous polarization of Sb Se$_{0.40}$S$_{0.60}$I can be seen in Fig. 2.
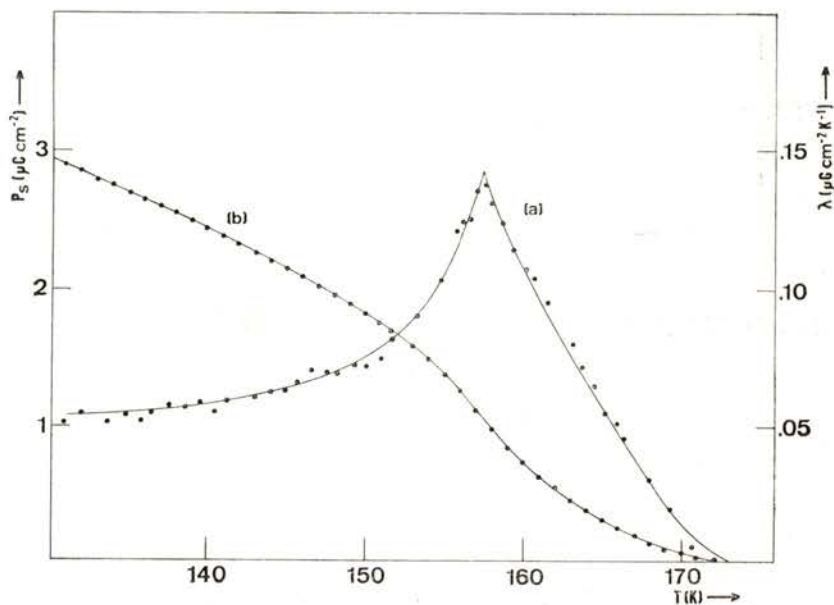
Fig. 2 — (a) Temperature dependence of pyroelectric coefficient $\lambda = |\, dP_s/dT \,|$ for Sb Se$_{0.40}$S$_{0.60}$I; (b) Temperature dependence of spontaneous polarization P$_s$(T) for Sb Se$_{0.40}$S$_{0.60}$I.

According to Landau's theory, for a second order transition, occuring at T$_0$, the squared spontaneous polarization, P$_s^2$(T), may be approximately represented by [7]

$$P_s^2(T) = A(T_0 - T) \qquad \text{for } T \leqslant T_0$$
$$P_s^2(T) = 0 \qquad\qquad \text{for } T > T_0$$

A plot of $P_s^2(T)$ versus T may be seen in Fig. 3 and shows that this representation is fairly good up to a few degrees below T_0.
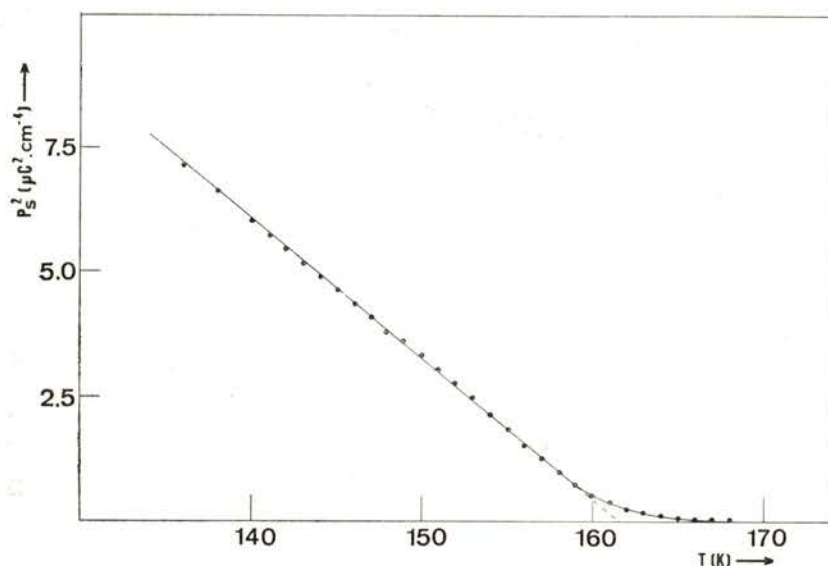
Fig. 3 — Temperature dependence of squared $P_s(T)$ for Sb Se$_{0.40}$S$_{0.60}$I.

3 — THEORETICAL MODEL

In the following we analyse the experimental data concerning Sb Se$_{0.40}$S$_{0.60}$I using a model in which we consider the crystal formed by non-interacting regions, each with a transition temperature T_0. This is, of course, a simplifying hypothesis since the real situation is certainly more complicated and these individual regions will not be, in practice, as independent as we are assuming but will interact with each other via depolarising fields, elastic strains or thermal fluctuations.

The usual procedure [8], [9] has been to define a density of probability, which we will call $g(T_0)$, and to consider the measured values of macroscopic properties of the crystal as some kind of average over the different regions of the crystal. A thermodynamical approach of the free energy with an apparent local field in the polarization direction has already been tried to fit

176

Portgal. Phys. — Vol. 13, fasc. 3-4, pp. 173-183, 1982

experimental data in Co-doped barium titanate, but without much success [9]. The fitting was better when using a truncated gaussian distribution of the Co-concentration. Taking these results into account we did not try the free energy approach.

Let T_m and T_M be the limiting transition temperatures; the probability density for finding a region of transition temperature in the vicinity of T_0 will be defined to satisfy the conditions

$$g(T_0) \neq 0 \quad \text{only for} \quad T_M > T_0 > T_m$$

and, of course,

$$\int_{T_m}^{T_M} g(T_0)\ dT_0 = 1.$$

If $P_s(T)$ represents the spontaneous polarization, at temperature T, of the region of the crystal whose transition temperature is T_0, the experimental value, measured over the whole crystal, will be an average value of $P_s(T)$, evaluated over the regions of the crystal still polarized at that temperature.

We have used two different approaches. In one of them we evaluated the average value of the square of the polarization (*a*) and in the other the average of the polarization itself (*b*).

a) Evaluation of $< P_s^2(T) >$

According to the way we defined $g(T_0)$, T_m and T_M the evaluation of $< P_s^2(T) >$ will give

$$< P_s^2(T) > = A \int_{T_m}^{T_M} (T_0 - T)\ g(T_0)\ dT_0 \quad \text{for } T < T_m$$

$$< P_s^2(T) > = A \int_{T}^{T_M} (T_0 - T)\ g(T_0)\ dT_0 \quad \text{for } T_m < T < T_M$$

$$< P_s^2(T) > = 0 \quad \text{for } T > T_M$$

If we choose for $g(T_0)$ any function symmetric around T_C and duely normalized we will have, for $T < T_m$

$$< P_s^2(T) > = A \int_{T_m}^{T_M} T_0\ g(T_0)\ dT_0 - A T \int_{T_m}^{T_M} g(T_0)\ dT_0$$

$$= A < T_0 > - A T = A (T_C - T)$$

For simplicity we have chosen $g(T_0)$ as a parabolic function, symmetric around T_C, defined between $T_m = T_C - \Theta$ and $T_M = T_C + \Theta$ by

$$g(T_0) = -\frac{3}{4\Theta^3}[(T_0 - T_C)^2 - \Theta^2]$$

We obtain

$$< P_s^2(T) > = A (T_C - T) \qquad\qquad T < T_m$$

$$< P_s^2(T) > = \frac{A}{16\Theta^3}[(T_C + \Theta) - T]^3 [T - (T_C - 3\Theta)]$$

$$< P_s^2(T) > = 0 \qquad\qquad T > T_M$$

The pyroelectric coefficient (λ), here taken as

$$\lambda = \frac{d}{dT}[< P_s^2(T) >]^{1/2}$$

has a maximum at a temperature

$$T_{max} = T_C - (2 - \sqrt{3})\Theta$$

To apply this model to our experimental results we assumed that $< P_s^2(T) > \simeq < P_s(T) >^2 \simeq P_{exp}^2(T)$. From the plot of P_{exp}^2 versus T (Fig. 3) we deduced the values $A = 0.287\ \mu C^2\ cm^{-4}\ K^{-1}$, $T_C = 161.4$ K and $\Theta = 7.9$ K. The fit may be seen in Fig. 4, curve (a): it shows a good agreement from 130 K up to 145 K. It also seems to indicate that a larger value of Θ should be used, as does the difference we find between the experimental value $T_{max} = 157.5$ K and the predicted value $T_C - (2 - \sqrt{3})\Theta = 159.3$ K. However, a theoretical curve using a larger value of Θ may also be seen in the same figure, curve (b), and it does not show a better agreement. This may be due either to the simplicity of the function we assumed for $g(T_0)$ or to the use of $< P_s^2(T) >$ instead of $< P_s(T) >^2$. In Fig. 5 we can see a
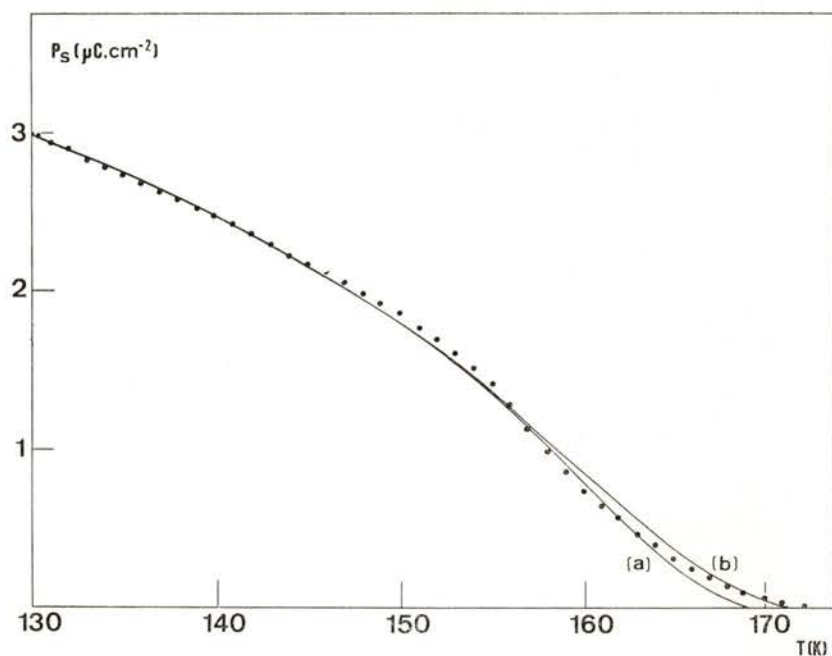
Fig. 4 — Temperature dependence of $P_s(T)$: Full circles, experimental results for Sb $Se_{0.40}S_{0.60}I$; Full lines, calculated values of $[< P_s^2(T) >]^{1/2}$ by taking a parabolic function as a density of probability.
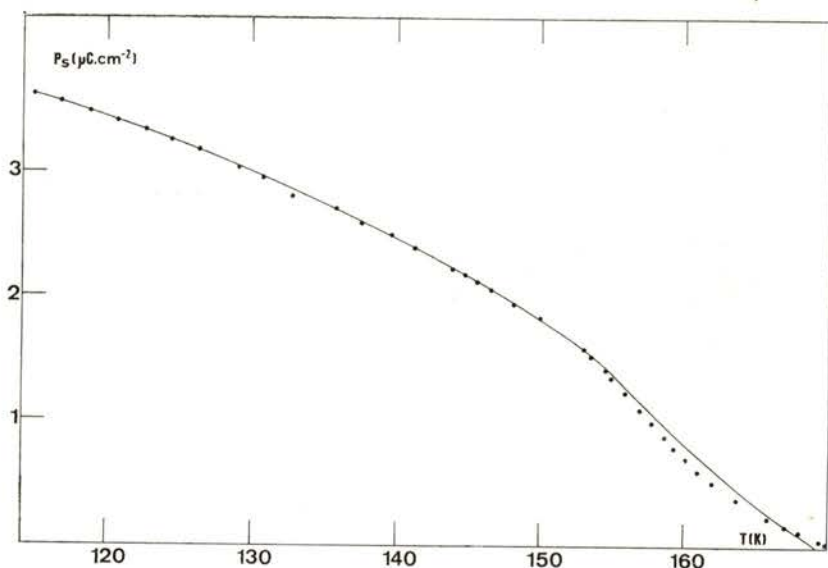
Fig. 5 — Temperature dependence of $P_s(T)$: Full circles, experimental results for Sb $Se_{0.40}S_{0.60}I$; Full line, calculated values of $[< P_s^2(T) >]^{1/2}$ by taking a truncated gaussian function as a density of probability.

another theoretical fit by taking a truncated gaussian function as a density of probability. As the situation has not improved significantly we tried another approach.

b)   Evaluation of $< P_s (T) >$

$P_s (T)$ may be written

$$P_s (T) = A^{1/2} \sqrt{T_0 - T} \qquad\qquad \text{for } T < T_0$$

$$P_s (T) = 0 \qquad\qquad \text{for } T > T_0$$

We will now define $g (T_0)$ by

$$g (T_0) = \frac{1}{\Phi_0} \exp \left[- \frac{(T_0 - T_C)^2}{\Theta^2} \right] \qquad T_m < T < T_M$$

$$g (T_0) = 0 \qquad\qquad\qquad\qquad \text{elsewhere}$$

where

$$\Phi_0 = \int_{T_m}^{T_M} \exp \left[- \frac{(T_0 - T_C)^2}{\Theta^2} \right] dT_0 .$$

The average value of P_s will then be

$$< P_s (T) > = \frac{A^{1/2}}{\Phi_0} \int_{\zeta}^{T_M} \sqrt{T_0 - T} \exp \left[- \frac{(T_0 - T_C)^2}{\Theta^2} \right] dT_0 ,$$

where $\zeta = T_m$ for $T < T_m$ and $\zeta = T$ for $T_m < T < T_M$;   and

$< P_s (T) > = 0$ for $T > T_M$.

All integrals shown were evaluated numerically. The fit to experimental results was done by trial and error: the best fit was found for $T_C = 163.0$ K and $\Theta = 8.5$ K and may be seen in Fig. 6 (b). Although some discrepancies persist the agreement has improved significantly. In Fig. 7 we can see a plot of $< P_s (T) >^2$ versus T calculated from the expression just given
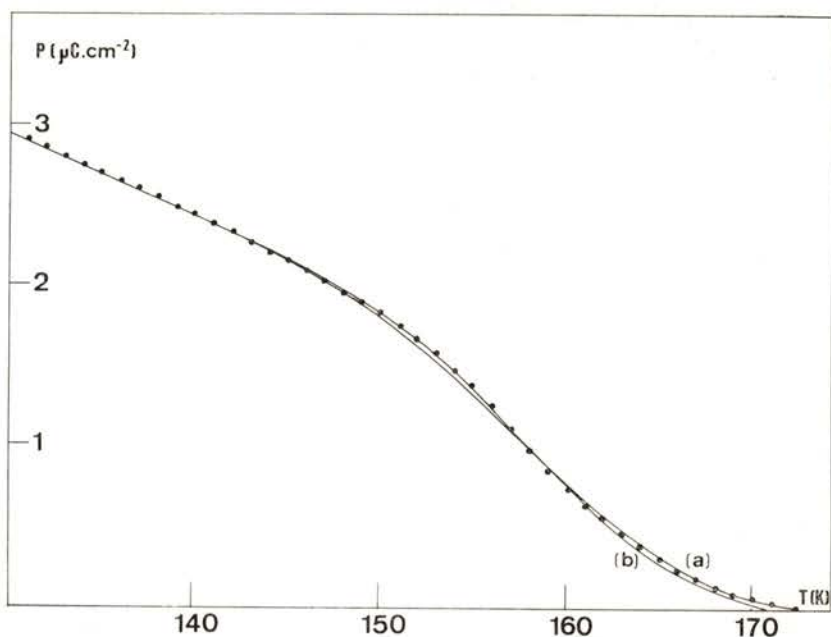
Fig. 6 — Temperature dependence of $P_s(T)$: Full circles, experimental points for $Sb\,Se_{0.40}S_{0.60}I$; Full lines, theoretical fit obtained by using a truncated gaussian function as a density of probability, (a) $\Theta = 10$ K; (b) $\Theta = 8.5$ K.

with an arbitrarily fixed value for A and for different values of Θ. As we can see, not too near the transition temperature $<P_s(T)>^2$ is still fairly well represented by a straight line, $<P(T)>^2 = \text{const.}\,(T_0 - T)$, which intercepts the T-axis the farther from T_C, the larger the value of Θ.

4 — CONCLUSIONS

In a diffuse phase transition the spreading of the transition temperature in a finite range of temperature has been ascribed to thermal and composition fluctuations, internal stresses, dispersion of the c-axis orientation and so on. As we observe a broadening of the transition in mixed compounds $SbSe_xS_{1-x}I$

increasing with x we think that fluctuations of Se composition may be an important reason for the diffuse character of the transition in those compounds. The model used explains two features
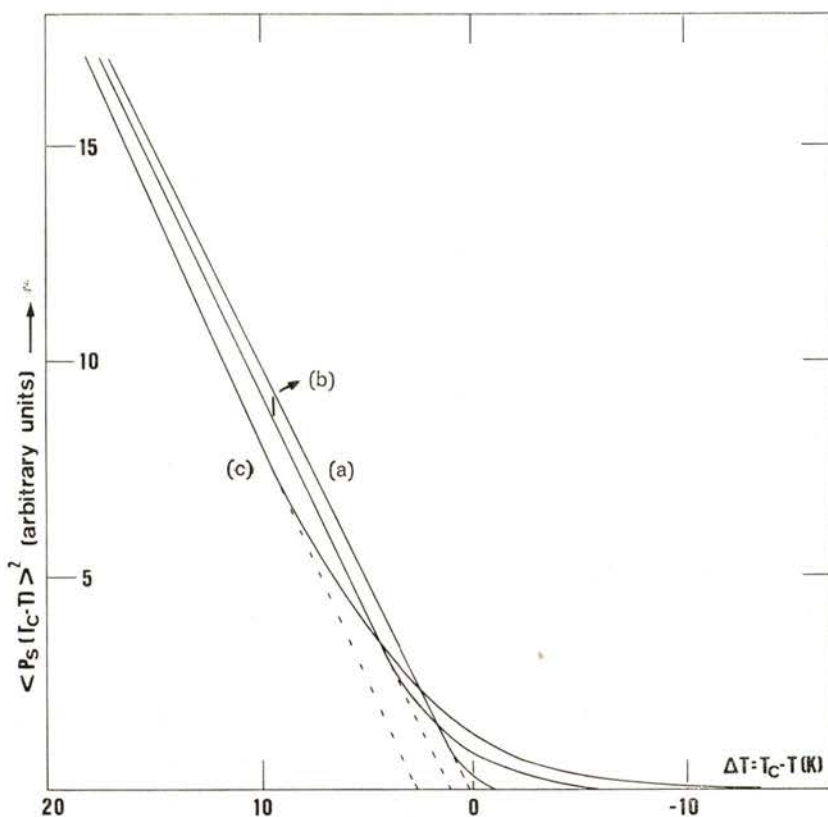
Fig. 7 — Temperature dependence of $< P_s(T_C-T) >^2$ obtained by using a truncated gaussian function as a density of probability, $A = 10$ (arbitrary units), (a) $\theta = 1$ K; (b) $\theta = 10$ K; (c) $\theta = 15$ K.

of the diffuse phase transition, namely that the pyroelectric effect does not go to zero just at T_0 but some degrees above it, and that far from the transition the averaged spontaneous polarization of the crystal will still behave approximately as if the transition temperature was unique.

The value of 8.5 K found for Θ, corresponds to a fluctuation of Se concentration of some 2.5 % around a mean value $\overline{x} \simeq 0.40$. This seems a reasonable value for composition fluctuations since, as we have already pointed out, the variation of the transition temperature T_C with the concentration x of Se is quite high (33 K for $\Delta x = 0.1$), so we expect that even small fluctuations of x will produce noticeable effects on the polarization of the crystal. Work is in progress to obtain a better fit to experimental data using other trial functions.

REFERENCES

[1] KIKUCHI, A, OKA, Y. and SAWAGUCHI, E., *J. Phys. Soc. Japan* **23**, 337 (1967) and references therein.

[2] FURMAN, E., BRAFMAN, O., and MAKOVSKY, J., *Phys. Rev.* **B8**, 2341 (1973).

[3] TENG, M. K., BALKANSKI, M., MASSOT, M. and ZIOLKIEWICZ, M. K., *Phys. Status Solidi* (b) **62**, 173 (1974).

[4] CHAVES, R., AMARAL, H. and ZIOLKIEWICZ, S., *J. Physique*, **41**, 259 (1980).

[5] NITSCHE, R., ROETSCHI H., WILD, P., *Appl. Physics Letters* **4**, 2101 (1964).

[6] CHAVES, M. R., AMARAL, M. H., (to be published).

[7] LINES, M. E., GLASS, A. M., *Principles and Applications of Ferroelectrics and Related Materials*, Clarendon Press, Oxford 1977.

[8] YURKEVICH, V. E., ROLOV, B. N., *Czech J. Phys.* **B25**, 701 (1975).

[9] GODEFROY, G., CHATRY, P., BENGUIGUI, L., *Ferroelectrics* **34**, 169 (1981).

MAGNETORESISTANCE NEAR THE CURIE POINT OF TbZn SINGLE CRYSTALS

Paulo P. Freitas, J. Bessa Sousa

Centro de Física da Universidade do Porto,
4000 Porto, Portugal

P. Morin

Laboratoire Louis Néel, CNRS, Grenoble, France

ABSTRACT — Magnetoresistance studies of the intermetallic ferromagnetic TbZn compound have been performed for the first time, with accurate measurements of $\Delta\rho$ (T, H) and ($d\rho/dT$) coefficients. The analysis of our results supports the theoretical predictions based on renormalization group calculations.

1 — INTRODUCTION

Previous studies of the critical behaviour of transport coefficients in TbZn ferromagnetic single crystals [1], [2] are now extended to include the effect of the magnetic field on the electrical resistivity (ρ) near the Curie point of TbZn. Since the critical features are better displayed by the temperature derivative $d\rho/dT$, this quantity was measured directly as a function of temperature under constant values of the applied magnetic field (H_a).

TbZn has a cubic CsCl type structure in the paramagnetic phase but at the Curie point it suffers a tetragonal distortion caused by magnetoelastic effects in the ferromagnetic phase. The magnetization (M) is then directed along a quarternary axis; at low T, it changes to a binary axis.

The internal magnetic field (H) can act in several ways. By imposing a preferential direction to the ionic spins S_i, the

Portgal. Phys. — Vol. 13, fasc. 3-4, pp. 185-192, 1982

185

field reduces the magnitude of the fluctuations near T_c and enhances the magnetization beyond its spontaneous zero field value. Also, multidomain structures below T_c are gradually destroyed, the domains parallel (or closer in direction) to H_a growing at the expense of the domains magnetized in other directions. Several characteristic energies play a role here, their relative strengths just determining the extent of the magnetic field perturbations.

The initial readjustment of the domains is the easiest process, since no anisotropy energy differences exist between the symmetry-equivalent easy directions in the sample. In good crystals, and near T_c, we can assume a single domain situation inside the sample. If H_a is not along an easy direction, further orientational effects follow this initial stage, depending on the differences in the anisotropy energies between easy and hard magnetic directions. All these domains effects are not expected to be easily observable in simple electronic transport property measurements, due to the smallness of the electron wavelength ($\lambda \sim$ Å) when compared with the large size of the magnetic domains ($\sim 10^4$ Å) and of the domain Bloch walls ($\sim 10^2$-10^3 Å).

On the other hand, changes in the magnetization and in the spin fluctuations, which directly affect the order 'seen' by the electrons as they travel within a mean free path, are expected to produce observable effects in the electronic transport coefficients.

In a mean field description of the electrical resistivity without fluctuations one assumes ρ to be a function of the magnetization components only (M_i). Since $\rho(M_i)$ must be an even function of M and M $\rightarrow 0$ as $T \rightarrow T_c$, one should have, to second order terms, in isotropic materials,

$$\rho/\rho_\infty = 1 + a \cdot M^2 \qquad (1)$$

with $\rho_\infty = \rho$ ($T \gg T_c$). For localized spin systems it can be shown [3] that $a = -[S/(S+1)]M_0^{-2}$. Describing the changes in M produced by the field and temperature through the usual mean field expression

$$\sigma = B_S (3S/(S+1) \cdot \sigma/t + h/t) \qquad (2)$$

where $\sigma = M(T\ H)/M(0,0)$, $t = T/T_c$, $h = \mu_0 mH/(kT_c)$, m is the magnetic moment associated to each ion, and B_S is the Brillouin

function, one can derive the mean field behaviour of ρ as a function of T and H. From such expression it results that the h-effects become negligible when $h \ll \sigma$ (or $H \ll M$).

The effect of the magnetic field on the fluctuations is far more complex; a thorough account of this problem can be found elsewhere [4]. Here we simply observe that the field effect in suppressing fluctuations will be maximum at T_c, where the difference in the free energies of the paramagnetic and ferromagnetic phases just vanishes. Also, the effect will be limited to a small range of temperatures (δT) close to T_c, imposed by the balance between the thermal energy $k\delta T$ and the magnetic energy per ion $\mu_0 m(H + M)$, so that $k\delta T \lesssim \mu_0 m(H + M)$. On the other hand the boundary between ferro and paramagnetism is not expected to be significantly altered (shift in the value of T_c), since we generally have $\mu_0 mH \ll kT_c$. Further comments on the role of fluctuations will be made in section 3.

2 — EXPERIMENTAL RESULTS

The single crystal used here ($1.2 \times 1.2 \times 12.9$ mm^3) had its long axis along a quaternary direction, the external magnetic field (H_a) and the electrical current being applied along it. The demagnetization factor (D) was below 0.1, so near T_c ($M \to 0$) the internal field H becomes approximately equal to H_a, i.e. $H = H_a - DM \simeq H_a$. Far below T_c, the situation is quite different if H_a is not sufficiently high, since $M(T)$ rises towards an high saturation value, $M(0) = 22.5$ KOe in TbZn.

Fig. 1 shows the temperature dependence of $d\rho/dT$ for $H_a = 0$, 100, 700, 1200 and 2500 Oe.

Under zero field, $d\rho/dT$ exibits a sharp positive peak at the Curie temperature of TbZn, $T_c = 200 \pm 0.5$ K, and a monotonic decrease in the paramagnetic phase towards a constant background due to phonon scattering. This variation of $d\rho/dT$ above T_c is, of course, due to short range correlation effects in the paramagnetic phase. For $H_a = 100$ Oe the $d\rho/dT$ curve in the ferromagnetic phase is practically the same as for $H_a = 0$, due to insufficient magnetic field to achieve penetration. However, in the paramagnetic phase the field effects are observed, producing an increase in $d\rho/dT$ values above the zero field curve.

For $H_a = 700$ Oe and above field penetration does occur in the ferromagnetic phase, originating a progressive rounding off in the experimental curves near T_c, and a systematic lowering
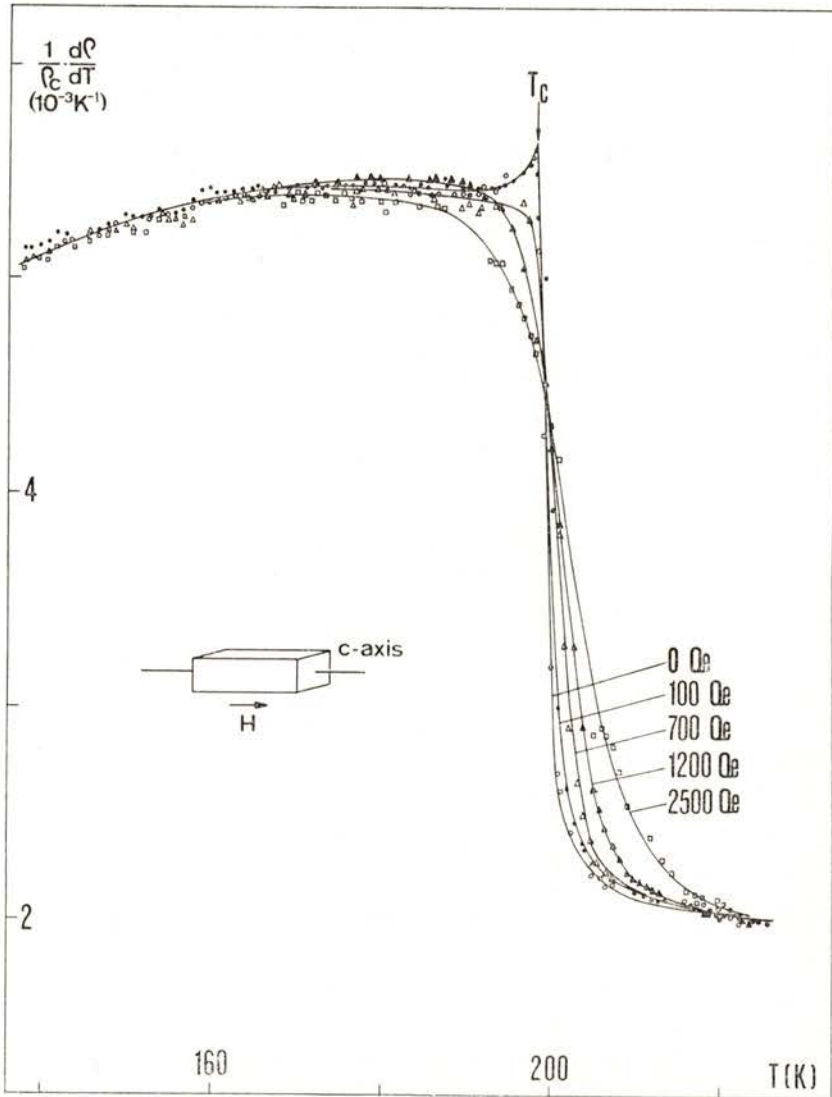
Fig. 1 — Critical behaviour of the normalized temperature derivative $(1/\rho_c)$ $(d\rho/dT)$ in Gd, near the Curie point, at different values of the applied magnetic field: $H_a = 0, 100, 700, 1200, 2500$ Oe.

of $d\rho/dT$ at temperatures close (and below) T_c. For the moderate fields used here, the field effects in the ferromagnetic phase are restricted to a small temperature range ($\lesssim 30K$) below T_c. This is due to the fact that the magnetic energy of an ionic moment under H_a becomes rapidly negligible when compared with the energy of the same moment under the increasing internal magnetization ($M(0) = 22.5$ KOe, whereas $H_a < 2.5$ KOe).

We have seen in section 1 that the effect of the magnetic field is expected to be maximum at T_c, where the critical fluctuations dominate the behaviour of the electrical resistivity. This is neatly evidenced by our results on $\Delta\rho(T, H)$, as shown in Fig. 2, for the normalized magnetoresistance $\Delta\rho/\rho = [\rho(T, H) - \rho(T, 0)]/\rho(T_c \ 0)$ as a function of temperature. The magnetoresistance is always negative and indeed exibits a sharp maximum at T_c; also, it increases with the applied field, due to the progressive increase in magnetic order in the system. We should note that $\Delta\rho/\rho$ curves are less accurate than the $d\rho/dT$ ones, since the latter are obtained directly, whereas $\Delta\rho/\rho$ is obtained by a subsequent subtraction of the corresponding resistivities at several temperatures obtained in different experimental runs. For this reason, the following analysis will be based on the $d\rho/dT$ results.

3 — ANALYSIS OF EXPERIMENTAL RESULTS

Our $d\rho/dT$ results show that H has opposite effects on both sides near T_c: whereas $d\rho/dT$ is below the zero field curve for $T < T_c$, the reverse occurs above T_c. This can be qualitatively understood if one recalls that $d\rho/dT$ depends strongly on the magnetization derivative $|dM/dT|$, a quantity which is smaller than its zero field value for $T < T_c$, and higher as soon as $T > T_c$.

Let us separate the magnetoresistivity term ($\Delta\rho$) out of the total electrical resistivity:

$$\rho(T, H) = \rho(T, 0) + \Delta\rho(T, H) \qquad (3)$$

In terms of the temperature derivatives we then get from (3):

$$(d\rho/dT)_H = (d\rho/dT)_0 + (d\Delta\rho/dT)_H \qquad (4)$$

The behaviour of the zero-field derivative $(d\rho/dT)_0$ in TbZn near T_c has been previously studied in detail [1], leading above T_c to a

$\ln(T\text{-}T_c)$ dependence in the immediate vicinity of T_c, and to a classical $(T\text{-}T_c)^{-1/2}$ dependence sufficiently away from the critical point. For this reason only the magnetoresistivity term
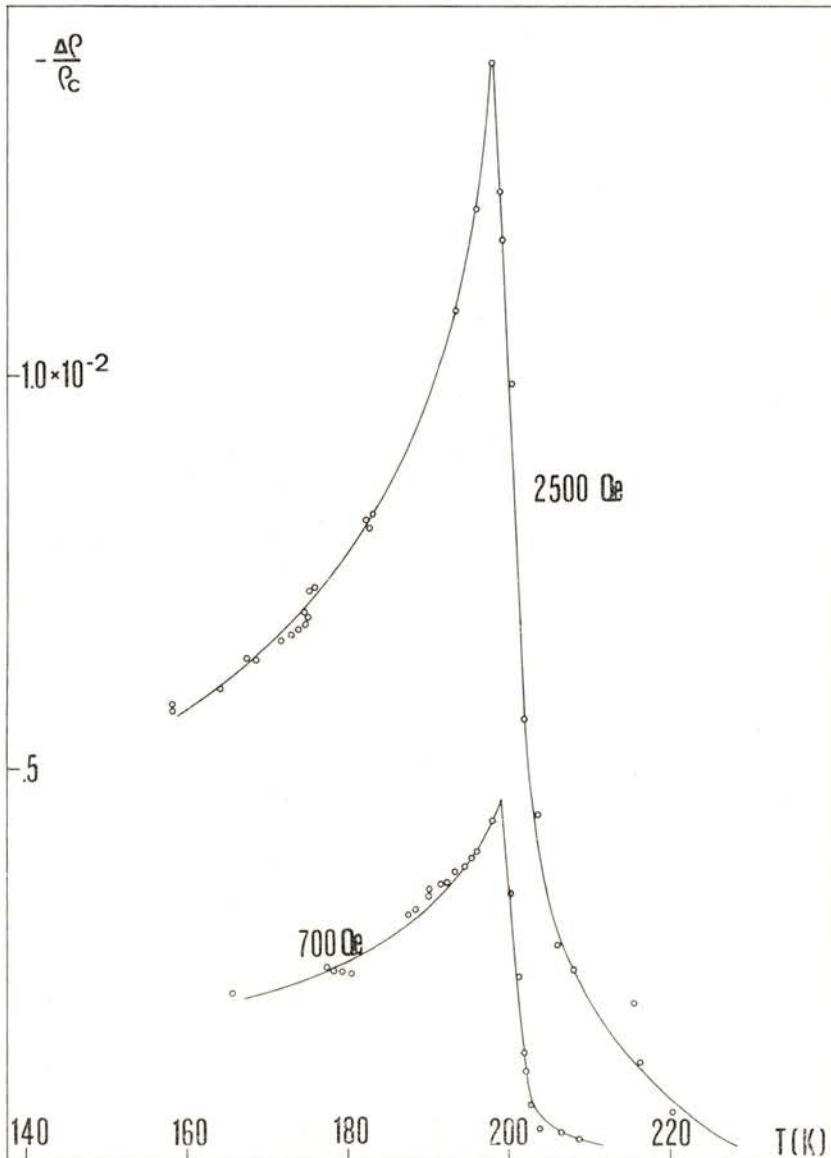
Fig. 2 — Critical behaviour of the normalized magnetoresistivity of Gd near the Curie point, at $H_a = 700$, 2500 Oe; $\Delta\rho(T, H_a) = \rho(T, H_a) - \rho(T, 0)$.

will be considered. Renormalization group results lead to the following theoretical predictions (with $\varepsilon = (T-T_c)/T_c$) [4]:

$$
\begin{array}{llll}
T > T_c & \text{(i)} & \varepsilon \gg h & : \quad d(\Delta\rho)/dT \propto h^2/\varepsilon^{\gamma+2} \\
& \text{(ii)} & \varepsilon \ll h & : \quad d(\Delta\rho)/dT = 0 \\
T < T_c & \text{(iii)} & |\varepsilon| \gg h & : \quad d(\Delta\rho)/dT \propto h/|\varepsilon|^{\alpha+\beta\delta} \\
& \text{(iv)} & |\varepsilon| \ll h & : \quad d(\Delta\rho)/dT = 0
\end{array}
\tag{5}
$$

where α, β, γ and δ are the critical exponents for the specific heat, spontaneous magnetization, correlation length and critical isotherm respectively. For example, in mean field approximation ($\alpha = 0$, $\beta = 1/2$, $\gamma = 1$, $\delta = 3$) one gets for ($d\Delta\rho/dT$):

(i) h^2/ε^3 , (ii) 0 , (iii) $h/|\varepsilon|^{3/2}$, (iv) 0.

In our case ($h = \mu_0 mH/kT_c \lesssim 0.001$) the temperature range $|\varepsilon| \ll h$ is not accessible with sufficient experimental data, and so only cases (i) and (iii) can be considered in detail.

The interesting check refers to the magnetic field dependence of $d(\Delta\rho)/dT$ (h^2 and h, cases i and iii respectively), because it should be independent of the particular values of α, β, γ and δ.

As shown in Fig. 3, an h^2-dependence is indeed observed in our $d\rho/dT$ data above T_c (case i), whereas an h-dependence is found
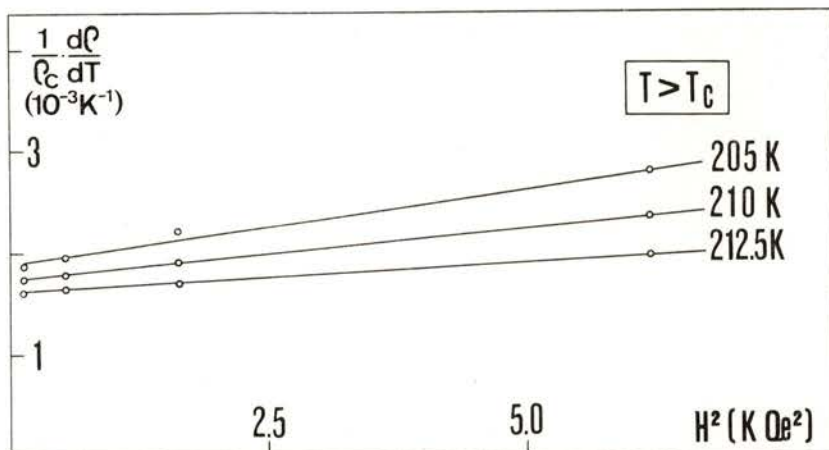
Fig. 3 — Above T_c, the normalized temperature derivative $(1/\rho_c)(d\rho/dT)$ follows a quadratic dependence on the magnetic field.

below T_c (Fig. 4; case iii). We also found that the magnitude of the slopes in the corresponding plots always increases as T approaches T_c, as predicted by theory.
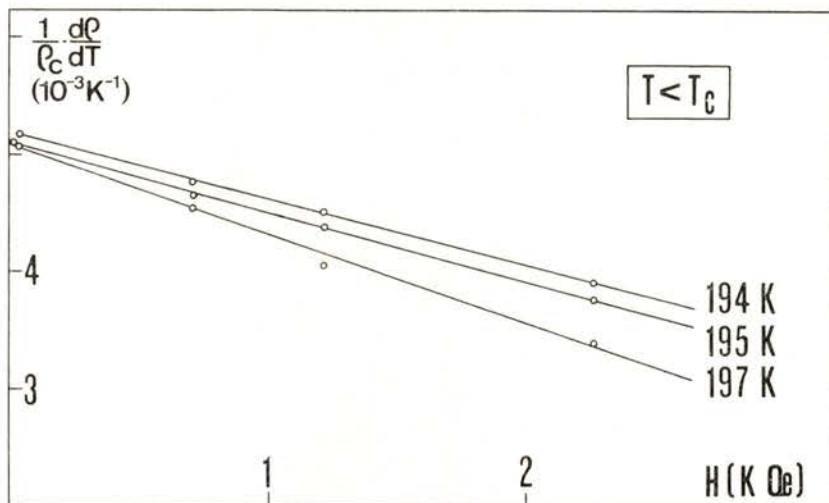
Fig. 4 — Below T_c, the normalized temperature derivative $(1/\rho_c)$ $(d\rho/dT)$ obeys a linear dependence on the magnetic field.

As a final comment, let us add that, within a molecular field approximation, the results $d(\Delta\rho)/dT \propto h^2/\varepsilon^3$, $h/\varepsilon^{3/2}$, and $d(\Delta\rho)/dT = 0$ simply follow from expressions (1) and (2) in the limits corresponding to cases (i), (iii) and (ii+iv) respectively.

REFERENCES

[1]   J. B. Sousa, M. M. Amado, R. P. Pinto, J. M. Moreira, M. E. Braga, M. Ausloos, J. P. Leburton, J. C. Van Hay, P. Clippe, J. P. Vigneron, P. Morin, *J. Phys.* **F10**, 933 (1980).
[2]   J. B. Sousa, R. P. Pinto, M. M. Amado, J. M. Moreira, M. E. Braga, P. Morin, M. Ausloos, *J. Phys.* **F10**, 1809 (1980).
[3]   P. G. De Gennes, J. Friedel, *J. Phys. Chem. Solids* **4**, 71 (1958).
[4]   I. Balberg, *Physica* **91B**, 71 (1977).

SOLID AND GASEOUS CARBON ALLOTROPES
IN ULTRAHIGH VACUUM AT 3 K

Carlo Reale

Metal Lux and Instituto di Fisica del Politecnico
Milan, Italy

ABSTRACT — In ultrahigh vacuum at 3 K (the ordinary condition of the interstellar matter) carbon can be quench-crystallized in A1-type and A3-type phases and may also become a gas with diatomic $C \equiv C$ molecules, similar to the $N \equiv N$, $O = O$ and $H - H$ molecules of the three other elements that give rise to life.

1 — INTRODUCTION AND GENERAL CONSIDERATIONS

In the temperature and pressure conditions of the earth, carbon, which is the element with the highest melting point, can crystallize in the form of diamond or graphite [1, 2] or be amorphous.

Diamond has a fcc A4-type structure, in which each atom is tetrahedrally bound to four others by single covalent bonds of equal lengths, and all the valence electrons are used in bonding. The result is the formation of a three-dimensional network of strong bonds that confer extreme hardness to the diamond, which is the hardest substance existing in nature. However, the diamond lattice is relatively empty, since the proportion of the available space filled by atoms thought of as hard spheres is only $\pi\sqrt{3}/16$, or about 46 % of the filling factor $\pi\sqrt{2}/6$ for the closest-packed fcc atom disposition, which is the A1-type arrangement.

Graphite has a characteristic hexagonal structure, in which planar layers of atoms composed of benzene-type rings with

single σ-bonds and held together by non-localized π-orbital electrons are formed. This structure is strongly anisotropic, because the inter-layer spacing is more than twice as large as the inter-atomic distance within a layer, and is still emptier than that of diamond, as its filling factor and axis ratio are 0.220 and 2.717, much lower and higher, respectively, than the filling factor $\pi\sqrt{2}/6$ and the axis ratio $\sqrt{8/3}$ for the closest-packed hexagonal atom disposition, which is the A3-type arrangement.

Amorphous carbon has a long-range random glassy structure (with a filling factor of 0.174 - 0.203, even lower than that of graphite) including short-range hexagonal aromatic cell networks, similar to pieces of graphite layers.

The large emptiness of diamond, graphite and amorphous carbon, together with the consideration that carbon belongs to group 4, which comprises three A3-type transition elements (titanium, zirconium and hafnium) and an A1-type non-transition element (lead), led us to try to force carbon to crystallize in closer-packing hexagonal or cubic phases by vapour-quenching in ultrahigh vacuum, at about 3 K, on materials able to promote pseudomorphism. The aim was attained by quench-condensation of carbon vapour, in the form of metastable A3-type or A1-type pseudomorphs, on glass substrates quench-coated with A3-type beryllium films or with double layers consisting of a B1-type LiF base film and a metastable A1-type boron overlay [3]: we have chosen beryllium and boron as they immediately precede carbon in the periodic table of the elements and pseudomorphism needs atom size similarity.

But the most interesting result was not the growth of unusual A3-type and A1-type carbon modifications, which is not a novelty, since we had already vapour-frozen A1-type phases of the three non-transition elements of group 4 immediately following carbon in the periodic table (silicon [4], germanium [4] and tin [5]), but the unexpected composition of the carbon vapour beam reflected from the impinged surfaces, which consists nearly completely of diatomic molecules. This means that in ultrahigh vacuum at about 3 K (which is the normal condition of the intersidereal matter) carbon may exist in the form of gaseous $C \equiv C$ molecules, like the $N \equiv N$, $O = O$ and $H - H$ molecules of the three other ele-

ments that give rise to life. Hence we are led to believe that in the interstellar space simple biochemical compounds such as glycine and other amino acids can arise spontaneously from direct synthesis of gaseous carbon, nitrogen, oxygen and hydrogen.

2 — EXPERIMENTAL DETAILS

Prior to the description of the results of the present study let us give some information about the method employed for evaporating carbon, analysing the vapour, growing the metastable A3-type and A1-type pseudomorphic films, and determining their crystal structure, thickness and condensation rate.

Carbon was sublimated from a liquid-nitrogen-cooled boron nitride crucible (suitably covered to avoid emission of solid sparks) by using a 270°-pencil-deflection electron gun. The evaporant consisted of ultrapure microcrystalline graphite granules, obtained by thermal decomposition of tetrachloromethane.

The sublimation took place in a vacuum coating chamber, at pressures from 10^{-10} to 10^{-6} torr, on very smooth, optically polished, square-shaped alkali-zinc borosilicate glass substrates held at 3 K inside a liquid helium-cryostat. Before carbon deposition, the substrates had been degassed by baking in vacuum at 350 °C for 6 hours, cleaned by both ultrasonic agitation at 50 kHz and ionic bombardment using a glow discharge of 5 kV, and quench-coated at 3 K with a single A3-type beryllium film or a double layer consisting of a B1-type LiF base film and a metastable A1-type boron overlay.

The presence of polyatomic molecules in the carbon vapour beams impinging on the beryllium or boron film and reflected from it was found out by analysing the vapour with a mass spectrometer whose ionizer converts molecules into cations through collisions with electrons extracted from an emission filament by means of a suitable electric field that gives them an energy of about 100 eV, eight times as high as the carbon first-ionization potential, but too low to affect the adsorbed percentages of the impinging molecules: the minimum detectable pressure was lowered by using an electron multiplier, so as to register currents

as low as 10^{-17} A, corresponding to pressures of 10^{-13} torr; the angle of impingement was kept large enough to avoid a perceptible mixing of the impinging and reflected beams. The disposition of the carbon atoms according to an A3-type or A1-type arrangement like that of beryllium or boron atoms was deduced from in situ electron-diffraction patterns; the thickness and growth rate of the deposits (which ranged from 100 to 2000 Å and from 1 to 30 Å/sec, respectively) were measured with a piezoelectric quartz-crystal monitor incorporated in the cryostat.

3 — RESULTS, DISCUSSION AND CONCLUSIONS

3.1 — *Sublimation temperature and emitted vapour composition*

Table 1 gives the sublimation temperature of carbon as a function of pressure over the range from 10^{-10} to 10^{-6} torr, together with vapour pressure data quoted by Glang [6]. The temperatures were measured with an accuracy of ± 2 K, by averaging a large number of values, which, excepting some small

TABLE 1 — Sublimation temperature of carbon at various pressures.

Pressure (torr)	Sublimation temperature (K)	
	This work	Glang [6]
10^{-10}	1680	1765
2.10^{-10}	1709	
5.10^{-10}	1752	
10^{-9}	1787	1845
2.10^{-9}	1824	
5.10^{-9}	1878	
10^{-8}	1921	1930
2.10^{-8}	1962	
5.10^{-8}	2022	
10^{-7}	2072	2030
2.10^{-7}	2121	
5.10^{-7}	2184	
10^{-6}	2235	2140

196

Portgal. Phys. — Vol. 13, fasc. 3-4, pp. 193-201, 1982

irregularities, were found to be continuously distributed in Gaussian fashion about the mean. A comparison shows that, with increasing pressure, the sublimation temperature rises somewhat more sharply than that of reference [6], and is lower or higher than it according to whether pressure is below or above 2.10^{-8} torr, as results from interpolation.

The composition of the vapour emitted from the crucible is given in the second column of table 2 : the values, which refer to evaporation at 10^{-10} torr from a source at 1680 K, were determined by averaging a large number of data obtained by analysing the beam with a precision of about $\pm 0.1 \%$. Note that the vapour consists of single atoms (71.15 %) and polyatomic molecules with an even number of atoms ranging from 2 to 20 with the exception of 8, 12 and 18 (28.85 %).

TABLE 2 — Composition of carbon vapour beams impinging and reflected on beryllium or boron films at 3 K; sticking coefficient.

Molecule	Impinging beam (%)	Reflected beam (%)		Sticking coefficient		Simplest corresponding hydrocarbon
		Be	B	Be	B	
C	71.15	4.25	6.05	0.994	0.991	Methane
C_2	11.85	95.15	92.45	0.193	0.174	Acetylene
C_4	0.60	0.00	0.00	1.000	1.000	Cyclobutadiene
C_6	6.15	0.35	0.90	0.994	0.985	Benzene
C_{10}	3.95	0.20	0.35	0.995	0.991	Naphthalene
C_{14}	3.55	0.05	0.15	0.999	0.996	Anthracene
C_{16}	0.35	0.00	0.00	1.000	1.000	Pyrene
C_{20}	2.40	0.05	0.10	0.998	0.996	Benzopyrene

3.2 — *Deposit crystal structure*

Tables 3 and 4 give crystal structure data of : (1) the vapour-quenched metastable A3-type and A1-type carbon, (2) A3-type and A1-type pseudomorphs with the same lattice constants as the beryllium and boron layers, (3) A3-type and A1-type modifications with the closest-packed filling factor $\pi \sqrt{2}/6$ (corresponding to an A3-type axis ratio $\sqrt{8/3}$), (4) graphite and diamond

(which crystallize in hexagonal and A4-type phases with filling factors 0.220 and $\pi\sqrt{3}/16$, respectively) and (5) A3-type (with axis ratio $\sqrt{8/3}$) and A1-type modifications with the same density as graphite and diamond.

TABLE 3 — Lattice constants a and c and unit cell volume V at 3 K, number of atoms per unit cell, n, and density d at 3 K of: A3-type carbon deposits vapour-quenched on A3-type beryllium layers; some hypothetical A3-type carbon phases; and graphite.

Material	a (Å)	c (Å)	c / a	V (Å³)	n	d (g / cm³)
A3 deposit	2.297	3.682	1.6030	50.473	6	2.3709
A3 pseudomorph	2.278	3.572	1.5680	48.158	6	2.4849
A3 close-packed phase	1.5444	2.5220	1.6330	15.628	6	7.6571
Graphite	2.4605	6.6841	2.7166	105.133	12	2.2765
A3 phase as dense as graphite	2.3140	3.7787	1.6330	52.567	6	2.2765

TABLE 4 — Lattice constant a and unit cell volume V at 3 K, number of atoms per unit cell, n, and density d at 3 K of: A1-type carbon deposits vapour-quenched on A1-type boron layers; some hypothetical A1-type carbon phases; and diamond.

Material	a (Å)	V (Å³)	n	d (g/cm³)
A1 deposit	2.755	20.911	4	3.8151
A1 pseudomorph	2.669	19.013	4	4.1960
A1 close-packed phase	2.1841	10.419	4	7.6571
Diamond	3.5666	45.369	8	3.5169
A1 phase as dense as diamond	2.8308	22.684	4	3.5169

The values of the lattice constants of (1) and (2) are means of those of a large number of samples whose lattice constants were determined with an accuracy of approximately $\pm$ 0.1 %; those of (3) were found by calculations; those of (4) were obtained from the values at room temperature by taking into account thermal

contraction; those of (5) were deduced from (4); all values of the unit cell volume and density were calculated from the lattice constants.

A glance shows that the A3-type and A1-type deposits are less dense than would be expected for no-lattice-misfit pseudomorphic growth, much less dense than ideal closest-packed phases (where the atoms, thought of as hard spheres, are arranged so as to fill the maximum proportion of the available volume), and only 1.041 and 1.085 times as dense as graphite and diamond, respectively; whereas the theoretical closest-packing A3-to-graphite and A1-to-diamond structure filling-factor ratios are 3.364 and 2.177.

These results are not surprising, since, in spite of the constraint imposed on the overlay lattice by the beryllium-carbon or boron-carbon interatomic bonds due to van der Waals forces, the overlay and base-film lattices cannot fit, as the distance between carbon atoms must be larger than those between beryllium or boron atoms, because beryllium, boron and carbon are consecutive elements with 4, 5 and 6 electrons, respectively, and the atom size increases with the number of electrons. Owing to the opposition of the electron shell repulsion to the above constraint, the lattice constants of the A3-type and A1-type carbon layers are only almost midway between those of a no-lattice-misfit pseudomorph and those of an ideal A3-type or A1-type modification with the same density as graphite or diamond.

A comparison of the data of table 4 with those given in references [4] and [5] shows that the A1-to-A4 phase density ratio of carbon (1.085) is much less than that of silicon (1.98), germanium (2.05) and tin (1.82 to 2.08, depending on the material of the base film), which are near the closest-packed theoretical value (2.177). As to the lattice misfit, let us point out that the base-film/overlay lattice-constant difference of carbon is negative, as that of tin, whereas those of silicon and germanium are positive.

3.3 — *Reflected vapour composition*

The film growth process may be envisaged as a vapour-to-solid transformation arising from the van der Waals attraction of the

impinging vapour molecules to the substrate or growing-film surface, due to the interaction of their fluctuating dipole and quadrupole moments (associated with the instantaneous position of the electrons in the atoms) with those induced in the surface atoms, or vice versa. As a result, the vapour molecules lose their velocity component orthogonal to the surface and are physically adsorbed, but may or may not be completely thermally equilibrated. In the latter case they move over the surface by jumping from one potential well to another till they interact with other adsorbed molecules to create stable solid clusters (whose growth and coalescence are the birth stages of the film), with release of the condensation heat; or the molecules recover, because of thermal agitation, a velocity component normal to the surface and desorb into the vapour phase. The probability that an impinging molecule will be incorporated into the film is given by the sticking coefficient, which corresponds to the ratio of the amount of material condensed on the surface to the total amount impinged [7].

The composition of the vapour desorbed from the carbon overlays growing on beryllium or boron base films is given in the third and fourth columns of table 2; the corresponding sticking coefficients, found out by calculation, are given in the fifth and sixth columns. As may be seen, the impinging molecules are completely (C_4 and C_{16}) or nearly completely (C, C_6, C_{10}, C_{14} and C_{20}) incorporated into the film, with the exception of the diatomic molecules, which are reflected in the proportion of 80.7 % (beryllium base layer) or 82.6 % (boron base layer).

These data show that in ultrahigh vacuum at about 3 K the $C \equiv C$ molecule is stabler in the gaseous than in the solid phase, so that in the interstellar space there should be anywhere $C \equiv C$, $N \equiv N$, $O = O$ and $H - H$ gaseous molecules. These may react to produce glycine, other amino acids and biochemical compounds associated with life; hence the conjecture that life may originate from intersidereal matter, and therefore be distributed throughout the whole universe.

REFERENCES

[1] C. F. Bell and K. A. K. Lott, *Modern Approach to Inorganic Chemistry* (Butterworths, London, 1972), pp. 100-104.

[2] P. J. Brown and J. B. Forsyth, *The Crystal Structure of Solids* (Arnold, London, 1973), pp. 115-117.

[3] C. Reale, *Vacuum*, **32**, 245 (1982).

[4] C. Reale, *Appl. Phys. Letters*, **27**, 157 (1975).

[5] C. Reale, *Phys. Letters*, **57A**, 65 (1976).

[6] R. Glang, *Handbook of Thin Film Technology* (Eds. L. I. Maissel and R. Glang, McGraw-Hill, New York, 1970) chap. 1, pp. 16-17.

[7] K. L. Chopra, *Thin Film Phenomena* (McGraw-Hill, New York, 1969), p. 138.
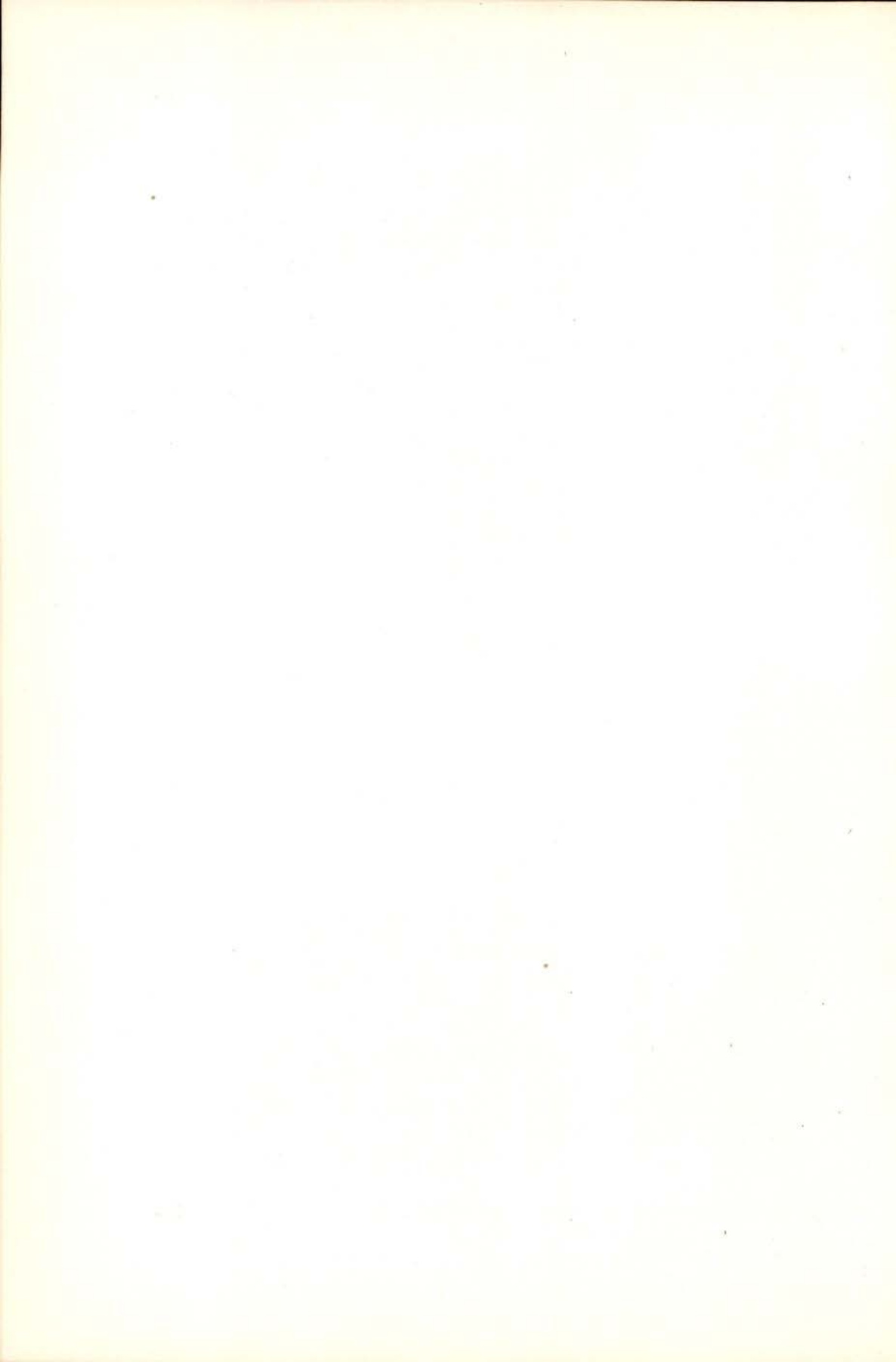
PHOTODYNAMIC EFFECTS ON THE MICROSOMAL ELECTRON TRANSPORT SYSTEM

Michael P. G. Nova and Alexandre T. Quintanilha

Membrane Bioenergetics Group, Lawrence Berkeley Laboratory
and
Department of Physiology — Anatomy, University of California
Berkeley CA 94720, U.S.A.

ABSTRACT — We studied the photodynamic action of singlet oxygen, generated by Rose Bengal bound to polystyrene beads, on the electron transport components of rat liver microsomes. The decrease in the levels of cytochrome P_{450} and in the activities of NADPH-cytochrome P_{450} reductase, NADH-cytochrome b_5 reductase and cytochrome P_{450} peroxidase during illumination ($\lambda > 400$ nm) at 10°C, was significantly greater when in the presence of Rose Bengal beads. The inactivation was enhanced when microsomes were suspended in D_2O, whereas dark controls showed no inactivation. Levels of cytochrome b_5 were not affected under any of the experimental conditions.

Sodium azide, a well known singlet oxygen scavenger, protected to varying extents against loss of activity of NADPH- and NADH-reductases, but had no significant effect on cytochrome P_{450} destruction, cytochrome P_{450} peroxidase inactivation and lipid peroxidation. Aminopyrene, a type II substrate for cytochrome P_{450}, when coupled with dithiothrietol, successfully prevented the destruction of cytochrome P_{450} and the process of lipid peroxidation, but only partially protected the reductases. Using the Nash reagent to assay for formaldehyde production, we also found evidence for singlet-oxygen, cytochrome P_{450} — mediated demethylation of aminopyrine. The antioxidant butylated hydroxytoluene successfully prevented lipid peroxidation but had no effect on the photoinactivation of cytochrome P_{450}.

1 — INTRODUCTION

The absorption of light in living organisms by endogenous or exogenous photosensitizers in the presence of oxygen causes oxidation which leads to many chemical and biological effects,

Portgal. Phys. — Vol. 13, fasc. 3-4, pp. 203-216, 1982

203

most of which are detrimental [1]. Recently, the use of photosensitizers for the destruction of cancerous tissue has received increasing attention from clinicians and photobiologists. The dye Rose Bengal is a powerful photosensitizer well known [2], [3] for its visible-light-induced generation of singlet oxygen ($^1O_2$). The short lifetime of $^1O_2$ in water ($\sim 2\mu s$) does not prevent it from destroying membranes and cells. In an aqueous suspension of membranes, Rose Bengal is usually found associated with the membrane component of the system. Since the membrane structure of microsomes is still unclear, the localization of the dye within such a system would be hard to determine. However, Rose Bengal covalently bound to polystyrene beads [4] still retains its photosensitizing properties and has already been used to photokill water-borne bacteria [5].

We have used Rose Bengal beads, as an exogenous photosensitizer, to study the photodynamic effects of visible light ($\lambda > 400$ nm) on the electron-carrying components and lipids of microsomal membranes.

Unsaturated fatty-acids and several amino acids are known to be susceptible to sensitized photooxidation even though the chemistry of such processes is not well understood [2]. Previous work [6], [7] has shown that endogenous flavins in microsomal reductases are capable of acting as photosensitizers. We have minimized this effect by working at lower temperatures and never exceeding incubation periods of 6 hours.

2 — MATERIALS AND METHODS

Chemicals: NADPH, NADH, cytochrome c, sodium azide, tryptophan, aminopyrine, dithiothrietol (DTT), butylated hydroxytoluene (BHT), tetramethyl phenylenediamine (TMPD), biphenyl, trichloroacetic acid (TCA), thiobarbituric acid (TBA), acetic acid, sodium phenobarbital and Rose Bengal were purchased from Sigma Chemical Company. Sodium dithionite was from Aldrich Chemicals. Deuterium oxide (D_2O) and Chelex 100 were purchased from Bio-Rad Laboratories.

Liver microsome preparations from phenobarbital pretreated Long Evans male rats were obtained by a previously reported protocol [8]; they were suspended in a 50 mM potassium phosphate ($pH = 7.5$) chelexed buffer and all incubations, except where otherwise noted, were carried out in this buffer. Deuterium oxide was also buffered with 50 mM potassium phosphate at an equivalent $pH \approx 7.5$.

Protein concentration was measured by the biuret method using defatted bovine serum albumin as a standard [9]. Lipid peroxidation was assayed by formation of TBA reactive material [10].

The activity of each component of the microsomal electron transport chain was followed independently of the other components; NADPH-cytochrome P_{450} reductase activity was measured using cytochrome c as an electron acceptor [11]; NADH-cytochrome b_5 reductase was assayed using ferricyanide as an electron acceptor [12]; peroxidase activity was assayed using cumene hydroperoxide as a hydrogen donor and tetramethylphenylenediamine as an electron donor [13]; cytochrome b_5 and cytochrome P_{450} were measured by difference spectra in an Aminco DW-2 dual wavelength/split beam spectrophotometer [14], [15]. Aminopyrine demethylation was determined via the production of formaldehyde [16]. Tryptophan degradation was determined by changes in the absorption difference at 279 nm - 240 nm [17].

Incubation of dark and light samples was as previously described [18]; the light source was a battery of 300 W quartz iodide lamps covered by a 400 nm cut-off filter (corning glass n.º 3389). The maximum light intensity as measured by a LI-COR LI-185 Radiometer was 17 mW cm^{-2} s^{-1}. A variable rheostat was used for variable light intensities.

Anaerobic conditions were otbained by flushing humidified N_2 over the samples before (during 2 hrs in an ice bath with occasional stirring) and during illumination; aliquots were taken with a syringe for assays. Control experiments were performed in which (a) polystyrene beads with no Rose Bengal, and (b) polystyrene beads and unreacted Rose Bengal were added during the incubations. All 2 ml samples of microsomes at 2 mg protein/ml were incubated at 10°C in a shaking waterbath. When used, 10 mg of polystyrene beads and 0.15 μmoles of Rose Bengal (either bound or not bound) were added per ml of suspension.

3 — RESULTS

The photoinactivation of the NADPH - cytochrome P_{450} reductase is shown in Figure 1.
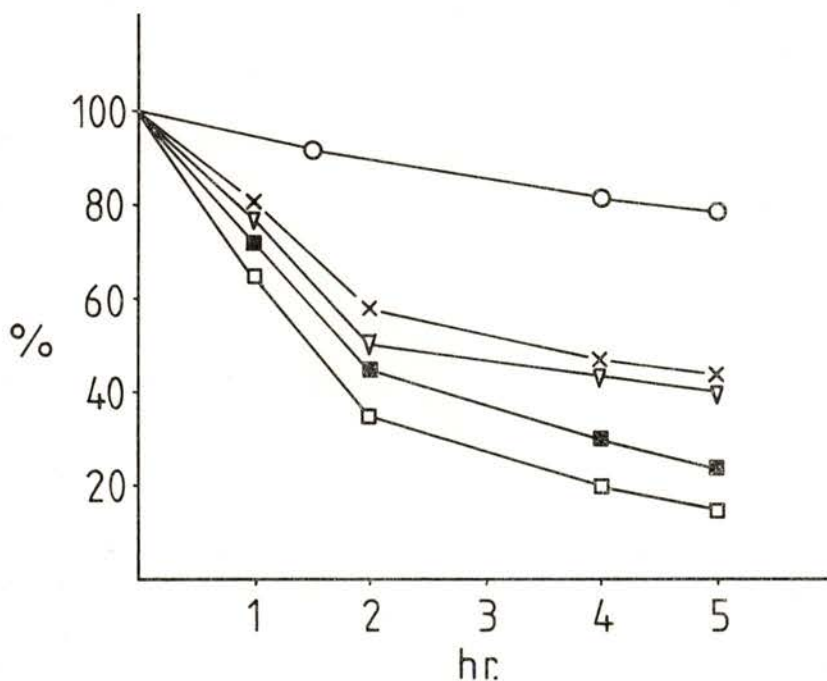
Fig. 1 — Photoinactivation of NADPH-cytochrome P_{450} reductase activity: 100 % corresponds to 164 ± 8 nmoles . min^{-1} . mg^{-1}; (O) in the absence of Rose Bengal beads. All others in the presence of Rose Bengal beads: (□) no further additions; (■) plus BHT ($10\mu M$); (v) plus azide (5mM); and (x) plus DTT (1mM).

Even in the absence of Rose Bengal beads there is some inactivation (~ 23 %) of this enzyme after 5 hrs of incubation at 10°C; in the presence of Rose Bengal beads, BHT ($10 \mu M$) affords no protection, while both DTT (1 mM) and sodium azide (5 mM) only partially protect the enzyme.

The effect of BHT, DTT and sodium azide on the photoinactivation of the NADH - cytochrome b_5 reductase is shown in Figure 2. In the case of this enzyme there is no inactivation in the absence of Rose Bengal beads and the extent of protection
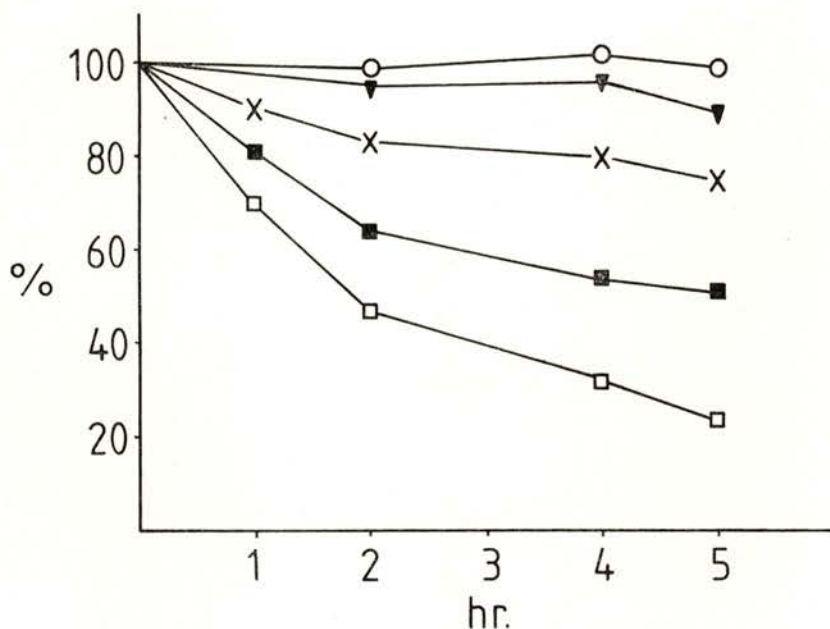
Fig. 2 — Photoinactivation of NADH-cytochrome b_5 reductase activity: 100 % corresponds to 2.7 ± 0.5 μmoles . min^{-1} . mg^{-1}; (○) in the absence of Rose Bengal beads. All others in the presence of Rose Bengal beads: (□) no further additions; (■) plus BHT (10μM); (▼) plus azide (5mM); and (×) plus DTT (1mM).

afforded by the compounds varies in the order BHT < DTT < azide with the latter protecting almost completely. Both reductases are therefore protected to varying degrees by azide and DTT while BHT only partially protects the NADH - cytochrome b_5 reductase.

The photoinactivation of cytochrome P_{450} is shown in Figure 3. Light by itself, in the absence of the photosensitizer destroys cytochrome P_{450} to some extent (~ 13 % in 5 hrs at 10°C) . In the presence of Rose Bengal beads the inactivation is far greater and is not protected by azide and/or BHT. DTT partially protects

and D_2O enhances the photoinactivation. The effects of two substrates of cytochrome P_{450}, biphenyl (1 mM) and aminopyrine (10 mM), on the photoinactivation of this enzyme were also
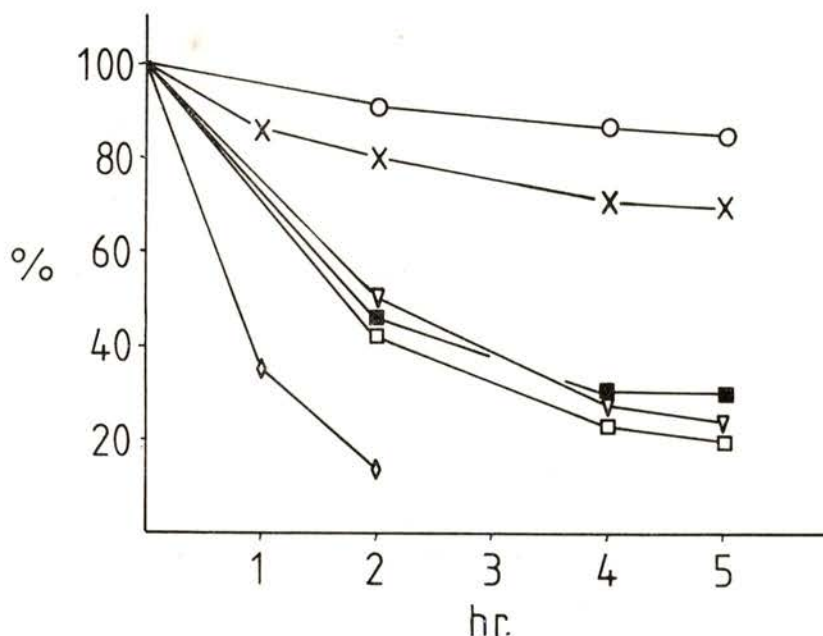
Fig. 3 — Photoinactivation of cytochrome P_{450}: 100 % corresponds to 1.4 ± 0.2 nmoles . mg^{-1}; (O) in the absence of Rose Bengal beads. All others in the presence of Rose Bengal beads: (□) no further additions; (■) plus BHT (10μM); (v) plus azide (5mM); (x) plus DTT (1mM); and (◊) in D_2O buffer with no additions.

studied. Figure 4 shows that both aminopyrine and DTT are required for complete protection of cytochrome P_{450}. By itself, aminopyrine does to some extent, whereas biphenyl does not prevent the photoinactivation of cytochrome P_{450}. Aminopyrine does not protect the photoinactivation of the reductases (data not shown).

The peroxidase activity of cytochrome P_{450} was also investigated; in this case, aminopyrine also partially protected but azide did not its photosensitized inactivation (Figure 5).
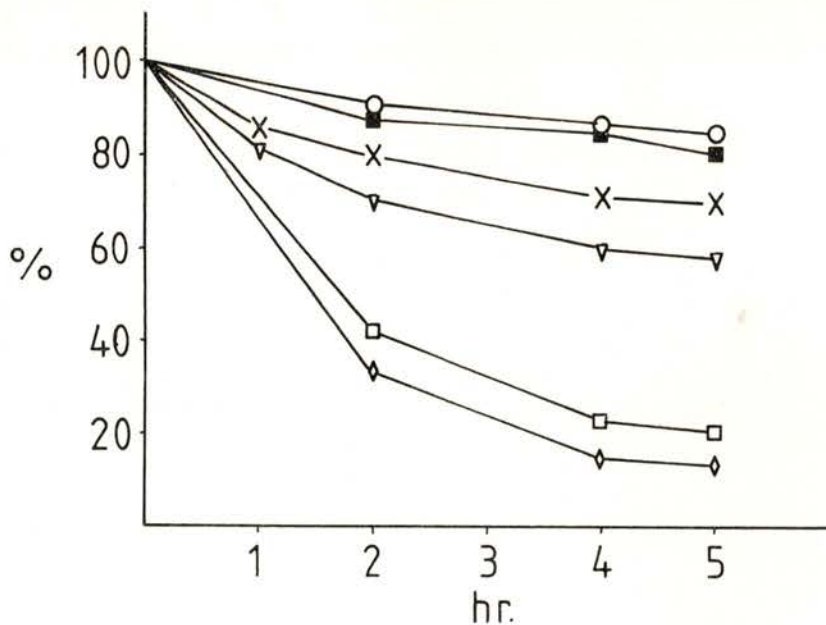
Fig 4 — Photoinactivation of cytochrome P_{450}: 100 % corresponds to 1.4 ± 0.2 nmoles . mg^{-1}; (O) in the absence of Rose Bengal beads. All others in the presence of Rose Bengal beads: (□) no further additions; (v) plus aminopyrine (10mM); (×) plus DTT (1mM); (■) plus aminopyrine (10mM) and DTT (1mM); and (◇) plus biphenyl (1mM).
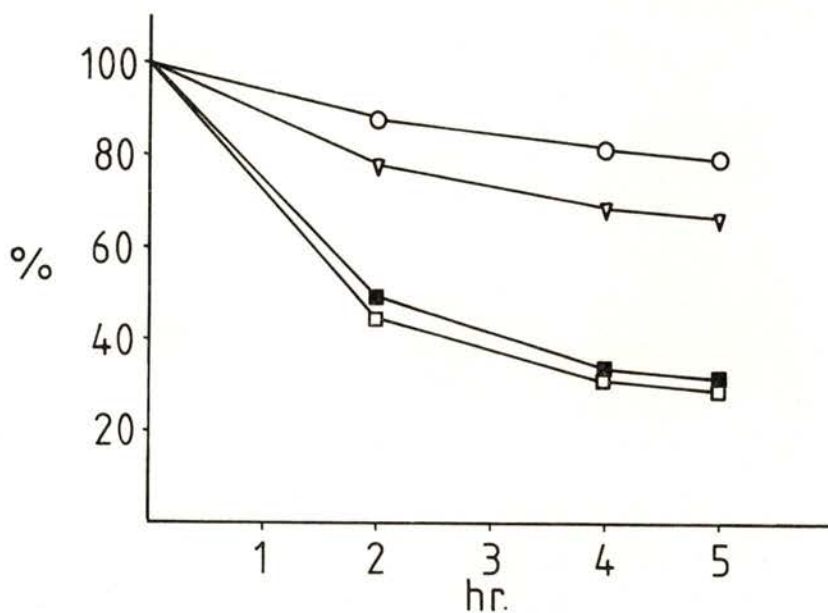
Fig. 5 — Photoinactivation of cytochrome P_{450} peroxidase activity: 100 % corresponds to 35 ± 3 nmoles . min^{-1} . mg^{-1}; (O) in the absence of Rose Bengal beads. All others in the presence of Rose Bengal beads: (□) no further additions; (v) plus aminopyrine (10mM); (■) plus azide (5mM).

Figure 6 shows the production of formaldehyde (monitored using the Nash reagent) during the illumination of microsomes in the presence of aminopyrine. Sodium azide or DTT had no effect on this mechanism. In addition, the NADPH rate of generation of formaldehyde in the dark was the same before and after the illumination of microsomes in the presence of Rose Bengal beads, DTT and aminopyrine (M. P. G. Nova, unpublished results). Formaldehyde could also be photogenerated in the presence of 10 μM haemoglobin and 10 mM aminopyrine showed an absolute requirement for Rose Bengal beads. Microsomal lipid peroxidation is
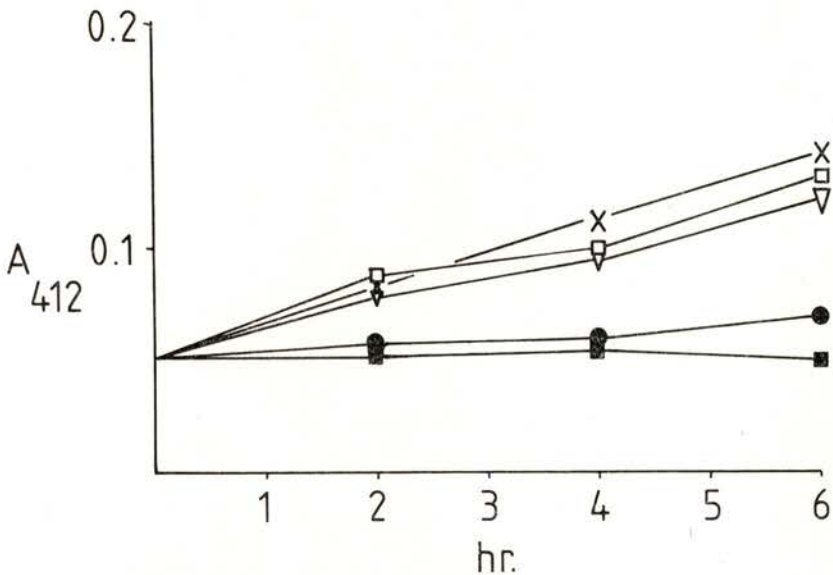
Fig. 6 — Generation of formaldehyde determined using the Nash reagent as described in Materials and Methods. Maximum rates correspond to 3.1 ± 0.5 nmoles . mg^{-1} . hr^{-1}; (■) in the absence of Rose Bengal beads and in the dark, (●) in the absence of Rose Bengal beads but in the light. All others in the presence of Rose Bengal beads: (v) no further additions; (□) plus azide (5mM); (×) plus DTT (1mM).

shown in Figure 7. Sodium azide prevents only very slightly, while DTT and BHT prevent almost completely the generation of TBA reactive material.

In the presence of unreacted Rose Bengal (0.15 mM) and polystyrene beads (10 mg/ml), at 1/3 of the light intensity (also at 10°C) the NADPH - cytochrome P_{450} reductase and the cytochrome P_{450} were inactivated by 70 % and 50 % respectively in just 1 hr, while cytochrome b_5 remained unaffected. Polystyrene beads alone did not enhance the photoinactivation.
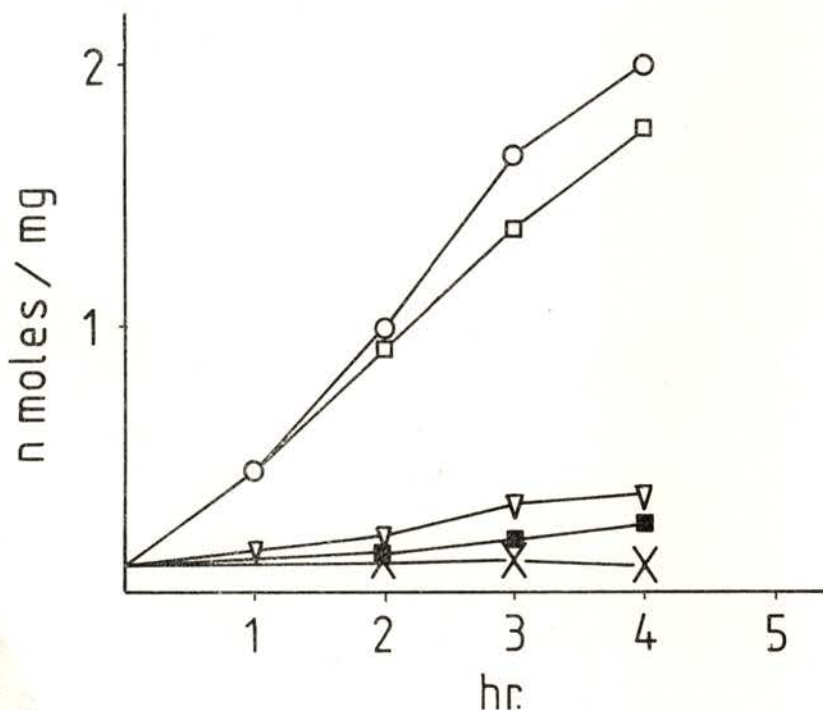
Fig. 7 — Photogeneration of TBA-reactants; (▽) in the absence of Rose Bengal beads. All others in the presence of Rose Bengal beads: (○) no further additions; (□) plus azide (5mM); (■) plus DTT (1mM); (×) plus BHT (10μM).

In the absence of oxygen, the photomediated effects on the electron transport and lipid components of microsomal membranes are abolished. Photooxidative effects are always enhanced in D_2O.

Table I shows changes in the difference between the absorbance at 279 nm and 240 nm for a 2 ml suspension of tryptophan (0.1 mM) after a 4 hr incubation at 10°C (Molar absorbance values used were 5580 at 279 nm and 1760 at 240 nm). Rose bengal beads are clearly required, and D_2O enhances the degradation of tryptophan during illumination.

TABLE I — Difference in absorption between 279 nm and 240 nm after a 4 hr incubation of tryptophan (0.1 mM) at 10°C (expressed as % of zero time value).

Dark	Light			
	H_2O (a)	D_2O (b)	H_2O+RB (c)	D_2O+RB
100 (d)	96	97	35	5

(a) H_2O — incubation in H_2O buffer
(b) D_2O — incubation in D_2O buffer
(c) RB — Rose Bengal beads (18 mg beads and 4 μmoles Rose Bengal per ml)
(d) 100 % corresponds to a value of 0.37 absorption units.

4 — DISCUSSION

The most interesting findings of the present investigation are:

a) That sodium azide, a well known scavenger of $^1O_2$, does not prevent the photodynamic action on cytochrome P_{450}, which in fact can only be fully protected by the combined presence of aminopyrine and dithiothrietol;

b) The photodynamic generation of formaldehyde when aminopyrine is added to an illuminated suspension of Rose Bengal beads and microsomes (or haemoglobin).

It is now well established that there is an important sulphydryl group near the haem of cytochrome P_{450} which contributes to the spectral characteristics of this cytochrome [19]. Dithiothrietol, a

strong sulphydryl reductant, is used as a protective agent during the isolation of cytochrome P_{450} [20] and will also, in some cases, regenerate P_{450} from its denatured P_{420} form [19]. It is not surprising therefore that dithiothrietol does afford some protection against the photodynamic inactivation of cytochrome P_{450} simply by maintaining the sulphydryl groups of the protein in the reduced state.

Substrates are also known to protect specific enzymes from denaturation and damage [21]. The reason why aminopyrine protects cytochrome P_{450} but biphenyl does not, may be due to the fact that biphenyl can only be added in a detergent solution, and detergents are well known for their denaturing action on this cytochrome [19]. Higher concentrations of biphenyl would also mean higher concentrations of detergent which would probably solubilize the membranes. Azide may not afford any protection against the photodynamic destruction of cytochrome P_{450} or the inactivation of its peroxidase activity simply because $^1O_2$ may have a higher reaction rate with cytochrome; β-carotene, one of the best $^1O_2$ quenchers [2], was not used since it also absorbs light in the visible range and would interfere with light absorption and with measurements of lipid peroxidation and cytochrome concentration. Azide does afford almost total protection to NADPH-cytochrome b_5 reductase, some protection to NADPH-cytochrome P_{450} reductase and negligible protection against lipid peroxidation. A strong correlation between lipid peroxidation and cytochrome P_{450} destruction has often been reported [22]. The fact that BHT prevents lipid peroxidation, but does not prevent cytochrome P_{450} destruction indicates that the photodynamic effect on this cytochrome is not mediated via lipid peroxidation. The varying levels of protection by azide to the different components in the microsomal system can always be explained in terms of varying reaction rates, even though we have no experimental data on such rates.

The results obtained with unreacted Rose Bengal and polystyrene beads show that the pattern of photodynamic inactivation of microsomal electron transport proteins depends largely on where the reactive oxygen species is generated. Unreacted Rose Bengal is found associated with microsomal membranes, most likely in the hydrophobic environment where the oxygen concentration is known to be higher and the life time of $^1O_2$ is longer [2];

this, and the fact that Rose Bengal in the membrane is likely to be closer to the membrane proteins, may explain the faster inactivation of the electron transport proteins observed in this case. The lack of a photodynamic effect on cytochrome b_5 is surprising, but has already been observed [6], [7].

The photodynamic demethylation of aminopyrine in the presence of microsomes or haemoglobin is interesting in so far as $^1O_2$ has often been suggested to be involved in many enzyme mediated oxidative reactions [23]-[25]. Its physiological relevance is far from being established [2], but it seems that in the presence of $^1O_2$, haemes are capable of demethylating aminopyrine. Cytochrome P_{450} is capable of accepting oxygen from a variety of donors, including hydroperoxides, hydrogen peroxide, sodium periodate and iodobenzene [26]-[31]. It may also accept $^1O_2$. On the other hand the effect could be totally unspecific, such that any haem would generate hydroxylamine oxides (in the presence of $^1O_2$ and secondary or tertiary amines) which would undergo rapid dehydration; the resulting nitrone intermediates would then liberate formaldehyde upon nonenzymatic hydrolisis. Our finding is however of sufficient importance to be reported, although a full understanding of the mechanism is still lacking.

We have no doubt that $^1O_2$ is being generated in our system. The unaerobic repression and the D_2O enhancement of all the effects (data not always shown) and the varying levels of protection afforded by azide provide strong evidence for the role of oxygen, particularly $^1O_2$ in the photodynamic damage to microsomal membrane components. Several enzymes have been inactivated by mechanisms involving $^1O_2$ [32]-[36]; unsaturated fatty acids have been photooxidized [37]-[39] to hydroperoxides [4] by mechanisms involving $^1O_2$. The possibility of generating other oxygen radicals from triplet sensitizers, such as Rose Bengal, cannot be ruled out, but electron transfer from sensitizer to oxygen leading to the superoxide ion is very inefficient [2]. In conclusion, it seems likely that the differential photodynamic effects on the components of the microsomal electron transport system are primarily singlet oxygen mediated and that further studies are required to determine the reaction rates of $^1O_2$ with the membrane components and to determine the involvement of other oxygen intermediates in the damage mechanisms.

REFERENCES

[1] H. F. BLUM, *Photodynamic Action and Diseases Caused by Light*, Hafner, N. Y., 1964.

[2] C. S. FOOTE, in *Free Radicals in Biology*, Vol. II Chpt. 3, Academic Press, N. Y., 1976.

[3] C. S. FOOTE, *Acc. Chem. Res.*, 1, 104 (1968).

[4] A. P. SCHAAP, A. F. THAYER, E. C. BLOSSEY and D. C. NECKERS, *J. Amer. Chem. Soc.*, 97, 3741 (1975).

[5] S. A. BEZMAN, P. A. BURTIS, P. J. IZOD and M. A. THAYER, *Photochem. Photobiol.*, 28, 325 (1978).

[6] O. AUGUSTO and L. PACKER, *Photochem. Photobiol.*, 33, 761 (1981).

[7] A. T. QUINTANILHA and K. J. A. DAVIES, *FEBS Lett.*, 139, 241 (1982).

[8] H. REMMIR, G. H. SCHENKMAN and R. W. ESTABROOK, in *Methods in Enzymology*, Vol. X, p. 703 (1967).

[9] A. G. GORNALL, C. J. BARDAWILL and M. M. DAVID, *J. Biol. Chem.*, 177, 751 (1949).

[10] J. A. BUEGE and S. D. AUST., in *Methods in Enzymology*, Vol. LII, p. 302 (1978).

[11] J. P. PHILLIPS and R. G. LANGDON, *J. Biol. Chem.*, 237, 2652 (1962).

[12] K. MIHARA and R. SATO, in *Methods in Enzymology*, Vol. LII, p. 102 (1978).

[13] P. J. O'BRIEN and A. D. RAHIMTULA, in *Methods in Enzymology*, Vol. LII, p. 407 (1978).

[14] R. W. ESTABROOK and J. WERRINGLOER, in *Methods in Enzymology*, Vol. LII, p. 212 (1978).

[15] W. LEVIN, A. Y. H. LU, M. JACOBSON and R. KUNZ, *Arch. Biochem. Biophys.*, 158, 842 (1973).

[16] J. WERRINGLOER, in *Methods in Enzymology*, Vol. LII, p. 297 (1978).

[17] *Handbook of Biochemistry and Molecular Biology*, Vol. I (Ed. G. D. Fasman) CRC Press, Cleveland, 1976.

[18] B. B. AGGARWAL, A. T. QUINTANILHA, R. CAMMACK and L. PACKER, *Biochim. Biophys. Acta*, 502, 367 (1978).

[19] R. SATO and T. OMURA, *Cytochrome P_{450}*, Academic Press, N. Y., 1978.

[20] D. RYAN, A. Y. H. LU and W. LEVIN, in *Methods in Enzymology*, Vol. LII, p. 117 (1978).

[21] W. J. RAY Jr. and D. E. KOSHLAND Jr., *J. Biol. Chem.*, 237, 2493 (1962).

[22] W. Levin, A. Y. H. Lu, M. Jacobson, R. Kuntzman, J. L. Poyer and P. B. McCay, *Arch. Biochem. Biophys.*, **158**, 842 (1973).

[23] O. Hayaishi and M. Nosaki, *Science*, **164**, 389 (1969).

[24] A. L. Tappel, P. D. Boyer and W. O. Lundberg, *J. Biol. Chem.*, **199**, 267 (1952).

[25] M. Hamberg and B. Samuelson, *Proc. Natl. Acad. Sci. U.S.A.*, **70**, 899 (1973).

[26] F. F. Kadlubar, K. C. Morton and D. M. Ziegler, *Biochem. Biophys. Res. Commun.*, **54**, 1255 (1973).

[27] A. D. Rahimtula and P. J. O'Brien, *Biochem. Biophys. Res. Commun.*, **60**, 440 (1974).

[28] A. D. Rahimtula and P. J. O'Brien, *Biochem. Biophys. Res. Commun.*, **62**, 268 (1975).

[29] E. G. Hrycay, J.-Å. Gustafsson, M. Ingelman-Sundberg and L. Ernster, *Eur. J. Biochem.*, **61**, 43 (1976).

[30] G. D. Nordblom, R. E. White and M. J. Coon, *Arch. Biochem. Biophys.*, **175**, 524 (1976).

[31] W. Duppel and V. Ullrich, *Biochim. Biophys. Acta*, **426**, 399 (1976).

[32] R. Nilsson and D. R. Kearns, *Photochem. Photobiol.*, **17**, 65 (1973).

[33] B. W. Glad and J. D. Spikes, *Radiot. Res.*, **27**, 237 (1966).

[34] H. Schmidt and P. Rosenkranz, *Z. Naturforsch.*, **B27**, 1436 (1972).

[35] A. Kepka and L. I. Grossweiner, *Photochem. Photobiol.*, **18**, 49 (1973).

[36] N. I. Churakova, N. A. Kravchenko, F. P. Serebryakov, I. A. Lavrov and E. D. Kaversneva, *Photochem. Photobiol.*, **18**, 201 (1973).

[37] A. Nickon and J. F. Bagli, *J. Amer. Chem. Soc.*, **81**, 6330 (1959).

[38] M. J. Kulig and L. L. Smith, *J. Org. Chem.*, **38**, 3639 (1973).

[39] A. H. Clements, R. H. Van den Engh, D. J. Frost, K. Hongenhout and J. R. Nooi, *J. Amer. Oil Chem. Soc.*, **50**, 325 (1973).

[40] B. Dowty, J. L. Laseter, G. W. Griffin, I. R. Politzer and C. H. Walkinshaw, *Science*, **181**, 669 (1973).

NON-OPTICAL SURFACE TOPOGRAPHY BY PROJECTED INTERFERENCE FRINGES

O. D. D. SOARES

Centro de Física, Universidade do Porto
4000 Porto, Portugal

ABSTRACT — Optical measurement techniques have always played an important role in precision metrology. Surface topography is a topic of great interest to science, technology and industry. Application of the technique of projected interference fringes in non-optical surface topography is described. Details and limitations of the technique are discussed. Prospects associated with the introduction of digital image processing are outlined.

1 — INTRODUCTION

In recent years several papers have been published on methods using projected fringes for various measurements on three-dimensional objects [1]-[9].

The projected fringes methods were mostly applied to problems of contouring, deformation measurement and vibration analysis. It has also been reported the application in dimensional metrology, surface inspection of parts used in mechanical engineering, and image recognition of surface defects.

In our case we were dealing with measurement of flatness of a plane surface of piston rings. The method was further tested on a dimensionally controlled cylindrical surface machined on

brass. The later results led to a more detailed examination of the method; its limitations were then established and the need for computer image processing emerged.

2 — PRINCIPLE OF THE METHOD

Fringe illumination is a spatially coded illumination of the object to obtain three-dimensional information.

Rowe and Welford [1] presented a method for the study of surface topography by projecting obliquely on a surface a set of interference fringes produced by two collimated coherent beams intersecting at an angle. The interference fringes are formed in the overlapping volume of the beams as planes parallel to the bisector of the angle, 2ϕ, between the beams. The intersection of these fringes' planes with the surface represents codified information of the surface topography.

The spatial invariance of the interference fringes means that there is no limit on the depth for application of the method, within the interfering volume of the two beams.

The fringe spacing, in principle, can have any value between $\lambda/2$ (λ being the radiation wavelength), and the major transversal dimension of the object area simultaneously illuminated by the two beams [10]. In pratice the method is applied with fringe spatial periods over a range from 1 μm to several millimeters so that the precision is variable over this range [2]. The papers quoted [1]-[9] describe methods of producing the fringes, optimum condition of use, extensions of the method and various applications. A detailed study of the method is presented in the following sections.

3 — FRINGE PATTERN CHARACTERISTICS
AND METHOD LIMITATIONS

The important features of the fringe pattern are:

   i)   Fringe visibility or contrast.

   ii) Fringe spatial frequency spectrum.

   iii) Fringe spatial orientation.

   iv) Fringe to surface topography correlation.

Fringe visibility is well studied in the scientific literature [11] in relation to its dependence on the degree of coherence between the interfering beams, the angle between the directions of polarization of the beams, and the intensity ratio of the beams. In some cases surface reflectivity can also be adjusted to enhance fringe contrast. Optimized fringe visibility should be attempted to facilitate experimental implementation and relax limitations on the viewing and recording system of the projected fringes.

The fringe frequency v for the two plane waves with normalized wave-vectors; $\mathbf{u}_1$ (u_{1x}, u_{1y}, u_{1z}) and $\mathbf{u}_2$ (u_{2x}, u_{2y}, u_{2z}), is given by [12]

$$v = (1/\lambda)\{|2(1 - u_{1x}\,u_{2x} - u_{1y}\,u_{2y}) - (u_{1z}^2 + u_{2z}^2)|\}^{1/2} \quad (1)$$

where λ is the radiation wavelength, and the z-axis was chosen normal to the surface of observation. In order to simplify the interpretation of the experimental results an incidence within a plane normal to the studied surface is assumed so that v comes

$$v = |(\sin \phi_1 + \sin \phi_2)/\lambda| = 1/d \quad (2)$$

where ϕ_1 and ϕ_2 are the angles between the beams and the normal to the surface of observation.

An equivalent formula in terms of 2ϕ, the angle between the beams, and β, the angle between the normal to the surface and the bisector of angle 2ϕ, is

$$v = 2|\sin \phi \, \cos \beta / \lambda| = 1/d \quad (3)$$

where d is again the fringe spatial period.

Experiments are performed under the assumption that it is valid to adopt expression (3), considering the angles defined through the local average normal to the surface under study and v representing the local average frequency of the fringes seen on the surface.

The spatial orientation of the fringes results from the geometry of interception of the surface under examination by

the fringe system. The fringe system is a family of parallel planes, within the interference field, equally spaced and normal to a plane parallel to the directions of the interfering beams. In a cartesian coordinate system, with the y-direction parallel to the fringe system, the object surface can be written

$$z = f(x, y) \qquad (4)$$

The set of equally spaced fringe planes is given by the equation

$$z' = (x - nd) / \operatorname{tg} \beta \qquad (5)$$

where $n = 0, 1, 2, 3...$, d is the spacing (in the x direction) of the planes, and β the angle of the planes with the z axis. The fringes on the surface are given by

$$x = f(x, y) \operatorname{tg} \beta + nd \qquad (6)$$

The analysis simplifies if the surface is assumed flat and the plane parallel to the directions of the interfering beams is normal to the surface. Thus, the fringes to surface topography correlation can be established in localized areas. If a step of height h exists, the fringe system will show a displacement

$$\Delta = h |\operatorname{tg} \beta| \qquad (7)$$

when viewed along the surface normal, Fig. 1. For $\beta = 0$ an oblique observation of the fringes on the surface must be done. This will be discussed further on. The fringe distance variation, Δ, in practice, could correspond to either a fringe interspace contraction or enlargement. This is certainly explained by the two possibilities of a down and up step surface accident. The distinction is not so simple to establish because it is relative to the direction in which the surface is explored and to the fringe illumination incidence. A possible way of giving a correct interpretation is to assume that an observer travels with the plane normal to the fringe system towards the surface under examination. If an enlargement is observed a down step has been localized. Alternatively, the fringe contraction would reveal an up step on the surface.
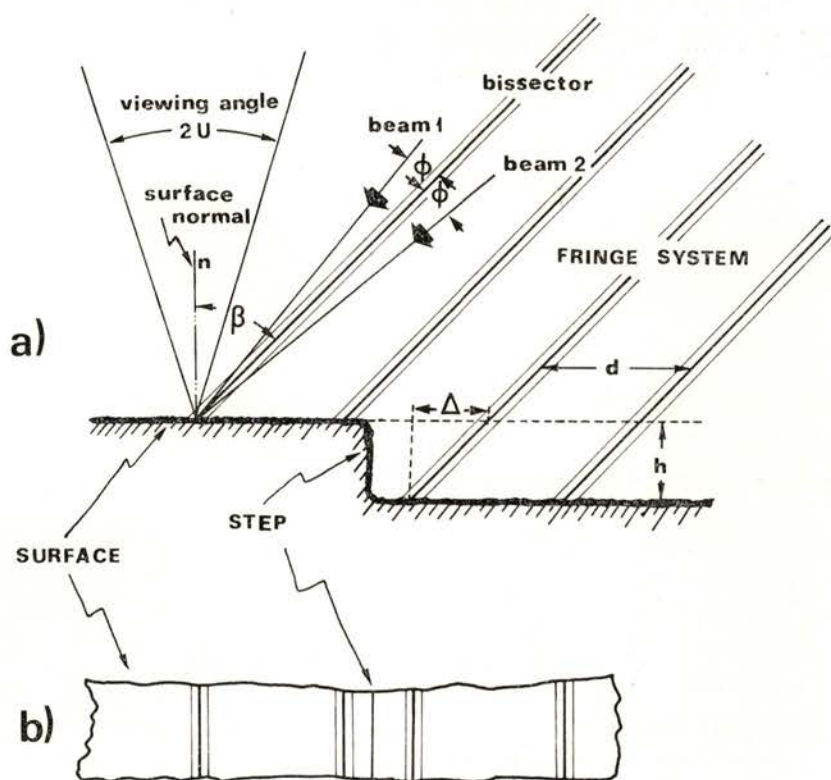
Fig. 1 — Displacement $\Delta = h \,|\, tg\,\beta\,|$ of the fringes on the surface due to a step of height h ; observation normal to the surface : *a)* Lateral view ; *b)* Top view.

The displacement Δ compares to the fringe period as

$$|\,\Delta\,/\,d\,| \;=\; 2\,|\,h\,\sin\phi\,\sin\beta\,/\,\lambda\,| \tag{8}$$

If observation is made at an angle γ (relative to the normal to the surface) the value of the recorded d_γ is then (Fig. 2)

$$d_\gamma = d\,\cos\gamma \tag{9}$$

and the fringe displacement Δ_γ comes as

$$\Delta_\gamma = h\,|\,\sin(\beta\text{-}\gamma)\,|\,/\cos\beta \tag{10}$$

It is seen that condition $\beta \neq \gamma$ should be satisfied.

The method limitations [2] in practice are imposed by the optical viewing system (microscope). The smallest fringe spacing that can be resolved by the optical system with a numerical
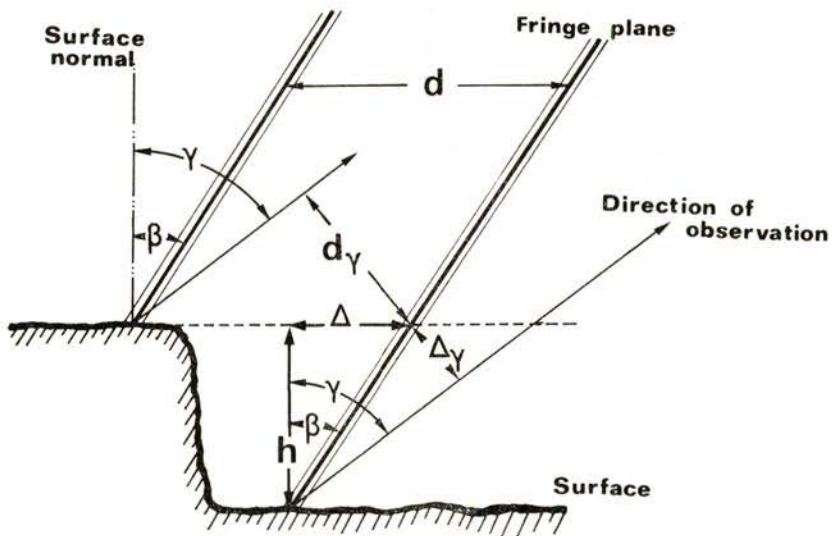
Fig. 2 — Displacement Δ_γ of the fringes on the surface due to a step of height h when observed at an angle γ.

aperture equal to $\sin U$ is $0.5 \lambda / \sin U$; the corresponding focal depth is $\pm \lambda / (8 \sin^2 U/2)$.

To resolve the fringes one should have

$$\sin U > \sin \phi \, \cos \beta \tag{11}$$

To see the fringes across a step of height h without refocusing one must have

$$\sin^2 (U/2) < \lambda / 8h \tag{12}$$

Therefore the fringes would have the lowest spatial frequency for the required purpose in order to resolve them, while ensuring fringe structure in focus throughout full depth (this also attenuates problems of vibration stability). A compromise should be sought between the two conflicting requirements, depth of field and

lateral resolution. If a depth of field $\pm h$ is desired then the smallest distance resolvable laterally is

$$[(\lambda h/2)/(1 - \lambda/8h)]^{1/2} \tag{13}$$

or, to an approximation acceptable for many purposes, $(\lambda h/2)^{1/2}$. This applies for an observing system not refocusable.

Fringe spacing has, in theory, no upper limit; but a lower limit is imposed by practical reasons as seen from Fig. 1, corresponding to $2\phi = \beta = 2U = 45°$. For $\lambda = 0.6328$ μm this gives for fringe spacing a value of 1.17 μm.

It should be noticed that the examinable area depends on the coherence of the source. For narrow fringe spacing the area has to be observed through a microscope so that coherence is not a major constraint in practice. However, the effect of speckle may impose cutting down the numerical aperture of the viewing system [2] with a spatial frequency cutoff beyond the projected fringes frequency and below the higher spatial frequencies corresponding to the speckle. The use of large fringes for the examination of large areas may be limited by the coherence of the source and could impose the use of a direct moiré technique.

The method relies on the assumption that the fringe system is a set of equidistant parallel planes. The interfering beams must then present a plane phase wavefront. In practice one should expect departures from the ideal conditions so that tolerance ranges have to be examined. In fact, a remanent angular divergence of the beam α could still be accounted for. From expression (2) it can be seen that the fringe spacing on the surface is perturbed within a range of

$$d(1 \pm \alpha/\sin\phi) \tag{14}$$

For simplicity of the analysis it was assumed $\gamma \neq \beta = 0$.
The divergence, α, should then be much smaller than

$$2(h/\lambda) \, \text{tg}\,\phi \, \sin\phi \, \text{tg}\,\gamma \tag{15}$$

a not very stringent condition in practice. A more general solution leads to the conclusion

$$|1/\sin(\phi + \alpha) - 1/\sin\phi| << (h/2\lambda)|\sin(\beta - \gamma)| \tag{16}$$

The divergence of the beams results, in practice, in a variation of the spatial frequency across the field; however, if proper care is taken, the method could still be applied.

The divergence has to be small, otherwise the fringe system will form on a curved family of surfaces adding, in general, unnecessary complexity to the problem.

From eq (10) one can easily establish the relation between the absolute errors (ε) of the quantities h, β, γ, Δ_γ:

$$\varepsilon(h)/h = \varepsilon(\Delta_\gamma)/\Delta_\gamma + \varepsilon(\gamma)|tg(\beta-\gamma)|^{-1} + \varepsilon(\beta)(tg\,\beta + |tg(\beta-\gamma)|^{-1})$$

$$(17)$$

The relative error on the measurement of h is of the same order as that obtained on the recording of Δ_γ assuming that β and γ are adequately measured (what does not present practical difficulties).
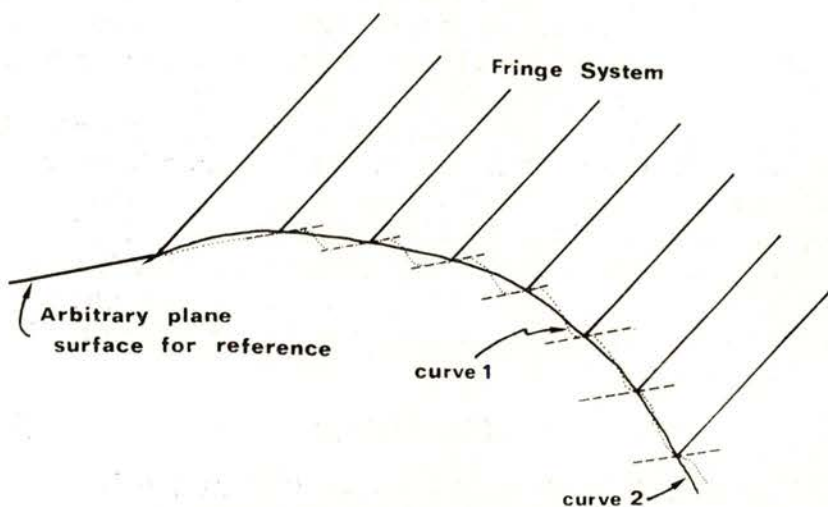
Fig. 3 — Fringe system interpretation with surface profile uncertainty resulting from a step by step method: curve 1 — step by step reading of the surface; curve 2 — real curved surface.

Another problem to be discussed relates to the process of observation of the fringes on the surface. Whether viewed directly

or photographed the fringes system suffers an anamorphic distortion which must be corrected. The photographic system, taken as example, is equivalent to a central point transformation of the points of the object photographed into the points of the plane of the photographic film. According to Fig. 2 and expression (10) the step of height h leads to a fringe spacing deviation on the photographic film Δ_γ which varies over $\delta_\gamma = U$ (Fig. 1), i.e. the range of permitted variation of the angle of observation. Care should then be taken in examining the implications of the recording geometry. Once β has been chosen to be large, γ very small and δ_γ small, this effect is negligible in most of the cases that were here considered. Alternatively a telecentric viewing system can be used. Nevertheless, for the general case, as the effect varies over the field of view it has to be compensated. This can easily be done through computer image processing techniques.

Finally, the spatial iterative character of the method leads to a step by step approximation — curve 1 of Fig. 3, of a curved surface under examination — curve 2. Therefore the localization of the step is undefined within the fringe interspacing. Such a limitation suggests the analysis of the surface by moving the fringes system over the surface (e.g. using phase modulation of one of the beams) and a computer based analysis. This constitutes one of the motivations for this work, namely the introduction of image processing techniques.

4 — EXPERIMENTAL RESULTS

The fringe system can be obtained by several methods described in detail in the literature [1], [2], [5]-[7].

The experimental arrangement we used is shown in Fig. 4. Two collimated beams intercept at a large angle (typical values, $\phi = 3°$, $\beta = 45°$) using a conventional expander, collimator, beam splitter and front surface mirror. Other types of interferometers could also be used, in particular those producing shearing of the interfering beams.

The surface under examination is placed within the beams interference volume and a microscope, with a photographic camera
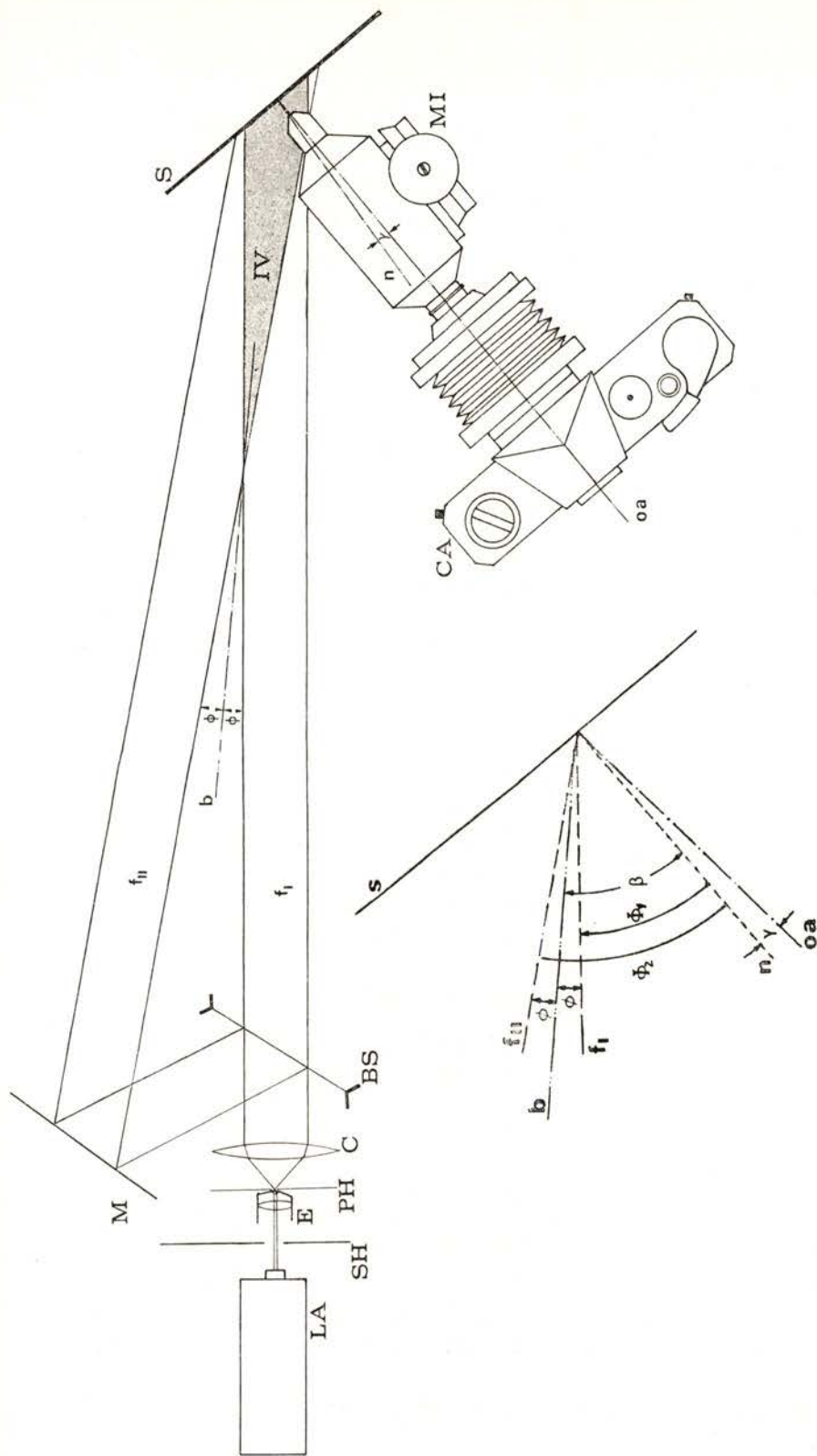
Fig. 4 — Schematic representation of the experimental arrangement: LA—laser; SH—shutter; E—expander; PH—pinhole; C—collimating lens; BS—beam splitter; M—mirror; MI—microscope; CA—photographic camera; S—surface under examination. The figure recalls also the definition of geometrical parameters.

attached, is used for viewing and recording the fringes over the surface (typical value $\gamma = 1°$).

The fringe spacing was adjusted in a range 5 μm — 16 μm. Figure 5 shows the projected fringes on the flat surface of a piston ring under study. The fringe planes distance was 8.1 μm ($\phi = 2.2°$) and the spatial period over the plane surface 11.5 μm ($\beta = 45°$); the photograph was taken along the normal to the surface ($\gamma = 0$). This image was explored using a graphic scale, Fig. 6, because the moiré technique showed very large fringes. The scale is made of parallel lines dimensionally equivalent to the fringe system over the surface and a set of small thicker traces. The edges of these traces were drawn to represent successive fringe spacing variations by one tenth of the fringe spacing. In the case illustrated a variation 'down' h = 6.9 μm on the surface relief was found. Certainly much more information is contained in Fig. 5, but it is most advisable to proceed by using a computer technique, the ultimate aim of our project; then a computed surface profile could be drawn.

5 — APPLICATIONS OF THE METHOD

The method finds application in dimensional metrology, mainly surface topography, vibration analysis [13] and contouring through combination with other techniques like moiré (in the comparison of surfaces). Changes in surface configuration either by distortion, deformation or substitution can be measured [14].

Non-destructive testing (micro-mechanics, crack and flaw detection, etc.) and the application, in a transmission arrangement, to phase objects is also considered relevant. Further, holographic recording of the fringe system on the surface and later analysis with real image projection may be of some value for some applications.

6 — CONCLUSION

A simple interference fringe projection technique has been described. It is quantitative, non-contact, requires no surface
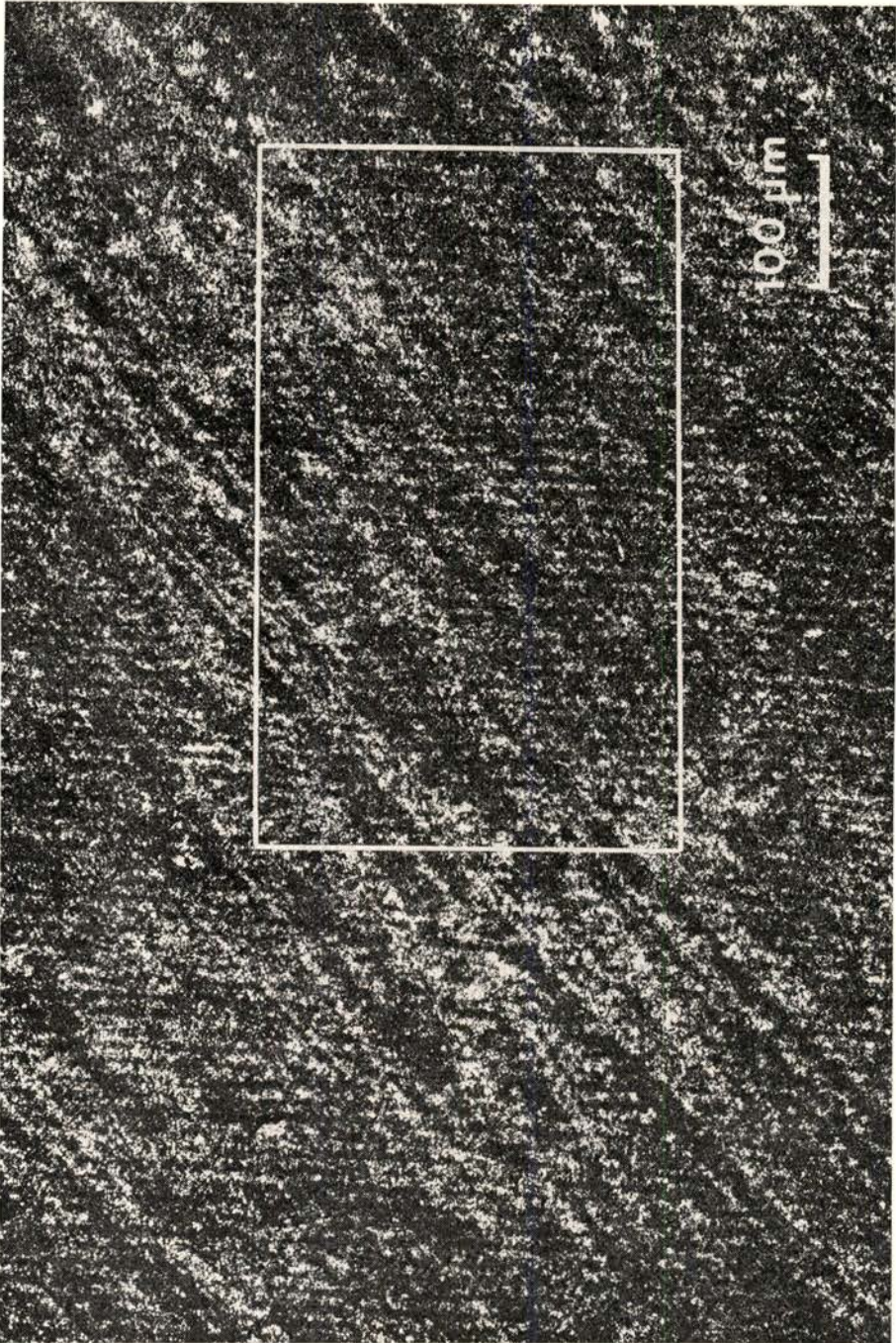
Fig. 5a — Projected fringes on a surface : general aspect of the microscopic field of view.
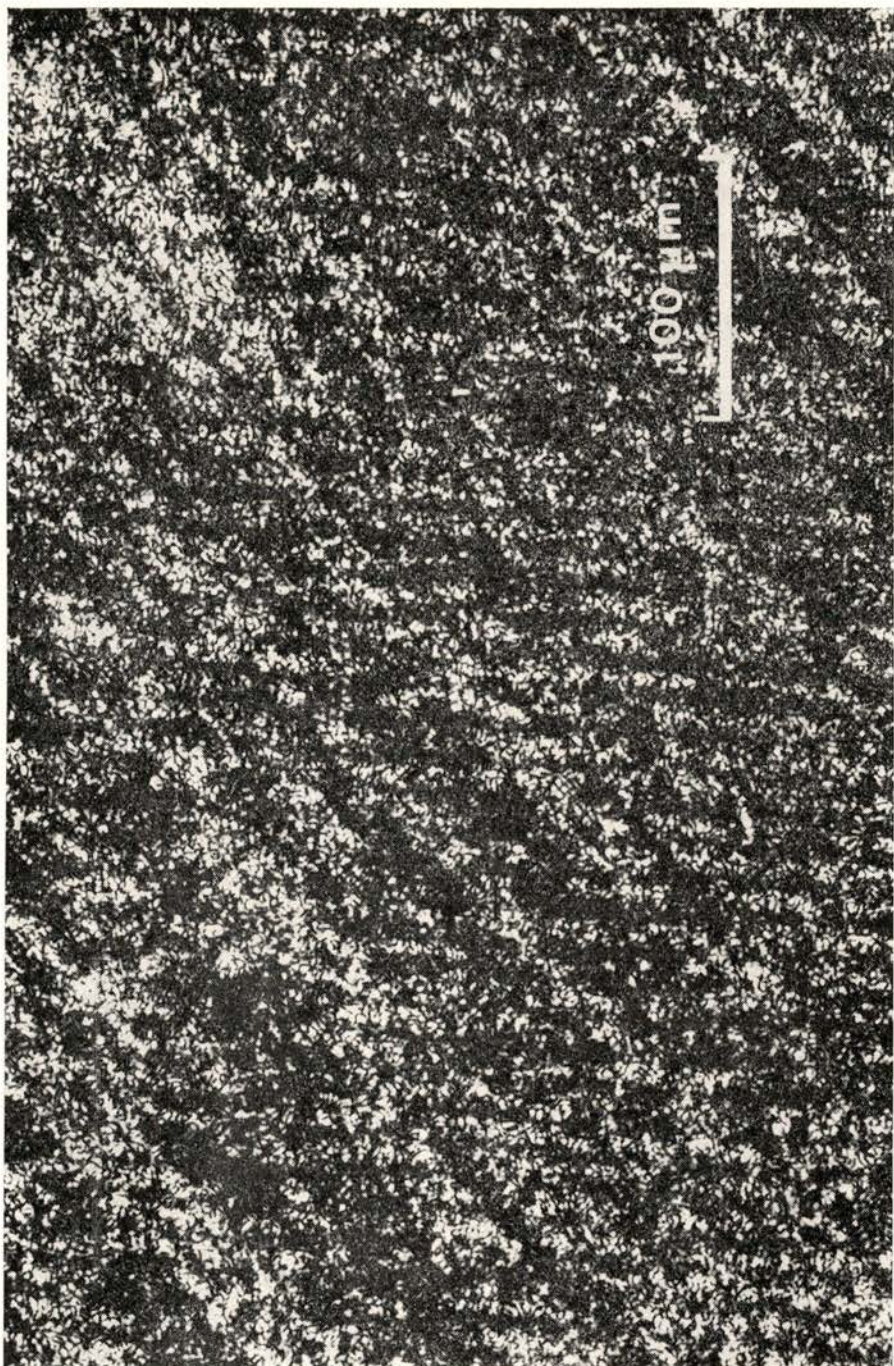
Fig. 5b — Projected fringes on a surface: enlarged detail corresponding to area marked in 5a.

preparation, is adequate for real time studies and for automatization, having a measurement sensitivity adjustable within a broad range. The fringe pattern has a simple quantitative de-
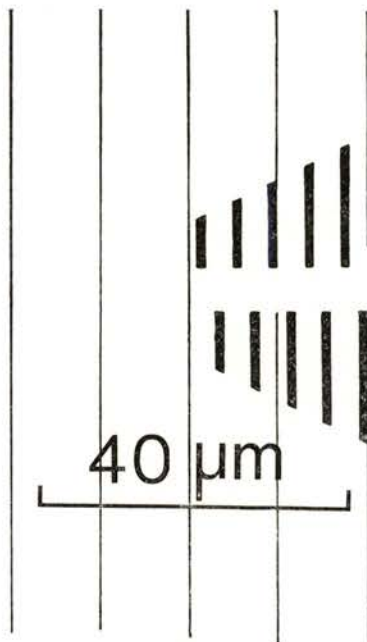
Fig. 6 — Graphic scale expressed on fringe interspacing tenths.

scription and interpretation. A detailed study of the method and its implementation revealed that result analysis must proceed by recourse to computer image processing techniques.

REFERENCES

[1] S. H. Rowe, W. T. Welford, *Nature,* **216** (1967), 786.

[2] W. T. Welford, *Optica Acta* **16** (1969), 371.

[3] S. H. Rowe, *J. Opt. Soc. Am.* **61** (1971), 1599.

[4] A. J. MacGovern, *Appl. Opt.* **11** (1972), 2972.

[5] C. G. Murphy, *ISA ASIT,* 74201 (1974), 1.

[6] P. Benoit, *Thèse,* Univ. Paris-Sud (1974).

[7] P. Benoit, E. Mathieu, J. Hormière, A. Thomas, *Nouv. Rev. Optique* **6** (1975). 67.

[8] B. Dessus, J. P. Gerardin, P. Mousselet, *Optical and Quantum Electr.* **7** (1975), 15.

[9] G. Indebetouw, *Appl. Opt.* **17** (1978), 2930.

[10] O. D. D. Soares, *Appl. Opt.* **18** (1978), 3838.

[11] K. Leonhardt, *Optik* **41** (1974), 344.

[12] O. D. D. Soares, *Thesis,* U. London (1976).

[13] P. Spicer, B. M. Watrasiewicz, *Optica Acta* **15** (1968), 521.

[14] R. E. Brooks, L. O. Heflinger, *Appl. Opt.* **8** (1969), 935.

SUR LA FORMULATION MAXWELLIENNE DE LA MÉCANIQUE DES FLUIDES INCOMPRESSIBLES

M. S. Garrido

CAUTL-INIC, BP 5176, 1704 Lisboa Codex, Portugal
Institut Maxwell, 1348 Louvain-la-Neuve, Belgique

RÉSUMÉ — Dans un formalisme maxwellien de la mécanique des fluides incompressibles on montre comme on peut passer des équations relativistes aux équations galiléennes par la conditions $c = \infty$.

ABSTRACT — Using a maxwellian formalism of the incompressible fluid mechanics, it is shown how to pass from the relativistic equations to the galilean equations by the condition $c = \infty$.

1 — INTRODUCTION

Les équations des fluides incompressibles peuvent se mettre sous une forme analogue aux équations de l'électromagnetisme, aussi bien au niveau relativiste qu'au niveau galiléen [1]: cette possibilité constitue une extension aux milieux continus de l'analogie existant entre la théorie des circuits électriques et la mécanique des solides rigides, bien connue depuis longtemps.

Dans cette Note nous allons montrer comment, dans la formulation maxwellienne de la mécanique des fluides, on passe du niveau relativiste au niveau galiléen par la condition $c = \infty$, ce passage n'étant pas aussi immédiat en mécanique qu'en électromagnetisme.

2 — ÉQUATIONS RELATIVISTES

En vue d'inclure le phénomène de gravitation et de retrouver l'équation de Newton au niveau galiléen, nous devons considérer les équations maxwelliennes de la mécanique des fluides incom-

pressibles au niveau de la relativité générale, donc dans un espace-temps dont la métrique est determinée par l'équation d'Einstein.

Ces équations ont été établies précedemment [1] et nous allons les reprendre directement.

Ainsi, on dispose en mécanique d'une loi d'Ohm, dont la forme la plus simple, valable pour des fluides peu visqueux avec des petits gradients de pression, est:

$$P^{\alpha}{}_{\gamma} \, J^{\gamma} = (\sigma/c) \, u_{\beta} \, F^{\alpha\beta} \tag{1}$$

oú $P_{\alpha\gamma} = g_{\alpha\gamma} + u_{\alpha} \, u_{\gamma}$ est le tenseur de projection, J^{γ} le quadricourant mécanique, u_{β} la quadrivitesse, $F^{\alpha\beta}$ le tenseur du champ mécanique et σ un paramêtre local dependant de la viscosité du fluide et transporté en accord avec l'équation de continuité de la matière.

Le champ mécanique $F_{\alpha\beta}$ satisfait les équations de Maxwell:

$$F^{\alpha\beta}{}_{;\,\beta} = J^{\alpha}/\varepsilon_0 \tag{2a}$$

$$F_{\alpha\beta\,;\,\gamma} + F_{\beta\gamma\,;\,\alpha} + F_{\gamma\alpha\,;\,\beta} = 0 \tag{2b}$$

où (;) represente la derivée covariante et $\varepsilon_0 = -1/4\,\pi\,x$ est une constante universelle obtenue à partir de la constante de gravitation x.

On peut introduire un quadripotentiel A^{α} tel que:

$$F_{\alpha\beta} = A_{\beta\,;\,\alpha} - A_{\alpha\,;\,\beta} \tag{3}$$

Pour un fluide incompressible, ce quadripotentiel satisfait les équations:

$$A^{\alpha\,;\,\beta}{}_{\beta} - R^{\alpha}{}_{\gamma} \, A^{\gamma} = -J^{\alpha}/\varepsilon_0 \tag{4a}$$

$$A^{\alpha}{}_{;\,\alpha} = 0 \tag{4b}$$

où $R^{\alpha}{}_{\gamma}$ est le tenseur de Ricci.

Les équations précedentes, formellement analogues aux équations classiques de l'électromagnetisme [2], doivent être comple-

tées en mécanique avec une relation reliant la quadrivitesse au champ mécanique:

$$A^\alpha = c^2 \, I \, u^\alpha \qquad (5)$$

où I represente l'indice du fluide.

L'indice du fluide est donné par [3]:

$$I = 1 + (i/c^2) \qquad (6)$$

où i represente l'enthalpie spécifique.

Si on néglige les phénomènes thérmiques, en supposant le mouvement isentropique, on a:

$$c^2 \, dI = di = dp/\rho \qquad (7)$$

où p represente la pression et ρ represente la densité de masse propre.

3 — PASSAGE À LA LIMITE GALILÉENNE

Si on se trouve dans le cadre des champs quasi-newtoniens [2], [4], le passage de l'espace-temps d'Einstein à celui de Galilée est assuré par la condition:

$$c = \infty \qquad (8)$$

Pour obtenir la notation vectorielle ordinaire dans l'espace tridimensionnel, on doit définir un potentiel vecteur $\mathbf{A}^*$ et un potentiel scalaire ϕ^*, ce que nous ferons par les composantes covariantes, en posant:

$$(A_1, A_2, A_3, A_0) = (c \, \mathbf{A}^*, - \phi^*) \qquad (9)$$

Si on fait le passage à la limite de l'équation (5), en utilisant la métrique quasi-newtonienne $ds^2 = - (1 + 2\varphi/c^2) \, c^2 \, dt^2 + (1 - 2\varphi/c^2) \, dr^2$, on obtient:

$$(c \, \mathbf{A}^*, - \phi^*) = (c \, \mathbf{v}, - \lim_{c \to \infty} c^2 I (1 + 2\varphi/c^2)^{1/2} (1 - v^2/c^2)^{-1/2}) \qquad (10)$$

où $\mathbf{v}$ represente la vitesse ordinaire et φ le potentiel de Newton.

On obtient donc:

$$\mathbf{A}^* = \mathbf{v} \quad , \quad \phi^* = c^2 I + v^2/2 + \varphi \qquad (11)$$

Portgal. Phys. — Vol. 13, fasc. 3-4, pp. 233-238, 1982

235

Nous devons remarquer que, contrairement à ce qui se passe en électromagnetisme, on obtient à la limite galiléenne $A_0 \neq - A^0$, de sorte que le choix des composantes covariantes pour introduire le potentiel scalaire n'est pas arbitraire.

En mécanique classique nous n'utilisons pas le potentiel ϕ^*, qui tends vers l'infini, mais un potentiel fini, que nous définirons par le changement de variables:

$$A = A^* = v \quad , \quad \phi = \phi^* - c^2 I = v^2/2 + \varphi \qquad (12)$$

Compte tenu de (3), ce changement implique un changement du champ mécanique $E_k^* = F_{k0}$ ($k = 1, 2, 3$), qui sera:

$$E_k = E_k^* + (c^2 I)_{,k} \qquad (13)$$

où, d'après (7), on a $(c^2 I)_{,k} \quad p_{,k}/\rho$.

La loi d'Ohm sera donc modifiée et on obtient dans le referentiel propre:

$$J_k = (\sigma/c) (E_k - p_{,k}/\rho) \quad , \quad \rho_G \quad - J_0 + \varepsilon_0 \nabla \cdot (\nabla p/\rho) \qquad (14)$$

le terme $- p_{,k}/\rho$ prennant la signification d'un champ appliqué E_k^a et ρ_G celle de la masse grave newtonienne.

On trouve dans ce changement de variables lors du passage à la limite galiéenne une deuxième différence formelle importante par rapport à ce qui se passe en électromagnetisme.

4 — ÉQUATIONS GALILÉENNES

Compte tenu des résultats précedents, on peut écrire les équations galiléennes de la mécanique des fluides incompressibles.

Si on associe à la constante universelle ε_0 une nouvelle constante μ_0 telle que $\varepsilon_0 \mu_0 = c^{-2}$, la condition (8) s'écrit:

$$\varepsilon_0 \mu_0 = 0 \qquad (15)$$

ce qui nous conduira, comme en électromagnetisme, à considérer deux limites galiléennes d'après qu'on annule ε_0 ou μ_0.

Comme en électromagnetisme, on peut introduire deux champs mécaniques **E**, **H**, auxquels on associe deux inductions mécaniques **D**, **B** telles que:

$$\mathbf{D} = \varepsilon_0 \, \mathbf{E} \qquad\qquad (16a)$$

$$\mathbf{B} = \mu_0 \, \mathbf{H} \qquad\qquad (16b)$$

La loi d'Ohm prends la forme:

$$\mathbf{J} = \sigma (\mathbf{E} + \mathbf{v} \times \mathbf{B} + \mathbf{E}^a) + \rho_G \, \mathbf{v} \qquad\qquad (17)$$

et les équations de Maxwell (2) donnent:

$$\nabla \times \mathbf{E} = - \partial \mathbf{B}/\partial t \qquad\qquad (18a)$$

$$\nabla \cdot \mathbf{D} = \rho_G \qquad\qquad (18b)$$

$$\nabla \times \mathbf{H} = \mathbf{J} + \partial \mathbf{D}/\partial t \qquad\qquad (18c)$$

$$\nabla \cdot \mathbf{B} = 0 \qquad\qquad (18d)$$

L'équation (3) donne:

$$\mathbf{B} = \nabla \times \mathbf{A} \qquad \mathbf{E} = - \partial \mathbf{A}/\partial t - \nabla \phi \qquad\qquad (19)$$

Les potentiels verifient les équations:

$$\nabla^2 \mathbf{A} = - \mu_0 \mathbf{J} \qquad \nabla^2 \phi = - \rho_G/\varepsilon_0 \qquad\qquad (20)$$

et la condition de Lorentz devient:

$$\nabla \cdot \mathbf{A} = 0 \qquad\qquad (21)$$

Aux équations précedentes, analogues à celles de l'électromagnetisme, on doit ajouter les relations (12) propres à la mécanique:

$$\mathbf{A} = \mathbf{v} \qquad \phi = \mathbf{v}^2/2 + \varphi \qquad\qquad (22)$$

Finalement, les équations doivent être completées avec l'équation de continuité de la matière qui est nécessaire, en particulier, pour determiner l'évolution du paramêtre σ.

Le formalisme galiléen obtenu a été étudié en détail préce-demment [1] et on a montré qu'il est équivalent au formalisme classique de la mécanique des fluides incompressibles, la gravi-tation comprise.

5 — CONCLUSION

Nous avons passé en revue les équation maxwelliennes de la mécanique des fluides incompressibles et montré comment on passe des équations relativistes au équations pré-relativistes.

Nous avons ignoré le niveau relativiste restreint dans la mesure où celui-ci exclu la gravitation et ne peut être consideré qu'une approximation du formalisme relativiste général lorsque la courbure de l'espace-temps est negligée.

RÉFÉRENCES

[1]   M. S. Garrido, *Técnica*, **54** (1979), 59; *Il Nuovo Cimento*, **68B** (1982), 252.

[2]   C. W. Misner, K. S. Thorne, J. A. Wheeler, *Gravitation*, ed. Freeman, 1973.

[3]   A. Lichnerowicz, *Proc. on the first Marcel Grossman meeting on General Relatively*, ed. North Holland, 1977.

[4]   L. Landau, E. Lifchitz, *Théorie des champs*, ed. MIR, 1970.

CONTENTS

FASCÍCULO 1-2

VII IBEROAMERICAN CONGRESS OF CRISTALLOGRAPHY

CONTENTS

FASCÍCULO 3-4

AUTHOR INDEX

PORTUGALIAE PHYSICA publishes articles or research notes with original results in theoretical, experimental or applied physics; invited review articles may also be included.

Manuscripts, with an abstract, may be written in English or French; they should be typewritten with two spaces and in duplicate. Figures or photographs must be presented in separate sheets and be suitable for reproduction with eventual reduction in size; captions should make the figures intelligible without reference to the text. Authors are requested to comply with the accepted codes concerning references.

There is no page charge. Author(s) will get 50 free reprints (without covers); these are to be shared among all the authors of the article. Authors interested in more reprints should say so when sending their manuscripts; quotations shall be sent with the proofs.

Subscription rates for volume 13:

> 1,700 Escudos (US$20) — individuals
> 4,250 Escudos (US$50) — libraries

PORTUGALIAE PHYSICA may also be sent on an exchange basis; we wellcome all suggestions to such effect.

All mail to be addressed to

PORTUGALIAE PHYSICA

CONTENTS